

**DAMAGE DEVELOPMENT IN THE ADHESIVE ZONE AND
MORTAR OF POROUS ASPHALT CONCRETE**

**SCHADEONTWIKKELING IN DE HECHTLAAG EN MASTIEK
VAN ZEER OPEN ASFALTBETON**

Proefschrift

ter verkrijging van de graad van doctor
aan de Technische Universiteit Delft
op gezag van de Rector Magnificus Prof. ir. K.C.A.M. Luyben
voorzitter van het College van Promoties,
in het openbaar te verdedigen op vrijdag 15 januari 2010 om 10.00 uur

door

Liantong MO

Master of Science in Materials Science & Engineering,
Wuhan University of Technology, China
geboren te Guangxi Zhuang Autonomous Region, China

Dit proefschrift is goedgekeurd door de promotor:
Prof.dr.ir. A.A.A. Molenaar
Prof.dr. S.P. Wu

Copromoter:
Dr.ir. M. Huurman

Samenstelling promotiecommissie:

Rector Magnificus,	Technische Universiteit Delft, voorzitter
Prof.dr.ir. A.A.A.Molenaar,	Technische Universiteit Delft, promotor
Prof.dr. S.P. Wu,	Technische Universiteit Wuhan, promotor
Dr.ir. M.Huurman,	Technische Universiteit Delft, copromotor
Prof.dr. S.J. Picken,	Technische Universiteit Delft
Prof.dr.ir. K. van Breugel,	Technische Universiteit Delft
Dr.ir. S.M.J.G. Erkens,	Rijkswaterstaat, DVS
Dr.ir. Z. Su,	ESHA Group bv, R&D
Prof.ir. F.S.K. Bijlaard,	Technische Universiteit Delft, reserve lid

Published and distributed by:

Liantong Mo
Road & Railway Engineering Section
Faculty of Civil Engineering and Geosciences
Delft University of Technology
P.O. Box 5048, 2600 GA Delft, the Netherlands
E-mail: l.mo@tudelft.nl, molt@whut.edu.cn, l.t.mo@hotmail.com

ISBN: 978-90-8570-444-7

Key words: Porous asphalt; Ravelling; Adhesive zone; Mortar; Fatigue damage

Printing: Wohrmann Print Service, Zutphen, the Netherlands

© 2009 by Liantong Mo

All rights reserved. No part of the material protected by this copyright notice may be reproduced or utilized in any form or by any means, electronic or mechanical, including photocopying, recording or by any information storage and retrieval system, without written context from the publisher.

I dedicate this thesis to my parents who are always proud of me and of whom I am proud.

ACKNOWLEDGEMENTS

The research described in this thesis is an integral part of the Lifetime Optimization Tool for porous asphalt (LOT project, DWW-2923) that was provided by the Delft University of Technology (TUD) to the Centre for Transport and Navigation (DVS), Dutch Ministry of Transport, Public Works and Water Management. This Ph.D research was carried out at the Laboratory of Road & Railway Engineering, TUD (65%) in cooperation with the Key Laboratory of Silicate Materials Science and Engineering of Ministry of Education, Wuhan University of Technology (WHUT), China (35%). Their support is gratefully acknowledged.

First of all, I would like to express my sincere gratitude to Prof. A.A.A. Molenaar and Prof. Shaopeng Wu, who provided me an invaluable chance to study at TUD. Without their enthusiasm and active involvement in international scientific cooperation I would not have undertaken this challenging research. Special thanks also go for their review work on my thesis. Comments and error corrections made by Prof. Molenaar are deeply appreciated.

I am very grateful to my day-to-day supervisor, Associate Prof. dr. M. Hurman, for his invaluable discussion, advice and encouragement throughout my study. I am very much indebted to him for his guidance and assistance on finite element modelling as well as data analysis. His review and comments of my manuscripts are also much appreciated.

Thanks the staff of the Laboratory of Road and Railway Engineering for their assistance while working at TUD. In particular, without the support offered by Radjan Khedoe, Jan Moraal and Jan-Willem Bientjes, the experimental work could not have been such a success. I really appreciate Milliyon Fekade Woldekidan for the perfect cooperation together in the LOT project. I benefited a lot from discussions with him. His research on mortar viscoelastic modelling made an important contribution to porous asphalt simulations. My gratitude is also given to associate Prof. Martin van de Ven for his concern and encouragement. The assistance provided by Abdol Miradi, Jacqueline Barnhoorn and Sonja van den Bos is appreciated.

I would like to thank Prof. Zhonghe Shui and Prof. Jianying Yu for providing their kind help on material testing at WHUT. My special thanks go to all staff members of Department of Road Materials at WHUT, in particular, Tingwei Cao, Yue Xiao, Quantao Liu, Jian Qiu, Gang Liu and Dongxing Xuan for the assistance with the experimental work on bitumen-stone adhesion testing, as well as many friends for their cooperation and support during my stay in Wuhan.

Dr. Lopez Arteaga at the Eindhoven University of Technology is appreciated for her comments on the tyre-pavement contact stresses that were used to simulate the STUVA loadings. Her research results play an important role on the simulation of the four STUVA mixtures. I would like to thank Dr. Christian Schulze for his great work and patience on determination of the Integral der Differenzen after different load repetitions at the STUVA APT experiment.

I would like to express my appreciation to Li Jing (as many of you may know, who was my ex-girlfriend) for what we had experienced together and her understanding and tolerance. Life is a learning process. Experiences in life teach us

new lessons and make us a better person.

I really appreciate Dr. Zhao Su, and his wife Fujin Pan, for their parent-like concern while staying in the Netherlands. Their support and encouragement helped me to overcome many difficulties during my first year in the Netherlands.

My deepest gratitude goes to my parents for their love and understanding, continuous support and encouragement. There are no words to express how much you mean to me and how much I love you. Many thanks are extended to my younger sister, Ronghua and her family for their good care of my parents when I studied abroad.

My special love goes to my wife, Xuming, for her understanding, continuous support and patience. I am lucky to have you in my life. My parents-in-law are also appreciated for their understanding and support.

Finally, I would like to thank for those who helped, encouraged and supported me in some way but not have been mentioned above by name.

A handwritten signature in black ink, appearing to read 'Liantong Mo', with a stylized flourish at the end.

Liantong Mo

Delft, 20 September 2009

SUMMARY

This research is focused on damage development in the adhesive zone and the mortar of porous asphalt concrete. The motive of this research is the loss of stone from the pavement surface, the so-called ravelling of noise reducing surface wearing courses. Ravelling is the dominant defect of porous asphalt resulting in huge costs of maintenance and resurfacing in the Netherlands. Ravelling is a mixture-associated problem and is directly related to the binding failure within the stone-to-stone contact regions. This research is thus towards a better understanding of the processes responsible for ravelling, i.e. cohesive failure in the mortar bridge and adhesive failure at the mortar/aggregate adhesive zone on the basis of meso-mechanics.

An intensive experimental program was carried out on various adhesive zones and mortars at a meso-scale of millimetres. This program was designed based on a better understanding of stress/strain states in porous asphalt concrete under moving traffic loadings. The aim was to develop fatigue/damage models for the adhesive zone and mortar which allows life expectancy to be predicted.

Tension and shear tests as well as tests in which tension and shear were combined were performed on the adhesive zones. Among these tests, uniaxial tension testing was conducted using Dynamic Mechanics Analyzer. Shear testing was performed using Dynamic Shear Rheometer. A test which combined tension and shear was specially designed. Various types of load signals were applied accounting for complex stress signals to which the adhesive zones are subjected in practice. A damage model based on a linear cumulative damage rule was used to explain the obtained test data. The proposed model is making use of the integration of an equivalent uniaxial tensile stress signal to compute the development of damage. To do this, an internal-friction theory was applied to translate any combination of shear and normal stresses into a simple equivalent uniaxial tensile stress. Model fit indicated that the predicted number of cycles to failure is in agreement with the measured data.

A practical mortar fatigue model based on the dissipated energy concept was developed for the life predictions under complex multiaxial loadings. The fatigue model is based on the initial dissipated energy per cycle. Model parameters can be determined on the basis of commonly used fatigue tests. The proposed model gave very good results in explaining the laboratory fatigue data.

By combining the mortar stress and strain signals provided by response calculations the dissipated energy per tyre passage can be calculated and the number of load repetitions to failure can be estimated using the mortar fatigue model.

The developed fatigue/damage models were applied to explain the ravelling damage of four different porous asphalt mixtures used in a full-scale accelerated pavement testing (APT) experiment. Finite element simulations of the behaviour of these four mixtures were made. A 2D idealized model was used for practical reasons. The life expectancy predicted by this way was in good agreement with the results of full scale ravelling tests.

The life time predictions as made explain the initiation of ravelling. In reality however maintenance will only be applied if ravelling has extended over a certain area and at a certain level of severity. To relate the computed life expectancy with the

actual lifespan of porous asphalt or the maintenance moment, a ravelling development model was proposed. By combining this model with the initial ravelling damage obtained from the simulations, the moment for maintenance and resurfacing can be estimated for planning pavement preservation strategies.

Finally, it was concluded that the meso-scale fatigue characterization of the adhesive zone and mortar is feasible. The developed adhesive zone damage model and mortar fatigue model together with the finite element model for the prediction of stress, strain and dissipated energy allow to arrive at a proper ranking in performance of porous asphalt mixtures. It has been shown that the developed models are very useful tools to design porous asphalt concrete with a better raveling resistance and a longer lifetime.

SAMENVATTING

Dit proefschrift beschrijft een onderzoek naar de ontwikkeling van schade in de mastiek en de hechtzone tussen mastiek en steen in Zeer Open Asfalt Beton, ZOAB, en andere typen open geluidreducerende deklagen. Rafeling, steenverlies aan het wegoppervlak, is het dominante schadebeeld van open deklagen en resulteert in een toename van verkeersgeluid. Herstel van rafeling vormt een omvangrijke jaarlijks terugkerende kostenpost. Rafeling ontstaat wanneer de hechtbruggen tussen steentjes bezwijken. Dit kan een gevolg zijn van zowel schade in de mastiek als schade in de mastiek/steen hechtzone. Rafeling is een mengsel gerelateerde schadevorm die direct verband houdt met het bezwijken van de hechtbruggen tussen steentjes. Dit onderzoek richt zich op de processen die rafeling veroorzaken - cohesief falen van de mastiekbruggen en adhesief falen van de mastiek/steen hechtzone - en maakt gebruik van meso mechanica principes.

Het onderzoek omvat een omvangrijk experimenteel programma, waarin verschillende hechtzones en typen mastiek zijn beproefd. Het betreft een experimenteel onderzoek op meso-schaal, de schaal van individuele steentjes.

Het onderzoek is gericht op interpretatie van de spanning-/reksignalen die in open deklagen onder belasting door rijdende wielen ontstaan. Daarom zijn vermoeiing-/schademodelen ontwikkeld die complexe berekende spanningsignalen als invoer gebruiken en waarmee de levensduur kan worden berekend.

Op de hechtzones zijn trek- en schuifproeven uitgevoerd. Ook proeven waarin combinaties van normaal- en schuifspanningen zijn opgelegd zijn uitgevoerd. De reeks aan proeven omvat onder andere: één-assige trekproeven op de Dynamic Mechanics Analyzer, DMA, en schuifproeven op de Dynaminc Shear Rheometer, DSR. Tevens zijn gecombineerde normaal-/schuifproeven ontworpen en uitgevoerd. De proeven zijn gedaan onder verschillende lastsignalen, dit omdat de spanningsignalen in de praktijk zeer grillig zijn. De ontwikkeling van schade in de hechtzones is beschreven met een schade-model dat gebaseerd is op de lineaire cumulatieve schaderegel. Het model bepaald schade door een equivalente trekspanning over de tijd te integreren. De equivalente trekspanning wordt bepaald met behulp van de Intern-onenigheidstheorie waarmee elke combinatie van nominaal- en schuifspanning wordt omgezet naar een equivalente trekspanning. Met regressietechnieken is aangetoond dat het model de beschikbare data goed beschrijft.

Voor mastiek is een praktisch vermoeiingsmodel ontwikkeld dat gebaseerd is op het concept van gedissipeerde energie. Met dit model worden complexe belastingsignalen vertaald in levensduur. De modelparameters kunnen worden bepaald met gangbare vermoeiingstests. Het model geeft een zeer goede voorspelling van laboratoriumdata.

Uit de combinatie van berekende spanning- en reksignalen afkomstig van mengselrespons simulaties kan de gedissipeerde energie per lastherhaling worden bepaald, zodat de vermoeiingslevensduur van mengsels berekend kan worden.

De ontwikkelde vermoeiings-/schademodelen zijn toegepast om rafelingschade in vier verschillende open asfalt mengsels te verklaren. De vier mengsels zijn in een full-scale versnelde verhardingstest beproefd. Ook zijn Eindige Elementen simulaties van de beproefde mengsels gemaakt. Om praktische reden is gebruik gemaakt van 2D

geïdealiseerde modellen. De aldus voorspelde levensduren vertoonde een grote overeenkomst met de resultaten van de versnelde verhardingstest.

De gemaakte simulaties verklaren allen het moment van schade-initiatie. In werkelijkheid echter wordt onderhand pas uitgevoerd als rafeling zich over een bepaald oppervlak en met een bepaalde ernst heeft ontwikkeld. Om een relatie te leggen tussen het moment van schade-initiatie en de werkelijke levensduur is een schade-ontwikkelingmodel voor rafeling ontwikkeld. Door dit model te configureren met het schade-initiatie-model kan het moment van onderhoud of reconstructie worden voorspeld.

Tot slot wordt geconcludeerd dat de karakterisering op meso schaal van de vermoeiingsweerstand van zowel mortel als hechtlaag zeer nuttig is. De ontwikkelde vermoeiing-/schademodellen maken een ranking mogelijk van ZOAB mengsels. Aangetoond is dat de modellen zeer bruikbaar zijn voor het ontwerp van ZOAB mengsels met een hogere rafelingsweerstand en een langere levensduur.

TABLE OF CONTENTS

1	INTRODUCTION	1 -
1.1	Problem definition	1 -
1.2	Potential causes for ravelling.....	2 -
1.3	Objectives of the research.....	3 -
1.4	Organization of this thesis	5 -
2	LITERATURE REVIEW	7 -
2.1	Introduction	7 -
2.2	Bitumen-substrate binding property	8 -
2.3	Summary of the literature review	23 -
2.4	General approach and test program	24 -
3	RAW MATERIALS	27 -
3.1	Stone.....	27 -
3.2	Fine sand and filler	30 -
3.3	Bitumen	30 -
3.4	Mortar.....	32 -
3.5	Summary	34 -
4	TEST PROGRAM & DESCRIPTION OF THE RESULTS	35 -
4.1	Introduction	35 -
4.2	Adhesive zone damage test.....	35 -
4.2.1	Introduction	35 -
4.2.2	DMA uniaxial tension test	37 -
4.2.2.1	Test description.....	37 -
4.2.2.2	Test interpretation	41 -
4.2.2.3	Test results	48 -
4.2.3	DSR shear test	49 -
4.2.3.1	Test description.....	49 -
4.2.3.2	Test interpretation	52 -
4.2.3.3	Test results	55 -
4.2.4	Combined normal-shear test.....	57 -
4.2.4.1	Test description.....	57 -
4.2.4.2	Test interpretation	60 -
4.2.4.3	Test results	60 -
4.3	Mortar fatigue test	62 -
4.3.1	Introduction	62 -
4.3.2	DSR shear test	63 -
4.3.2.1	Test description.....	63 -
4.3.2.2	Test interpretation	65 -
4.3.2.3	Test results	70 -
4.3.3	DMA dual cantilever bending test	71 -
4.4	Fatigue test on stone-mortar-stone.....	73 -
4.5	Summary and conclusions	75 -

5	INSTRUMENT CALIBRATION	- 77 -
5.1	Introduction	- 77 -
5.2	Theory	- 78 -
5.2.1	Instrument parameters	- 79 -
5.2.1.1	Mass and moment of inertia	- 79 -
5.2.1.3	Air-bearing friction	- 80 -
5.2.1.4	Compliance of clamp	- 80 -
5.2.1.5	Resonant frequency	- 80 -
5.2.1.6	Specimen force and deformation	- 81 -
5.2.2	Shape factors	- 84 -
5.2.2.1	Introduction	- 84 -
5.2.2.2	Bitumen films	- 85 -
5.2.2.3	Cylindrical torsion	- 86 -
5.2.2.4	Steel strip	- 86 -
5.3	Calibration	- 87 -
5.3.1	Standard parallel plates	- 88 -
5.3.2	Cylindrical torsion	- 94 -
5.3.2.1	Introduction	- 94 -
5.3.2.2	Results and discussion	- 97 -
5.3.2.3	Rectangular torsion	- 101 -
5.3.2.4	Dual cantilever bending	- 105 -
5.3.2.5	Correlation between DSR and DMA instruments	- 107 -
5.4	Data correction	- 112 -
5.5	Conclusions	- 116 -
6	ADHESIVE ZONE DAMAGE MODEL	- 125 -
6.1	Introduction	- 125 -
6.2	Damage model	- 125 -
6.2.1	Failure criterion	- 125 -
6.2.2	Fatigue damage under regular signals	- 131 -
6.2.3	Damage accumulation model for complex signals	- 134 -
6.3	Model parameter determination and model verification	- 141 -
6.3.1	Introduction	- 141 -
6.3.2	Model parameter determination	- 143 -
6.3.3	Model verification	- 147 -
6.4	Observations on the basis of the model	- 148 -
6.4.1	Temperature dependence of model parameters	- 148 -
6.4.2	Model interpretation on effects of aging, water and type of stone	- 152 -
6.4.3	Failure mechanisms	- 155 -
6.5	Conclusions	- 157 -
7	MORTAR FATIGUE MODEL	- 159 -
7.1	Introduction	- 159 -
7.2	Multiaxial fatigue failure	- 159 -
7.2.1	Energy criteria	- 159 -
7.2.2	Hysteresis energy criteria	- 160 -

7.3	Mortar multiaxial fatigue model.....	162 -
7.4	Mortar fatigue results	165 -
7.5	Determination of model parameters	167 -
7.5.1	Initial dissipated energy per cycle	167 -
7.5.2	Mean dissipated energy per cycle	169 -
7.5.3	Practical mortar fatigue model.....	173 -
7.6	Conclusions	174 -
8	MODEL APPLICATION & VERIFICATION	175 -
8.1	Introduction	175 -
8.2	Finite element simulation	176 -
8.2.1	Geometry	176 -
8.2.1.1	Structural geometry of porous asphalt	176 -
8.2.1.2	Simplified structural geometry for simulations	177 -
8.2.1.3	STUVA mixtures and simulations.....	179 -
8.2.2	Loading.....	180 -
8.2.2.1	LOT Loading	180 -
8.2.2.2	STUVA Loading	181 -
8.2.2.3	New insights into STUVA loading.....	181 -
8.2.2.3	Determination of new model loading	184 -
8.2.3	Material properties.....	185 -
8.2.3.1	Mortar response	185 -
8.2.3.2	Adhesive zone Response	188 -
8.3	Material fatigue and damage models	188 -
8.3.1	Mortar fatigue model	188 -
8.3.2	Adhesive zone damage model	189 -
8.4	Results and discussions	190 -
8.4.1	Life estimation based on adhesive zone damage	191 -
8.4.2	Life estimation based on mortar fatigue	194 -
8.4.3	Causes of ravelling	198 -
8.4.3.1	Adhesive failure vs cohesive failure.....	198 -
8.4.3.2	Effect of void content	200 -
8.4.4	Ravelling damage prediction	201 -
8.4.5	Prediction of lifespan and the maintenance moment	203 -
8.4.5.1	Ravelling evolution in real pavements.....	204 -
8.4.5.2	Ravelling evolution model.....	205 -
8.5	Conclusions	210 -
9	CONCLUSIONS & RECOMENDATIONS	213 -
9.1	Introduction	213 -
9.2	Conclusions	213 -
9.2.1	Conclusions related to experimental work.....	213 -
9.2.2	Conclusions related to fatigue/damage models.....	213 -
9.2.3	Conclusions related to model application and verification	214 -
9.3	Recommendations	214 -
9.3.1	Recommendations related to experimental work.....	214 -

9.3.2	Recommendations related to fatigue/damage models.....	- 214 -
9.3.3	Recommendations related to model application and verification.....	- 215 -
References	- 217 -

LIST OF USED SYMBOLS AND ABBREVIATIONS

Symbols

a_T	= the temperature shift factor
A	= model constant
b	= model constant
C_1, C_2	= model constants
d	= the equivalent grain diameter, [mm]
d_s	= the distance between stones, [mm]
D	= the accumulated damage
\dot{D}	= the damage rate, [s^{-1}]
ΔE_a	= the apparent activation energy, [J/mol]
E	= Young's modulus, [MPa]
E_0	= the instantaneous stiffness, [MPa]
f	= frequency, [Hz]
f_c	= location parameter, [Hz]
f'	= the reduced frequency, function of temperature, [Hz]
f_n	= the natural frequency, [Hz]
F	= force, [N]
F_0	= force amplitude, [N]
G	= shear modulus, MPa or torsion stiffness, [N.m/rad]
G^*	= complex modulus, [Pa]
G_e^*	= the equilibrium complex modulus, [Pa]
G_g^*	= the glass complex modulus, [Pa]
h	= the gap width between two parallel plates, [mm]
h_{eff}	= the specimen effective height, [mm]
I	= moment of inertia, [N.m.s ²]
IDD	= Integral der differenzen, [mm]
J	= clamp compliance, [rad/(N.m)]
K	= the stiffness of beam, [N/m]
k_1, k_2, k_3	= the factors
k_n	= the normal stiffness of the adhesive zone, [MPa/mm]
k_s	= the shear stiffness of the adhesive zone, [MPa/mm]
l	= the effective length of the solid rectangular sample, [mm]
Lft	= serve life, [year]
M	= the mass of weight, [Kg]
m_e	= shape parameter
n	= model constant
N	= number of cycles
N_f	= number of cycles to failure

r	= specimen radius, [mm]
R	= universal gas constant, 8.314 J/(K.mol)
R_a	= the arithmetic average of the absolute values of surface deviations, [μm]
R_q	= the root mean square average of height deviation, [μm]
Raf	= percentage of ravelling, [%]
t	= the thickness of the solid rectangular sample, [mm]
t	= time, [s]
t_1, t_2	= time constants, [s]
T	= torque, [N.mm]
T_0	= torque amplitude, [N.m]
T_{raw}	= raw torque that is applied by machine, [N.m]
T_{sample}	= torque in sample, [N.m]
T_I	= torque induced by moment of inertia, [N.m]
T_μ	= torque induced by air-bearing friction, [N.m]
T_0	= reference temperature, [K]
T	= test temperature, [K] or [$^{\circ}\text{C}$]
w	= the width of the solid rectangular sample, [mm]
W_{total}	= the sum of hysteresis loop areas from the nine stress components, [MPa]
W_0	= the energy limit, [MPa]
$W_{initial_cycle}$	= initial dissipated energy per cycle, [MPa]
x	= displacement, [mm]
Z	= model constant
α_1, α_2	= stiffness reduction parameters
σ	= tensile stress, [MPa]
σ_0	= the nominal strength that material will fail within a second, [MPa]
σ_e	= the equivalent tensile stress, [MPa]
σ_n	= normal stress, [MPa]
σ_{ij}	= stress components, [MPa]
ε_{ij}	= strain components
τ	= shear stress, [MPa]
τ_0	= amplitude of shear stress, [MPa]
τ_1	= the longitudinal shear components, [MPa]
τ_2	= the transverse shear components, [MPa]
γ	= shear strain
γ_0	= the amplitude of shear strain
β_0, β_1	= model constants
θ	= radial deflection angle, [rad]
θ_0	= amplitude of radial deflection angle, [rad]
θ_{raw}	= raw radial deflection angle, [rad]

δ	= the phase lag between stress and strain in sample, [°]
φ	= the raw phase lag between displacement amplitude and torque amplitude, [°]
ϕ	= the internal friction angle for adhesive zone damage model, [°]
Ψ	= material parameter
ν	= Poisson's ratio
ω	= angle velocity, [rad/s]

Abbreviations

1D	= One-Dimensional
2D	= Two-Dimensional
3D	= Three-Dimensional
APT	= Accelerated Pavement Test
DMA	= Dynamic Mechanical Analyzer
DSR	= Dynamic Shear Rheometer
LB	= Long-term aged Bitumen
LM	= Long-term aged Mortar
LOT	= Lifetime Optimization Tool
SB	= Short-term aged Bitumen
SM	= Short-term aged Mortar
STUVA	= Research Association for Underground Transportation Facility, Germany
TUD	= Delft University of Technology
WHUT	= Wuhan University of Technology

1 INTRODUCTION

1.1 Problem definition

Unlike traditional dense-graded asphalt mixes and gap-graded stone mastic asphalt, porous asphalt is an open-graded asphalt mixture. Its aggregate gradation consists of a large amount of coarse aggregates combined with a small amount of fine materials resulting in a very open structure. After laying and compaction, porous asphalt concrete typically has an air void content higher than 20% by volume. As a result, a large amount of interconnected voids or pores is created, which are essential to the fundamental functions of porous asphalt, i.e. noise reduction, water drainage as well as driving safety in wet weather [Elvik & Greibe 2005; Nielsen 2006].

Porous asphalt was firstly applied on the Dutch primary road network in the early eighties and in 1987 it was decided to start applying porous asphalt wearing courses on a larger scale in the Netherlands. The application on the Dutch primary road network has increased rapidly and nowadays close to 90% of the primary road network has been surfaced with this type of wearing course. Noise reduction, driving comfort and driving safety in wet weather are obvious reasons for this extensive application. The road user satisfaction with porous asphalt is forcing a change in attitude and will lead to a general application in the future [van der Zwan, Goeman et al 1990; Swart 1997].

Durability of porous asphalt has been a matter of concern due to its open mix design. Among other durability issues, the loss of stone from the pavement surface (see Figure 1.1), so-called ravelling, is the dominant defect resulting in frequent road maintenance and thus in reduced road network availability [van der Zwan, Goeman et al 1990; Swart 1997; Miradi 2004; Miradi & Molenaar 2006]. The average life span of porous asphalt on the slow lanes of Dutch motorways is currently about 10-12 years. Compared to dense asphalt mixtures that have a service life of approximately 18 years, the service life of porous asphalt is limited.

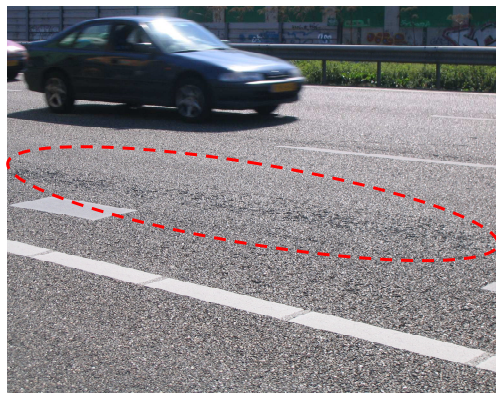


Figure 1.1 Ravelling damage on porous asphalt surface wearing courses

Ravelling occurs on the pavement surface due to traffic and environmental loadings. Therefore, it is much more a problem of material damage rather than structural damage, i.e. typical fatigue cracking that initiates at the bottom of asphalt layer and then propagates gradually upwards to the surface. This means that conventional pavement structural design, i.e. giving strength to the pavement by increasing the structural layer thickness, can not prevent this type of pavement distress. Ravelling is in fact a type of failure that finds its cause within stone-to-stone contact regions. Therefore, it is more likely to be a mixture-associated problem and thus information about the mechanical behaviour of the related material components in the stone contact region is of great importance for ravelling investigation. Apart from this, the states of stress/strain in the material components under moving traffic loadings are also of importance. By combining these two factors, better insight into ravelling resistance can be obtained.

1.2 Potential causes for ravelling

It is believed that ravelling is related to binding failure within the stone contact region. Therefore, the potential types of failure in stone contact regions must be considered. It is known that the coarse stone fraction in porous asphalt is bonded in small localized regions, referred as stone-to-stone contact regions earlier. As schematically indicated in Figure 1.2, a typical contact region may consist of three components including an interface, an adhesive interlayer and the mortar. The interface is formed by direct adhesion between the aggregate and the bitumen. A bit further from the aggregate surface the bitumen forms a very thin adhesive interlayer that binds the smaller mineral particles in the mortar to the bitumen covered coarse stone surface. Such a bituminous interlayer is believed to exist because edge effects prevent the larger mineral particles in the mortar to be present in this interlayer. Definition of this bituminous interlayer would be difficult. However, it is known from theory that this bitumen-rich interlayer must be very thin and may only contain a limited amount of very fine mineral particles. Even further away from the stone surface the third component is distinguished, i.e. pure mortar consisting of fine sand, filler and bitumen.

At meso-scale, ravelling is directly related to the performance of the material components within the stone contact region. Failures may occur in the interface, the bitumen-rich interlayer and in the mortar, which are further described as follows:

- (1) Interfacial failure (adhesive failure) - this is purely debonding at the stone-bitumen interface. The stone surface is separated completely without bitumen binder remaining on its surface.
- (2) Cohesive failure through the bitumen-rich interlayer - this implies that bonding fracture occurs very close to stone surface and the fractured surfaces are still coated with bituminous material after failure.
- (3) Cohesive failure through pure mortar - this implies that the location of fracture is not close to stone surface; the fractured surfaces are coated by mortar.

Failure might also happen through the stone particles if an internal crack already exists. However, the probability of such a failure is believed to be fairly small and is thus not taken into account in this study. The type of failure that will lead to ravelling

damage depends on the mechanical behaviour of the material components (response, strength/fatigue) and mixture geometry and loading. It should be clear that failure will firstly happen in the weakest link of the local materials mentioned above. Figure 1.3 shows that failure types 2 and 3 as described previously really occur in practice. As observed, pure interfacial failure is not predominant, while cohesive failure in the bitumen-rich interlayer or pure mortar is important issues leading to ravelling.

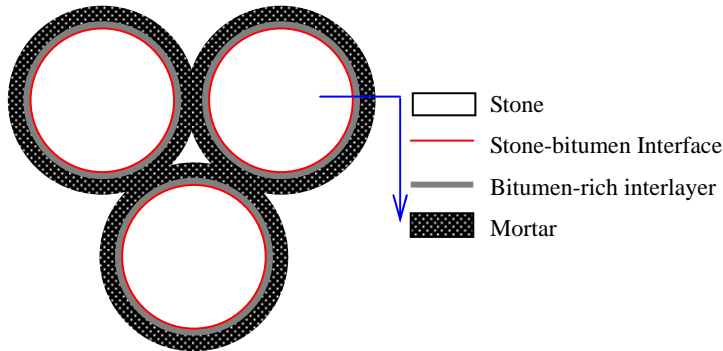


Figure 1.2 Schematic illustration of idealized grain-grain contact model



Figure 1.3 Ravelled coarse aggregates indicate the type of failure

1.3 Objectives of the research

This Ph.D research is an integral part of research project “Lifetime Optimization Tool of Porous Asphalt”, which is called the LOT project for short hereafter. The LOT project, which was commissioned to the Road and Railway Engineering Group of the Delft University of Technology by the Dutch Ministry of Transport in 2007, aimed for the development of a meso-mechanical tool that gives insight into the phenomena that take place in porous asphalt mixes when subjected to moving tyre loads. By

application of finite element modelling, the model basically translates the tire-pavement contact loads, mixture geometry and mortar response into signals of stress/strain at various locations within the mixture. The life expectancy of porous asphalt is estimated by interpretation of the in-mixture stress/strain signals. More information on the LOT project can be found elsewhere [Huurman 2008]. Figure 1.4 gives a simplified schematic of the LOT design strategy. At the end, LOT predicts the type of failure that results in ravelling and the number of tire passages that are required to cause this type of failure. It also provides information on which material component properties should be changed to achieve a better ravelling resistance.

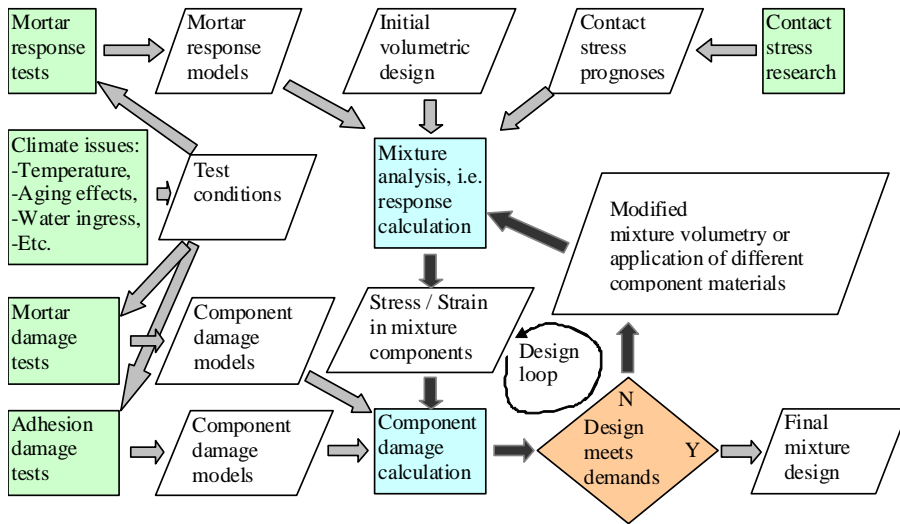


Figure 1.4 Simplified schematic of LOT design strategy[Huurman 2008]

The LOT project consists of the following parts: laboratory tests, mortar response models, component damage models, numerical simulations of porous asphalt and in-door accelerated ravelling tests. In this Ph.D research, the focus is on damage models for the mortar and the adhesive zone. Hereafter, the mortar is referred to the mixture consisting of fine sand, filler and bitumen; the adhesive zone is defined as the region where the mortar meets the stone surface. As discussed earlier, such an adhesive zone includes the bitumen-stone interface plus the bitumen interlayer, thus two potential types of failure can be investigated. In this study, the adhesive zone is represented by using two stone columns bound together by a very thin bitumen layer with a thickness of 15 μ m.

As stated, the LOT project focused on the meso-scale structure consisting of stone chippings. It is common practice to characterize the fatigue resistance of asphalt mixture on, e.g. beam specimens. Such a macro scale approach however is not good enough for analyzing the ravelling resistance of porous asphalt mixtures. Fatigue characterization on meso-scale implying the fatigue characterization of the mortar and the adhesive zone is required. Therefore, new set-ups that allow meso-scale fatigue testing have to be developed.

Finite element simulations on road surfacing seals and porous asphalt indicated that the adhesive zone is subjected to a complex combination of shear and normal stresses [Huurman, Milne et al 2003; Huurman, Mo et al. 2007; Mo, Huurman et al. 2007, 2008]. Furthermore the stress signals due to the moving tyre loadings are complex. Therefore, a damage model that takes into account the combined action of normal and shear stresses as well as the complex stress signal is needed for the adhesive zone.

With respect to the mortar, the traffic loads create complex 3D states of stress and strain, which change from one location to another within the mixture [Huurman, Mo et al. 2007; Mo, Huurman et al. 2007, 2008]. Meanwhile, there is no predominant stress or strain component that accounts for mortar fatigue; the stress/strain signals are complex and far from sinusoidal as commonly applied in classical fatigue tests. By combining these factors, it is clear that mortar fatigue in this study is a problem of multiaxial fatigue under complex stress/strain signals. A mortar fatigue model that is capable to explain such stress/strain states is thus required.

As an integral part of the LOT project, the developed fatigue or damage models in this research will be combined into a design tool for porous asphalt (see Figure 1.4).

For the purpose of model verification, full scale ravelling test sections were conducted in Cologne, Germany [van Hinthem 2008; RWTH 2007; Huurman, Molenaar et al. 2008]. The entire tool is validated by comparing the computed life with the ravelling behaviour as observed in the accelerated pavement test (APT).

1.4 Organization of this thesis

This thesis consists of three parts: an experimental part, a part in which fatigue or damage models are developed and a model application and verification part.

After this introductory chapter, Chapter 2 presents a literature review on the binding properties of bitumen-aggregate systems. Chapter 3 briefly introduces the materials used in this study including stone, fine sand, filler, bitumen and mortar.

Material testing for the development of the fatigue/damage models for the adhesive zone and the mortar is described in the next chapter. Information on the test description, test interpretation and the obtained results is presented there too.

Chapter 5 provides information on the calibration of various test instruments used in this study. Differences in the data produced by different instruments are thus understood, allowing to minimize their effects. Data correction is carried out and the loss of accuracy due to improper test interpretation in the LOT project is investigated.

The development of the damage model for the adhesive zone is discussed in Chapter 6. For reasons of simplicity, the proposed model is making use of a linear cumulative damage rule to explain the damage behaviour of the adhesive zone in combination with the internal-friction theory.

In Chapter 7 mortar fatigue models based on the concept of dissipated energy are presented. The initial dissipated energy per cycle and the total dissipated energy are used as the fatigue damage parameter. A practical mortar fatigue model that is capable of translating complex multiaxial loadings into life expectancy is given.

In Chapter 8 the model predictions are compared with the actual ravelling that developed during the APT and which was measured by means of laser texture

measurements and determined by means of visual inspection performed after completion of the APT.

Finally, conclusions and recommendations are given in Chapter 9.

2 LITERATURE REVIEW

2.1 Introduction

Bitumen serves as binder for mineral aggregates in bituminous paving mixtures. Bitumen is present in bituminous mixtures in the form of a thin film with various thicknesses around the aggregate particles. As a binder, bitumen sticks to the aggregate surfaces, thus bitumen-stone adhesion is defined at their boundaries. Bitumen in thin films has properties that differ from those of the bulk bitumen.

Furthermore, fine aggregates and filler can be regarded as part of the binder phase. In this study, the mixture containing fine aggregates, filler and bitumen is defined as mortar; the mixture that only consists of filler and bitumen is called mastic. The critical size that divides the contribution of fine fraction into part of binder or aggregate skeleton is dependent upon type of mixture. Muraya (2007), in his study concluded that for porous asphalt concrete, all aggregate particles smaller than 0.5mm, i.e. fine sand, belong to the mortar.

The introduction of the fine fraction and filler usually changes the rheological properties and improves the stiffness and the toughness of the binder phase. Addition of these materials sometimes imparts drawbacks to the resulting composites such as making them brittle.

In asphalt mixtures, stone aggregates are much stiffer and stronger than other material components, i.e. the bituminous binder. The possibility of failure through aggregates tends to be very small. Most of the failure can be found in the binder phase that connects neighbouring particles. The potential failures may be as follows:

- (1) Interfacial failure at the bitumen-stone boundaries;
- (2) Cohesive failure through the bituminous interphase in the adhesive zone;
- (3) Cohesive failure through the mortar or mastic.

The actual type of failure that occurs in asphalt mixtures may be one or a combination of these failure modes. In any case failure happens at the weak locations in the mixture.

Porous asphalt concrete is an open, bitumen bonded material. The binding is generated at the stone-stone contact regions where a limited amount of mortar acts as binding agent. Ravelling is the result of failure of the weakest link within the stone contact region. This binding failure may be introduced by repeated traffic loads only. Although non mechanical associated effects, especially aging, moisture, chemical attack, etc. may enhance the development of ravelling, it is believed that ravelling is directly related to fatigue damage of material components within the stone contact regions. Therefore, a critical parameter relevant to ravelling resistance is the binding properties of bitumen-aggregate system.

The aim of this chapter is to review the binding properties of bitumen-aggregate systems. In such systems, the binder phase can be bitumen in a thin film, a mastic and a mortar. The substrates can be various solids including steel, aluminium, glass and stone. The focus is on test methods that could be used to measure the binding properties of bitumen-aggregate systems as well as relevant issues that affect the

binding fatigue/strength and failure characteristics.

2.2 Bitumen-substrate binding property

Mack (1957) is the pioneer to measure the strength of bitumen films. Use was made of steel plates as substrate and a thin bitumen film as adhesive. Uniaxial tensile tests were done under force-controlled mode with a constant rate of loading of 5 pounds per second and at a temperature of 25°C. The bitumen film thickness varied from 20 μm to 200 μm . The average film thickness was calculated by dividing the volume of bitumen used by the actual area between the two steel plates. Mack found that the strength of a thin film of bitumen varied linearly with the film thickness to a maximum and then decreased. The strength also increased with surface tension. Figure 2.1 shows an example of the film strength as the function of film thickness. Mack concluded that at film thickness between 70 μm to 200 μm , bitumen behaved like a solid. Another finding was that the optimum film thickness increased with the viscosity of bitumen. As the viscosity varied with temperature, the optimum film thickness was considered to depend upon temperature. As a result, the optimum film thickness for certain bitumen increased as temperature reduced. Mack also discussed the relation of film strength to mechanical properties of asphalt mixtures. It was found that the ratio of maximum film strength to maximum bearing strength of sand-asphalt mixtures is approximately 3.00.

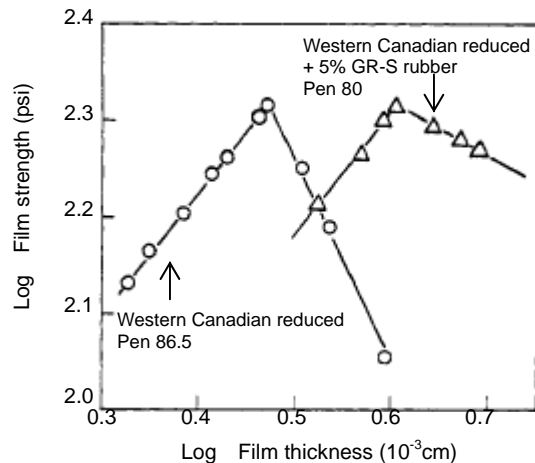


Figure 2.1 Film tensile strength as function of film thickness [Mack 1957]

Majidzadeh and Herrin (1965) investigated the behaviour of thin films of bitumen subjected to uniaxial tensile stresses. The focus was on the effects of film thickness, rate of extension and temperature. All tests were conducted by using a butt-type specimen arrangement. A small amount of bitumen was placed between two aluminium blocks of known area and weight. The average bitumen film thickness was calculated using the same method as reported by Mack (1957). By doing this, an average film thickness ranging from 10 μm to 1000 μm was obtained. The rates of

extension varied from 0.005 to 1.0 inch/min. A wide range of temperatures from 0°C to 45°C was considered. Several important results as obtained from this study are given below.

- (1) The tensile strength of thin bitumen films decreased as the film thickness increased, and finally the tensile strength approached a constant value that did not change as the film thickness further increased. The hydrodynamic theory can be used to predict the tensile strength of thick films of bitumen. The theory of potential energy and cavities with certain assumptions can be applied to very thin films of bitumen which tend to behave as a solid. Figure 2.2 presents the influence of film thickness on tensile strength and the theoretical prediction.
- (2) The behaviour of bitumen over a wide range of film thicknesses can be explained by the restraining action, flaws and cavities. The restraining action of the boundary conditions produced transverse tensile stresses in the specimen which changed the state of simple tension to triaxial tension. This change, occurring gradually as the film thickness decreased was partly responsible for the different types of behaviour observed in the bitumen films. In addition, the influence of the flaws and cavities that might be present in the bitumen on the behaviour of specimen was more pronounced in thin films where the material behaved more as a solid than thick films where bitumen behaved more as a plastic material.
- (3) Three types of failure were observed in the bitumen specimens: brittle fracture, tensile rupture and failure by flow and necking. Depending on the test conditions, brittle fracture occurred in thin films, whereas thick films failed predominately by flow and necking. The failure of intermediate film thicknesses is by tensile rupture which is characterized by the formation of cavities and filaments in the film. The range of film thickness at which different types of failure occurred depended on the test variables, e.g. temperature, rate of extension and size of specimen. As the temperature decreased or the rate of extension increased, the limits of brittle failure and flow condition were shifted to the thicker film range. Figures 2.3 and 2.4 give an example. As indicated, the tensile strength increases as the rate of extension increases or the temperature decreases.

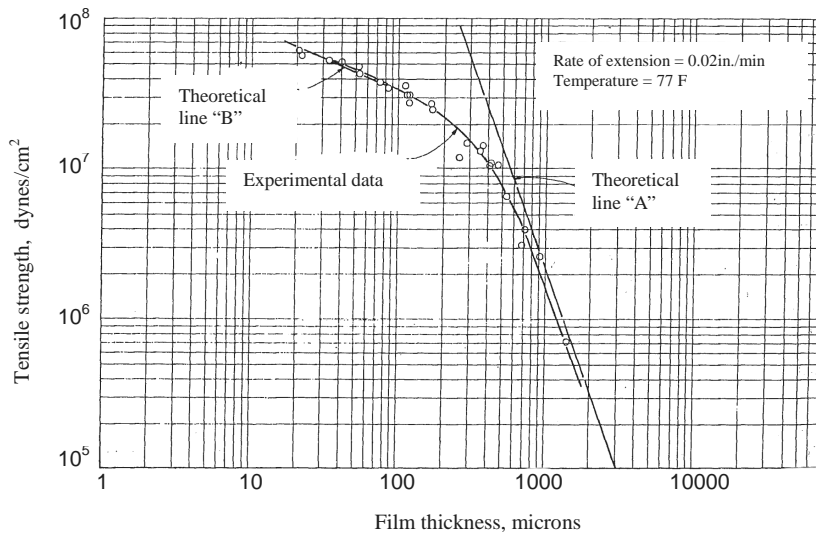


Figure 2.2 Influence of film thickness on tensile strength and theoretical predictions (A: hydrodynamic theory; B: the theory of potential and cavities) [Majidzadeh & Herrin 1965]

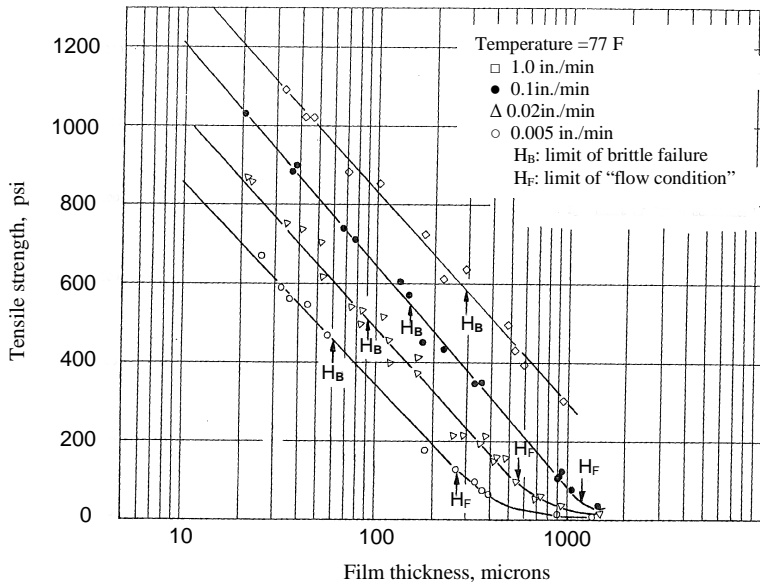


Figure 2.3 Influence of rate of extension on tensile strength and limits of brittle failure and flow condition [Majidzadeh & Herrin 1965]

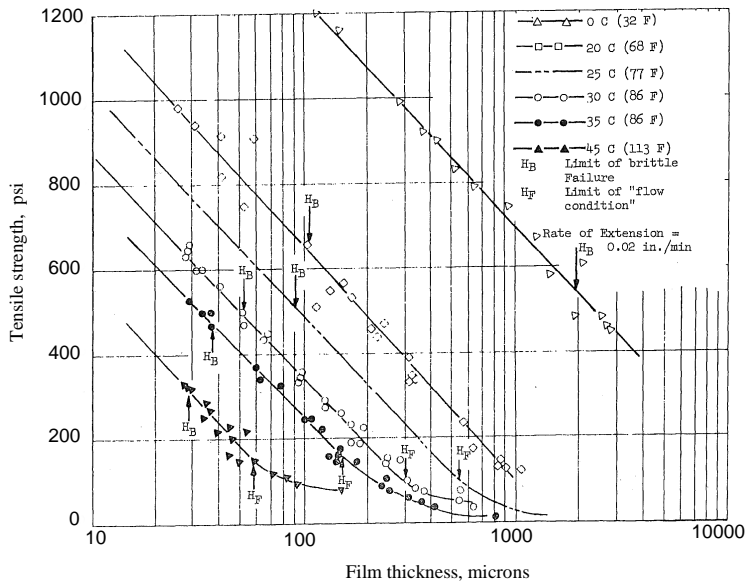


Figure 2.4 Influence of temperature on tensile strength and limits of brittle failure and flow condition [Majidzadeh & Herrin 1965]

Sisko (1968) conducted a study on the tensile strength of thin films of 12 types of bitumen in different conditions of aging. Specimens were aged in the thin film oven test (TFOT), and aged specimens were taken from roads being up to eleven years in service. All uniaxial tensile tests were performed on 13 μ m thick bitumen films between two aluminium holders at an extension rate of 0.10inch/min. These conditions were selected to cause failure by brittle failure. The spacers of aluminium foil are used to control the film thickness by means of spacer legs (see Figure 2.5). Besides of aluminium substrate, Sisko also stated that an attempt to use holders with stone faces in contact with the bitumen film was unsuccessful. The reasons were due to the problem of holder preparation and the inconsistent failure modes occurring at low temperatures.

The tensile strength of thin bitumen films increased with decrease in temperature to a maximum value which was about the same at low temperatures for all bitumen binders in newly constructed roads (see Figure 2.5). Subsequent weathering developed appreciable differences in tensile strength between bitumen binders. The TFOT aging showed that there was no correlation between tensile strength and the source of the bitumen or its composition. Changes in bitumen composition were not significant enough to show the contribution that the individual components made to the tensile strength of bitumen. Sisko finally stated that the failure of thin films was a complicated mixture of cohesive and adhesive failure.

Based on the extensions measured by means of linear variable differential transformer (LVDT), Sisko found that the tensile modulus of bitumen in very thin films was within an order of magnitude of that of aluminium. Due to this, extension measurements may not reflect the actual deformation in the bitumen film and thus

were discontinued. Determination of the strain in the thin bitumen film seemed much more troublesome than that of the stress.

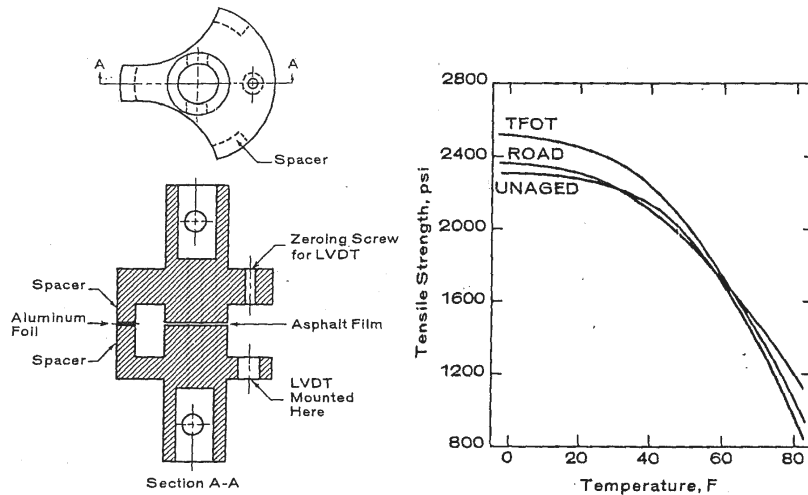


Figure 2.5 Section view of holder(left) and general dependence of tensile strength on temperature (right) [Sisko 1968]

Marek and Herrin (1968) presented an extensive study on the tensile behaviour and failure characteristics of eleven bitumen binders in thin films. Variables in their study included film thickness (20~600 μm), rate of extension (0.005~1.0inch/min), temperature (0~50°C), consistency and source of the bitumen binders (50~210 penetration). Two types of substrates, aluminium and Lucite cylindrical blocks were employed. Again, the average film thickness was controlled by a procedure quite similar to the procedures described previously [Mack 1957]. Besides the tensile strength, the extent of cavity formation prior to specimen failure, the amount of volume change to failure caused by tensile stressing and the magnitude of specimen necking to failure were measured by means of photographic techniques. Some important conclusions from Marek's study are as follows.

- (1) The tensile strength of bitumen in thin films was a function of film thickness and three regions can be classified as shown in Figure 2.6. In very thin film region, the tensile strength appeared to increase as the film thickness was increased. Tests in this region were limited because of limitations of the experimental technique and the inability to form very thin films that were uniform. In the next region, the tensile strength decreased with increasing film thickness and followed a linear relation in a semilogarithmic plot. In the very thick film region the tensile strength approached to a constant value and a cohesion type of failure was always observed.
- (2) The tensile strength of thin bitumen films increased with increasing deformation rate or with decreasing temperature. This is in agreement with the conclusions from Majidzadeh's research.
- (3) The penetration grade of the bitumen binder had a more significant influence

on tensile strength compared with the source of the bitumen binder. Generally the lower penetration bitumen binders had a higher tensile strength than the high penetration bitumen binders. Bitumen binders from the same source which possess higher asphaltene contents exhibited a greater tensile strength.

- (4) The type of material used in the test block construction did not significantly affect the apparent tensile strength. This effect prevailed as long as cohesive failure was observed.
- (5) Three modes of failure were observed and the range of film thickness exhibiting each failure mode was dependent upon the combinations of test conditions. Each failure mode showed a distinct failure surface characteristic.
- (6) As the temperature was decreased and as the rate of deformation was increased, or as the bitumen penetration grade became harder, the limits of brittle fracture or flow failure occurred at increasingly thicker film thicknesses.
- (7) The type of failure that occurred in thin bitumen films subjected to tensile stresses can generally be classified as cohesive failure rather than adhesive failure. Exceptions to this latter failure phenomenon occurred at very thin films, at low temperature, and/or rapid deformation.
- (8) A constant rate of loading test appeared to be a more desirable test method than a constant rate of deformation test for determining bitumen behaviour characteristics. The use of a stiff enough but not perfect rigid testing apparatus may result in a significant influence on the rate of deformation.
- (9) Bitumen in thin films subjected to tensile stresses exhibited a cavitation phenomenon. Visible internal cavities developed and grew until specimen failure. Specimens which exhibited the brittle failure never had cavity development progress to the extent that one cavity interfered with the growth of another. There was no apparent sign of a crack propagation phenomenon on the separated fracture surfaces.
- (10) The strain at maximum load increased as the film thickness was increased in the thin film region. After some limiting film thickness was reached, the strain to failure tended to remain constant.

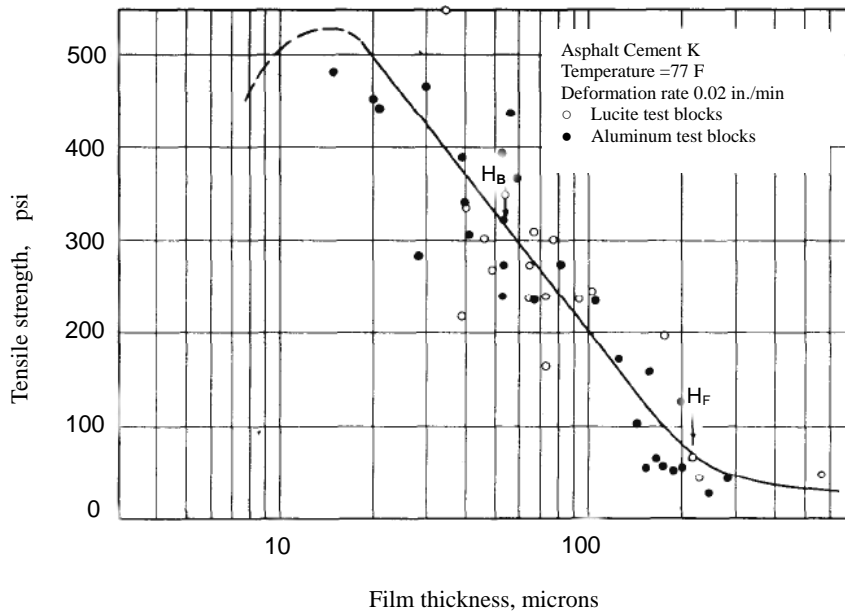


Figure 2.6 Influence of film thickness on tensile strength and limits of brittle failure and failure caused by flow (H_B : brittle failure; H_F : failure caused by flow.) [Marek & Herrin 1968]

Frolov and Vasieva et al. (1983) presented a research on the strength and structure of thin bitumen films. Steel and marble cylinders were used as substrate surfaces. The displacement rates varied from 100mm/min to 1000mm/min. Various film thicknesses up to 400 μ m were considered. All tests were conducted at a temperature of 24°C. At high displacement rates attempts were made to increase the possibility of adhesive failure. However, it was found that determination of the conditions of the formation of adhesive detachment was troublesome. In the region of adhesive detachment, cohesive detachment may also take place. Adhesive detachment required higher speeds and higher stresses at thinner film thickness compared with cohesive detachment. Frolov et al. concluded that the strength in adhesive detachment exceeded the strength in cohesive detachment by a factor of 1.1~1.5.

Frolov et al. proposed a complete curve to explain the relation between strength and film thickness. Figure 2.7 gives an example. Among 9 types of bitumen with different grades, the maximum cohesive strengths were obtained from film thicknesses ranging from 20 μ m to 36 μ m and in most cases, 25 μ m was found to be the average film thickness. The film strength increased when the samples were stored for 3 months. The force of detachment of the asphalt film from the marble substrate was considerably greater than that from steel. Frolov et al. related the sharp rise of film strength at 20~25 μ m to the start of intense formation of strong bitumen structures.

In a later study, Frolov and Frolova et al. (1984) presented the relationship between the film strength- thickness curves and photomicrographs of bitumen films separated by direct detachment. From the optimal tensile strength and the

microstructure of the film after failure, it was possible to estimate the physicommechanical properties of the bitumen and to predict its properties in an asphaltic concrete.

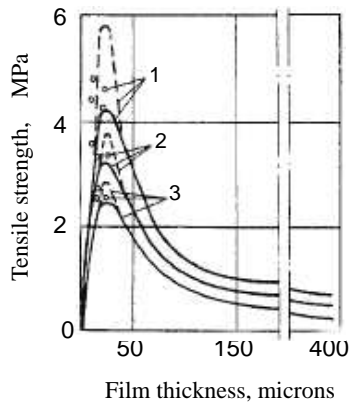


Figure 2.7 Relationship between strength and film thickness (BND bitumen, steel substrate, 24°C and 100mm/min) continuous curves are for fresh bitumen, cohesive detachment; points plotted as circles are for bitumen after holding for 3 months, cohesive detachment; 1= Bitumen Pen 50; 2= Bitumen Pen 69; 3=Bitumen Pen 163) [Frolov & Vasieva et al. 1983]

Chang (1994) studied the cohesive and adhesive strength of various bitumen binders using a poker-chip geometry, i.e. the bitumen is used to bind two rigid steel plates together. Two types of steel plates, 15.24cm and 5.08mm in diameter, were used. Three ranges of film thickness were involved: thicknesses larger than 2mm, thicknesses between 120 μ m and 2mm, and thicknesses thinner than 120 μ m. These film thicknesses were controlled by casting, compression with spacer control and compression with extensometer control respectively. Experimental variables included the rate of loading, temperature, film thickness and preparation conditions. Uniaxial tensile, uniaxial compression and repeated load tests were performed. Some conclusions from Chang's study are given below.

- (1) The mechanical properties were strongly affected by the specimen preparation temperature.
- (2) Based on the load-deformation characteristic and the nature of the fracture surface, four types of failure, i.e. brittle fracture, tenacious rupture, semiflow rupture and failure by flow were observed.
- (3) The tensile strength increased as the film thickness decreased. When a specimen was really thick, however, depending on the test condition, the tensile strength can approach quite a small value as shown in Figure 2.8.
- (4) The cavities in the central region were larger and denser than at the edge. Most of the failures were due to cavitations. Some cohesive and adhesive failures were observed. Strength properties of poker-chip specimens depended on the bitumen's cavitation resistance.
- (5) Long stabilizing/equilibrium time introduced the so-called physical

hardening effect, which was reflected by the greater stiffness, the tendency of interfacial failure and brittle bulk failure.

- (6) The mechanical properties of bitumen in the poker-chip geometry subjected to a stress significantly lower than the yield stress can be described by means of a linear viscoelastic model.

Chang stated that the measurements of deformation and apparent stiffness of the bitumen films, especially when the films were very thin, were difficult. Since the stiffness of bitumen in thin film was very high, the compliance of the measurement system can not be neglected. Thus the stress seemed to be the most reliable parameter that can be used.

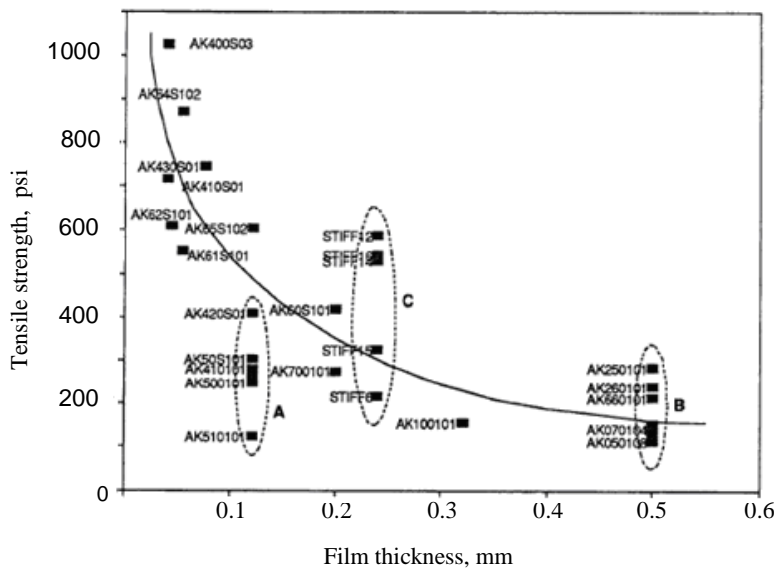


Figure 2.8 The influence of thickness on the break strength of bitumen films in tensile tests [Chang 1994]

A modified blister test was developed for evaluating the adhesive strength of bitumen-aggregate systems [Chang 1994; Anderson & Cristensen et al. 1994]. This test consisted of a coating of bitumen binder over a flat aggregate surface. A hole, drilled through the aggregate under the coating, allowed the application of steady or varying water pressure to the underside of the coating. To prevent a “blow out” of the bitumen film during pressurization, an aluminium film was placed on top of the bitumen film. Adhesion is measured by the force required to displace the film from the aggregate. It was expected that in the presence of water adhesive failure would occur along the bitumen-aggregate interfaces. Eight bitumen binders and two types of aggregates were tested using this blister test. It was found that no adhesive failure was observed with either of the aggregates or any of the eight bitumen binders. After

adding a freezing step, adhesive failure was produced. However, it failed to differentiate between two aggregates with radically different susceptibility to water damage.

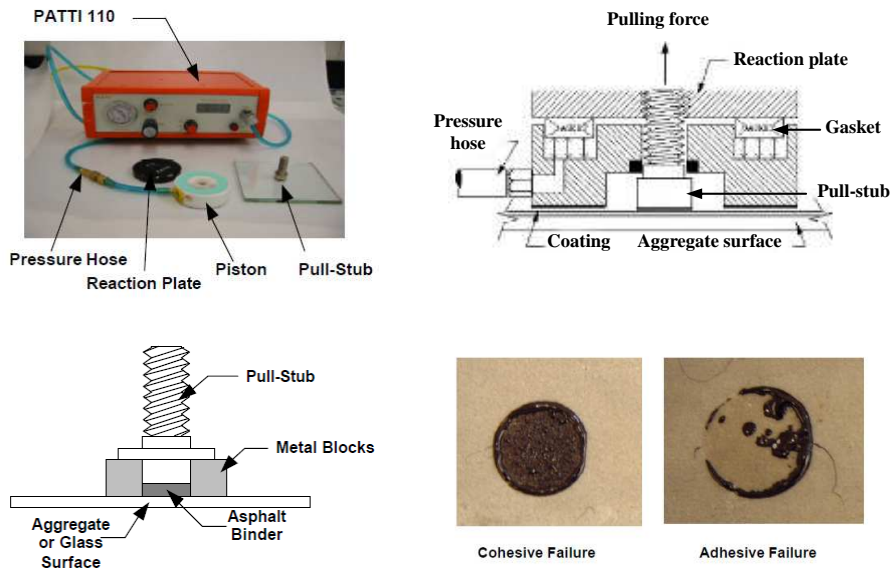


Figure 2.9 Main features (left-upper) of the PATTI, schematic drawing (right-upper), specimen preparation (left-bottom) and type of failure (right-bottom) [Kanitpong & Bahia 2003]

Some researchers used the Pneumatic Adhesion Tensile Testing Instrument (PATTI) to evaluate the adhesive loss of bitumen-aggregate systems exposed to water [Nguyen & Byrd 1996; Youtcheff & Aurilio 1997]. The tests were performed according to ASTM D 4541 “Pull-Off Strength of Coating using Portable Adhesion Testers”. Figure 2.9 gives an impression of pull-off testing using the PATTI. Pull-off tests were usually done at room temperature on a bitumen or mastic layer with a thickness of 200 μm . Specimens were prepared at a temperature of approximately 100°C [Youtcheff & Aurilio 1997; Kanitpong & Bahia 2003, 2004, 2005; Copeland & Youtcheff et al. 2006, 2007; Copeland 2007]. In bitumen-aggregate systems, some researchers found that the weakest link in the dry condition and after moisture conditioning is the bitumen binder since all dry specimens had cohesive failure and adhesive failure between the bitumen-substrate interfaces could only be found in a few water conditioned specimens [; Kanitpong & Bahia 2003, 2004, 2005; Copeland & Youtcheff et al. 2006, 2007; Copeland 2007]. Moisture conditioning was shown to influence the bond strength of the bitumen-aggregate systems as determined by means of pull-off test method; however, it did not always degrade the bond strength [Copeland 2007].

The bond strength of mastic-aggregate systems using the same pull-off test was

also reported [Copeland & Youtcheff et al. 2006, 2007; Copeland 2007]. Copeland (2007) reported that the mastic used consisted of mineral filler smaller than $75\mu\text{m}$ and bitumen at a volume ratio of filler: bitumen=30:70. The addition of filler increased the bond strength at dry conditions but did not change the failure mode. All dry specimens failed cohesively within mastic. After moisture condition, most of the tested specimens experienced a clear adhesive failure.

Kanitpong and Bahia (2003) suggested differentiating the bitumen-stone adhesion and the cohesion of bitumen by using different test methods. Pull-off tests were proposed to measure adhesion while the DSR was applied to measure the tackiness of thin bitumen films. A tack factor, which was calculated by integrating the area under the force vs. time curve, was used to evaluate the tackiness of bitumen in thin films. It was found that the tack factor increased as temperature decreased from 64°C to 16°C . A strong relationship between the indirect tensile strength of asphalt mixtures and the tack factor of related bitumen binders was reported.

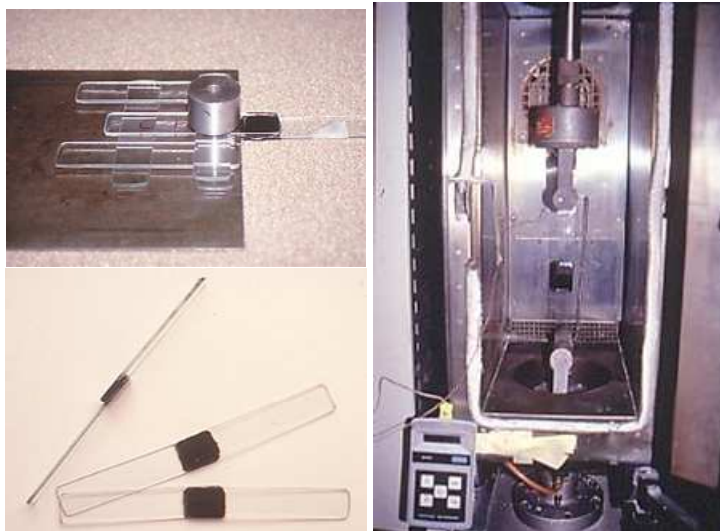


Figure 2.10 Specimen preparation (left-upper), overview of specimen (left-bottom), and test setup with an environmental chamber [Babcock & Statz et al. 1998]

Babcock and Statz et al. (1998) conducted a study of various asphalt binders using lap shear bonds as shown in Figure 2.10. One base bitumen and three types of polymer modified bitumen binders were used. Glass slides were used at a temperature range of $0\text{--}64^{\circ}\text{C}$, while metal slides were applied at temperatures between -6°C and 6°C since the glass slides broke prior to the asphalt failing in lap shear at very low temperatures. The thickness of bitumen layer between the two slides was 1.6mm . Tests were done by pulling the specimens at a speed of 0.51cm/min . All the tests showed that lap shear testing is reproducible with various polymers and temperatures. Polymer modification increased the tensile strength of the binder at temperatures

above 12 °C. At temperatures of 12 °C and below, the strength of all the bitumens became approximately equal. Specimens failed in an adhesive manner at low-temperature, while cohesive failure was observed at temperatures above 6°C.

Yan and Liang (2001) measured the shear adhesiveness between bitumen and rock by using the lap shear test. Two types of bitumen and two types of rock (limestone and granite) were used. Test specimens were prepared by using two stone slices (10cm×5cm×1cm) sandwiching with a bitumen film with an overlap area of 5cm×5cm. Various temperatures (0°C~30°C) and displacement rates (1.0~9.0mm/min) were applied. It was found that the maximum shear strength decreased exponentially with temperature and increased exponentially with displacement rate. Bitumen-rock combinations with better adhesiveness can be differentiated by the shear strength and the moisture susceptibility can be evaluated by water conditioning.

Little and Jones (2003) stated that the types of failure that occurred had a strong relationship with the nature of the bitumen/mortar and the binder film thickness (see Figure 2.11). Asphalt mixtures with thin asphalt films fail in tension by adhesive bond rupture, while those with thicker asphalt films (or mastic films) fail because of damage within the mastic (cohesive failure) as opposed to interfacial debonding (adhesive failure).

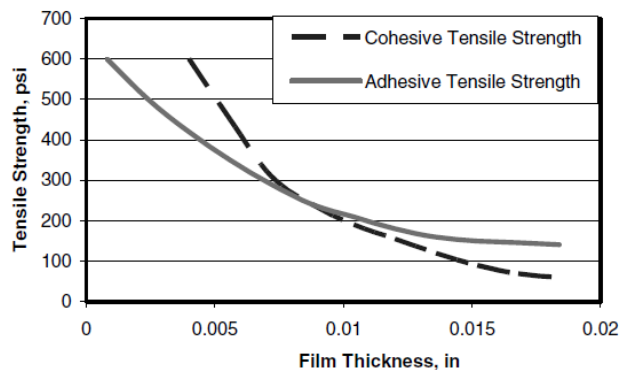


Figure 2.11 Adhesive versus cohesive bond failure in relation to bitumen film thickness [Little & Jones 2003]

In the pre-LOT phase, uniaxial tensile and shear tests on bitumen-stone adhesion samples were performed using Dynamic Mechanical Analyzer (DMA) (see Figure 2.14) [Mo & Huurman et al. 2006, 2007; Cao 2007; Mo 2007]. Two types of stone (Greywacke and Basalt) and two types of bitumen (70/100 Pen and 60/80 Pen) were used. Both monotonic and repeated load force-controlled tests were performed at temperatures of 25°C and 5°C. The stone surfaces were polished using fine carborundum powders and thus the obtained surface might not be the same to the actual surface of crushed stone. The thickness of bitumen film was 20µm. A specially designed clamp was used to press the bitumen between the ends of the two blocks down to the required thickness by means of a spacer. It was found that some tests at

5°C were difficult to perform because of the increased bond strength of the bitumen-stone systems and the limited loading capacity of the used instrument. It was found that the bond strength increased with increased rate of stress, or reduced temperatures. The fatigue resistance of the bitumen-stone bond was increased as temperature decreased from 25°C to 5°C. For the shear tests, cohesive failure seemed to be the predominant failure mode, while mixed failure was observed for tensile tests. Finite element simulations showed that the bitumen film thickness and the change of the bitumen properties due to temperature did not affect the stress states significantly. However, the local loss of interfacial bonding between bitumen and stone would be significant to the overall interfacial fracture. Mo & Huurman et al. (2006) also proposed a damage accumulation model for interpretation of monotonic and repeated load data based on the stress-time histories.

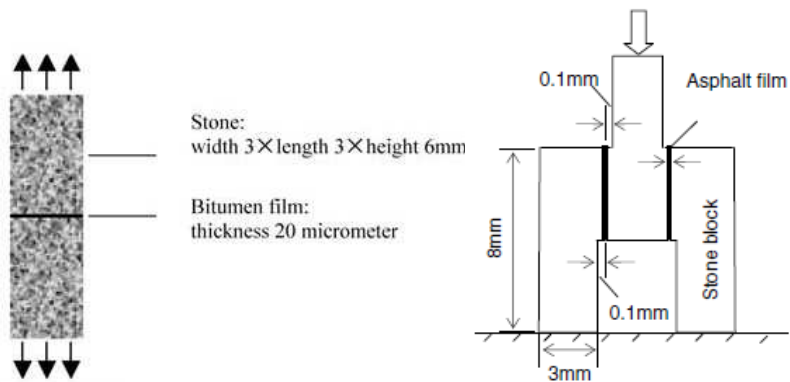


Figure 2.12 Schematic illustration of test specimens (left: uniaxial tensile test; right: shear test) [Mo & Huurman et al. 2006, 2007]

Khattak and Baladi et al. (2007) performed a study on the binder-aggregate adhesion and mechanical characteristics of polymer modified asphalt mixtures at low temperatures. The lap-shear test was used to study the interfacial adhesion between bitumen binder and aggregate. As shown in Figure 2.13, the bitumen binder with a thickness of 0.13mm was sandwiched between two granite rock substrates and a tensile force was applied to break the bond between bitumen and stone. Two types of bitumen and five types of polymer modified systems were involved. Test temperature varied from 20°C to -20°C. In situ tensile tests in Environmental Scanning Electron Microscope (ESEM) were conducted on the cut sections of asphalt concrete (see Figure 2.14).

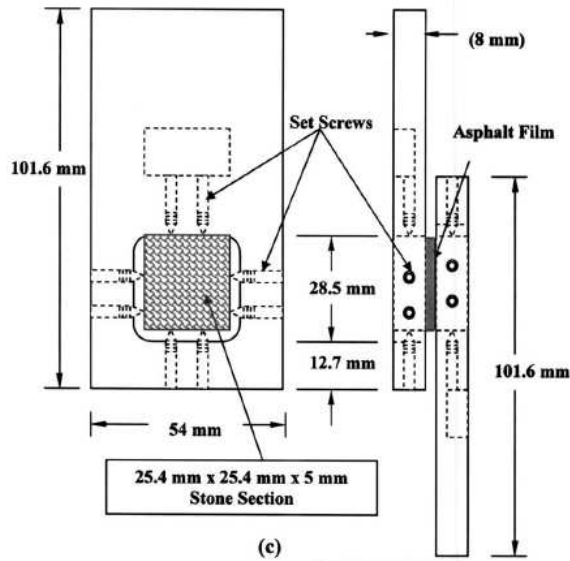


Figure 2.13 Fixture schematics of lap-shear test [Khattak & Baladi et al. 2007]

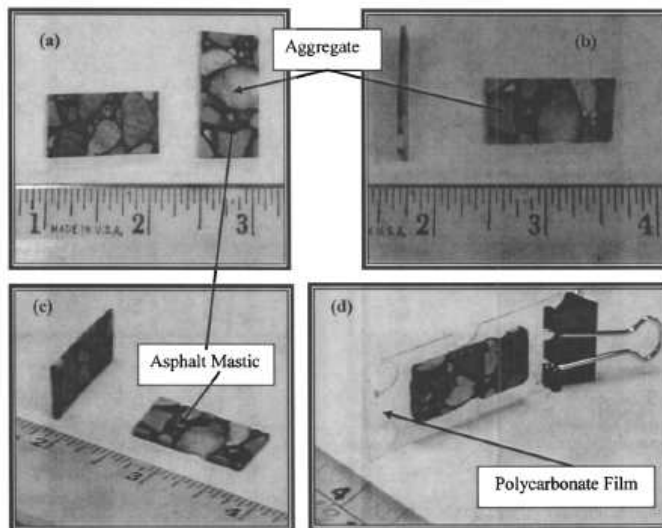


Figure 2.14 Test specimens used for in situ tensile [Khattak & Baladi et al. 2007]

It was found that the failure mode of bitumen-aggregate systems changed from cohesive failure (0~20°C) to adhesive failure with the decrease in temperature (at -10°C and -20°C). The polymer modification slightly improved the low-temperature adhesive properties of the processed binders.

In situ tensile tests in ESEM showed that cracks tended to propagate along the interface. The exposed aggregate surface, which was crazed by the crack, reveals

some bitumen residues. Bitumen fibrils along the failure surface were formed. Based on these observations, Khattak stated better adhesion properties were obtained by the use of polymer modified binders. Figure 2.15 gives an example of the ESEM micrographs showing the failure processes and fibril formation.

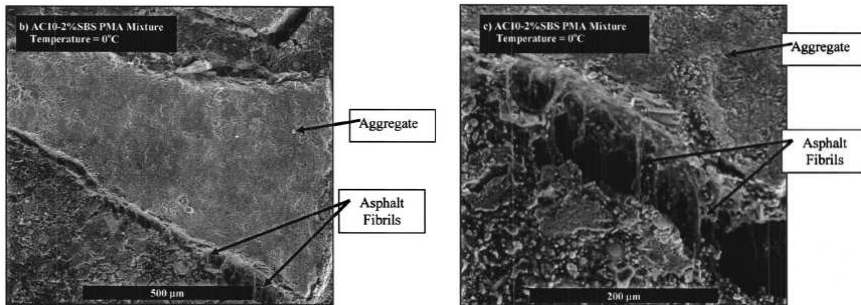


Figure 2.15 ESEM micrographs showing failure processes and fibrils of AC10 mixture modified with 2% SBS polymer content at 0°C [Khattak & Baladi et al. 2007]

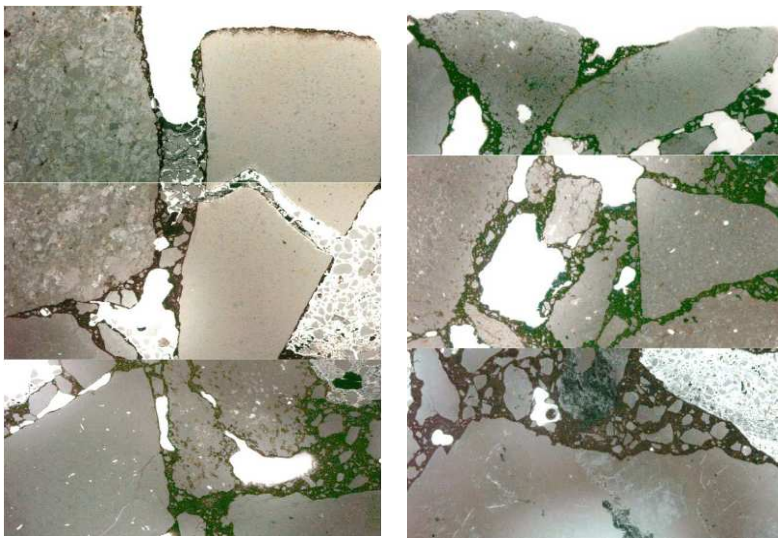


Figure 2.16 Thin section images from road sections with poor (left) and good (right) performances. From top to bottom: slow lane, surface and top zone; slow lane, bottom zone [Nielsen & Bendtsen 2006; Nielson 2007; Nielsen and Raaberg et al. 2007].

Nielsen and Raaberg et al. presented an analysis and assessment of cores drilled from road sections in the Netherlands with single layer porous asphalt. Figure 2.16 gives an example. It was found that the main overall deterioration mechanism was related to the adhesion and cohesion between mastic and aggregate. Deterioration of

the mortar was also observed. The finding that it is necessary to improve the adhesion between aggregate and mastic in order to avoid ravelling is certainly valid. However, improving materials requires an appropriate set of laboratory test and assessment methods that reflect and simulate the behaviour in the field [Nielsen & Bendtsen 2006; Nielson 2007; Nielsen and Raaberg et al. 2007].

2.3 Summary of the literature review

A substantial amount of research has been performed on the binding behaviour of bitumen-substrate systems. Many different test methods have been developed to measure the bitumen-substrate binding properties. Most of the used substrates are metal solids and thin bitumen films are used as adhesive. Based on the literature review, the following observations are made.

- (1) The direct measurement of the interfacial adhesion between bitumen and stone is very troublesome. In most studies, cohesive failure or mixed failure mode is reported. It indicates that the adhesion strength may exceed the cohesive strength.
- (2) The strength of thin bitumen films increases with reducing film thickness and cohesive failure was observed when the bitumen film is thick. This indicates that the measurement on bitumen-stone adhesion should focus on very thin films to obtain a high possibility of adhesive failure.
- (3) The failure mode of thin bitumen films subjected to tensile stresses depends on the film thickness, temperature, rate of extension as well as the consistency of bitumen. In very thin films, brittle fracture may occur with no apparent sign of crack propagation. Very thick films fail by excessive flow. In intermediate film thicknesses, cavitation may play an important role on tensile rupture.
- (4) Bitumen in very thin films behaves like a solid. The stiffness of bitumen in thin films may be within an order of magnitude of that of aluminium, or two orders of magnitude of that of steel. This implies that the compliance of the measurement system can not be neglected when performing measurements on very thin films. The real deformation of the thin bitumen film is very difficult to determine. Therefore, the stress seems to be the most reliable parameter to be measured in such tests compared to strain.
- (5) The above indicates that force-controlled mode tests should be performed to evaluate bitumen-stone adhesion because of the very thin bitumen film.
- (6) The laboratory aging effect on bitumen tends to improve the adhesive strength of bitumen-stone systems. However, water immersion shows a great influence on adhesive failure, i.e. stripping. Since water increases the possibility of adhesive failure, it implies that bitumen-stone adhesion is more sensitive to water damage than the cohesion of bitumen.
- (7) The bitumen-stone binding tends to fail in an adhesive way at low temperatures, while in a cohesive way at relatively high temperatures. The temperature at which the failure changes from cohesive failure to adhesive failure depends on the combination of bitumen and stone. This temperature can be changed by modifying the bitumen with polymer. Freeze-thaw cycles tend to increase the chance of adhesive failure.

- (8) Most studies have focused on the binding strength of bitumen-substrate systems. In practice, repeated traffic loads play an important role on the bonding failure. This is especially true for loss of aggregate from the pavement surfaces. It indicates that fatigue behaviour is of great importance for ravelling investigation.
- (9) Most of tests were performed at a scale larger than the size of aggregate. It should be noted that ravelling is a type of failure within the stone contact regions. This indicates that tests on larger specimens are not good enough for ravelling investigation and thus new test setups that allow meso-scale fatigue characterization have to be developed.
- (10) Previous researches were focused on uniaxial tensile testing of bitumen-substrate systems. It should be noted that ravelling occurs on pavement surface. This indicates that the material components may experience very complex shear stress induced by direct tyre-pavement interaction. Finite element simulations of porous asphalt concrete showed that the effect of shear stress is more significant than the effect of tensile stress. As a result, shear tests become very important for analyzing such a problem.

2.4 General approach and test program

Figure 2.17 (see at the end of this chapter) gives the general approaches to problem analysis in the field of asphalt pavements. As indicated, the scale of modelling, macro, meso or micro scale, is dependent on the scale of the problem in which one wants to have insight. At each scale, a tool is needed to bring structural geometry, loading and material properties together to allow for mechanics analysis. The life expectancy is usually estimated combining the computed stress or strain with the corresponding material fatigue/damage models. The mechanics analysis allows to bring up material measurement data (i.e. response) one level of scale. However, the loadings of a model at a certain level of scale can be derived from the modelling results at the upper level of scale. The objectives of modelling at different scales are briefly described as follows

- (1) Pavement thickness design is to solve the load bearing capacity, or structural support by the determination of the overall thickness of the road and the thickness of the individual layers. The scale of such problems is in an order of meter.
- (2) Bulk mixture design aims to achieve high-quality asphalt mixtures by improving deformation resistance, fatigue resistance, low temperature cracking resistance, durability, moisture damage resistance, workability, etc. The scale of such problems is in an order of decimetre.
- (3) Meso scale research aims to improve asphalt mixture performance by analyzing the mixture as if it were a structure. Performance is dependant on mixture geometry (structural geometry) and component behaviour (i.e. mortar and adhesive zone). The scale of such problems is in an order of millimetre.
- (4) Micro-scale design aims to improve the performance of asphalt mixtures via insights into the chemical/physical properties of the binder-stone combination.

In this case, a scale of at least micrometer may be required.

With respect to ravelling damage as is discussed in this study, the focus is on meso-scale with a structural geometry of stone chippings bonded by the mortar. As a result, the adhesive zone and mortar are the important material components that account for fatigue damage. Based on the previous literature review, it is known that basic knowledge on meso-scale fatigue characterization of the adhesive zone is needed. Therefore, a test program taking into account the following issues is required:

- (1) the scale level of millimetres;
- (2) complex stress states and shape of stress signal;
- (3) fatigue behaviour rather than material strength;
- (4) shear stress in the mix close to pavement surface;
- (5) temperature;
- (6) aging;
- (7) water immersion.

Table 2.1 Test program on bitumen-stone adhesion

Bitumen	Short-term aging & long-term aging
Stone	Sandstone & greywacke
Water conditioning	Water immersion
Temperature	From -10°C to 20°C
Uniaxial tensile tests	Various load signals, force controlled
Shear tests	Various load signals, force controlled

The above discussion resulted in the following test program on the bitumen-stone adhesion as shown in Table 2.1. This table lists some important issues that were analyzed in the test program. Specimens will be made use of small stone substrates sandwiching a very thin bitumen film. Uniaxial tensile and shear fatigue tests will be considered since shear and tensile stresses are two important issues that account for the debonding of bitumen-stone adhesion. All tests are planned to be conducted in force controlled mode and various load signals will be considered to account for the complex state of stress to which the adhesive zone is subjected in the actual mixture. Furthermore, non-mechanical effects, such as aging and moisture will be taken into account in the test program. Laboratory accelerated aging protocols will be applied to simulate the effects of short-term and long-term aging of bitumen. Similarly, a laboratory water immersion protocol will be used to investigate the water susceptibility of bitumen-stone adhesion. To differentiate between various bitumen-stone combinations with different susceptibilities to water damage and aging, different types of stone and bitumen should be considered. Finally, a wide range of temperature e.g. from -10°C to 20°C is also considered.

A similar test program is also required for mortar fatigue characterization at meso-scale. As shown in Table 2.2, the test program will take into account the effect of aging (short-term aging and long-term aging), water immersion, temperature, complex stress state (shear and tensile) and stress signal (i.e. frequencies of 10Hz and 40Hz).

Table 2.2 Test program on mortar fatigue

Mortar	Short-term aging & long-term aging
Water conditioning	Water immersion
Temperature	0°C and 10°C
Bending tests	Various load signals (i.e. frequencies), force controlled
Shear tests	Various load signals (i.e. frequencies), force controlled

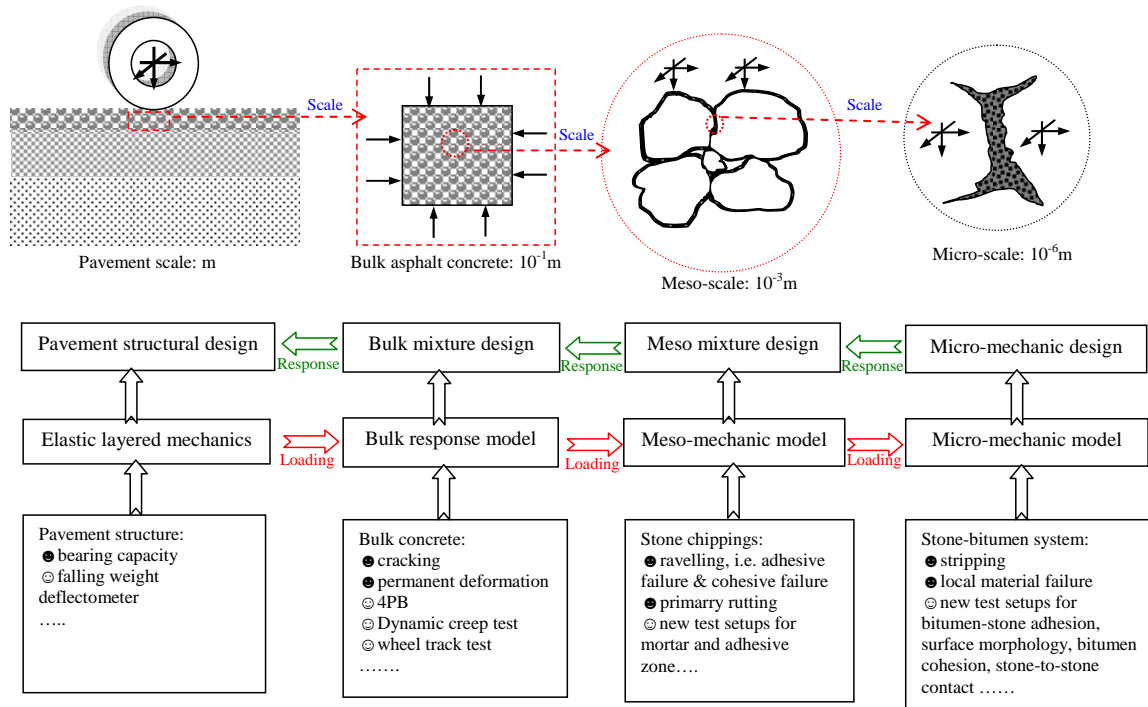


Figure 2.17 General approaches to problem analysis in the field of asphalt pavements

3 RAW MATERIALS

In this chapter, the materials used in this study including stone, fine sand, filler, bitumen and mortar, are briefly introduced. Some of these materials were also used in other researches that have been completed at the Lab of Road and Railway Engineering of the Delft University of Technology (TUD) and in this study, use was made of those data. A limited amount of additional tests was done to provide extra information. More detailed information on the material properties can be found via the given references.

3.1 Stone

Two types of stone, i.e. sandstone and greywacke, were used in the LOT project and this research. The adhesive zone is defined as the adhesive interface zone plus a bitumen interlayer. As will be described in more detail later in Chapter 4, the characteristics of the adhesive zone in relation to the type of stone, were determined using specially designed specimens. These specimens consisted of two stone columns with a thin layer of bitumen in between (see Figure 3.1-i). For specimen preparation, boulders of each stone were casted in cement and then the stones were sawn into slices with a thickness of approximately 10 mm (see Figure 3.1-a). To obtain a relatively constant surface roughness, one side of the slice was sand-blasted. After that, stone columns were drilled from the slices (see Figure 3.1-c). Due to limitations in loading capacity of the various test machines that were used in this study, two different diameters of stone columns, i.e. 2.7mm and 6.8mm were drilled from the stone slices (see Figure 3.1-e). All stone columns were cleaned in boiling distilled water for 15minutes and dried in an oven at a temperature of 105°C for half an hour. After cooling the stone columns were stored in clean plastic bags. Specimens were produced by using the DSR at a temperature of 175°C. A pair of stone columns was clamped into the open-hole in the upper and lower clamps. A small drop of bitumen was placed between two surfaces and then pressed to the required film thickness (see Figure 3.1-e). After cooling, specimens were removed from the DSR and stored at 5°C before testing. More details on the preparation of stone columns can be found elsewhere [Khedoe & Moraal 2007].

Among other properties, the surface morphology, surface energy and the mineral composition may be of great interest. Figure 3.2 shows images of crushed aggregate surfaces and the treated surfaces of stone columns used in this study. These images were captured by a Scanning Electron Microscopy (SEM) and an Atomic Force Microscopy (AFM). As observed, the surface morphology of the crushed aggregate is much rougher than that of the prepared stone columns. The 3D AFM images show that the maximum roughness depth, that is, the peak-to-valley height is approximately 3~5µm [Mo & Huurman et al. 2009]. Table 2.1 lists the roughness of the sand-blasted surfaces of stone columns at macro-level and meso-level as determined by van Lent (2008). The table shows that the sandstone and greywacke specimens show a similar surface morphology.

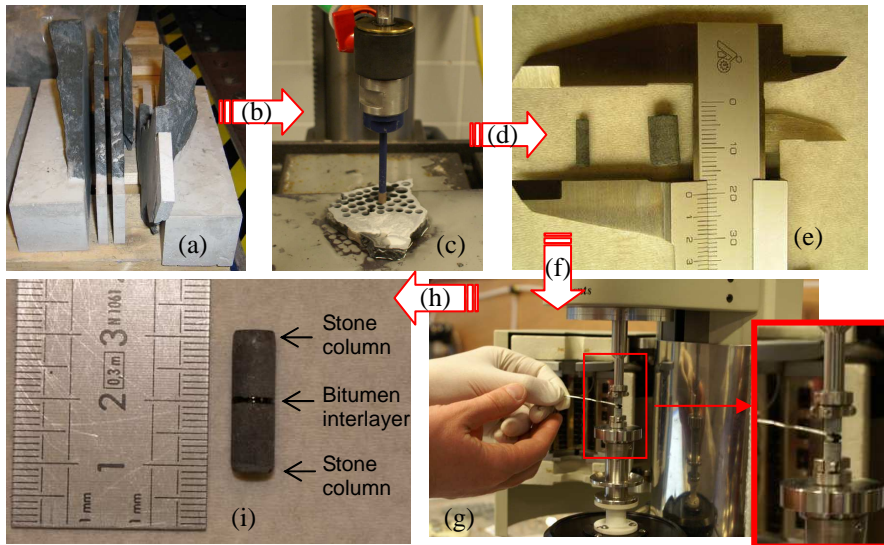


Figure 3.1 Impressions of the specimen preparation and size for adhesive zone (a: cement casting and slices; b: sand-blasting treatment; c: drilling cores; d: cleaning; e: stone columns; f: select stone pairs; g: prepare specimen using DSR; h: cooling and remove specimen from DSR; i: 6.8mm diameter stone columns) [Khedoe & Moraal 2007]

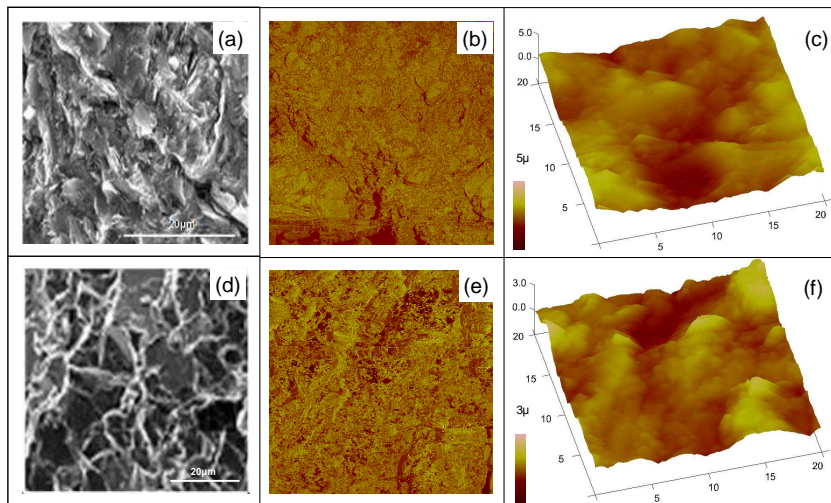


Figure 3.2 Surface morphology analysis using SEM and AFM images (a: SEM, sandstone aggregate; b and c: 2D and 3D AFM, sandstone column; d: SEM, greywacke aggregate; e and f: 2D and 3D AFM, greywacke column) [Mo & Hurman et al. 2009]

Table 3.1 Morphology measurement results reported by van Lent

Magnification	Type of stone	R _a [μ m]	R _q [μ m]
7X	Greywacke	50.67	59.47
	Sandstone	49.07	58.51
20X	Greywacke	4.99	6.85
	Sandstone	6.63	8.57
50X	Greywacke	5.15	7.00
	Sandstone	7.45	9.60

Note: R_a = Arithmetic average of the absolute values of surface deviations
R_q = Root mean square average of height deviation

Table 3.2 Chemical composition of sandstone and greywacke reported by van Lent

Composition	Sandstone	Greywacke	Composition	Sandstone	Greywacke
	Wt %			Wt %	
SiO ₂	60.628	53.052	S	0.00	0.268
CO ₂	10.776	8.446	P ₂ O ₅	0.117	0.077
CaO	8.244	8.27	TiO ₂	0.4196	0.7896
Al ₂ O ₃	10.368	15.67	V ₂ O ₅	0.0082	0.0212
K ₂ O	2.114	3.326	Cr ₂ O ₃	0.0588	0.0444
MgO	1.886	2.832	MnO	0.1638	0.0978
Na ₂ O	2.022	0.6624	NiO	0.1874	0.1046
Fe ₂ O ₃	2.908	6.128	BaO	0.1034	0.0986

Table 3.3 Surface energy components of stone columns reported by van Lent

Stone	Greywacke	Sandstone
γ_s^{TOT} /Stdev	63.71/0.42	60.05/3.8
γ_s^{LW} /Stdev	50.53/0.09	48.49/0.22
γ_s^{AB} /Stdev	13.18/0.36	11.56/3.72
γ_s^+ /Stdev	0.95/0.06	0.68/0.41
γ_s^- /Stdev	45.57/0.55	48.98/2.98

γ_s^{TOT} = total surface free energy; γ_s^{LW} =free energy of Lifshitz-van der Waals force;

γ_s^{AB} =surface energy of polar acid-base interactions; γ_s^+ =contribution of Lewis acid;

γ_s^- = contribution of Lewis base; unit=mJ/mm²; Stdev= standard deviation

Tables 3.2 and 3.3 (see above) give the chemical composition and surface energy components reported by van Lent. As listed in Table 3.2, sandstone shows a higher SiO₂ content compared with greywacke stone, indicating that sandstone is slightly more acidic, that is, less basic than greywacke. With respect to the surface

energy as indicated in Table 3.3, it can be concluded that there are not distinct differences between these two types of stone.

3.2 Fine sand and filler

In this study, fine sand and filler was blended with bitumen to prepare mortar. The composition of the mortar is discussed in Section 3.4. The sand used is crushed sand with a nominal maximum aggregate size of 2mm. The grading is shown in Table 3.4. The density of the fine sand is 2.677kg/m³ [van Hinthem 2008].

Table 3.4 The grading of fine sand [van Hinthem 2008]

Sieve size [mm]	4.0	2.0	1.0	0.5	0.18
passing percentage	100	85-99	50-70	20-45	5-20

The applied filler is a Wigro 60 limestone filler with 25wt% hydrated lime [van Hinthem 2008]. Its characteristics are listed in Table 3.5.

Table 3.5 Characteristics of Wigro 60 filler

Bitumen number	Voids	Density	Hydrated lime	Limestone	Solvability in HCL	Cumulative retained
ml/100g	vol%	Kg/m ³	wt%	wt%	wt%	%
56-62	44-50	2475-2675	65-75	25-35	68-88	2mm: 0 0.09mm: 0-15 0.063mm: 5-25

3.3 Bitumen

In this study, use is made of Cariphalte XS, a SBS polymer modified bitumen provided by Shell. Some of its specifications are as follows: Penetration 50-85 at 25°C, softening point higher than 65 °C and ductility at 5 °C larger than 35cm [Shell 2003]. This polymer modified bitumen is commonly used in the top layer of double layer porous asphalt concrete in the Netherlands. Table 3.6 gives the measurement results of surface energy reported by van Lent.

Table 3.6 Surface energy components of the short-term aged bitumen reported by van Lent

	$\gamma_s^{TOT} / \text{Stdev}$	$\gamma_s^{LW} / \text{Stdev}$	$\gamma_s^{AB} / \text{Stdev}$	$\gamma_s^+ / \text{Stdev}$	$\gamma_s^- / \text{Stdev}$
SDM	35.28/0.56	35.09/0.49	0.19/0.08	0.01/0.00	0.86/0.39
WPT_A	34.38/3.10	31.73/2.77	2.65/0.62	2.17/0.24	0.81/0.63
WPT_R	45.18/4.02	41.62/3.38	3.84/1.82	-0.44/0.32	8.40/0.63

Note: unit=mJ/mm²; SDM= Sessile Drop Method; WPT_A= Wilhelmy Plate Test from advancing contact angle; WPT_R= Wilhelmy Plate Test from receding contact angle.

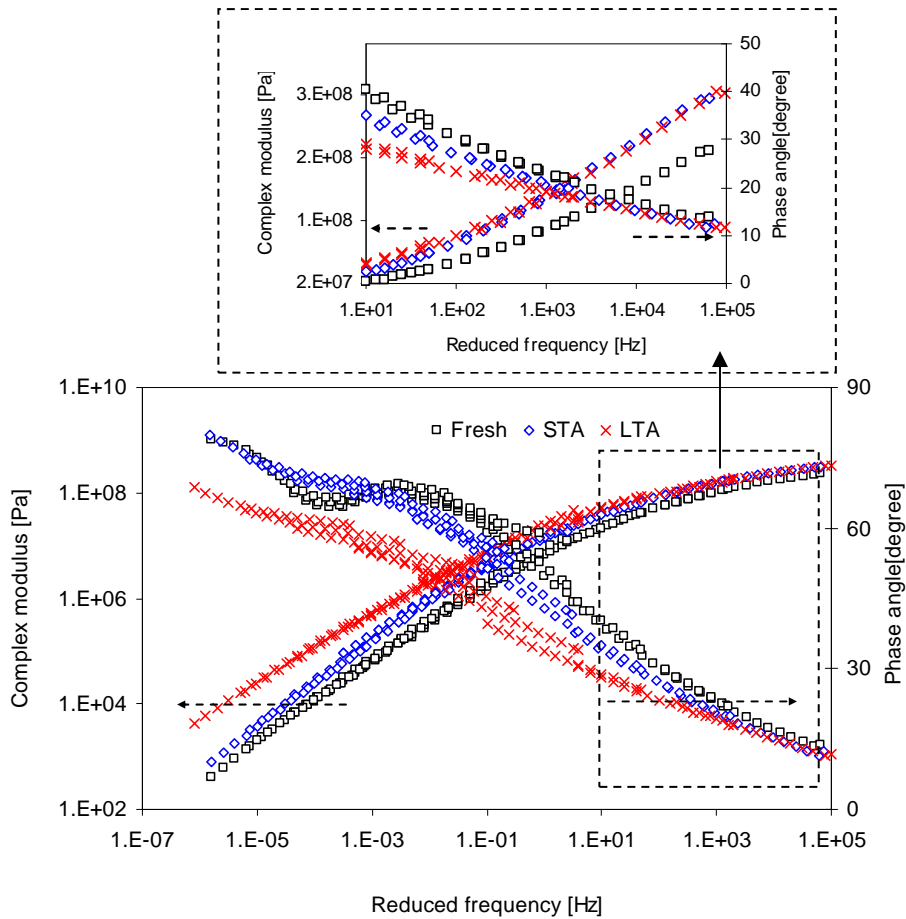


Figure 3.3 Master curves of the complex shear modulus and phase angle for the fresh bitumen, short-term aged bitumen (STA) and long-term aged (LTA) bitumen at a reference temperature of 10°C

To investigate the effect of aging, the SBS modified bitumen was subjected to a short-term and long-term laboratory accelerated aging protocol. In the short-term aging protocol, the bitumen is spread in a 2 mm thick film (which reflects the nominal maximum size of sand used in porous asphalt mixture) and stored in an oven at 175°C (which is equal to the mixing temperature) for 1.5 hours. This was done to simulate the aging during mixing, transportation, laying and compaction. The long-term aging regime consists of a 1000-hour aging by using a combination of ultraviolet light (60W/m², 300~400nm wavelength), a temperature of 40 °C, 70% relative humidity and oxygen (open environment). Long-term aging was performed on specimens that were already subjected to the short-term aging protocol. According to Hagos' research, the used long-term aging reflects the initial 3-year field aging of porous asphalt in the Netherlands [Hagos 2008]. More details on the aging regimes can be

found elsewhere [Khedoe & Moraal 2007; Hagos 2008].

Figure 3.3 gives the master curves of the complex shear modulus and phase angle for the fresh bitumen, the short-term and long-term aged bitumen. Hereafter, the phase angle is defined as the phase lag between the maximum stress and strain. The reference temperature is 10 °C. It is shown that the complex modulus increases with extending aging while the phase angle decreases. These trends are especially strong at low frequencies. At high frequencies the effect of extending aging is relatively limited as shown in the zoom-in linear-scale plot. The master curves of the phase angle of the fresh bitumen and the short-term aged bitumen exhibit a plateau region. According to other studies on aging of polymer modified bitumen, it is known that such a plateau region can be used as a sensitive indicator of the existence of a polymeric network structure in the base bitumen [Airey & Brown 1998; Wu & Pang et al. 2009]. Obviously, this plateau region becomes indistinct in the master curve of long-term aged bitumen, indicating the network structure of SBS modified binder was damaged by long-term aging.

3.4 Mortar

The mortar used in this study consists of bitumen, filler and fine sand mixed at a mass ratio of 0.34:0.30:0.36 (bitumen: filler: fine sand). The fine sand used to prepare the mortar is smaller than 0.5mm. The reason for this is that according to Muraya's research, the aggregate skeleton of porous asphalt only consists of aggregates larger than 0.5mm [Muraya 2007]. It means that the mortar in porous asphalt can be defined as a mixture of bitumen and any of aggregates smaller than 0.5mm. The filler and fine sand is uniformly blended with bitumen at a temperature of 175°C. The obtained fresh mortar is aged using the same aging regimes that were applied to the bitumen as described before. Therefore, two types of mortar, short-term aged mortar and long-term aged mortar were considered. More information on mortar preparation and aging can be found elsewhere [Khedoe & Moraal 2007].

Figure 3.4 gives the master curves of the complex modulus and phase angle for the fresh mortar, short-term aged mortar and long-term aged mortar. For the purpose of comparison, the corresponding master curves of fresh bitumen are also plotted in this figure. The data for short-term aged and long-term aged mortar are obtained elsewhere [Huurman & Woldekidan 2007]. Small strains were applied to assure that measurements were done within the linear viscoelastic region. By comparing the master curves of the mortar with the fresh bitumen, it is shown that the introduction of the fine sand and filler increases the complex modulus. However the effects of the fine sand and filler on phase angle are limited. Mortar aging also results in a complex modulus increase and a phase angle decrease, but the order of aging effect on mortar is not consistent with the order of aging effect on bitumen based on the limited amount of tests available. Long-term aging shows to have a smaller effect on mortar's rheological properties than short-term aging. This unexpected phenomenon was further examined by execution of extra tests on short- and long-term aged mortar. The extra data is shown in Figure 3.5. The difference between two short-term aged mortar tests strongly indicates that the reproducibility of tests on the mortar is not as good as for tests on the bitumen. It is believed that this is due to the heterogeneity in mortar specimen preparation due to the introduction of the

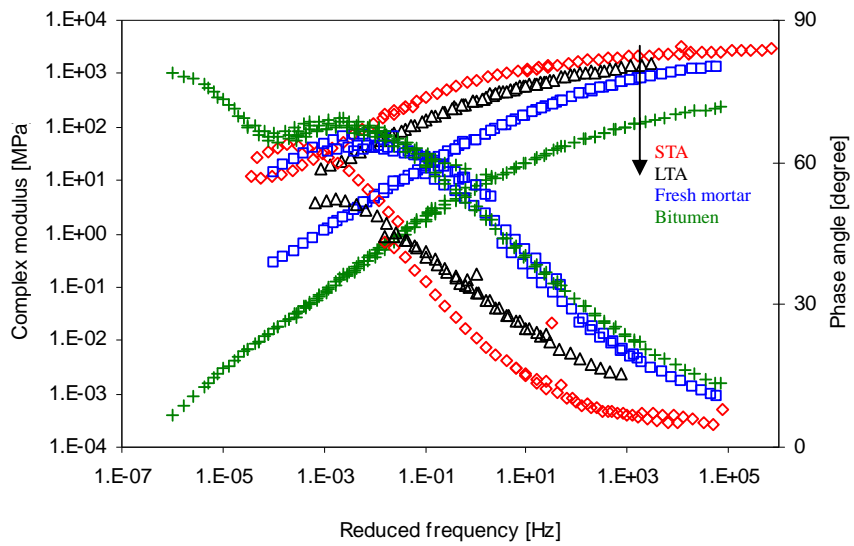


Figure 3.4 Master curves for the fresh bitumen, fresh mortar, short-term aged (STA) mortar and long-term aged (LTA) mortar at a reference temperature of 10°C

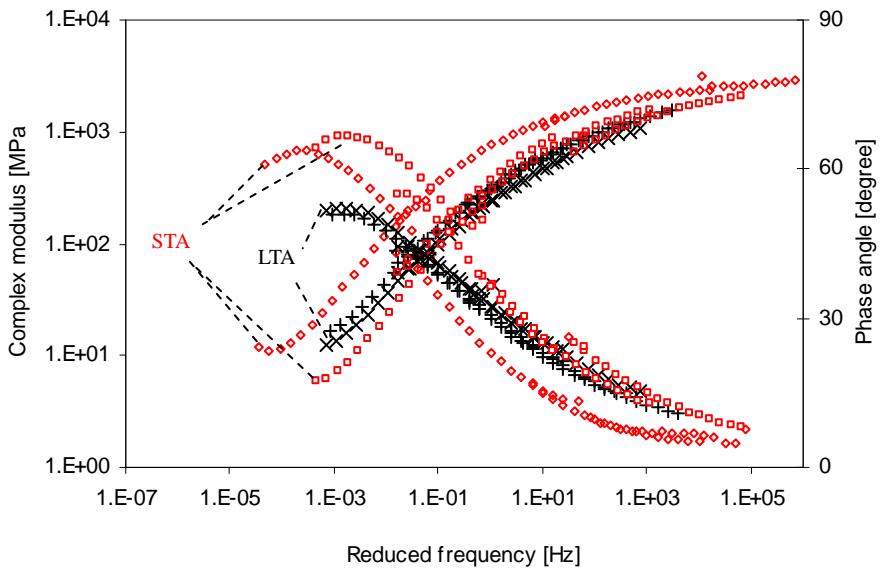


Figure 3.5 Extra data on the short-term aged (STA) mortar and long-term aged (LTA) mortar at a reference temperature of 10°C

filler and fine sand. Since only a limited amount of test data is available, conclusions regarding the effect of short- and long-term aging on the mortar's characterization are hard to establish. In any case, the results show that ample attention should be paid to the preparation of mortar specimens.

3.5 Summary

Two types of stone, i.e. sandstone and Greywacke and one type of SBS modified bitumen were used in this study. Based on surface morphology measurements, surface energy measurements and chemical composition analysis, it was concluded that no distinct differences exist between the sandstone and greywacke specimens. The bitumen was subjected to short-term aging and long-term aging, thus in effect two different binders were considered for the fatigue testing of adhesive zones. The fresh bitumen was blended with one type of filler and one type of fine sand at a mass ratio of 0.34:0.30:0.36 (bitumen: filler: sand) to produce a fresh mortar. This fresh mortar was subjected to short-term and long-term laboratory aging. As a result, two types of mortar, i.e. short-term aged mortar and long-term aged mortar were involved in this study.

4 TEST PROGRAM & DESCRIPTION OF THE RESULTS

4.1 Introduction

The LOT project aimed at the development of a design strategy for ravelling resistant porous asphalt concrete wearing courses [Huurman 2008]. Because a strategy in which porous asphalt mixture is modelled on macro level is not good enough to fully understand the behaviour of skeleton type mixtures like porous asphalt, this design strategy should focus on the meso-mechanical structure consisting of individual stone particles being bonded by mortar. Such a meso-scale structure allows to analyze the potential crack paths which are expected to develop in the mortar bridges or/and the adhesive zones when the meso-scale structure is subjected to repeated traffic loadings. The so-called cohesive failure occurs when the crack initiates and propagates within the mortar bridge and adhesive failure happens when the crack grows along the mortar-stone interface zone.

The model that enables to analyze ravelling makes use of finite element modelling to translate the tire-pavement contact load, mixture geometry and mortar response into signals of stress and strain at various locations within the modelled mixture [Huurman & Mo et al. 2006; Huurman 2008]. From the stress and strain signals, the life expectancy of porous asphalt is then estimated. It is obvious that fatigue/damage models for the mortar and the adhesive zone need to be available in order to be able to perform such analyses.

In previous chapter the materials used in this study are briefly introduced. In this chapter, material testing for the development of fatigue/damage models for the mortar and the adhesive zone is addressed. Information on the test methods, test interpretation and the obtained results is presented.

4.2 Adhesive zone damage test

4.2.1 Introduction

Initial finite element simulations of porous asphalt mixtures showed that the adhesive zones are subjected to complex 3D states of stress with a combination of one normal stress and two shear components. Since the thickness of the adhesive zone is far smaller than the other dimensions, 2D state of stress is a sufficient representation by using one normal stress and one shear stress (i.e. the resultant stress of two shear components). The stress states within the adhesive zones are fully dependent on where these zones are located in the mixtures. Figure 4.1 gives an example and more data can be found elsewhere [Mo & Huurman et al. 2007, 2008; Huurman 2008]. Besides the location, the aforementioned stress states also vary over time during tire passages. Therefore, complex stress signals of normal and shear components can be expected. Apart from the observation that shear and normal stresses coexist it is difficult to distinguish the predominant stress component between these two stresses. Furthermore, the stress signals to which the adhesive zones are subjected are far from sinusoidal, a shape that is commonly applied in classical fatigue tests on asphalt mixtures. In conclusion, it can be stated that the effects of 3D states of stress and

complex stress signals must be taken into account for the damage model of the adhesive zone. For these reasons, tests using normal and shear stresses as well as combinations hereof were planned. Among these tests, uniaxial tension testing was conducted using Dynamic Mechanical Analyzers (DMA). Shear testing was performed by Dynamic Shear Rheometers (DSR). Combined normal-shear tests were also carefully and specially designed. Various types of load signals were applied accounting for complex stress histories.

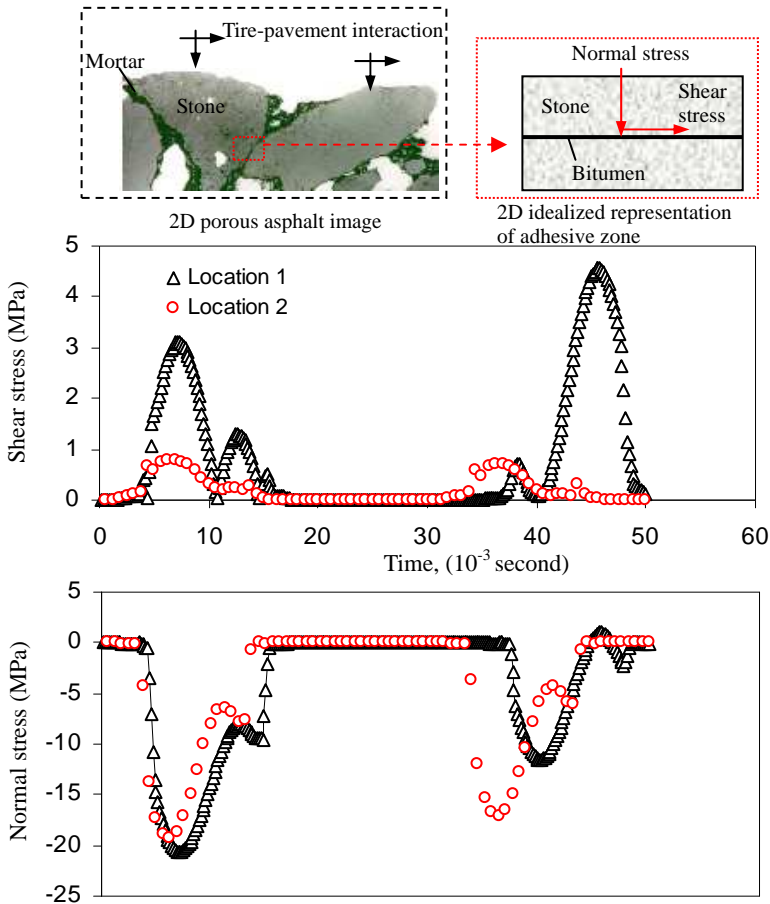


Figure 4.1 Porous asphalt is loaded via tire-pavement interaction (upper-left) which results in normal and shear stresses in 2D idealized representation of the adhesive zone (upper-right). The shear stresses are shown in the middle figure. The normal stresses are shown in the bottom figure. These stresses are due to two tyre passages and are calculated for two locations by means of finite element analysis [Mo & Huurman et al. 2008]

4.2.2 DMA uniaxial tension test

4.2.2.1 Test description

The specimens that were prepared for DMA uniaxial tension testing consisted of two stone columns as shown in Figure 4.2 (right). Each stone column had a diameter of 2.7 mm and a height of approximately 10mm. The size of the specimen used for this type of testing is determined by the maximum loading capacity of the machine of approximately 15N in combination with a rough estimation of bitumen fatigue strength of 2.5MPa. The stone columns were glued together at two ends using a thin layer of bitumen. The thickness of the bitumen interlayer was controlled during specimen preparation and was set to a thickness of 15 μ m by means of a DSR machine (see Figure 4.2-left). The reason for this selected film thickness is due to the fact that the bitumen films showed a peak strength value at 15~25 μ m and thicker film tended to result in cohesive failure prior to adhesive failure [Marek & Herrin 1968; Frolov & Vasieva et al. 1983].



Figure 4.2 Specimen preparation by means of DSR (left) and the overview of the specimen that is used for DMA uniaxial tensile testing (right)

To obtain the desired thickness of the bitumen interlayer between two stone columns, a special clamp system was designed, which can easily be assembled in the DSR instrument by just replacing the upper and lower standard parallel plates. A pair of stone columns is clamped into the open-hole in the upper and lower clamps (see Figure 4.2). Care should be taken to make sure that these stone columns are well centred and the contact surfaces are parallel and horizontal. A zero gap between the upper and lower stone columns can be estimated automatically by spinning down the moveable top clamp. The zero gap was reached when the moveable stone column is in full contact with the stone column fixed at the bottom. Finally, a gap setting of 20 mm was established by spinning the stone columns apart. This gap will facilitate putting a small bitumen drop on the contact surfaces. The stone columns were heated to 175 °C using the DSR temperature control chamber. After reaching a constant temperature for half an hour, the temperature chamber was opened and a small drop of hot bitumen was quickly placed on the contact surface of the bottom fixed stone column. The upper clamp was then lowered to the required gap width of 15 μ m. After cooling down to room temperature for at least 1 hour, the specimen was removed from the clamp

system and stored at a temperature of 5 °C. More details on the specimen preparation can be found elsewhere [Khedoe & Moraal 2007].

It must be noted that the aforementioned thickness (i.e. 15 μ m) of the bitumen interlayer is the minimum layer thickness between the two stone surfaces. This thickness is controlled by the peak-to-peak height between the two surfaces. It is obvious that the actual distribution of film thickness is different from one point to another dependent on the surface morphology. To illustrate this, a sketch was made of the 2D surface morphology and the corresponding thickness of the bitumen interlayer (Figure 4.3). If the surface morphology is defined as the maximum roughness depth, that is, the peak-to-valley height R_{max} , the maximum value of film thickness h_{max} is approximately equal to $h_{max} = h_{min} + 2R_{max}$. As shown in the previous chapter, the results of roughness measurement on stone surface really depend on the scale level. As a result, the thickness distribution of the bitumen interlayer is also dependent upon which scale level is considered. Using the data of roughness measurements which were given in Chapter 3, the extrema of the average thickness distribution of the bitumen interlayer at various scale levels are given in Table 4.1.

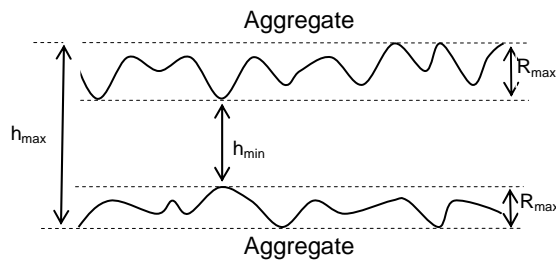


Figure 4.3 Schematic of 2D surface morphology and the thickness distribution of bitumen layer

Table 4.1 Surface roughness and thickness distribution of bituminous layer

Magnification	Type of stone	R_a [μ m]	$h_{min} \sim h_{max}$ [μ m]
7X	Greywacke	50.67	15~116.3
	Sandstone	49.07	15~113.1
20X	Greywacke	4.99	15~25.0
	Sandstone	6.63	15~28.3
50X	Greywacke	5.15	15~25.3
	Sandstone	7.45	15~29.9

Note: R_a = Arithmetic average of the absolute values of surface deviations

Figure 4.4 shows the DMA set-ups for tests on adhesive zones. Due to the limited time that was allowed for testing and given the relatively large number of tests, two DMA instruments were used to perform uniaxial tension tests. One is the DMA 800 (TA Instruments Ltd., USA) located at the Wuhan University of Technology (WHUT), China. The other is the DMA 2980 (TA Instruments Ltd., USA) at the Delft University of Technology (TUD). To perform this type of testing, special clamp

systems were designed to clamp the specimens into these two DMA instruments. Specimens were firstly fastened at the upper clamp, but the bottom end of the specimen was glued using adhesives. The used adhesives were capable to solidify within minutes. The reason for using adhesive was to avoid specimens to be damaged when attached to the lower clamp.

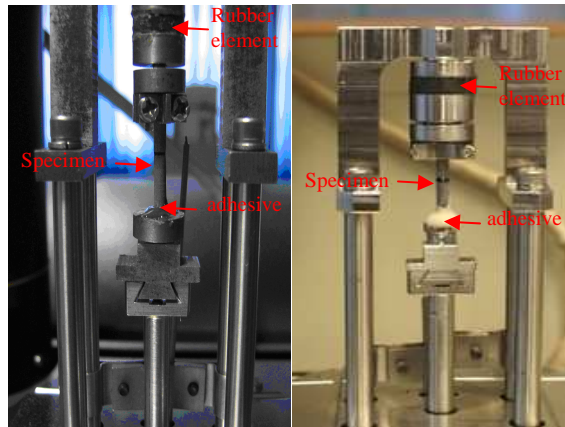


Figure 4.4 DMA test set-ups for tests on adhesive zones (left: DMA 800; Right: DMA 2980)

The test program for adhesive zones was conducted on the materials mentioned in the previous chapter. Two types of stone columns (sandstone and greywacke) and two types of bitumen (short-term aged bitumen and long-term aged bitumen) were involved. To investigate the effect of water on the adhesive zone, the specimens that were prepared by using the stones and the bitumen mentioned above were subjected to water conditioning. Based on measurements on bitumen/aggregate system exposed to water, Nguyen found that bitumen lost adhesion on both soda glass and granite substrates within a few hours by immersing 12mm-diameter specimens in distilled water at room temperature [Nguyen & Byrd et al. 1996]. For this reason and the fact that the specimens used in this study are much smaller, a laboratory water conditioning was considered. This protocol consisted of submerging the specimens in 5 °C water under vacuum for 1 hour. As a result, a total of 8 material combinations were tested.

- (1) Sandstone + short-term aged bitumen
- (2) Sandstone + long-term aged bitumen
- (3) Sandstone + short-term aged bitumen, water immersion
- (4) Sandstone + long-term aged bitumen, water immersion
- (5) Greywacke + short-term aged bitumen
- (6) Greywacke + long-term aged bitumen
- (7) Greywacke + short-term aged bitumen, water immersion
- (8) Greywacke + long-term aged bitumen, water immersion

In order to investigate the effect of temperature, tests were done at temperatures ranging from -10°C to 20°C .

Three different types of test were planned. The first type is DMA dynamic testing performed at 10 Hz by using a repeated load signal i.e. $F_0(\sin \omega t + 1.25)$ (see Figure 4.5). The second type is DMA monotonic testing. Constant static testing was performed by applying a constant tension force to the specimens. Finally, additional DMA repeated load tests were performed by applying pure sinusoidal-wave stress signal, i.e. $F_0 \sin \omega t$.

The thickness of the adhesive zone is so thin and its distribution is so complex that an accurate definition of strain is not possible. It was thus decided that tests need to be performed in force controlled mode. This is also believed to be more consistent with the loading conditions to which the individual stones in the pavement surface are subjected in practice.

The signals as applied in the various tests mentioned above are graphically shown in Figure 4.5. Table 4.2 summarizes the test program for all of DMA uniaxial tension tests.

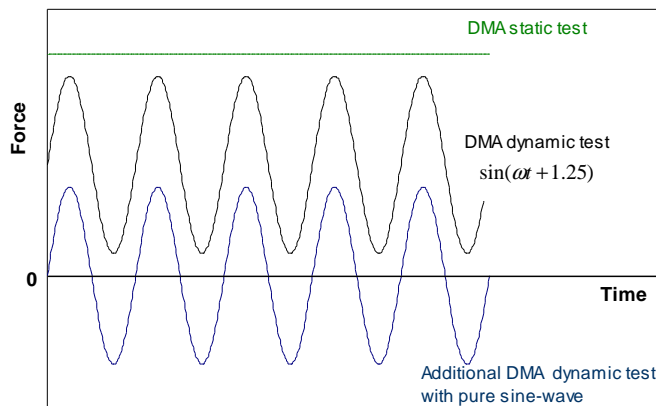


Figure 4.5 Schematic of applied signals for DMA uniaxial tension tests

Table 4.2 Test program for DMA uniaxial tension tests

Stone	Sandstone (B)				Greywacke (G)			
Bitumen	Short-term aged bitumen (SB) , Long-term aged bitumen (LB)							
Water condition	Water ingress (W)							
Test combination	B+SB	B+LB	B+SB_W	B+LB_W	G+SB	G+LB	G+SB_W	G+LB_W
	Temperature (°C)							
DMA dynamic tests	-10,0, 10,20	-10,0, 10,20	0,10,20	0,10,20	-10,0, 10,20	-10,0, 10,20	0,10,20	0,10,20
DMA static tests	-10, 20	-10, 20	-	-	-10, 20	-10, 20	-	-
Additional DMA tests	10	10	-	-	10	10	-	-

Note: the number e.g. -10, 0,10 and 20 indicates the test temperature.

4.2.2.2 Test interpretation

As mentioned above, uniaxial tensile tests on the adhesive zones were performed under force controlled mode. However, it was found that the available DMA machines had difficulties in performing force controlled tests in a straight forward way. The DMA 800 at WHUT may operate in the so-called force tracking controlled mode. This mode requires that a certain deformation is applied under displacement controlled mode at the start of the test. The machine then measures the required force and computes the stiffness of the tested item accordingly. As the stiffness decreases the machine automatically increases the applied deformation (and thus the force remains constant) accordingly. Effectively the test has now become, in an indirect way, a force controlled test.

The force tracking control mode can only operate when a substantial deformation is measured. It might be clear that the stone columns are too stiff to deform and the bitumen interlayer is too thin to develop considerable deformation. To introduce ample deformation, a soft material, e.g. rubber, is therefore introduced into the set-up; this is shown in Figure 4.4. The deformation over this soft material remains fairly constant during the test. Furthermore, almost all of the displacement measured by the machine follows from the deformation in the rubber element. As a result the DMA machine does no longer experience difficulties to perform a force tracking controlled test.

Figure 4.6 gives a typical example of the force and displacement signals obtained by the DMA machine at WHUT under the force tracking control mode. As indicated, the total displacement measured by the machine increases during the test, while the measured force still remains relatively constant. The increase of the measured displacement is in good agreement with the analysis mentioned above since the machine tries to compensate the increasing deformation due to the reduction of stiffness, thus inducing a constant force. The exact moment of failure is obtained by

forward and backward extrapolation of the measured displacement signal as indicated in Figures 4.6 by arrows.

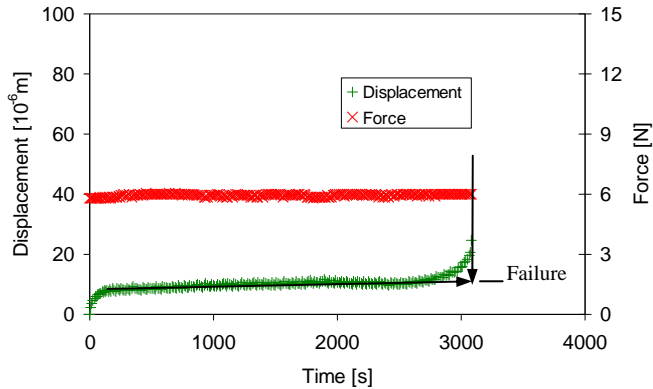


Figure 4.6 Typical displacement and force signals done by DMA machine at WHUT under force-tracked controlled mode

The DMA at TUD it is only capable to operate under the displacement controlled mode. Like was done for the DMA 800 at WHUT, a rubber element was also introduced in the TUD DMA (see Figure 4.4). Fortunately, it appeared that the force during the displacement controlled test remained quite constant during the test; only a slight decrease happened at the end of the test. This implies that although only displacement controlled tests could be performed with the TUD DMA, these tests almost “looked like” force controlled tests

To demonstrate this, finite element simulations of the test setup were performed using the finite element software package ABAQUS (Version 6.6). In Figure 4.7 the simulations of the test item before and after loading are shown. All of the materials involved are defined as deformable bodies with the following properties (Young's modulus and Poisson's ratio):

- Stainless steel: $E = 2 \times 10^5 \text{MPa}$ and $\nu = 0.3$
- Rubber: $E = 50 \text{MPa}$ and $\nu = 0.48$
- Bitumen: $E = 10 \text{MPa}$ and $\nu = 0.45$
- Stone: $E = 4 \times 10^4 \text{MPa}$ and $\nu = 0.25$

A 20-node hex-structured element was used for the analysis. As shown in Figure 4.7, the boundary conditions were that the movements at the bottom of the model were fully restrained. A dynamic force was applied at the top of the model. The effect of mesh refinement was checked to reach a fairly constant result. Figure 4.8 shows the simulation results of the total displacement of the test setup, the deformation in rubber element and bitumen interlayer respectively. As can be seen from this figure, the total displacement is almost identical with the deformation in the rubber. 99.5 percent of the total deformation is due to the deformation of the rubber. This value is dependent upon the stiffness of the rubber element.

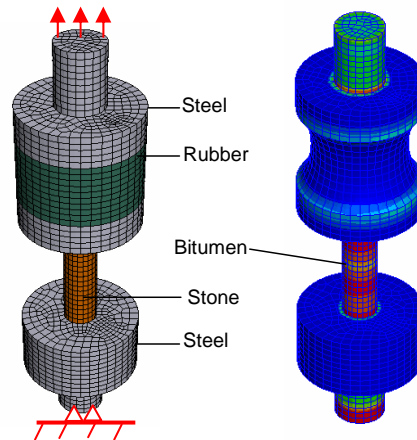


Figure 4.7 Finite element simulation of the test setup including the rubber element (left: material sections, boundary conditions and load; right: calculated stress and deformation)

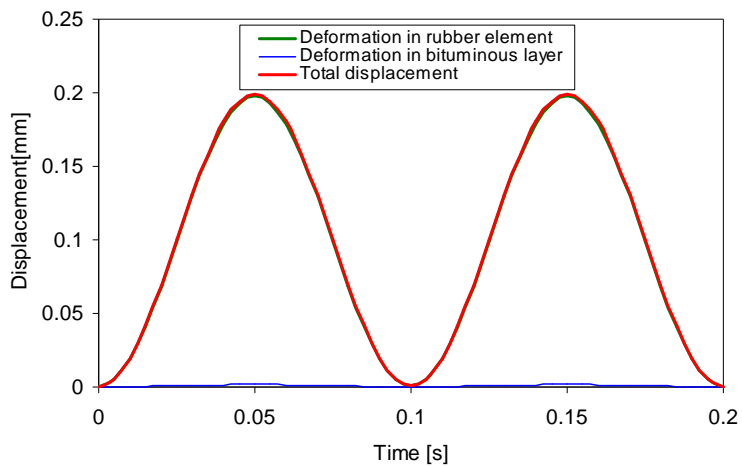


Figure 4.8 Computed total displacement and deformation in bitumen interlayer and rubber element

Figure 4.9 shows a typical example of the displacement and force signals as obtained by the DMA machine at TUD under displacement controlled mode. After introducing the rubber element, relatively high displacement amplitudes can be applied. Taking into account the very thin bitumen interlayer and its limited deformation before failure, the force induced by the rubber deformation remains relatively constant. A significant reduction of the measured force is only observed during a short period of time before the two stone columns are separated. For this type

of test, failure is defined as the point at which the measured force is reduced to 90 percent of the steady-state force. The load time or cycle at which failure occurs is interpolated from the test data.

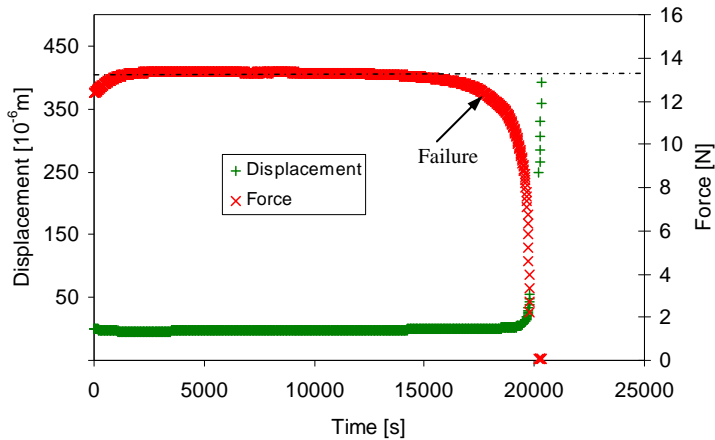


Figure 4.9 Typical displacement and force signals obtained from the DMA 2980 at TUD under displacement controlled mode

Figure 4.10 gives an impression of the stress distributions in the cross-section of the adhesive zone when subjected to an average tensile stress of 1 MPa. The data are obtained from a finite element simulation of the DMA uniaxial tensile test. The model consists of two stone columns that are bonded together by a bitumen interlayer with a thickness of $15\mu\text{m}$ (see Figure 4.10). The material properties of stone and bitumen are the same as those used in the previous model. In this simulation, the stone columns are defined as rigid bodies. Since the bitumen interlayer is very thin, a very fine mesh is needed to meet the requirement of the aspect ratio being less than 10. Due to such a fine mesh the whole model setup with mesh generation is not visible. Only an example of the cross-section is given (see Figure 4.10). The boundary conditions are such that the movements of one of the stone columns are fully restricted; the other stone column is loaded at the end surface with a tensile stress of 1 MPa as shown in Figure 4.10. The effect of mesh refinement on the computational results has been checked to obtain a stable value by using multiple models, e.g. coarse, fine and double fine meshes (see Figure 4.11).

Figure 4.11 shows the stress distributions from the centre to the edge of the cross section of the adhesive zone. As shown, there is no significant difference between the stress distributions as observed with the various meshes. Except for the edge of the cross-section, a very uniform stress distribution is obtained. The effect of the edge on the stress distribution is very limited. For example, the model is loaded with a uniform tensile stress of 1 MPa via the cross-section of the stone column. The computed tensile stress in the bitumen interlayer is 1.01 MPa.

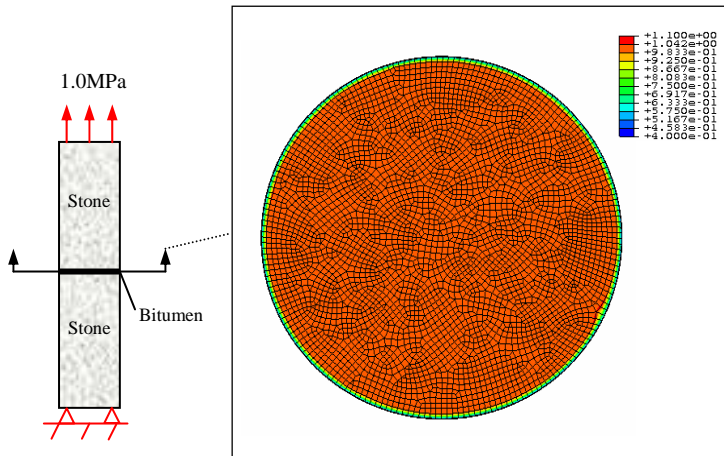


Figure 4.10 Stress distributions in the cross-section in the adhesive zone

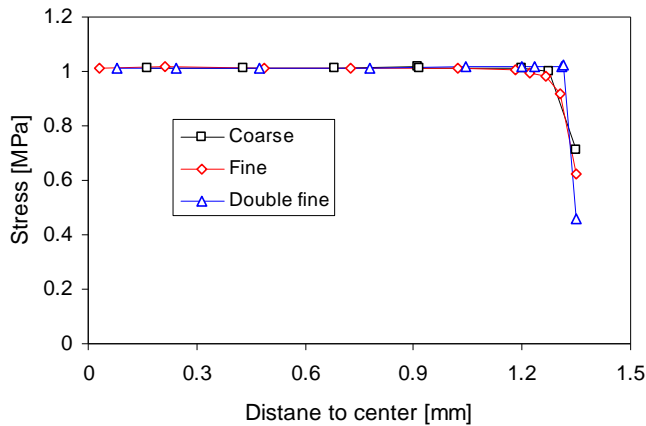


Figure 4.11 Effects of mesh refinement on stress distributions from the centre to the edge

Besides the effect of the edge, the stone surface morphology may also have a great influence on the stress distribution within the adhesive zone. This concern arises because the bitumen interlayer has a minimum thickness of 15 μm and the roughness of the stone morphology ranges from 5 μm to 10 μm as measured at meso-scale. As a result, the thickness of the bitumen interlayer within the adhesive zone is different from point to point. When such an adhesive zone is subjected to a tensile loading, very complex stress states that are far from being uniform can thus be expected. To get insight into the stress states at a meso-scale level taking into account the stone surface morphology and the actual thickness of the bitumen interlayer, two finite element simulations were performed, the results of which are shown in Figure 4.12.

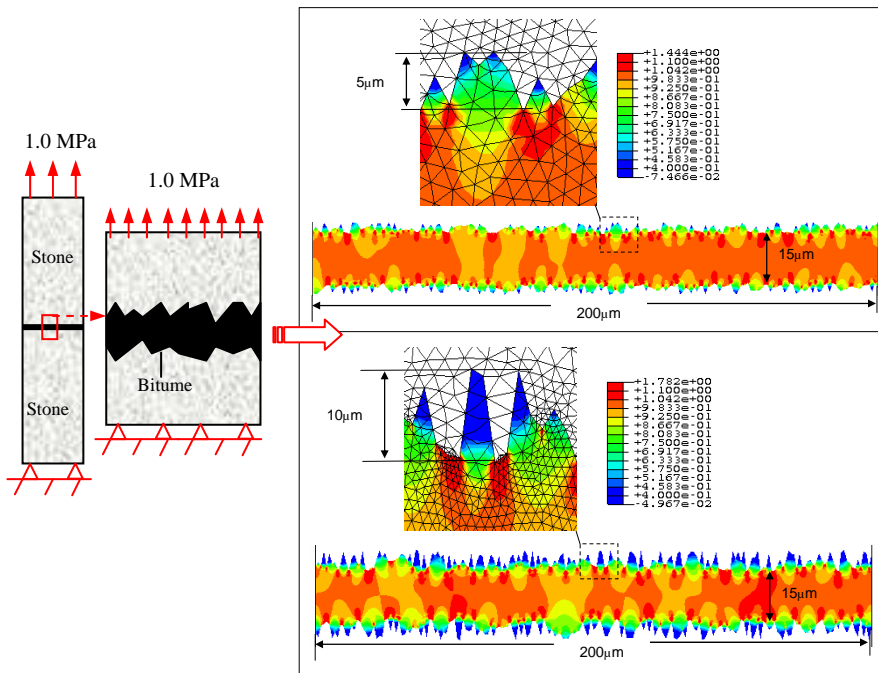


Figure 4.12 Stress distributions in the adhesive zones with different stone surface roughnesses (left: schematic of uniaxial tensile test; middle: a small local section of the adhesive zone; right-upper: 5µm roughness; right-down: 10µm roughness)

As discussed in Chapter 3, the stone morphology in 3D nature is very complex. Due to this a huge amount of degrees of freedom is required to model a small section of stone morphology. Compared to 2D models, 3D models are complex and expensive to use in terms of data preparation and computational time.

For practical reasons, a 2D stress analysis was therefore made. The length of the model was selected as 200µm. This length was believed to be long enough since the morphology measurement described in the previous chapter indicated that a square section of several hundreds microns was good enough for morphology analyses. The rough surface was generated by using a random function. The increment of distance was 1µm, which is in the same order of the resolution of the roughness measurements. The model consisted of two stone plates with length of 200µm and height of 600µm. These two stone plates were bonded together by a bitumen interlayer of 15µm thickness. Two different levels of stone roughness, e.g. the maximum peak-to-valley height, 5µm and 10µm were considered. Again, the material properties used in this model are the same ones as mentioned earlier. Stone sections were defined as rigid bodies due the huge difference of stiffness between stone and bitumen. One of the ends of the model was fully restricted and the other end was loaded with a tensile stress of 1MPa as shown in Figure 4.12. Due to the irregular shape, an 8-node triangle element was used and very fine meshes were generated as shown in image zooms.

Figure 4.12 gives an impression of the non-uniform stress distributions. High stress levels are found to occur at the peaks that point to the bitumen interlayer and low stress levels happen at the valleys that point to the stone. The stress levels at the peaks also differ from location to location. This figure also indicates that cavitation is likely to occur in these types of tension test.

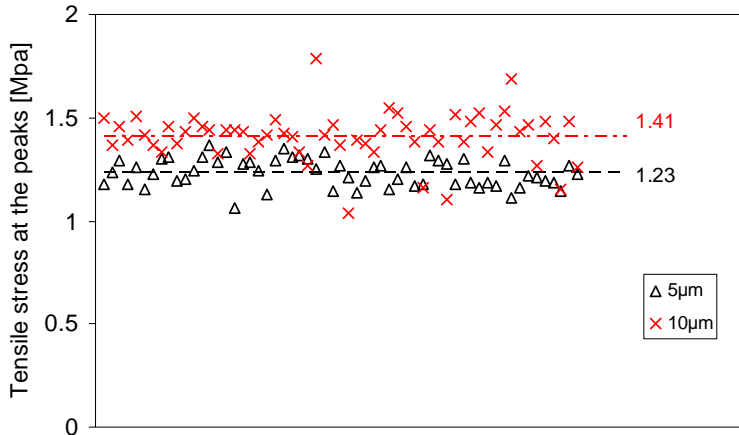


Figure 4.13 Computational tensile stresses at the peaks

In order to investigate the differences among these high stress levels, data points at the peaks were selected for each model and plotted in Figure 4.13. When comparing the data obtained with the 5µm roughness model and 10µm roughness model, it is found that the rougher surface results in a higher stress level as well as a larger scatter. The average of data obtained from the 5µm roughness model is 1.23MPa and a higher value of 1.41MPa can be found for the 10µm roughness model.

Based upon the analysis above, it is clear that the stress experienced by the adhesive zone can not simply be determined by using the so-called uniform stress approach, which is determined using the force divided by the cross-sectional area. The factors that may affect the stress should be taken into account. Among these, the edge effect of the adhesive zone can be neglected; this is shown by the computational results given in Figure 4.11. However, the stone roughness shows to have a significant influence on the stress distributions. Hereto, the following transfer function is given for interpretation of the tensile stress in the adhesive zone.

$$\sigma = k_1 \times \frac{F}{\pi \times r^2} \quad (4.1)$$

Where

σ = tensile stress, [MPa];

k_1 = the factor that accounts for surface roughness, $k_1 = 0.5 \times (1.23 + 1.41) = 1.32$;

F = force, [N];

r = specimen radius, 1.35mm.

4.2.2.3 Test results

Figure 4.14 shows the data from DMA dynamic testing over a temperature range of 0 to 20°C. Please note that the applied stress signal is $\sigma_0(\sin \omega t + 1.25)$. The results show some scatter, but clearly indicate trends. Tests at -10°C could not be performed due to limitations of the loading capacity of the machine. In total, 8 material combinations and three different temperatures were involved.

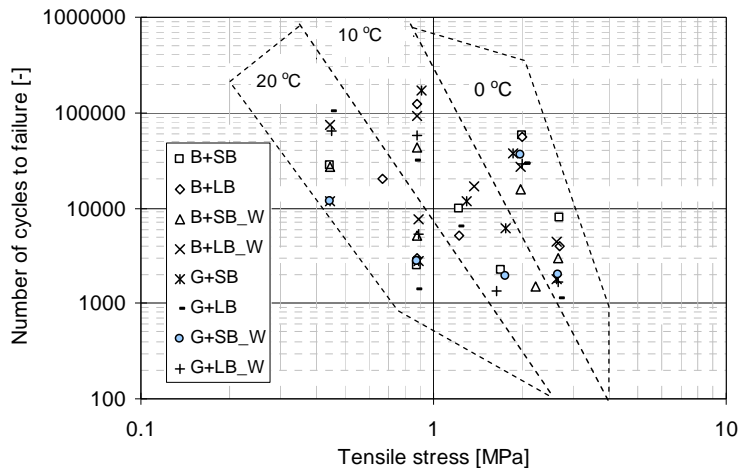


Figure 4.14 DMA dynamic test results using a stress signal of $\sigma_0(\sin \omega t + 1.25)$ (The legend of test series is given in Table 4.2. tensile stress is determined according to Equation 4.1)

Figure 4.15 shows the data from DMA static testing performed at -10°C and 20 °C. The data obtained from DMA additional testing performed at 10 °C using a sinusoidal-wave stress signal are also plotted. With respect to DMA static testing, the time to failure was recorded in seconds, while the number of cycles to failure is used for DMA additional testing.

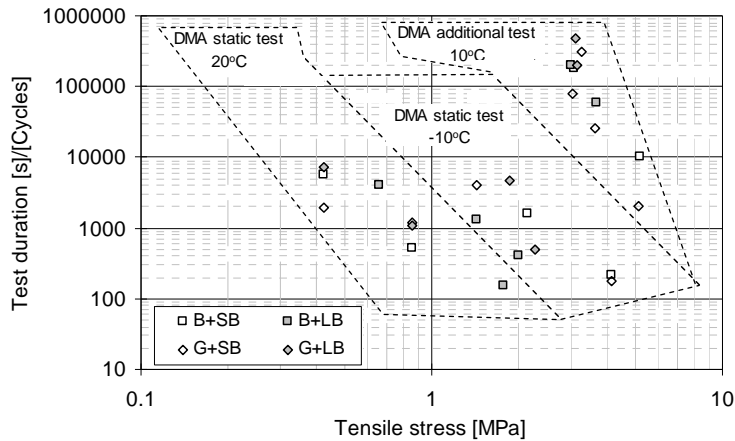


Figure 4.15 Time to failure for DMA static tests and number of cycles to failure for DMA additional test results using a pure sine signal, $\sigma_0 \sin \omega t$ (The legend of test series is given in Table 4.2. tensile stress is determined according to Equation 4.1)

4.2.3 DSR shear test

4.2.3.1 Test description

Shear tests on adhesive zones are also performed by means of DSR instruments. The specimens used for DSR testing are similar to the specimens used for DMA testing. The difference is that two stone columns with a diameter of 6.7mm replace the stone columns with a diameter of 2.7mm. The size of specimens used for DSR testing is determined based on a machine capacity (maximum torque) of about 150N.mm and estimated maximum bitumen strength of 2.5MPa. Again, these larger stone columns are glued together using a bitumen interlayer with the same minimum thickness as described in Section 4.2.2.1. The procedures of specimen preparation for DSR testing are similar to those for DMA testing and are thus not described here. Detailed information can be found elsewhere [Khedoe & Moraal 2007].

Figure 4.16 gives the DSR set-ups for adhesive zone testing. As can be seen, two DSR instruments were used to perform shear tests. One is a DSR Physical MCR 101 (Anton Paar Ltd., German) located at the Wuhan University of Technology (WHUT), China. The other is a DSR AR 2000ex (TA Instruments Ltd., USA) at the Delft University of Technology. The used test procedures are similar for both instruments. Special clamp systems are required to clamp the specimens into the DSR instruments. One end of the specimen was fixed into the upper clamp via the stone column, but the bottom end was glued using adhesives.

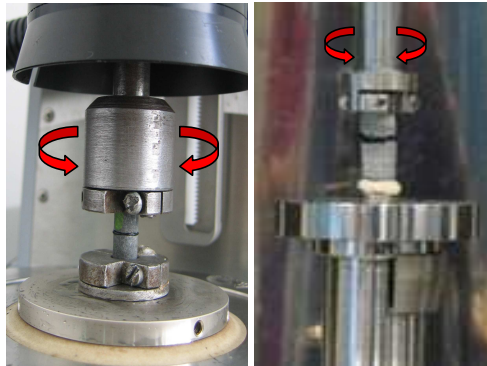


Figure 4.16 DSR set-ups for adhesive zone shear testing (left: DSR Physical MCR 101; right: DSR AR 2000ex)

In total, 8 material combinations including 2 types of stone (sandstone and greywacke), 2 types of bituminous binders (short-term aged bitumen and long-term aged bitumen) and water immersion, were considered:

- (1) Sandstone + short-term aged bitumen
- (2) Sandstone + long-term aged bitumen
- (3) Sandstone + short-term aged bitumen, water immersion
- (4) Sandstone + long-term aged bitumen, water immersion
- (5) Greywacke + short-term aged bitumen
- (6) Greywacke + long-term aged bitumen
- (7) Greywacke + short-term aged bitumen, water immersion
- (8) Greywacke + long-term aged bitumen, water immersion

Shear testing was performed under torque controlled mode. As shown in Figure 4.17, two different torque signals were applied. One is pure sinusoidal oscillatory torque $T_0 \sin \omega t$ and the other is haversine signal, $T_0(\sin \omega t + 1)$. To obtain such a haversine torque signal, a combination of oscillatory torque $T_0 \sin \omega t$ and constant rotation torque T_0 was used. Both torque signals were performed at a same frequency of 10 Hz. Most of the shear tests were performed using the pure sinusoidal signal under the so-called standard operation mode. Therefore, these tests hereafter are defined as DSR standard shear tests. Only a limited number of tests were carried out by using haversine torque signal $T_0(\sin \omega t + 1)$. This part of the tests is hereafter defined as additional DSR shear testing.

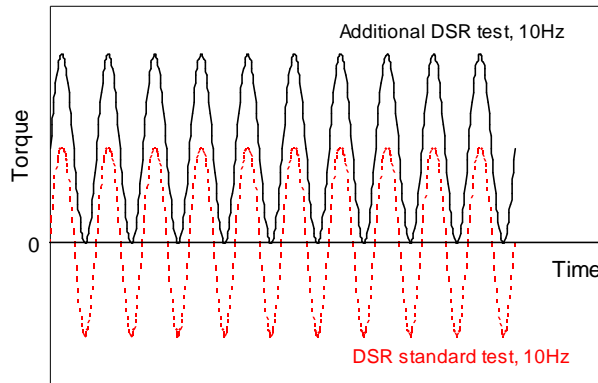


Figure 4.17 Applied torque signals for DSR shear testing on the adhesive zone

Test temperatures ranging from -10°C to 20°C were considered. However, it was found that tests at -10°C proved to be difficult to perform due to the strength of the adhesive zone and the limited machine capacity. The adhesive zone is so strong at -10°C that the DSR instruments can only bring specimens to failure after a very long period of loading at the maximum torque output. For this reason, only limited data is available at -10°C . To compensate for this loss, it was decided to perform a complete series of DSR standard tests at 5°C .

Most of the DSR standard tests were performed by the DSR Physical MCR 101 at WHUT except for the tests at -10°C . The reason is that the DSR AR 2000ex at TUD has a more powerful torque output than the DSR Physical MCR 101 and the former DSR was applied for standard tests at -10°C . Additional tests also were performed by the DSR AR 2000ex. Table 4.3 summarizes the DSR shear test program.

Table 4.3 Test program for DSR shear tests

Stone	Sandstone (B)				Greywacke (G)			
Bitumen	Short-term aged bitumen (SB), Long-term aged bitumen (LB)							
Water condition	Water immersion (W)							
Test combination	B+SB	B+LB	B+SB_W	B+LB_W	G+SB	G+LB	G+SB_W	G+LB_W
	Temperature ($^{\circ}\text{C}$)							
Standard tests (DSR 301)	0,5, 10,20	0,5, 10,20	0,5, 10,20	0,5, 10,20	0,5, 10,20	0,5, 10,20	0,5, 10,20	0,5, 10,20
Standard tests (DSR 2000ex)	-10	-10	-	-	-10	-10	-	-
Additional tests (DSR 2000ex)	10	10	-	-	10	10	-	-

Note: the number e.g. -10, 0,5,10 and 20 indicates the test temperature.

4.2.3.2 Test interpretation

The following steps were undertaken for test interpretation: firstly, insight into the edge effect on the stress states within the adhesive zone is required. To do this, finite element modelling was used to investigate if there are high stress gradients occurring at the free boundaries of the bitumen interlayer. Secondly, the non-uniform stress state in the adhesive zone will be taken into account by means of finite element models at meso-scale. Again, the morphology of the stone surface was considered in the models.

Figure 4.18 gives the computational results on the shear stress distributions within the adhesive zone. As indicated, the model consists of two stone columns glued by a thin bitumen interlayer of 15 μm thickness. The modelled stone columns are 6.8mm diameter by 10 mm height. The material properties used as model input are the same as those used in the previous simulations. Both of these materials are defined as deformable bodies.

As shown in Figure 4.18, the movement of the bottom stone column is fully restricted. However, the movement of upper stone column is only restricted in the horizontal direction; it is allowed to rotate around the central axis. A 20-node hex-structured mesh element was used. The torque is applied at the end of the upper stone column by means of forces. As a result, a total torque of 61.739N.mm was applied to the adhesive zone and the corresponding maximum shear stress to which the adhesive zone is subjected is, in theory, 1MPa. As can be seen from Figure 4.18, the shear stress varies linearly with the distance to the centre and the maximum shear stress that occurs at the edge is the same as the theoretical value. It thus indicates that the edge effect of the bitumen interlayer on the stress state is negligible.

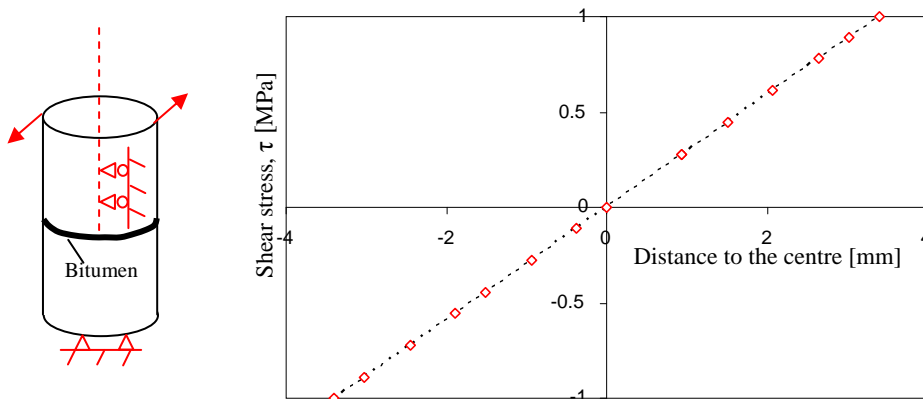


Figure 4.18 Schematic illustration of the shear test (left) and linear variation of the shear stress with the distance to centre (right) (where: $\tau = [\tau_{zx} + \tau_{zy}]^{0.5}$ with z axis normal to the bitumen film).

Figure 4.19 gives the computed stresses in the adhesive zone when stone surface morphology is taken into account. For the similar reasons as mentioned earlier, the

meso-scale model hereof is making use of a limited arc section of the adhesive zone (see Figure 4.19). The shear stress in this limited arc section can be regarded as constant since the distance of each point to the centre is the same. This limited arc section can be further simplified by using a small plate section when the length is limited. Finally, the meso-scale model only consisted of two small stone plates glued with a bitumen layer (see Figure 4.19).

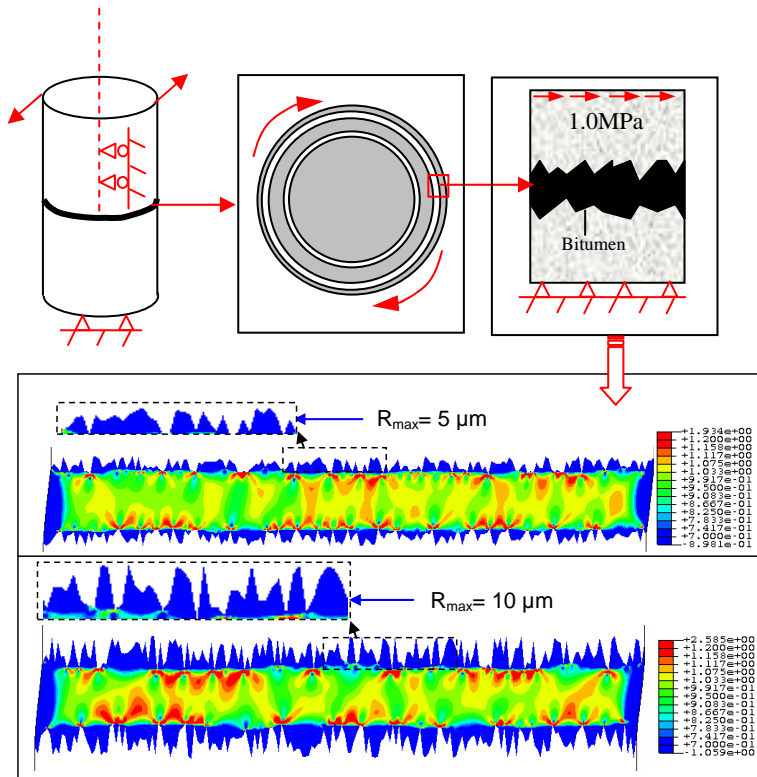


Figure 4.19 Schematic illustration of the shear test (upper-left) modelling, a small arc section where the shear stress is constant (upper-middle), 2D illustration of a limited arc of the adhesive zone(upper-right), non-uniform state of shear stress within the adhesive zone taking into account the surface morphology (bottom)

For reasons of simplicity, use is made of the same morphologies as used for the tension simulations described in Section 4.2.2.2. However, the boundary conditions and the loading are different. As shown in Figure 4.19, the bottom stone section is fully restricted. The upper stone section is limited in rotation while the vertical and longitudinal movements are free.

A shear force of 0.2 N was applied on the upper stone section. The corresponding theoretical value of shear stress in the adhesive zone is then equal to 1MPa (see Figure 4.19). As a result, the computed stress in the adhesive zone is based on a

reference stress of 1MPa. For any other applied stress, the resulting stress in the adhesive zone can be calculated by means of the linear rule.

Figure 4.19 shows that the states of shear stress within the adhesive zone are highly non-uniform as indicated by the various colours. The red parts in the plots show high stress concentrations. These stress concentrations occur at the peaks of the bitumen-stone boundaries in the direction that they point to the bitumen. The bitumen that is embedded in the texture of the stone surface seems to experience very small to no shear stress. As one can find, the stress concentrations are much larger than the uniform shear stress of 1MPa calculated theoretically. Furthermore, the rougher stone surface will result in a higher level of shear within the adhesive zone. For example, the maximum shear stress is 1.934MPa when $R_{max}=5\mu\text{m}$; while the maximum value becomes 2.585MPa when $R_{max}=10\mu\text{m}$.

Figure 4.20 gives an impression of the data scatter of the shear stress concentrations due to surface textures. Large scatter can be observed in this plot. The average value of the stresses concentrations is about 1.34MPa when $R_{max}=5\mu\text{m}$. The rougher surface with $R_{max}=10\mu\text{m}$ shows a higher average value of 1.46MPa.

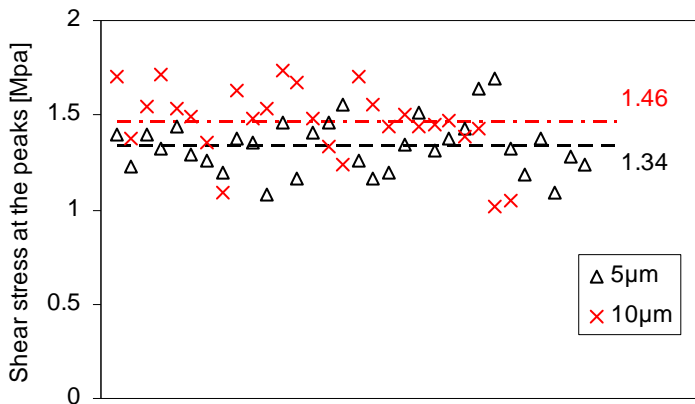


Figure 4.20 Data scatter of shear stresses concentrations due to different surface morphology

The analysis considering the edge effect on the stress state indicates that the shear stress can be calculated using the conventional analytic function. However, high stress concentrations due to are surface morphology are found through finite element simulations at meso-scale. A combined function is proposed to calculate the shear stress at the outside edge of the adhesive zone, that is, the so-called maximum value.

$$\tau = k_2 \times \frac{2 \times T}{\pi \times r^3} \tag{4.2}$$

Where:

τ = shear stress, [MPa];

k_2 = the factor that accounts for surface roughness, $k_2 = 0.5 \times (1.34 + 1.46) = 1.40$;
 T = torque, [Nmm];
 r = specimen radius, 3.4mm.

It is expected that the stress concentrations may govern the failure of the adhesive zone. In Equation 4.2 the actual value of k_2 that stands for the factor of stress concentration is difficult or impossible to determine due to complex morphology of stone surface. Finite element simulations show that k_2 can range from 1 to 2.6. For the reason of simplicity, the average of both factors determined from the models is used.

4.2.3.3 Test results

Figure 4.21 shows the data obtained from DSR standard fatigue testing using a sinusoidal-wave stress signal. The number of cycles to failure is plotted on log-log scale against the shear stress determined by Equation 4.2. The scatter and temperature effect can clearly be observed. Again tests at -10°C proved to be difficult to perform due to the strength of the adhesive zone and the limited machine capacity. Most of the data at -10°C were thus obtained by setting the machine to its full capacity. Due to time constraints, only a limited amount of tests at lower stress levels is performed at -10°C . Considering the large scatter of the fatigue data, the effects of the type of stone, aging and water conditioning cannot be clearly distinguished in this plot. Only temperature effects are visible. Five distinct temperature trends are observed by drawing straight lines in this log-log plot. In this way the effect of temperature on the shear fatigue behaviour of bitumen-stone adhesion has been established. As temperature drops, all of the material combinations show a better fatigue resistance. The slope of straight line tends to be steeper with a decline in temperature.

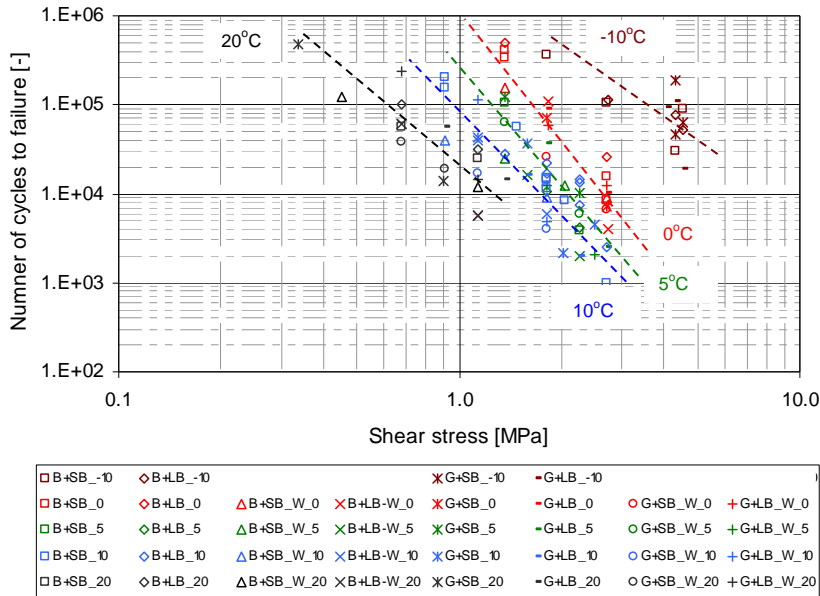


Figure 4.21 DSR standard fatigue test results under sine-wave stress signal (shear stress is determined using Equation 4.2. the legend of test series is referred to Table 4.3)

Figure 4.22 shows the DSR additional fatigue test results obtained at 10°C under a haversine signal $T_0(\sin \omega t + 1)$. For the purpose of comparison, the DSR standard fatigue test results at 10°C under a pure sinusoidal-wave stress signal $T_0 \sin \omega t$ are also plotted in this figure. Generally speaking, the additional shear fatigue tests tend to result into a smaller number of cycles to failure than those done by standard shear fatigue tests. The lower number of cycles to failure obtained in the additional tests is most probably caused by creep effects. It indicates that the shape of stress signal has a significant influence on the fatigue life of the adhesive zone. This strongly demonstrates the premise that the desired damage model for the adhesive zone must take into account the stress history to which the adhesive zone is subjected. The data obtained from additional fatigue tests will be used for the purpose of model verification but not for the determination of model parameters.

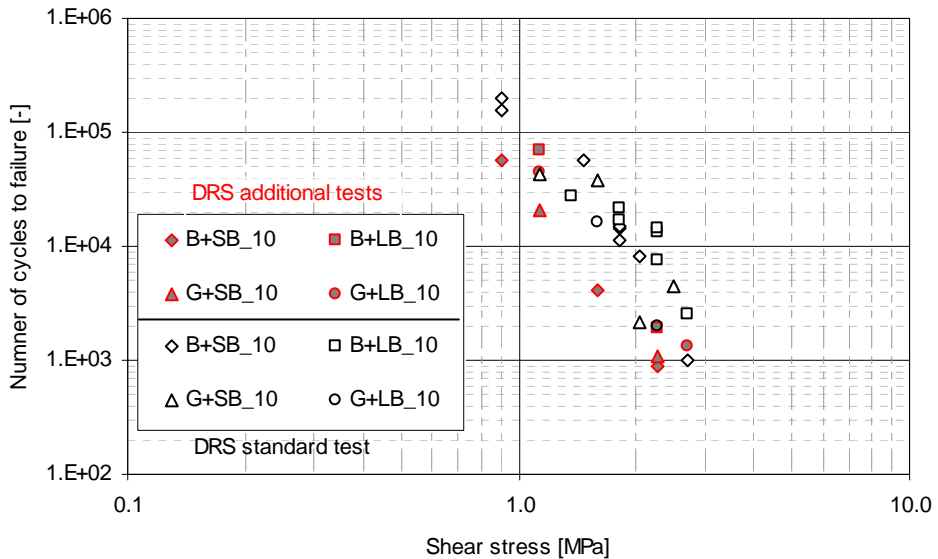


Figure 4.22 Comparison of DSR additional test results using haversine torque signal $T_0(\sin \omega t + 1)$ with DSR standard test results using pure sine signal $T_0 \sin \omega t$ at 10°C (Shear stress is determined using Equation 4.2. The legend of test series is given in Table 4.3)

4.2.4 Combined normal-shear test

4.2.4.1 Test description

As stated earlier, the adhesive zone is subjected to a combination of normal and shear stresses. The test plans for DMA testing and DSR testing only provided information on the damage development of the adhesive zone when experiencing either pure tension or shear. Insight into the effect of the combined stresses on fatigue damage is thus of great importance. A new type of test that allows for application of a combination of shear and normal stresses on the adhesive zone is required. For this reason, two different test set-ups were developed as shown in Figure 4.23. Firstly, a special test set-up with an oblique angle of 45° to vertical was designed at the Adhesion Institute of the Faculty of Aerospace Engineering, TUD. Tests were carried out on a hydraulic machine in the force controlled mode. The used specimens are the same as the ones used in the DSR testing mentioned earlier. Before the specimens were placed into the machine they were first glued to special socket head cap screws. During the whole process alignment is assured by using a simple but effective V-shape alignment tool. More detailed information on these tests can be found elsewhere [Hofstede 2007]. Due to the oblique angle of 45° , the normal and shear forces acting on the adhesive zone can be determined by decomposing the applied hydraulic force according to the parallelogram rule. A schematic impression of these force signals is given in Figure 4.24. Hereafter, this type of test is called oblique shear

test in short.

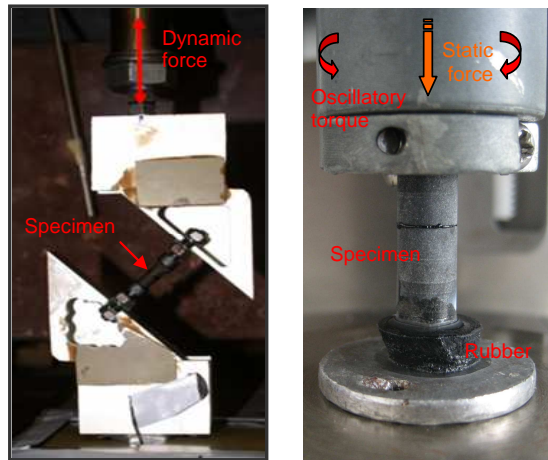


Figure 4.23 Combined normal-shear test setups (left: 45° oblique test; right: DSR combined test)

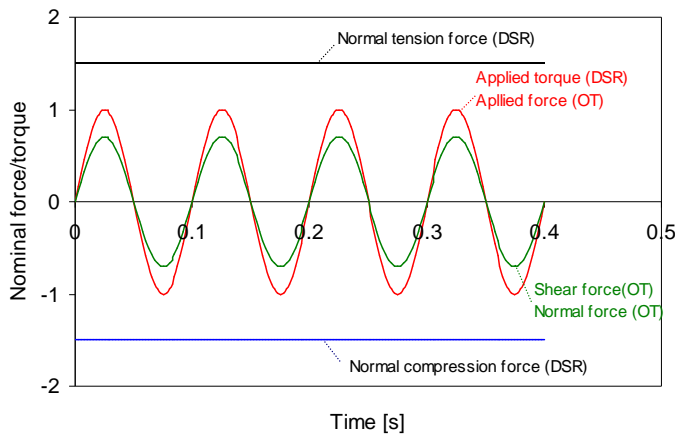


Figure 4.24 Schematic representation of the loading signals used for the combined normal-shear testing on the adhesive zone (OT: oblique shear test)

An attempt to achieve a combination of normal and shear stresses was also made by application of the DSR instruments in the way as shown in the right hand side of Figure 4.23. To do this, both normal and shear forces needs to be applied on the specimens. The available DSR instruments can only apply a constant static force, while an oscillatory torque can be applied at the same time. The applied static force and oscillatory torque signals are graphically shown in Figure 4.24.

As can be seen in Figure 4.23, the main difference between the DSR test and the

normal-shear combined test on the adhesive zone is the introduction of a rubber element for the latter. The reason for this is that the thickness of the adhesive zone is very thin and thus hardly deforms. As a result, the applied normal force was quite difficult to control by adjusting the vertical deformation during the test. A small change in the vertical deformation may result in a significant change of the applied normal force. Initial trials indicated that the normal force signal is fairly noisy. After introduction of the rubber element, ample deformation is allowed for the whole set-up thus making the machine more flexible to control the vertical deformation and the normal force accordingly.

Table 4.4 gives a summary of the test program for the combined normal-shear testing. Please note that data obtained from these two types of combined stress tests will be used for model verification purposes. Only a limited amount of tests were planned and the effect of water immersion was not considered.

Table 4.4 Test program for combined normal-shear testing

Stone	Sandstone (B)		Greywacke (G)	
Bitumen	Short-term aged bitumen (SB) or Long-term aged bitumen (LB)			
Test combination	B+SB	B+LB	G+SB	G+LB
	Temperature (°C)			
Oblique test	-10,0, 10,20	-10,0, 10,20	-10,0, 10,20	-10,0, 10,20
DSR combined test	10	-	10	-

Note: the number e.g. -10, 0,5,10 and 20 indicates the test temperature.

For the oblique shear tests, four material combinations including 2 types of stone (sandstone and greywacke), 2 types of bituminous binders (short-term aged bitumen and long-term aged bitumen) were considered:

- (1) Sandstone + short-term aged bitumen
- (2) Sandstone + long-term aged bitumen
- (3) Greywacke + short-term aged bitumen
- (4) Greywacke + long-term aged bitumen

Test temperature varied from -10°C to 20°C. All the oblique shear tests were done at a frequency of 10Hz with a pure sine-wave.

DSR combined normal-shear tests were done on two material combinations:

- (1) Sandstone + short-term aged bitumen
- (2) Greywacke + short-term aged bitumen

The tests were only done at a temperature of 10°C. The frequency of the oscillatory torque is 10Hz with a pure sine-wave.

4.2.4.2 Test interpretation

As stated earlier, the stone surface morphology has a great influence on the stress states for both DMA tension testing and DSR shear testing. It is expected that the same influence also holds for the combined normal-shear testing. For this reason, the same factors that account for the effect of the surface roughness on tension and shear stresses will be applied to the stress components acting on the adhesive zone during the combined normal-shear testing. Due to the oblique angle of 45°, the normal and shear stresses that the adhesive zone is subjected are expressed as follows.

$$\sigma_n = k_1 \times \frac{F \sin 45^\circ}{\pi r^2} \text{ and } \tau = k_2 \times \frac{F \cos 45^\circ}{\pi r^2} \quad (4.3)$$

Where

σ_n = normal stress, [MPa];

τ = shear stress, [MPa];

k_1 = the factor of normal stress due to surface roughness, $k_1 = 1.32$;

k_2 = the factor of shear stress due to surface roughness, $k_2 = 1.40$;

F = applied force via the machine, [N];

r = specimen radius, $r = 3.4\text{mm}$.

With respect to DSR combined normal-shear tests, the normal and shear stresses are calculated by using Equations 4.1 and 4.2 respectively.

4.2.4.3 Test results

Figure 4.25 shows the results obtained from the oblique shear tests. The number of cycles to failure is plotted against the net stress that consists of the normal and shear stresses acting on the adhesive zone. Due to the limited number of data points and scatter, the temperature trends could not be well distinguished. Dashed lines are used to indicate the temperature trends.

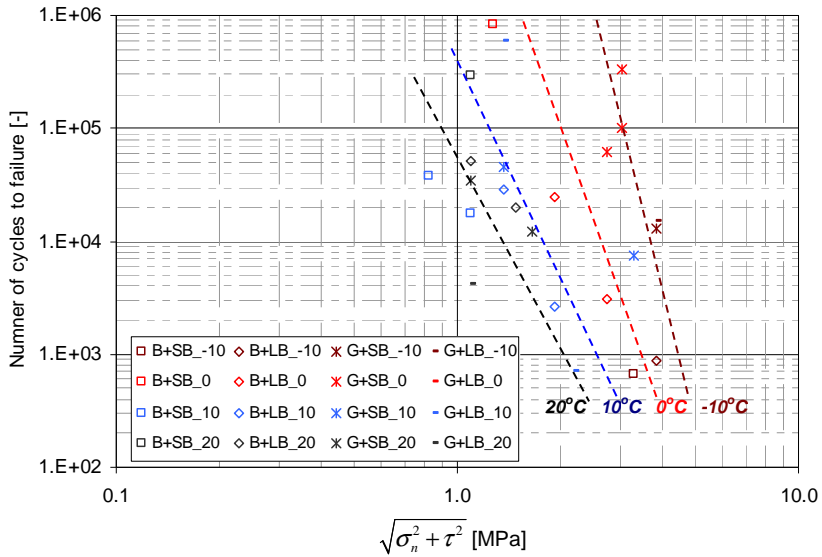


Figure 4.25 Fatigue test results of the oblique tests (σ_n : normal stress; τ : shear stress. k_1 and k_2 are applied for stress calculation.)

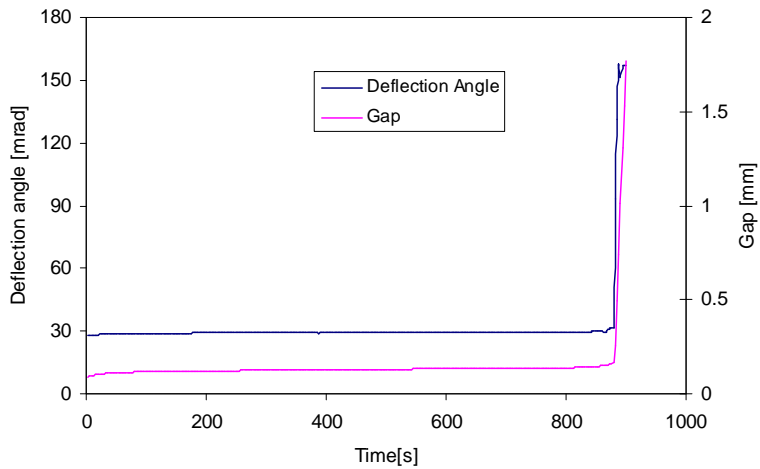


Figure 4.26 Typical deflection and gap (vertical displacement) signals for the combined tension-shear testing

Figure 4.26 gives a typical result from DSR combined tension-shear testing. As can be seen, the radial deflection angle (e.g. torsion angle) and the gap distance, that is, the vertical displacement, remain fairly constant until the two stone columns are separated. The combined compression-shear testing was found to be difficult to

perform. The reason for this is that the two stone surfaces that are glued together by the bitumen interlayer can not be perfectly parallel and horizontal. Furthermore, a normal compressive force will further reduce the thickness of the bituminous interlayer. Direct contact of the two stone surfaces may occur when the stone columns try to rotate. As a result, the friction induced by this direct stone to stone contact is so large that it is able to resist the applied torque. This phenomenon has been proven by doing tests on two bare stone columns without bitumen binding them together. It was found that this type of testing lasted a very long time and the moment of failure was very hard to define. As a result, only data under the combined tension-shear testing are available, as listed in Table 4.5. The table shows that tests were done using three tension-shear combinations.

Table 4.5 DSR combined tension-shear test results at 10°C

Bitumen	Stone	Shear stress [MPa]	Normal stress [MPa]	Fatigue life [cycle]
SB	B	0.80	0.40	8790
SB	B	0.80	0.80	4860
SB	B	0.40	0.80	2070
SB	G	0.80	0.40	2610
SB	G	0.80	0.80	2580
SB	G	0.40	0.80	600

4.3 Mortar fatigue test

4.3.1 Introduction

Ravelling is a surface defect caused by repeated contact loads occurring between the tire and the road surface due to moving wheels. As a result of this, the mortar bridges connecting the coarse particles are subjected to complex 3D states of stress, changing from point to point. Figure 4.27 gives an impression of the stress state in the mortar bridges as determined by means of finite element simulations of porous asphalt concrete [Mo & Huurman et al. 2007, 2008]. Further analysis of the stress/strain signals indicated that there is no predominant direction of stress that allows for the prediction of mortar failure. Also the stress/strain signals are far from sinusoidal as commonly applied in classical fatigue tests.

It was foreseen that a model that is able to explain mortar fatigue under any 3D state of stress requires laboratory data obtained under a range of stress states. Therefore, the fatigue behaviour of the mortar was determined using a combination of DSR shear testing and DMA bending testing.

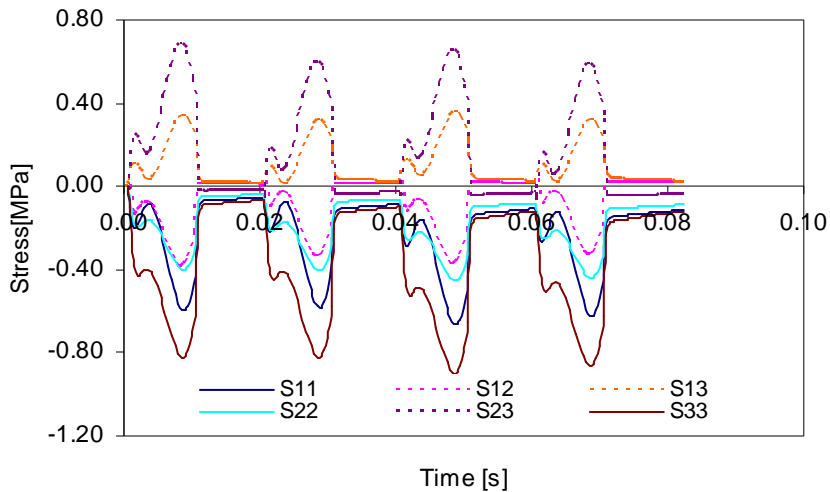


Figure 4.27 Complex stress development during four tyre passages (S_{ij} ($i,j=1,2,3$): stress components in 3D nature) [Mo & Huurman et al. 2008]

4.3.2 DSR shear test

4.3.2.1 Test description

The mortar discussed hereafter is described in the previous chapter. Two types of mortar being, short-term aged and long-term aged mortar were subjected to fatigue testing. After aging, the mortar was heated to 175°C and agitated until it was ready to pour. The mortar was carefully poured into a special designed mould made of silicone plastic to prepare samples as shown in Figure 4.28. After casting, the mould was placed in an oven with a temperature of 175°C for 5 minutes to remove air voids in the specimen. Then, the mould was first cooled down at room temperature and then stored at -10°C for 2 hours before the mould was opened to remove the samples. Further information on specimen preparation can be found elsewhere [Khedoe & Moraal 2007].

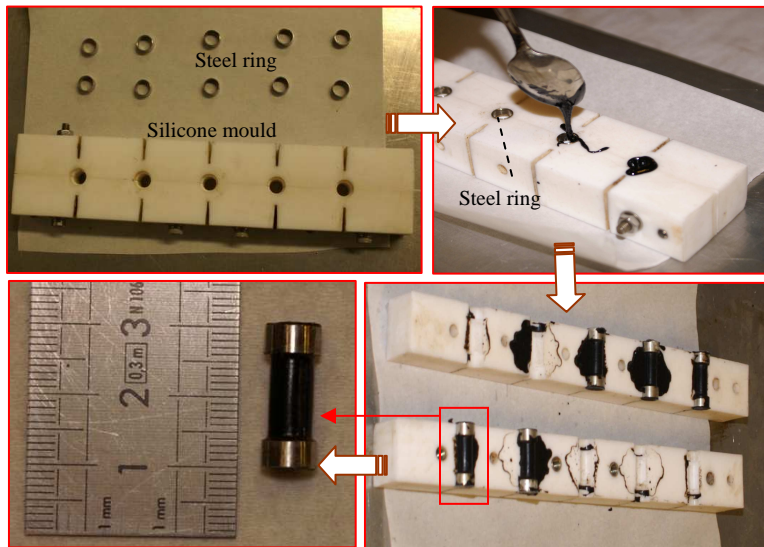


Figure 4.28 Preparation of the mortar specimens (upper-left: steel rings and silicone mould; upper-right: casting hot mortar into the mould; bottom-right: opening the mould to remove the samples; bottom-left: the obtained sample.) [Khedoe & Moraal 2007]

Figure 4.29 shows the entire test set-up and the specimen. The total height of the specimen is 20mm, in which a column with 10 mm height and 6 mm diameter is the effective section for testing. At each end, a steel ring with an inner diameter of 7mm, an outer-diameter of 8 mm and a height of 4mm was placed for the purpose of clamping. Therefore, the clamps did not touch the mortar directly, but only touched the two steel rings at both ends. This was done because the elastic-visco characteristics of mortar would result in loose contact due to relaxation effects. The adhesion between the mortar and steel ring was found to be strong enough and no failure between the ring and the mortar was observed during testing.

The mortar shear fatigue tests were performed on short-term aged and long-term aged mortar as well as the samples which had received a water conditioning treatment. The water conditioning protocol consisted of submerging the specimens in 5 °C water under vacuum for 1 hour. As a result, the following 4 combinations were tested:

- (1) Short-term aged mortar;
- (2) Long-term aged mortar;
- (3) Short-term aged mortar plus water immersion;
- (4) Long-term aged mortar plus water immersion.

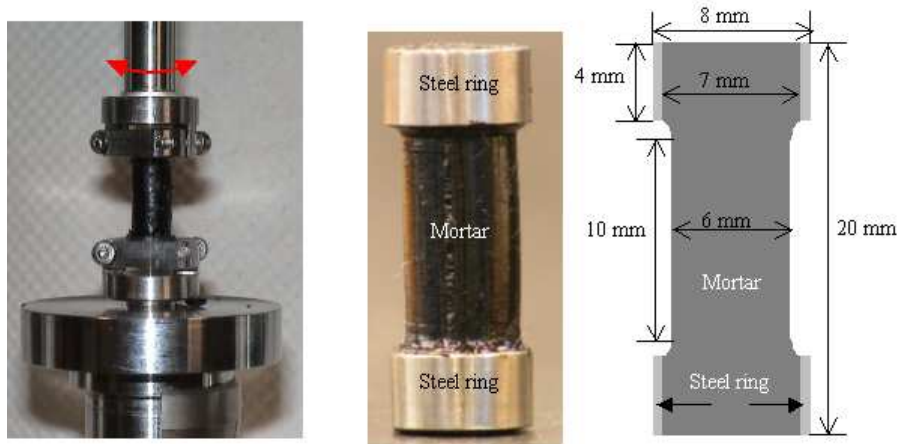


Figure 4.29 Mortar shear fatigue testing (left: specimen assembled in modified DSR test set-up; middle: overview of specimen; right: relevant sizes of specimen section)

The tests were performed at two temperatures (0°C and 10 °C) and two frequencies (10Hz and 40Hz). The applied torque-time signal was a pure sinusoidal wave under torque controlled mode. Table 4.6 gives a summary of the mortar shear fatigue tests. Given the number of tests that had to be performed, two DRS instruments, the DSR AR 1000 and DSR AR 2000ex were used to perform the tests. The DSR AR 1000 has smaller torque capacity and was mainly used to carry out the tests at 10 °C, whereas the DSR AR 2000ex is more powerful, and was mainly used for tests at 0 °C and for tests for which a relatively high stress levels were required.

Table 4.6 Summary of mortar shear fatigue tests

Mortar	Short-term aged mortar (SM)		Long-term aged mortar (LM)	
Water conditioning	5 °C water, vacuum, 1 hour			
Test combination	SM	SM_W	LM	LM_W
Temperature	0 °C and 10 °C			
Frequency	10Hz and 40Hz			

4.3.2.2 Test interpretation

Mortar shear fatigue testing was performed under torque controlled mode using a pure sinusoidal-wave oscillatory torque. During testing, the applied torque was continuously recorded. Also the induced radial deflection angle (torsional angle) was measured and recorded accordingly. The phase angle between the torque signal and the displacement signal also was recorded. Figure 4.30 gives typical results of these

signals. The moment of failure is obtained by forward and backward extrapolation of the measured displacement signal as indicated in Figures 4.6 by the arrows.

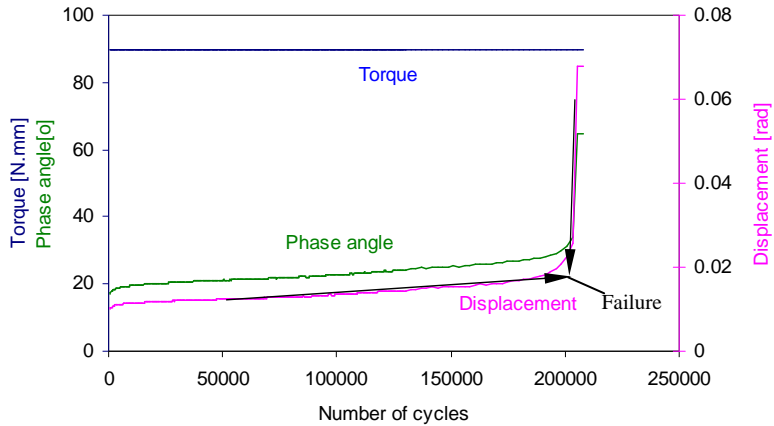


Figure 4.30 Typical results of mortar shear fatigue testing

For fatigue life analysis, the applied torque and the measured displacement were translated into shear stress and strain respectively by taking into account the geometry of the specimen.

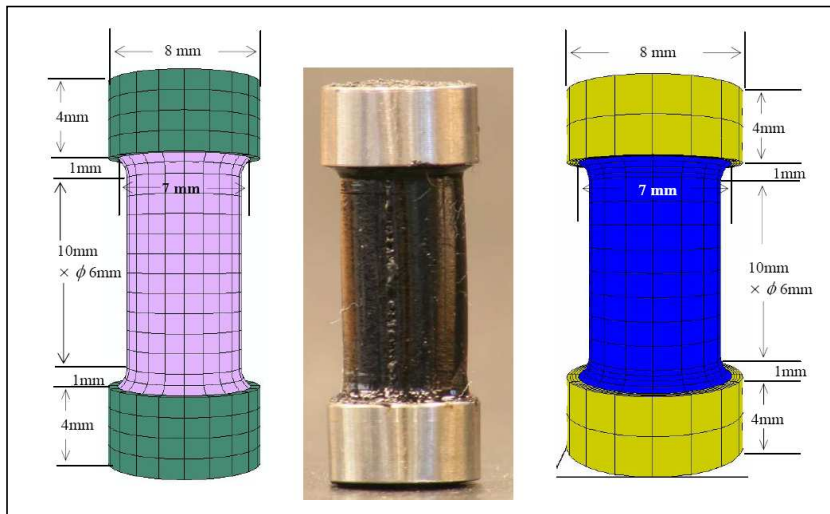


Figure 4.31 Mortar specimen for DSR shear testing (left: ABAQUS representation; Middle: real specimen; right: CAPA 3D representation)

In order to determine the relevant geometry factors, finite element simulations

were performed. Both the ABAQUS and CAPA-3D [Scarpas 1993] programs were used to perform the analysis. In both cases, the model was subjected to a torque of 70N.mm acting on the upper steel ring while restraining the bottom ring. The material properties of mortar were: shear modulus $G = 100\text{MPa}$ (that is $E = 290\text{MPa}$) and $\nu = 0.45$. The computed displacement is 0.06967 rad and 0.06951 rad for the CAPA-3D and ABAQUS simulation respectively. The difference between these two computations in the computed radial deflection angle is only 0.2%, which indicates the accuracy of the finite element models. Only the results from CAPA-3D simulations were used for the following analysis.

Figure 4.32 shows that the highest shear stress occurs along the curved edge in the vicinity of the steel ring where the diameter of the sample is varied from 6mm to 7mm. It is stated explicitly that the observed phenomenon is independent of the mesh topology; this was demonstrated by varying the mesh generation. Due to the stress concentration, the redesign of the specimen was considered with the aim of achieving a specimen shape in which the stresses would be fully homogeneous. However, various finite element simulations with different specimen shapes shown that the concentrated shear stress will always develop at the specific location where the middle part of the cylinder specimen widens to meet the rings. An indication hereof is given in Figure 4.33.

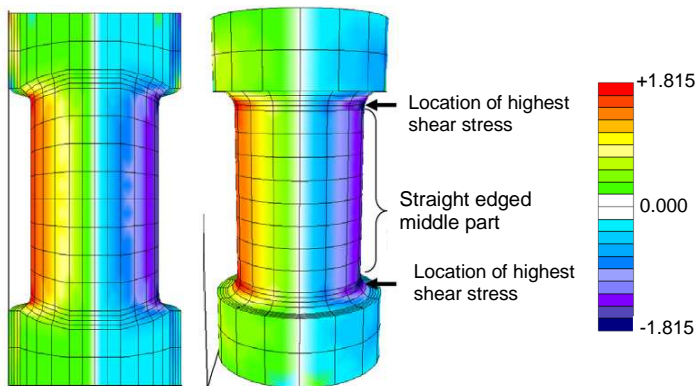


Figure 4.32 Shear stress distributions along the mortar column

The analysis above showed that a redesign of the specimens was needed. This however was not an option because of time limitations. It was therefore decided to determine the significance of the observed phenomenon by means of finite element modelling. In this way, the transfer functions for stress and strain can be determined.

Figure 4.34 gives an impression of the shear stress distributions at the mid height of the mortar column (middle section) and at the location where the highest stress occurs (edge section), when the specimen is subjected to a torque of 70N.mm. The maximum shear stress at the middle section is 1.645MPa, which is almost identical with the theoretical value of 1.650MPa. However, the maximum shear stress in the edge section is 1.812MPa, approximately 10 percent higher than the one in the middle section. Figure 4.34 also shows that except for the small area close to the outer edge, the main area of the edge section is subjected to a lower stress level than the middle

section. This observation leads to a conclusion that the effect of stress concentrations would probably remain limited as specimen failure demands for material failure over a full cross section. On the other hand, the stress concentrations might lead to early failure at these locations resulting in a redistribution of stress at those locations. If this is the case, failure near the caps is likely to occur. After observing the location of failure in numerous specimens, it was found that approximately 50% of the specimens failed at the location where the highest stress was computed (see Figure 4.35). The other 50% failed in the straight edged middle part of the specimens.

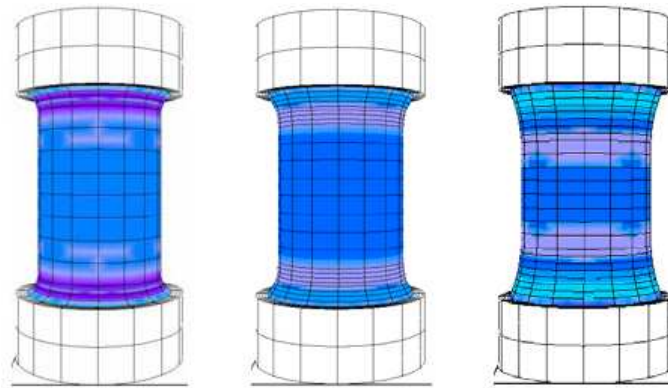


Figure 4.33 Shear stress concentrations in different specimen shapes

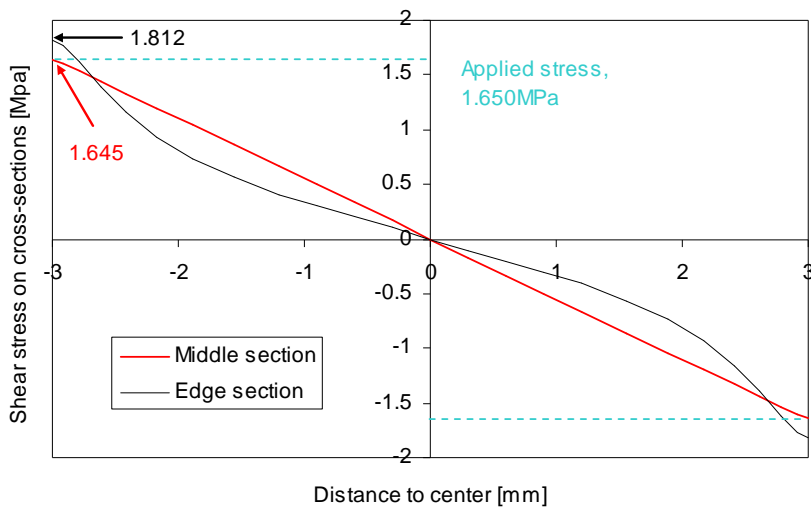


Figure 4.34 Shear stress distributions in the middle and edge sections

The transfer functions to relate the torque and the displacement to shear stress and strain at the outer edge of the mortar column can be explained using the following standard equations.

$$\tau = \frac{2 \times T}{\pi \times r^3} \quad (4.4)$$

$$\gamma = \frac{r \times \theta}{h_{\text{eff}}} \quad (4.5)$$

Where

- τ = shear stress, [MPa];
- T = torque, [N.mm];
- r = specimen radius, 3mm;
- γ = shear strain;
- θ = measured deflection angle, [rad];
- h_{eff} = specimen effective height, 12.742mm.

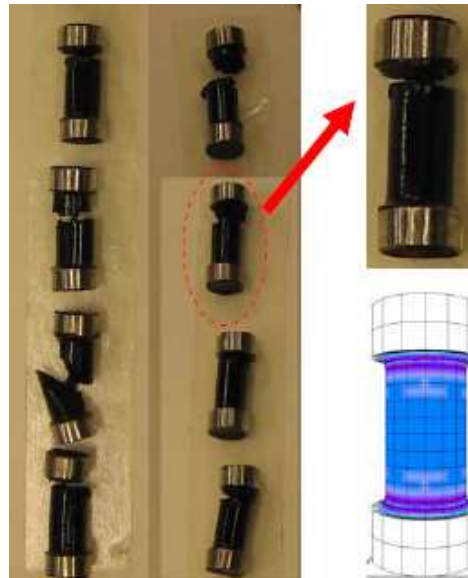


Figure 4.35 Impression of locations of specimen failure

The CAPA-3D simulation mentioned above showed that a torque of 70N.mm induced a radial deformation angle of 0.06971 rad. Accordingly, the computed shear stress and strain at the outer edge of the mortar column are equal to 1.645MPa and 0.01640, respectively. Combining the applied torque with the induced stress, one can calculated backward that the stress factor that accounts for the sample geometry is equal to 0.02357 MPa/(N.mm), which is identical with $\frac{2}{\pi \times r^3}$. Similarly, the strain

factor can be calculated as 0.2354 /rad. Since the strain factor stands for $\frac{r}{h_{\text{eff}}}$, the effective height h_{eff} is thus equal to 12.742mm. This value is larger than the total height between two steel rings, 12mm, indicating that the mortar embedded in steel rings contributes a little bit to the total deformation. This is demonstrated by the shear stress distributions in the vertical cross-section as shown in the left-hand plot of Figure 4.32.

Please note that Equations 4.4 and 4.5 are used to calculate the stress and strain at the straight edged middle part of the specimen. To take into account the effect of stress concentrations at the location close to the rings, a calibration factor is introduced.

$$\tau = k_3 \frac{2 \times T}{\pi \times r^3} \quad (4.6)$$

$$\gamma = k_3 \frac{r \times \theta}{h_{\text{eff}}} \quad (4.7)$$

Where:

k_3 = the calibration factor that accounts for stress concentration, $k_3 = 1.10$.

The analysis above indicates that determination of the stress/strain for a mortar fatigue test can only be performed in combination with the torque/deformation and the failure location which is known after the completion of test. In the cases that failure occurs at the middle section, Equations 4.4 and 4.5 can be used for the calculation of stress/strain. In the cases that failure occurs close to the steel ring, Equations 4.6 and 4.7 must be used.

It must be noted that this knowledge was not available at the early stage of the mortar fatigue testing and information on the failure location of each specimen was not reported in relation to the specimen number.

Due to lack of information of the failure location of each specimen and taking into account that approximately 50 percent of the specimens failed at the middle section and 50 percent failed at the edge section, the value of k_3 is determined as the average between 1 and 1.10 to minimize the effect of stress concentrations. For this reason, Equations 4.6 and 4.7 are applied for test interpretation together with $k_3 = (1+1.10)/2=1.05$.

It must state that this method is conservative to some extent and it is not suggested for the future mortar fatigue tests. Different equations should be applied for the calculation of the stress and strain dependent on the failure location. For each specimen this location should also be reported together with other data.

4.3.2.3 Test results

Figure 4.36 shows the results of mortar fatigue tests done at temperatures of 0 and 10 °C and frequencies of 10 and 40Hz. It must be noted that the shear stress shown on the x-axis was determined by Equation 4.6 with $k_3=1.05$. Due to data scatter, the effects of frequency and water conditioning can not be clearly distinguished in this

plot. Only temperature and aging effects could be made visible. These are indicated by means of the trend lines. The figure shows that the mortar exhibits a better fatigue resistance under torque controlled mode when the temperature decreases. This figure also indicates that aging has a positive effect on the fatigue life at 10°C. However, when the test temperature reduces to 0°C, the effect of aging becomes mixed. In general, the effects of aging or temperature are dependent on the applied stress levels and both of them tend to be negative at relatively low stress levels. This may be explained by the fact that damage grows more rapidly as bituminous materials become harder.

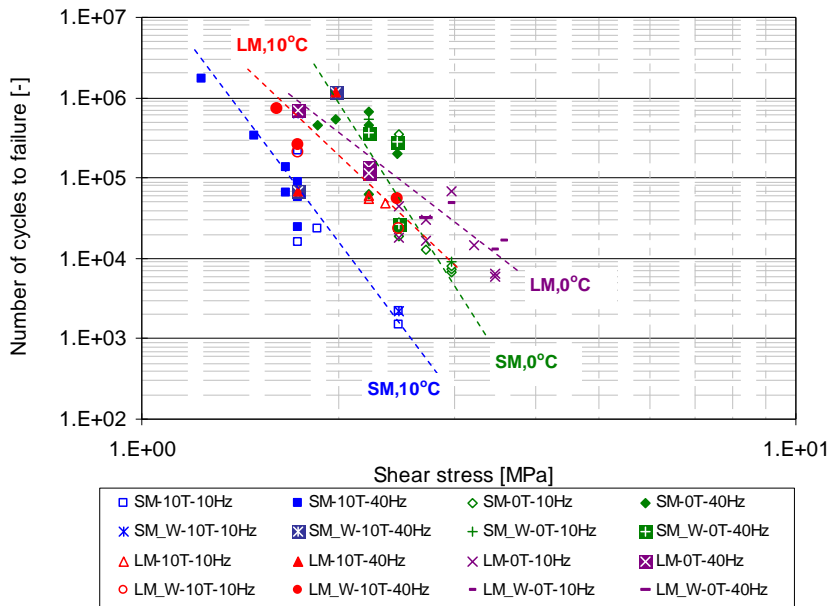


Figure 4.36 Results of mortar shear fatigue tests at various test conditions (Shear stress = theoretical shear stress \times 1.05; the legend is referred to Table 4.5)

4.3.3 DMA dual cantilever bending test

DMA dual cantilever bending tests were performed to provide information on fatigue behaviour under stress states which differ from the shear stress conditions as mentioned above. The bending test was chosen because uniaxial tension fatigue tests are difficult to perform by using the available DMA instruments due to the limitations of the machine capacity. Figure 4.37 gives an impression of the specimens and the test set-up. It was found that these tests could not be performed successfully. The reason for this is that the contacts between the specimen and the clamp became loose during testing because of the stress relaxation of the mortar. The confining stress acting on the specimen via the clamps was relaxing over time. As a result, the measured data was very noisy and the moment of failure proved impossible to be clearly defined. Further efforts were made to overcome this problem. As shown in the left-bottom plot

of Figure 4.38, one of the improvements tried was the embedment of brass elements at the locations where the clamps needed to make contact with the specimen. By doing this, the problem of contact was solved. However, another problem arose from the mortar-brass interface zone. Specimens repeatedly showed failure at the locations where the mortar meets the brass elements.

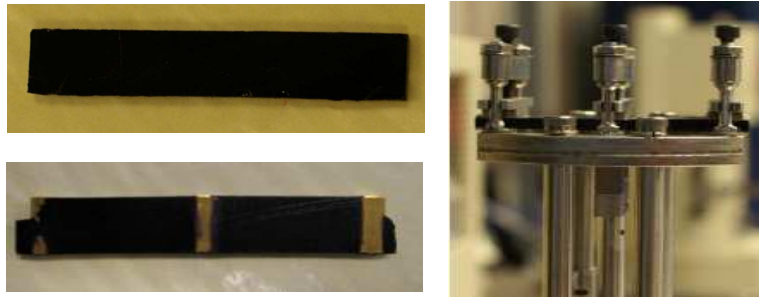


Figure 4.37 Mortar bending specimens (left-up: normal specimen; left-bottom: specimen embedded with brass elements) and DMA test setup

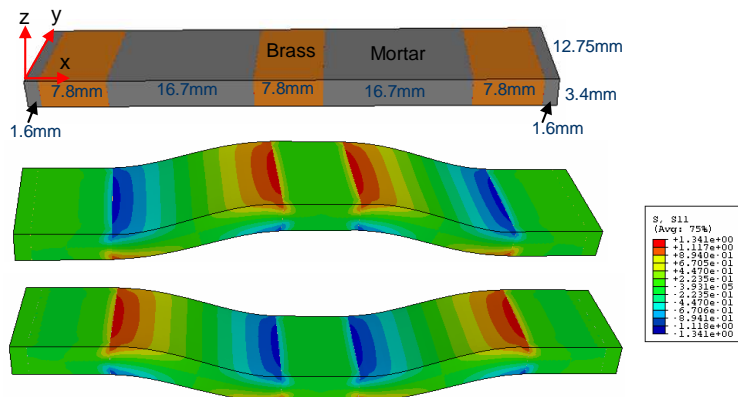


Figure 4.38 Finite element simulation of specimen with brass embedment (upper: specimen geometry; middle and bottom: computed bending tensile stress from top and bottom views; S11: stress component, σ_{xx})

Figure 4.38 shows the finite element simulation of tests done on the specimens with embedded brass elements. In this model, the following material properties were used:

Brass: $E = 1 \times 10^5 \text{ MPa}$ $\nu = 0.35$

Mortar: $E = 300 \text{ MPa}$ $\nu = 0.45$

Movement of the brass elements at both ends was fully restricted. The middle

brass element was loaded by a force of 10N. Computational results show that the highest bending tensile stress occurs at the locations around the mortar-brass boundaries. Apparently, the mortar-brass interface is subjected to unfavourable stress conditions. Failure at such a location can only be prevented by improving the bonding properties between brass and mortar. Further efforts, e.g. using rough brass surface were tried on this issue, but failed to solve the interface problem. The analysis described here resulted in the conclusion that DMA bending tests on the mortar using this test setup could not be performed.

4.4 Fatigue test on stone-mortar-stone system

The test program described above focused on the adhesive zone (adhesive interface plus pure bitumen layer) and the pure mortar separately. To obtain insight into the actual bitumen-rich interlayer, the fatigue behaviour of two stone columns glued by a thin mortar layer was also investigated. In this case, an entire system including the interfacial adhesion, bitumen-rich interlayer and pure mortar was tested. Obviously, failure could only occur at the weakest link among the different material components. Specimens used for this testing were similar to those for adhesive zone testing. The only difference is a mortar layer of 1mm instead of the bitumen film. Therefore, the procedures of specimen preparation were similar and will not be explained further. For the stone-mortar-stone system, only a few tests were performed. Effects of aging and water conditioning were also involved. Again, the water conditioning is the same as described before. Three test temperatures, 0, 10 and 20°C were selected. Table 4.7 gives a summary of fatigue test results of stone-mortar-stone systems. The stress listed in this table is the theoretical maximum shear stress at the outer edge of the sample column. Based on the limited amount of data listed in Table 4.7, the following observations are made: (1) the fatigue lives of long-term aged specimens are generally higher than those of short-term aged specimens; (2) water conditioning tends to impair the fatigue life; (3) the effect of type of stone is not clear.

Table 4.7 Fatigue test results of stone-mortar-stone system

Tem.		B+SM	B+LM	B+SM_W	G+SM	G+LM	G+SM_W
20°C	Stress [MPa]	0.81	0.81	0.81	-	-	-
	N	1920	3060	540	-	-	-
10°C	Stress [MPa]	1.296	1.296	1.296	1.296	1.296	1.296
	N	2220	6420	1740	2070	1920	1440
0°C	Stress [MPa]	1.944	1.944	1.944	1.944	1.944	1.944
	N	1410	6210	200	4590	10500	1410

Note: N= number of cycles to failure. B=sandstone; G=greywacke; W=water condition
SM=short-term aged mortar; LM=long-term aged mortar;

The examination of the fractured surfaces of the stone-mortar-stone system were also performed and showed that all of the specimens had failed at a location which is very close to the stone surface. To illustrate this, Figure 4.39 visualises the difference in fracture surfaces obtained from the adhesive zone and mortar-stone-mortar testing. The images were captured using an AXIOSHOP 40, made by CarlZeiss Far East Co.

Ltd., Hong Kong.

As indicated, adhesive failure only occurs in the binder-stone interface, resulting in bare stones after failure. Cohesive failure may occur through the bitumen-rich interlayer so that the stone surface is still covered with bituminous material after failure. The remaining binder on one of the fractured surfaces of the stone-mortar-stone system (see Figure 4.39c) is similar to that remnant on the adhesive zone tested by DMA and DSR instruments (see Figures 4.39a and b) and some local areas are uncovered by bitumen, thus the stone surface can be inspected. On the other fractured surface (see Fig 4.38d) of the mortar-stone-mortar system, the filler particles embedded in bituminous binder can be observed. The analysis above indicates that the bitumen-rich interlayer between stone surface and mortar may contains much fewer (if any) fine mineral particles than the undisturbed mortar far from stone surface and the mechanical behaviour of this bitumen-rich interlayer is more like the bitumen film than the mortar. Such a bitumen-rich interlayer seems to be the potential weak zone.

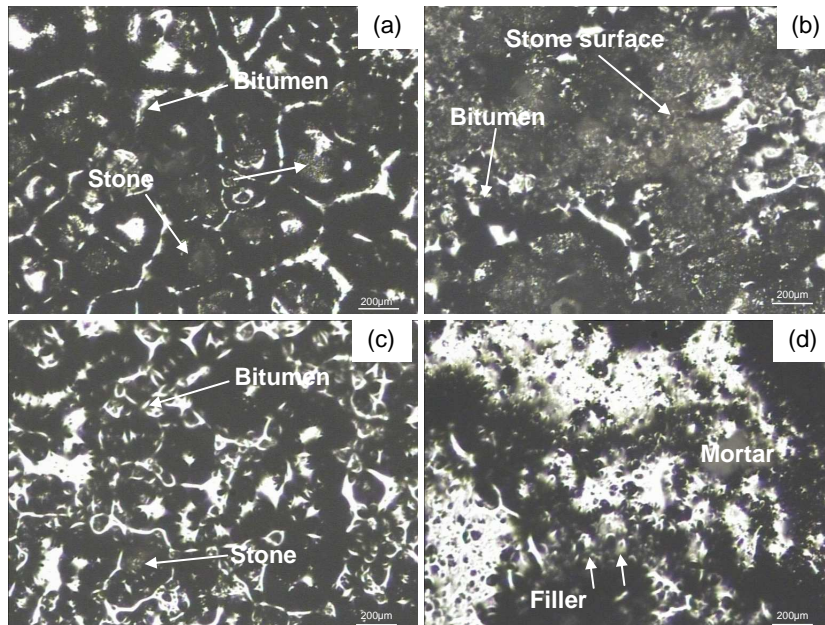


Figure 4.39 Typical fractured surfaces after failure at 10 °C (a: DMA tensile testing of adhesive zone; b: DSR shear testing of adhesive zone; c and d: DSR shear testing of stone-mortar-stone system)

Table 4.8 gives a comparison of the fatigue life of the adhesive zone, the stone-mortar-stone system and the mortar under DSR fatigue testing. Since the stone-mortar-system tended to fail at a location close to the stone surface, its fatigue life should be determined by the lifetime of the adhesive zone that is represented by the stone plus bitumen interlayer, while much smaller than the one of the mortar. This

expectation is in agreement with the data listed in Table 4.8. For example, the ratios of N_1/N_2 are in a range of 10^{-1} to 10^{-2} . However, the ratios of N_1/N_3 are much smaller.

Table 4.8 Life comparison of the adhesive zone, the idealized stone-mortar-stone system and the mortar under DSR testing

Test conditions	Shear stress	SMS	AZ	Mortar	N_1/N_2	N_1/N_3
	MPa	N_1	N_2	N_3		
B_SB_20°C	0.810	1.92E+03	2.51E+04	-	7.66E-02	-
B_LB_20°C	0.810	3.06E+03	3.13E+04	-	9.78E-02	-
B_SB_W_20°C	0.810	5.40E+02	1.21E+04	-	4.47E-02	-
B_SB_10°C	1.296	2.22E+03	3.00E+04	1.10E+07	7.40E-02	2.02E-04
B_LB_10°C	1.296	6.42E+03	2.00E+04	4.30E+07	3.21E-01	1.49E-04
B_SB_W_10°C	1.296	1.74E+03	9.00E+03	8.50E+06	1.93E-01	2.05E-04
G_SB_10°C	1.296	2.07E+03	4.20E+03	1.10E+07	4.93E-01	1.88E-04
G_LB_10°C	1.296	1.92E+03	5.20E+03	4.30E+07	3.69E-01	4.47E-05
G_SB_W_10°C	1.296	1.44E+03	4.05E+03	8.50E+06	3.56E-01	1.69E-04
B_SB_0°C	1.944	1.41E+03	1.50E+04	1.00E+06	9.40E-02	1.41E-03
B_LB_0°C	1.944	6.21E+03	5.00E+04	1.28E+06	1.24E-01	4.85E-03
B_SB_W_0°C	1.944	2.00E+02	9.00E+03	7.50E+05	2.22E-02	2.67E-04
G_SB_0°C	1.944	4.59E+03	7.01E+04	1.00E+06	6.55E-02	4.59E-03
G_LB_0°C	1.944	1.05E+04	8.96E+04	1.28E+06	1.17E-01	8.20E-03
G_SB_W_0°C	1.944	1.41E+03	2.56E+04	7.50E+05	5.51E-02	1.88E-03

Note: SMS= stone-mortar-stone system; AZ= adhesive zone; $N_{1,2,3}$ = fatigue life of SMS, adhesive zone and mortar.

4.5 Summary and conclusions

In total, two types of stone and the effects of aging (short-term aging and long-term aging) and water immersion were considered for adhesive zone testing. A wide range of test temperatures from -10°C to 20°C was used.

New test set-ups were developed to perform adhesive zone testing at meso-scale level. For this purpose, DMA instruments were used for uniaxial tension testing and DSR instruments were applied for shear testing. The oblique shear tests were performed, in which a combination of normal stress and shear stress were successfully applied. Meanwhile, a simple and practical normal-shear combined test set-up was developed within the platform of DSR instruments.

Finite element modelling was carried out to get insight into the stress states within the adhesive zone. It was found that the edge effect was negligible, while the effect of stone surface morphology on the stress distributions was significant. The stress acting on the adhesive zone can not be regarded as a uniform stress since local

stress concentrations occurred. A factor that accounts for these stress concentrations was thus introduced.

The fatigue data of the adhesive zone showed large scatter, but the effect of temperature was clearly visible. Data scatter indicated that the testing was not fully under control. This is logical because it is difficult or impossible to fully control the thickness of bitumen film and the stone surface morphology. Non-uniform stress distributions will have contributed to the data scatter.

In the mortar fatigue tests, the effects of aging (short-term and long-term), temperature (0 °C and 10 °C), frequency (10Hz and 40Hz) and water immersion were taken into account. Shear and bending fatigue tests were performed using the DSR oscillation shear testing and the DMA dual cantilever bending testing respectively. However, the DMA bending test was not successful and thus only DSR shear fatigue tests could be performed.

Finite element simulations on the mortar shear fatigue showed that local stress concentrations occurred indicating that such regions may be potential locations of failure. The computational results were in agreement with the laboratory observation that approximately 50% of the cases of failure happened in the section where the stress concentrations occurred. To take into account the effect of stress concentrations, a factor accounting for this was thus introduced.

Fatigue tests were also done on the idealized stone-mortar-stone systems in order to find out the weak link in the stone contact region. Results showed that failure happened at a location which was very close to the stone surface. Compared with the mortar, the fatigue life of the adhesive zone was much shorter and this zone thus tends to be the potential weak link. Image analysis showed that the adhesive zone where the mortar meets the stone surface was a bitumen-rich layer, which can be represented by stone plus a thin bitumen film.

5 INSTRUMENT CALIBRATION

5.1 Introduction

In this study, tests were performed using various DSR and DMA instruments located at WHUT, China and TUD, the Netherlands. Concerns arose whether these instruments lead to the same results. The instrument factor theoretically becomes 1 when all instruments are equal. To obtain insight into the differences between the instruments an instrument calibration procedure was followed.

Furthermore, tests in this research were specially designed and they differ from the standard tests for which the instruments are designed. Theoretically, the instruments should be capable to perform the specially designed tests since the measurement principles do not change. Special clamp systems were designed to clamp the desired test specimens into the instruments. In the case of data analysis, reliable stress and strain in the specimen become important. To obtain this information, the following two issues arise: (1) specimen force and deformation; (2) specimen geometry that translates the specimen force and deformation into stress and strain in the specimen.

For standard tests, the stress and strain are provided by the instrument software automatically. In the case of the non-standard tests that were done in this study, more effort is required to obtain the real stress and strain in the specimen. For this purpose, the post-processing approaches that have been developed to determine the true stress and strain values will be discussed hereafter.

In general, test equipment must be calibrated at intervals by comparison with a standard or a calibrated testing apparatus. This calibration also applies to DSR and DMA instruments. In this case, different reference samples are available for the comparison with the corresponding reference equipment. This so-called instrument self-calibration assures that the instrument is in good condition.

Table 5.1 Instrument multipliers for various test instruments

Instrument	Test mode	Multiplier [-]
DMA 800, WHUT	static test	0.969
	dynamic test	1.135
DMA 2980*, TUD	static test	1.000
	dynamic test	0.964
DSR MCR 101, WHUT	dynamic test	0.831
DSR 2000, TUD	dynamic test	0.894
DSR 1000, TUD	dynamic test	0.796

Note: DMA 2980 is the reference instrument.

Unfortunately, there is neither a universal reference sample nor a clamp system that is available for both DSR and DMA calibrations. For this reason, a calibration study was carried out by using different reference samples as well as different clamp systems. By doing this, the differences between the instruments used in this study are obtained as given in Table 5.1. It indicates that the instrument accuracy is within $\pm 20\%$ in terms of stiffness measurement. An instrument multiplier larger than

1 indicates the instrument underestimates the material stiffness, while an instrument having a multiplier factor smaller than 1 overestimates the material stiffness when comparing to the reference instrument. To minimize the data spread, the measurement data obtained from various instruments should be multiplied by the corresponding instrument factors listed in Table 5.1. More information on these instrument multipliers is given hereafter

5.2 Theory

In this section, the theories related to DSR and DMA testing will be discussed by means of an example. Figure 5.1 gives the flowchart representing the data collection and processing by the DSR instrument. As indicated in this figure, information about translation of the raw torque (T_{raw}) and the raw radial deflection angle (θ_{raw}) into the corresponding specimen torque (T_{sample}) and the real radial deflection angle (θ_{sample}) is required. Sitting in between is machine input including moment of inertia(I), air-bearing friction (μ) and compliance of clamp(J). Also the T_{sample} and θ_{sample} needs to be translated into stress and strain. Shape factors of the specimen geometry are needed in order to be able to do so. Finally, the known shear stress (τ_{sample}) and strain (γ_{sample}) allow to calculate the shear modulus G^*_{sample} .

Since the mathematical models are identical, the approach described in Figure 5.1 also holds for DMA testing. Table 5.2 shows the analogous quantities in the DMA and DSR mechanical systems in mechanics [Wiki, Humonic oscillator].

Table 5.2 Analogous quantities in DMA and DSR mechanical systems

DMA testing	DSR testing
Position x	Angle θ
Velocity $\frac{dx}{dt}$	Angular velocity $\frac{d\theta}{dt}$
Mass M	Moment of inertia I
Spring constant K	Torsion constant G
Friction μ	Rotational friction μ
Drive force F	Drive torque T
Resonant frequency	
$\frac{1}{2\pi} \sqrt{\frac{K}{M}}$	$\frac{1}{2\pi} \sqrt{\frac{G}{I}}$
Differential equation	
$M \ddot{x} + \mu \dot{x} + Kx = F$	$I \ddot{\theta} + \mu \dot{\theta} + G\theta = T$

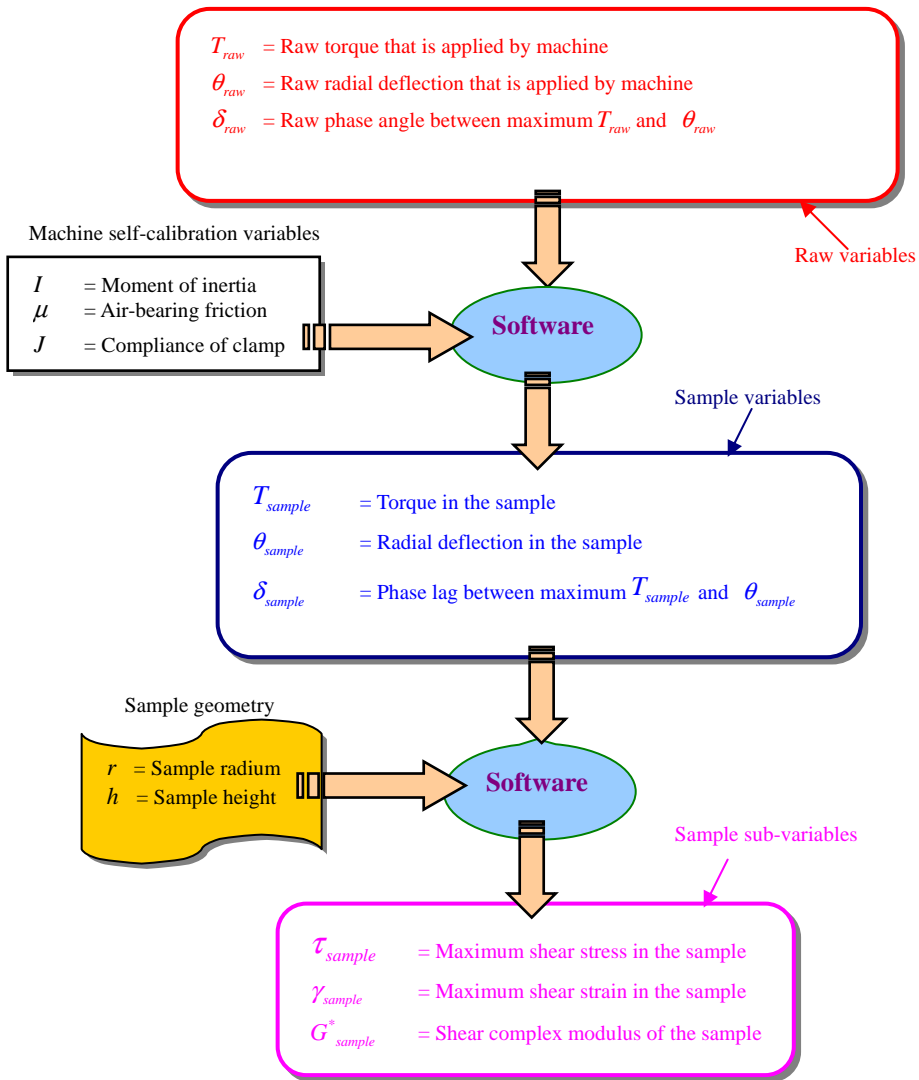


Figure 5.1 Flowchart for data collection and processing of DSR parallel-plate testing

5.2.1 Instrument parameters

5.2.1.1 Mass and moment of inertia

Inertial mass is the mass of an object measured by its resistance to acceleration. Similarly, moment of inertia is a measure of an object's resistance to changes in its

rotation rate. The mass can be measured directly by weighing the object. However, the moment of inertia (with respect to a given axis of rotation) of any object is given by:

$$I = \int r^2 dm \quad (5.1)$$

Where:

m = mass, [kg];

r = the perpendicular distance to the axis of rotation, [m].

When friction is neglected, the moment of inertia can be measured by combining a constant drive torque with the angular acceleration.

$$I = T / \ddot{\theta} \quad (5.2)$$

5.2.1.3 Air-bearing friction

Air friction is velocity dependent and is always directly opposite the velocity. At low speeds and for small particles, air resistance is approximately proportional to velocity and can be expressed in the form

$$T_\mu = -\mu \dot{\theta} \quad \text{or} \quad F_\mu = -\mu \dot{x} \quad (5.3)$$

Equation 5.3 indicates that an object will continue to accelerate to higher speeds until it encounters an amount of frictional resistance which is equal to the drive force or torque. In this way, the coefficient of friction, μ , can be determined. In general, the value of μ is fairly low and thus the frictional resistance can be neglected for practical reasons.

5.2.1.4 Compliance of clamp

The clamp system is very stiff but not rigid. As a result, the actual deformation measured by the instrument consists of the contributions of the clamp system as well as the test specimen. The deformation of the clamp is approximately proportional to the drive force and can be expressed in the form

$$\theta_c = T \times J \quad \text{or} \quad x_c = F \times J \quad (5.4)$$

The value of J can be approximately determined by performing a test on a specimen having a much higher stiffness when compared to the clamp system. In this case, the clamp system is responsible for almost all of the deformation.

5.2.1.5 Resonant frequency

Resonance is the tendency of a system to oscillate at larger amplitudes at some frequencies than at others. These frequencies are defined as the system's resonant frequencies. At resonant frequencies, even small periodic drive forces can produce

huge amplitude vibrations, because the system stores vibration energy. When the damping of the system is small, the resonant frequency is approximately equal to the natural frequency as determined as follows.

$$f_n = \frac{1}{2\pi} \sqrt{\frac{K}{M}} \quad \text{or} \quad \frac{1}{2\pi} \sqrt{\frac{G}{I}} \quad (5.5)$$

The ratio of the frequency of the drive force over the natural frequency can be used as an indicator of the resonance effect. A very low ratio indicates that the effect of resonance is very limited and the force to which the test specimen is subjected is approximately equal to the drive force and no corrections need to be made for the resonance effect.

5.2.1.6 Specimen force and deformation

During the steady state, the following differential equations hold for the DMA and DSR test system.

$$M \ddot{x} + \mu \dot{x} + Kx = F \quad \text{or} \quad I \ddot{\theta} + \mu \dot{\theta} + G\theta = T \quad (5.6)$$

As mentioned earlier, these two systems are equivalent. For this reason, the DSR test system is chosen as an example for the following discussions.

According to the differential equation above, the value T_{sample} can be determined as

$$T_{sample} = T_{raw} - I \frac{d^2\theta_{raw}}{dt^2} - \mu \frac{d\theta_{raw}}{dt} = T_{raw} - T_I - T_\mu \quad (5.7)$$

Where:

$T_I = I \frac{d^2\theta_{raw}}{dt^2}$, the torque induced by moment of inertia, [N.m];

$T_\mu = \mu \frac{d\theta_{raw}}{dt}$, the torque induced by air-bearing friction, [N.m].

The values of θ_{sample} is equal to the total measured displacement θ_{raw} minus the contribution of the clamp system.

$$\theta_{sample} = \theta_{raw} - T_{raw} \times J \quad (5.8)$$

When the external torque is applied to the specimen using a pure sinusoidal wave

$$T_{raw}(t) = T_0 \sin(\omega t) \quad (5.9)$$

Where:

T_0 = torque amplitude, [N.m];

ω = angle velocity, [rad/s].

The displacement induced by the sinusoidal torque can be written as:

$$\theta_{raw}(t) = \theta_0 \sin(\omega t + \delta_{raw}) \quad (5.10)$$

Where:

θ_0 = displacement amplitude, [rad];

δ_{raw} = raw phase angle between the displacement and torque amplitude, [degree].

The signals of T_{sample} and θ_{sample} over time can be computed as:

$$T_{sample}(t) = T_{raw}(t) - I \frac{d^2 \theta_{raw}(t)}{dt^2} - \mu \frac{d \theta_{raw}(t)}{dt} = T_{raw}(t) - T_i(t) - T_\mu(t) \quad (5.11)$$

$$\theta_{sample}(t) = \theta_{raw}(t) - T_{raw}(t) \times J \quad (5.12)$$

When θ_{sample} reaches a peak value within a cycle, the displacement amplitude can be determined by

$$\theta_{sample_max} = \max[\theta_{sample}(t)] \text{ at } t = t_\theta \text{ or } \delta_\theta = t_\theta \times \omega \quad (5.13)$$

Where:

t_θ, δ_θ = the time and angle at which the peak displacement occurs, [s] and [degree] respectively.

Similarly, the torque amplitude in the sample can be expressed by the peak value within a cycle

$$T_{sample_max} = \max[T_{sample}(t)] \text{ at } t = t_T \text{ or } \delta_T = t_T \times \omega \quad (5.14)$$

Where:

t_T, δ_T = the time and angle at which the maximum displacement occurs, [s] and [degree] respectively.

Combining the angles at which the maximum displacement and torque in the sample occur, the phase angle δ_{sample} between the displacement θ_{sample} and the torque T_{sample} can be determined.

$$\delta_{sample} = \delta_\theta - \delta_T \quad (5.15)$$

To obtain the displacement and the torque signals in the sample (T_{sample} and θ_{sample}), it was decided to use an Excel spreadsheet to solve the above equations in

combination of the instrument input parameters given in Table 5.2.

Table 5.2 DSR instrument input parameters for mortar testing

Instrument	Inertia I 10^{-6} N.m.s^2	Air-bearing friction μ N.m/(rad/s)	clamp compliance J rad/(N.m)
DSR mortar tests			
DSR 1000, TUD	14.96	0.969	0.008040
DSR 2000, TUD	16.64	1.046	0.006961
DSR adhesive zone tests			
DSR 1000, TUD	14.92	0.942	-
DSR 2000, TUD	16.63	-	-
DSR 301, WHUT	96.26	-	-
Instrument	Inertia M kg	Air-bearing friction μ N/(m/s)	clamp compliance J m/(N)
DMA adhesive zone tests			
DMA 800, WHUT	0.0301	-	-
DMA 2980, TUD	0.0305	-	-

Figure 5.2 gives a typical example of the computational results based on the raw variables including T_{raw} , θ_{raw} and δ_{raw} . As one can observe, the torque and the displacement in the sample (T_{sample} and θ_{sample}), the torque induced by the inertia and the air-bearing friction of the test system (T_i and T_μ) are computed and plotted against time within a complete cycle. Compared with the raw torque T_{raw} , the torque induced by inertia effect T_i is quite significant, while the torque induced by friction effect T_μ is very limited and thus can be neglected. The curve of T_{sample} clearly differs from the raw torque T_{raw} . This demonstrates that the raw torque T_{raw} may not well represent T_{sample} to which the sample is subjected. Based on the signals of T_{sample} and θ_{sample} , the peak values of these two variables within a cycle can be defined and the angles (δ_θ and δ_r) at which the maximum values take place are obtained accordingly. As indicated in Figure 5.2, the difference of these two angles denotes the phase angle δ_{sample} between the torque and the displacement in the sample.

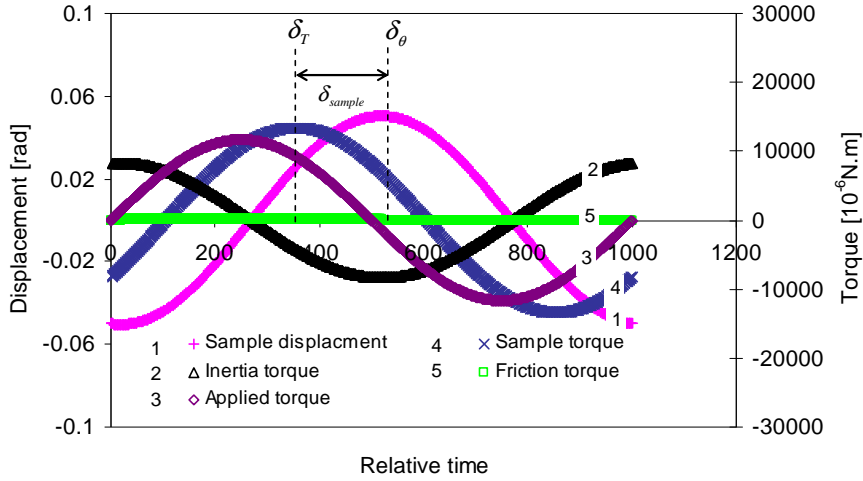


Figure 5.2 Computational results based on raw variables ($\theta_{raw} = 0.0504\text{rad}$, $T_{raw} = 11671\mu\text{N.m}$ and $\delta_{raw} = 96.9^\circ$) and instrument inputs of the DSR 2000 (1: θ_{sample} ; 2: T_I ; 3: T_{raw} ; 4: T_{sample} ; 5: T_{μ} ;)

In this way, the following information relating to the test specimen can be obtained or calculated:

- the amplitude of the torque in the sample, T_{sample} ;
- the amplitude of the deformation in the sample, θ_{sample} ;
- the phase angle between the torque and the displacement in the sample, δ_{sample} ;
- the maximum stress in the sample τ_{sample} , calculated by multiplying the torque amplitude by the shape factor;
- the maximum strain in the sample γ_{sample} , calculated by multiplying the displacement amplitude by the shape factor;
- complex modulus G^*_{sample} , using the maximum stress divided by the maximum strain.

Proof of the approach discussed above will be given later by combining with test data.

5.2.2 Shape factors

5.2.2.1 Introduction

DSR and DMA instruments performed tests in different loading modes. Furthermore, there is no unique clamp system available for all of the instruments. Therefore, several standard materials were considered combining with the available clamp systems of the various instruments. Figure 5.3 shows the samples and the test setups for the following instrument calibration. As indicated, some of them are making use of the special designed clamp systems (see Figures 5.3 b and c) in the study.

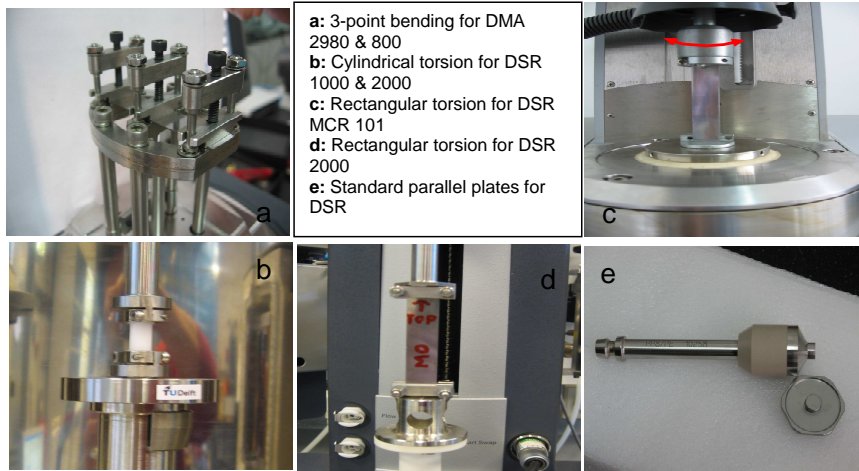


Figure 5.3 Test setups for various instrument calibrations

Stress and strain cannot be measured directly and are derived from measured force and deformation signals. Transfer functions that take into account specimen geometry are applied to transfer specimen load and deformation into desired stress and strain. Equation 5.16 gives the general equations that may be applied.

$$\sigma = k_1 \times F \text{ and } \varepsilon = k_2 \times \Delta x \quad (5.16)$$

Where:

k_1, k_2 = Shape factors dependent on specimen geometry.

Hereafter, the determination of the shape factors of various test setups that were used for instrument calibration will be discussed.

5.2.2.2 Bitumen films

When bitumen films are tested by DSR standard parallel plates, the shear strain and the shear stress are calculated at the outside edge of the disc using

$$\gamma = \frac{\theta \times r}{h} \quad (5.17)$$

$$\tau = \frac{2T}{\pi \times r^3} \quad (5.18)$$

Where:

r = specimen radius, mm;

h = film thickness, mm;

T = torque, N.mm.

5.2.2.3 Cylindrical torsion

For cylindrical torsion test, use is made of a delrin sample and the clamp system that was used for the mortar tests. Figure 5.4 shows the delrin sample and test setup. The equations that relate the specimen torque and deformation to stress and strain are as follows:

$$\gamma = \frac{\theta \times r}{h_{eff}} \quad (5.19)$$

$$\tau = \frac{2T}{\pi \times r^3} \quad (5.20)$$

Where:

h_{eff} = specimen effective height, [mm].

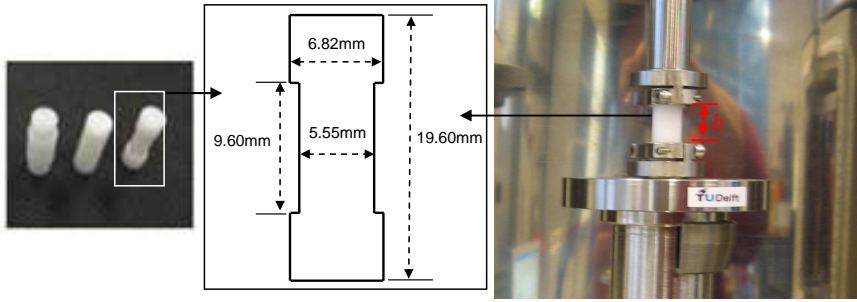


Figure 5.4 Cylindrical delrin sample and test setup (left: delrin sample; middle: specimen size; right: test set-up)

By means of finite element simulations, the value of h_{eff} is determined equal to be 10.727mm taking into account the specimen geometry given in Figure 5.4. Here, this value is obtained when delrin specimen was loaded by $\theta = 5.110 \times 10^{-5}$ rad, resulting in γ equal to 1.3220×10^{-4} . Since the finite element modelling of the cylindrical torsion test is similar to the response calculation performed on the mortar as described in the previous chapter, detailed information is not given here.

5.2.2.4 Steel strip

As shown in Figure 5.3, a stainless steel strip (60mm×12.41mm×0.43mm) was used to perform DSR rectangular torsion test and DMA dual cantilever bending test. With respect to the rectangular torsion, the maximum stress and strain in the specimen was determined by using the following equations [TA instrument, DSR]:

$$\tau = \frac{3A \times T}{Bwt^2} \quad (5.21)$$

$$\gamma = \frac{\theta \times A}{l} \quad (5.22)$$

Where:

l, w, t = the effective length, width and thickness of the solid rectangular sample, [mm]

A, B = geometry factor, $A \cong [(\frac{t}{c})^2 + (\frac{w}{2})^2]^{0.5}$ and $B = [1 - \frac{195}{\pi^5} \frac{t}{w} \tan(\frac{\pi w}{t})]$.

When using the DMA dual cantilever clamp, the stress and strain are not constant throughout the sample thickness. The maximum level of strain occurs at the sample surface, while the center experiences no strain at all. This also means that both stress and strain can have a positive or negative sign, depending on whether it is on the top or bottom surface of the sample. The following equations express the maximum stress and strain levels and do not include any contribution from the clamp [TA instrument, DMA]:

$$\sigma = \frac{3Fl}{2wt^2} \tag{5.23}$$

$$\varepsilon = \frac{3xtF_c}{l^2[1 + \frac{12}{5}(1+\nu)(\frac{t}{l})^2]} \quad \text{with } F_c = 0.7616 - 0.02713 \times \sqrt{\frac{l}{t}} + 0.1083 \ln(\frac{l}{t}) \tag{5.24}$$

Where:

l = sample length (one side), [mm];

ν = Poison's ratio, [-];

F_c = clamping correction factor, [-].

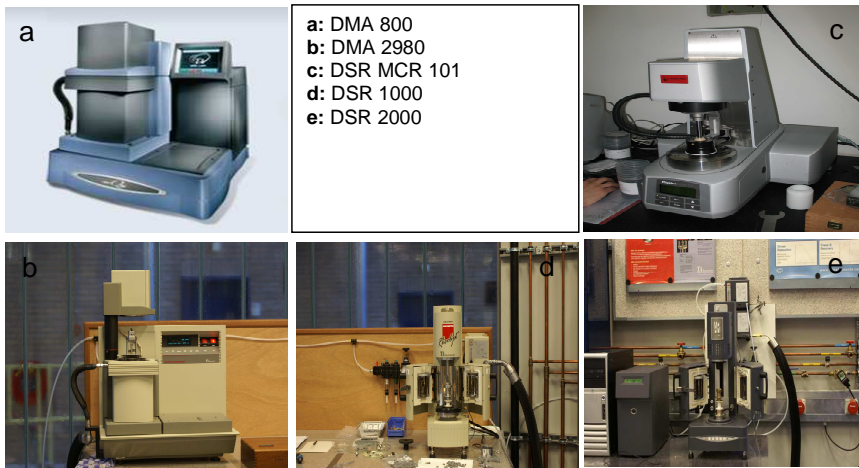


Figure 5.5 Image of the used test instruments

5.3 Calibration

Figure 5.5 gives an image of the various DSR and DMA instruments used in this study. The test conditions that were used for mortar or adhesive zone tests by

application of these instruments are summarised in Table 5.3. Here the instrument calibration will also focus on these test conditions.

Table 5.3 Test conditions for various instruments

Type of test	Instrument	Loading Mode	Frequency
Mortar fatigue test	DSR 1000 DSR 2000	Oscillatory torque controlled	10Hz and 40Hz
Adhesive zone shear fatigue test	DSR MCR 101 DSR 1000 DSR 2000	Oscillatory torque controlled	10Hz
	DSR 2000	Rotational+ Oscillatory Torque controlled	10Hz
Adhesive zone tension fatigue test	DMA 800	Dynamic force -controlled	10Hz
	DMA 2980	Dynamic displacement -controlled	10Hz
Adhesive zone static test	DMA 800	Static force-controlled	-
	DMA 2980	Static force-controlled	-

Table 5.4 gives the calibration plan for the various instruments. First of all, four different types of bitumen were used as test samples to compare the DSR 2000 with the DSR MCR 101 by using the standard parallel plates. Secondly, a cylindrical delrin specimen was used to relate the DSR 1000 with the DSR 2000 by means of the specially designed clamp system used for the mortar tests. A stainless steel strip (60mm×12.41mm×0.43mm) was applied to compare the DSR with the DMA instruments. These strips were used in DMA dual cantilever bending test and the DSR 2000 and DSR MCR101 torsion tests. By doing all these tests, the relation between the four instruments could well be established.

Table 5.4 Calibration plan for various instruments

Location	TUD			WHUT	
	DMA 2980	DSR 1000	DSR 2000	DSR MCR101	DMA 800
bitumen	-	-	S 5.3.1 Standard parallel plates		-
Stainless steel strip	S 5.3.4 DCB	-	S 5.3.3 Rectangular torsion		S 5.3.4 DCB
Cylindrical delrin	-	S 5.3.2 Cylindrical torsion		-	-

Note: DCB = dual cantilever bending

5.3.1 Standard parallel plates

In this instrument calibration procedure, four bitumen types; 30/45 Pen, 40/60 Pen, 70/100 Pen and 160/200 Pen produced by Q8, were used. To allow for proper comparison, parallel sampling was carried out from the bitumen of the same batch. The sample of each type of bitumen was stored in two small cans. One of the cans was brought to WHUT for testing and the other was used at TUD. The following tests

were performed using standard parallel plates:

- (1) Check of the measured linear visco-elastic behaviour by means of a small strain amplitude sweep testing at an interval of 10 °C from -10°C to 60°C. The obtained data are used to determine the strain levels which are within the linear visco-elastic range at various test temperatures.
- (2) Frequency sweep tests: for temperatures below 30 °C, 8mm diameter parallel plates used with 2mm gap width; for temperatures above 20 °C , 25mm diameter parallel plates used with 1mm gap width. The overlap temperatures for these test geometries are at 20°C and 30°C. Test frequency ranged from 0.05 to 50Hz.
- (3) The difference between the DSR 2000 and DSR MCR 101 was evaluated based on the shear complex modulus obtained from the two instruments.

Figure 5.6 gives the typical results of frequency sweep tests at various temperatures as conducted on the 35/40 Pen bitumen. Both DSR instruments produced similar data. However, a direct comparison of the data is not possible because the output is at different frequencies. As a result, the data produced by one DSR instrument needs to be well described by a model. The model must be accurate and flexible to calculate the complex moduli under various conditions. With the aid of the model, the complex modulus that should be measured by the other instrument can be back-calculated. By doing this, the modulus values can be compared.

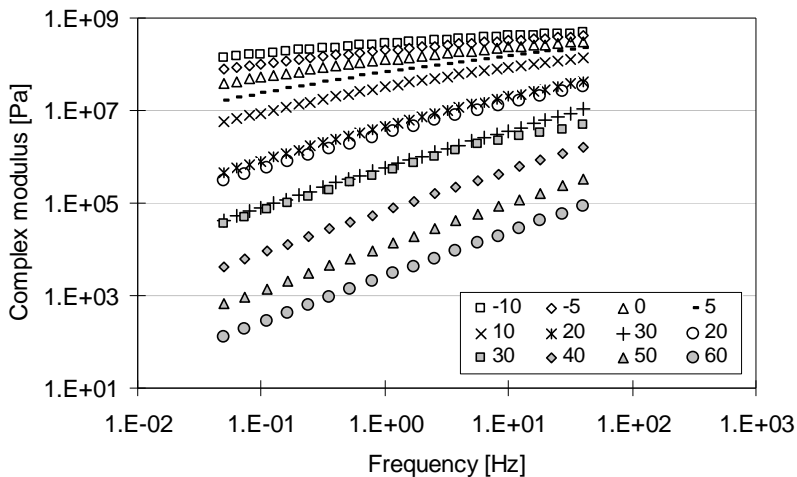


Figure 5.6 Complex modulus of 30/45 Pen bitumen under frequency sweep tests at various temperatures

It is known that the rheological properties of bituminous binders can be well described by a master curve using the time-temperature superposition principle. This principle allows to shift data obtained at various temperatures with respect to time. The master curve of the complex modulus constructed at a reference temperature in this manner, usually is a function of reduced time or frequency. In general, this curve can be mathematically modelled by a sigmoidal-shape function described as [Bahia, Hanson et al 2001]:

$$G^* = G_e^* + \frac{G_g^* - G_e^*}{[1 + (f_c / f')^k]^{m_e/k}} \quad (5.25)$$

Where

$G_e^* = G^*(f \rightarrow 0)$, equilibrium complex modulus, $G_e^* = 0$;

$G_g^* = G^*(f \rightarrow \infty)$, glass complex modulus;

f_c = location parameter with dimensions of frequency;

f' = reduced frequency, function of temperature;

k, m_e = shape parameters, dimensionless

The reduced frequency is determined by multiplying the test frequency by a temperature shift factor, a_T :

$$f' = f \times a_T \quad (5.26)$$

This shift factor is usually described using the Williams–Landel–Ferry (WLF) formulation:

$$\log(a_T) = -\frac{C_1(T - T_0)}{C_2 + (T - T_0)} \quad (5.27)$$

Where:

T_0 = reference temperature, [K];

T = test temperature, [K];

C_1, C_2 = model constant.

or using the Arrhenius Equation:

$$\log(a_T) = \frac{\Delta E_a}{2.303R} \left(\frac{1}{T} - \frac{1}{T_0} \right) \quad (5.28)$$

Where:

ΔE_a = apparent activation energy, [J/mol];

R = universal gas constant $R = 8.314 \text{ J/(K.mol)}$.

To construct the complex modulus master curves of these four types of bitumen, a reference temperature of 10°C was chosen. The experimental data were then fitted to the sigmoidal-shape function given by Equation 5.25 in combination with a shift factor as per Equation 5.27 or Equation 5.28. All of the model parameters or constants can be automatically obtained by minimizing the mean relative error using the Solver function in the Excel spreadsheet.

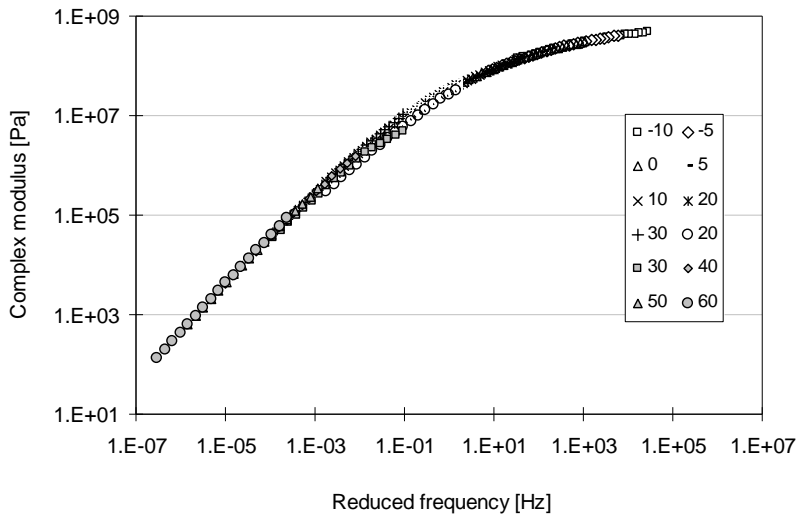


Figure 5.7 Complex modulus master curve of the 30/45 Pen bitumen constructed by using the optimal temperature shift factors a reference temperature of 10°C

Table 5.5 Temperature shift factors for various types of bitumen

Temperature [°C]	Bitumen			
	30/45 Pen	40/60 Pen	70/100 Pen	160/220 Pen
-10	698.8	482.5	336.2	196.8
-5	149.2	146.9	113.0	122.2
0	27.1	25.5	25.2	25.2
5	5.2	5.0	4.7	5.1
10	1	1	1	1
20	3.67E-02	3.85E-02	4.07E-02	4.46E-02
30	2.34E-03	2.56E-03	3.04E-03	4.06E-03
40	1.98E-04	2.30E-04	2.94E-04	5.04E-04
50	2.94E-05	3.37E-05	4.85E-05	9.00E-05
60	5.99E-06	6.81E-06	1.08E-05	2.24E-05

Initial fitting results indicated that neither the WLF formulation nor the Arrhenius Equation is capable to acceptably describe the measured rheological behaviour. The data at high temperatures (low reduced frequencies) do not fit the model perfectly. This indicates that both Equations 5.27 and 5.28 can't describe the temperature dependence of the bituminous binders over the wide range of test temperatures.

To get a better model fit, the shift factor for each temperature was determined

without applying any temperature shift equation to minimize the error. Figure 5.7 gives an impression of fitting results obtained. The temperature shift factors are listed in Table 5.5. As shown in Figure 5.7, a perfect fit is obtained for all test data over the wide temperature range.

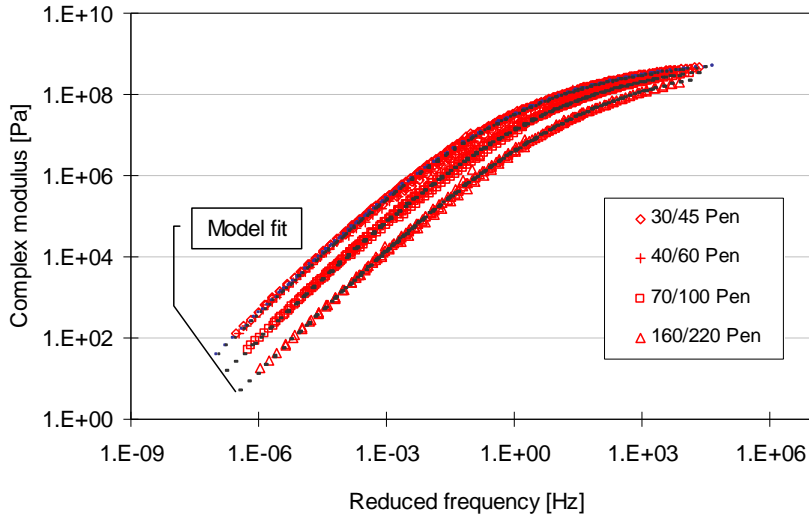


Figure 5.8 Model accuracy of master curves from the DSR MCR 301

Table 5.6 Determination of model parameters for master curves

Model parameters	30/45 Pen	40/60 Pen	70/100 Pen	160/220 Pen
G_e^*	0			
G_g^* [Pa]	7.411E+08	6.959E+08	6.511E+08	6.386E+08
f_c [Hz]	0.5642	0.7045	2.521	12.352
m_e [-]	1.062	1.053	1.055	1.066
k [-]	0.2147	0.2202	0.2165	0.2086
R^2	1.000	0.999	0.999	0.999

Figure 5.8 gives an impression of the model accuracy for the master curves for these four different types of bitumen. Due to very similar properties, the difference between the data obtained from the 30/45 Pen bitumen and those of the 40/60 Pen bitumen is so small that they are not clearly distinguished in this log-log plot. The statistic results listed in Table 5.6 demonstrate that the fit of the master curves is very good with R^2 values very close to 1.

To obtain the difference between these two DSR instruments, the mean percentage relative error (MPRE) between the modulus data measured by the DSR 2000 and the DSR MCR 301 is evaluated:

$$\text{MPRE} = \frac{\sum_{i=1}^m \sum_{j=1}^n \left| \frac{G_{1-j}^* - G_{2-j}^*}{G_{1-j}^*} \right|}{\sum_{i=1}^m n_i} \times 100 \quad (5.29)$$

Where:

- j = the j -th test data;
- i = the i -th type of bitumen;
- n = the total number of test data for each bitumen;
- m = the total number of types of bitumen, $m = 4$.

The mean percentage relative errors are listed in Table 5.7. The overall mean percentage relative error is equal to 3.4%. Such a small error indicates that the DSR 2000 and DSR MCR 301 are comparable with each other.

Table 5.7 Mean percentage relative errors

MPRE, %				
Overall	30/45 Pen	40/60 Pen	70/100 Pen	160/220 Pen
3.4	3.5	2.8	3.2	4.3

Figure 5.9 gives a comparison between the complex modulus measured by the DSR 2000 and the complex modulus estimated based on the model for the DSR MCR 301. As one can observe, the data obtained from both DSR instruments are identical with each other. Thus it is concluded that there is no clear distinction between these two DSR instruments as used for bitumen measurements by means of parallel plates.

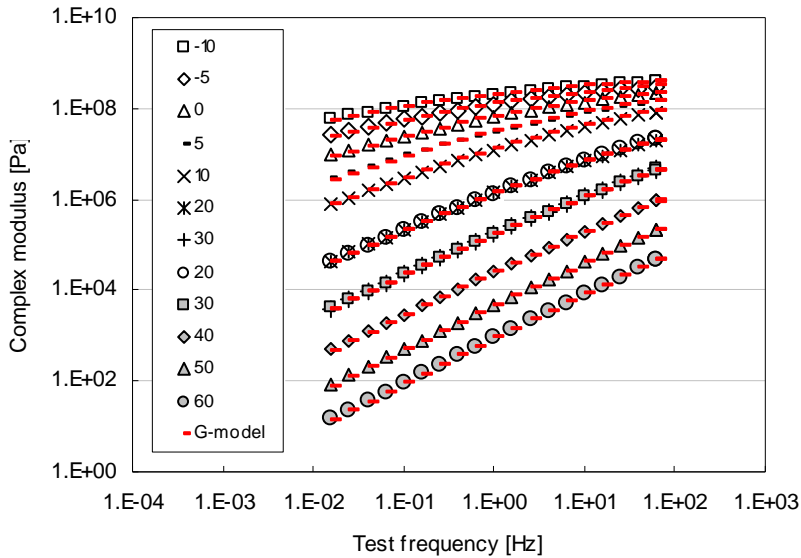


Figure 5.9 Comparison between the modulus measured by the DSR 2000 and the modulus estimated based on the model for the DSR MCR 301

5.3.2 Cylindrical torsion

5.3.2.1 Introduction

In previous section, the two DSR instruments were compared when using the standard parallel plates as well as the standard test procedure. In this case, the data outputs, i.e. stress, strain, complex modulus as well as phase angle between stress and strain are automatically processed and generated based on the black box behind the instrument, (see Figure 5.10). However, these functions are believed not to be valid any more for non-standard tests because of complex specimen geometry. This concern was evaluated and the results will be discussed hereafter.

For non-standard tests, the tough problem is the definition of the so-called gap distance, i.e. the distance between two parallel plates. Figure 5.11 gives an illustration of the gap distances in the DSR standard parallel plates and the non-standard tests, i.e. mortar and adhesive zone tests. As indicated, the gap distances in the mortar and adhesive zone are really dependent on the location where the specimen was clamped. Furthermore, the geometries of these test specimens are beyond the DSR standard parallel plates that are used for bitumen testing. As a result, the gap that was determined by the DSR instrument is not really reflecting the effective specimen height that allows the instrument to determine the shape factors. For example, the effective height of the mortar specimen is 12.742mm as determined in the previous chapter. With respect to the adhesive zone, its effective height may be very small, i.e. 15 μ m.

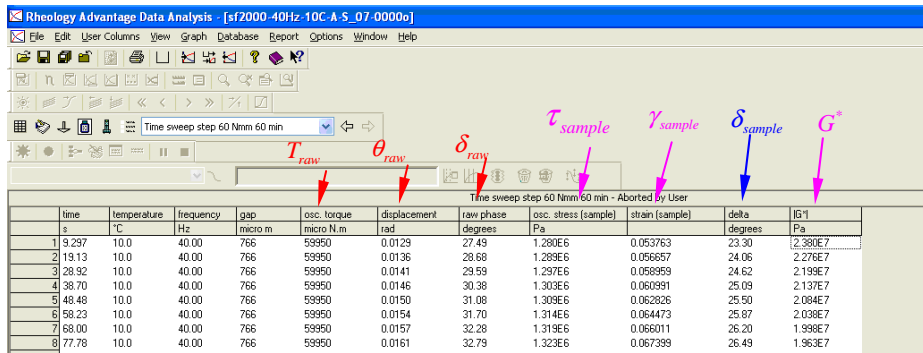


Figure 5.10 Typical data output obtained from the DSR 2000

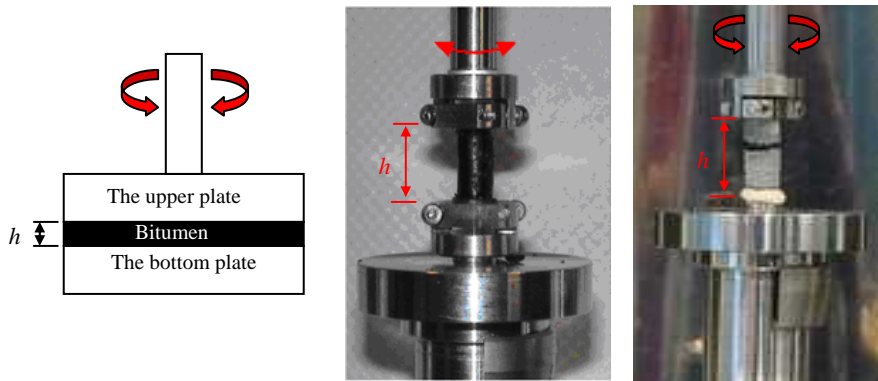


Figure 5.11 Illustration of the gap distances in the DSR standard parallel plates (left), the shear mortar test (middle) and the shear test on the adhesive zoon (right)

The difference between the actual gap distance and the effective specimen height indicates that the test procedure for non-standard tests can not fully copy those of the standard parallel-plate mode for bitumen testing. As a result, the data output of some variables, especially those having a relation with the specimen geometry, need to be corrected. Data post processing for non-standard DSR testing is discussed hereafter.

As shown in Figure 5.12, the sample variables (T_{sample} , θ_{sample} and δ_{sample}) are dependent on the input of instrument including I , μ and J and have nothing to do with the input of specimen geometry (i.e. r and h) during data processing by the black box of the instruments. However, as the terminal data, both the specimen stress τ_{sample} and strain γ_{sample} is influenced by the input of instrument parameters as well as the specimen geometry as mentioned above. By realizing this, it is clear that proper instrument parameters (I , μ and J) must be used for any tests. It also indicates that when proper instrument parameters are used as input, the sample variables (T_{sample} and θ_{sample}), which may be output by the instrument if possible, are the corrected

values for direct stress and strain analysis.

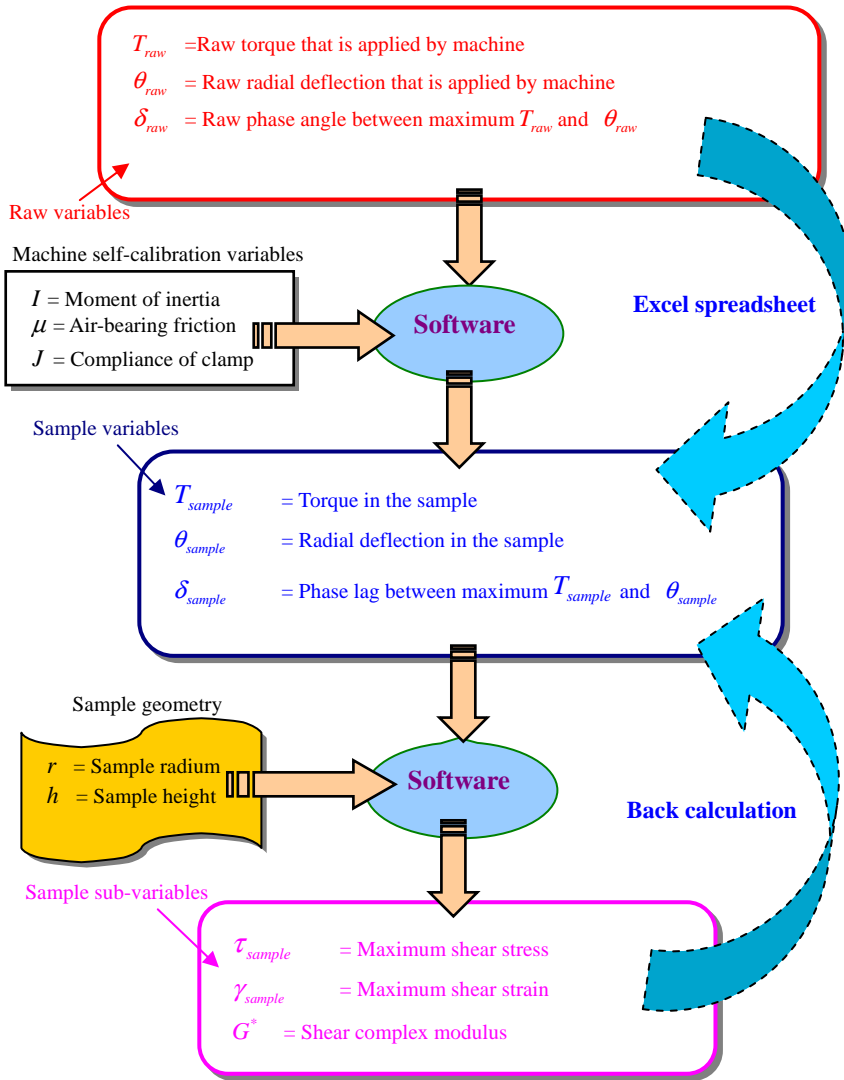


Figure 5.12 Two potential approaches of data post processing including straight-forward and back calculation of T_{sample} and θ_{sample}

Unfortunately, this kind of knowledge was not available during the LOT project. As a result, the raw outputs (T_{raw} , θ_{raw} and δ_{raw}) were mistaken for the sample outputs (T_{sample} , θ_{sample} and δ_{sample}) and were used directly to calculate the stress and strain. The error of this mistake is still unknown and thus need to be evaluated. For this reason, data correction will be discussed after ample insight into various instruments is

obtained.

Figure 5.12 shows two potential approaches for data post processing that allows to calculate the real specimen loading and deformation T_{sample} and θ_{sample} . Besides the straight-forward approach based on the raw variables combining with the instrument parameters, the other approach is back-calculation by using the “wrong” outputs of the sample sub-variables (τ_{sample} and γ_{sample}) together with the “wrong” specimen geometrical inputs. This approach seems to be crazy, but it is very practical indeed.

As indicated by the flowchart in Figure 5.12, τ_{sample} and γ_{sample} are firstly affected by various instrument parameters (i.e. I , μ and J) and thus proper instrument parameters must be used as input. After that, data processing will only deal with the influence of the specimen geometry. As mentioned earlier, the correct input related to the specimen geometry is not available for non-standard tests during this procedure. The instrument just continues the data processing by using the wrong input since it is outwitted to perform the testing. This implies that the cause of error in τ_{sample} and γ_{sample} only roots in the specimen geometrical inputs if the instrument parameters are correct.

The above discussion results in the conclusion that the real specimen torque T_{sample} and deformation θ_{sample} can be obtained by means of back-calculation. In this case, a relatively simple data post processing is needed. For example, dividing the “wrong” τ_{sample} by the “wrong” stress factor leads to the real T_{sample} ; similarly, dividing the “wrong” γ_{sample} by the “wrong” strain factor leads to the real θ_{sample} . After obtaining the real T_{sample} and θ_{sample} , the actual τ_{sample} and γ_{sample} in the sample can be determined by using the correct shape factors as discussed in Section 5.2. For practical reasons, this approach appears to be very promising. Proof of this will be given later. An appendix will be given at the end of this chapter shows how to use this practical approach for data post processing.

5.3.2.2 Results and discussion

In the following, the cylindrical delrin specimen was used for calibration tests on the DSR 2000 and DSR 1000 instruments. To get insight into the instrument performances the test conditions below were considered:

- frequency sweep tests from 1 to 100Hz in displacement-controlled mode;
- frequency sweep tests from 1 to 100Hz in torque-controlled mode.

Figures 5.13 and 5.14 show the frequency sweep test results under displacement and torque controlled modes by means of the DSR 2000. It must be noted that in these figures, the raw torque and displacement are referred to the output of torque and radial deflection angle, T_{raw} and θ_{raw} obtained from the instrument directly. The torque in the sample and the displacement in the sample, T_{sample} and θ_{sample} , were computed by using the two approaches for data post processing as shown in Figure 5.12.

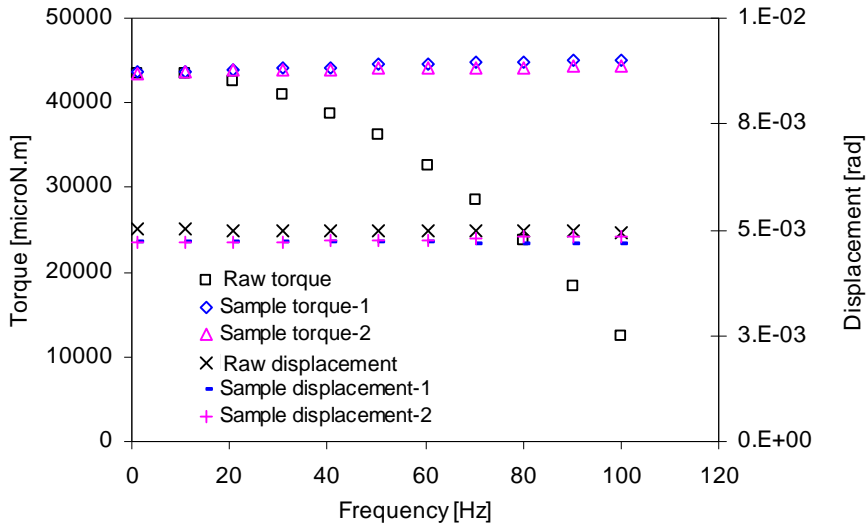


Figure 5.13 Frequency sweep test results under displacement-controlled done by using DSR 2000 (hereafter, raw torque and displacement: T_{raw} and θ_{raw} ; sample torque and displacement: T_{sample} and θ_{sample} ; 1: straight-forward calculation; 2: back-calculation)

Figure 5.13 shows that T_{raw} exhibits a strong frequency dependence, while the computed T_{sample} remains fairly constant. The latter is in good agreement with the constant applied displacement θ_{raw} . Moreover, there is a slight difference between θ_{raw} and θ_{sample} . This is due to the contribution of the clamp system. However, such a contribution is limited compared with the actual deformation of the specimen.

Similar trends can also be observed in the case of frequency sweep testing in torque controlled mode, as indicated in Figure 5.14. When the applied torque remains constant, the measured displacement shows a strong frequency dependence. The trends among θ_{raw} , T_{sample} and θ_{sample} are all logical. Again, a small gap exists between the displacement in the sample and the total measured displacement.

The computed T_{sample} and θ_{sample} on the basis of the proposed approaches are comparable with each other, indicating that both of approaches are capable to derive the correct values of T_{sample} and θ_{sample} dependent on different output data obtained from the instrument. This is important for the data correction in the case of the LOT project in which only the raw measured value were reported from the laboratory.

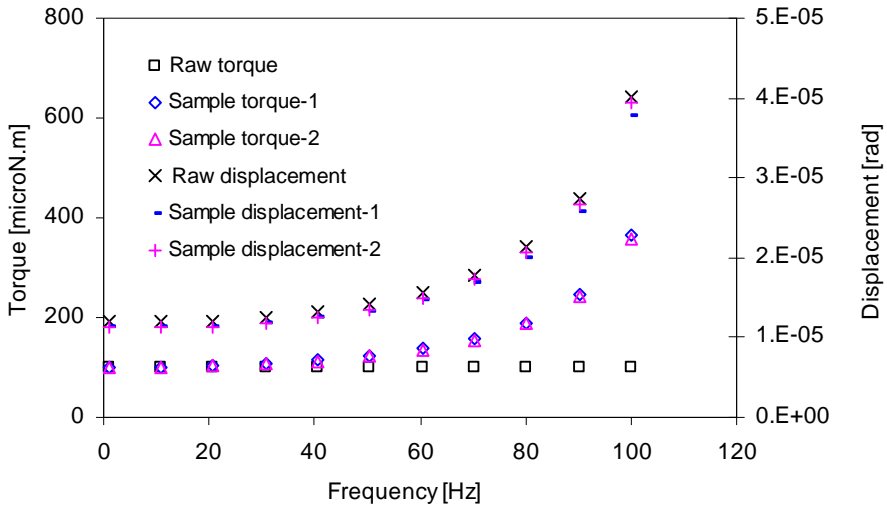


Figure 5.14 Frequency sweep test results under torque-controlled done by using DSR 2000

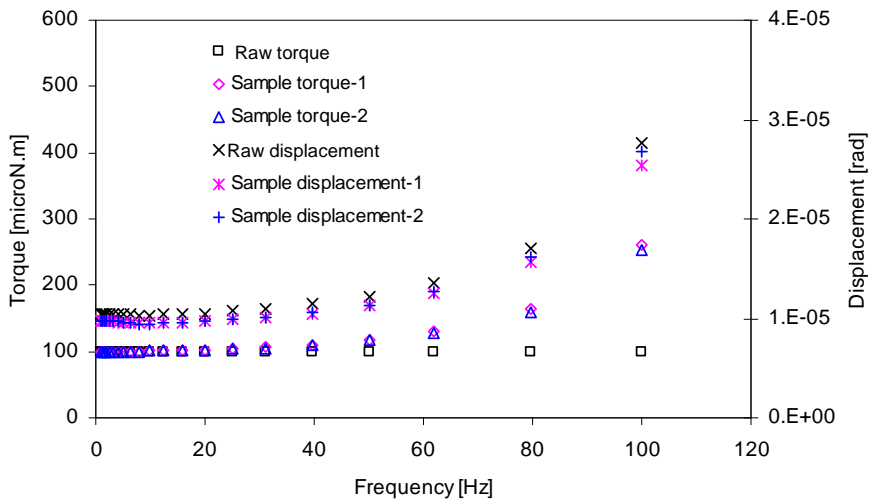


Figure 5.15 Frequency sweep test results in torque-controlled mode done by using the DSR 1000

The above tests that were performed by using the DSR 2000, were also carried out by using the DSR 1000. Figures 5.15 shows frequency sweep test results in the torque-controlled mode done by means of the DSR 1000. Compared to the data obtained from the DSR 2000 (see Figure 5.14), it is concluded that the DSR 1000

behaves in the same way as the DSR 2000.

Another important remark is that don't mistake δ_{raw} for δ_{sample} during the data analysis. It must be noted that the definitions of these two parameters are different. Figure 5.16 gives an example using the delrin sample. As the applied frequency increases, the raw phase angle δ_{raw} deflects from the sample phase angle δ_{sample} more obviously. Only when the applied frequency is much smaller than the resonance frequency, the δ_{raw} is comparable with the δ_{sample} . This will be demonstrated by means of the test data obtained on the steel strip which is discussed in the following section.

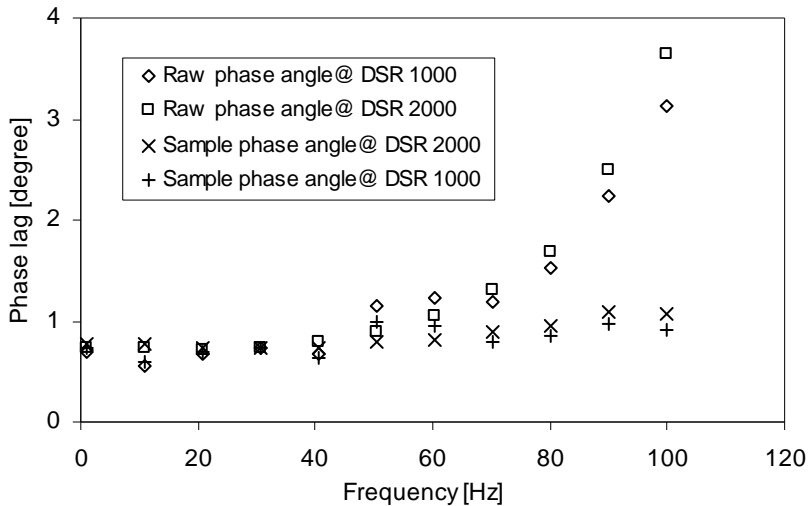


Figure 5.16 Impression of the differences between δ_{raw} and δ_{sample}

For the purpose of comparison between the two DSR instruments, the stiffness measurement results in Figures 5.14 and 5.15 were used. It should be noted that these tests were done under the same conditions, i.e. delrin sample, frequency sweep from 1Hz to 100Hz with an applied torque of 100 microN.m.

As indicated in Figure 5.17, the DSR 1000 tends to measure a higher stiffness than the DSR 2000. If the mean value of the stiffness is selected as the reference value, then the stiffness values measured by the DSR 1000 is approximately 12.5% higher than those measured by the DSR 2000.

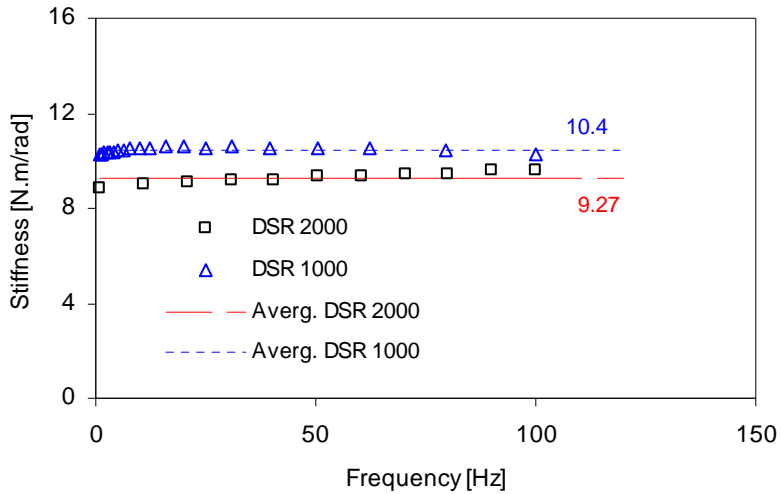


Figure 5.17 Indication of instrument differences by means of stiffness measurements

5.3.2.3 Rectangular torsion

This section will focus on the comparison between the DSR 2000 and the DSR MCR 301. Emphasis is on investigating the instrument performances with application of the special designed clamp system. Use was made of a stainless steel strip with a length of 60mm and a width of 12.41mm and a thickness of 0.43mm in stead of the thin bitumen film. For the DSR MCR 301, the specially designed clamp system for adhesive zone testing was utilized. However, for the DSR 2000 its standard rectangular clamp system was used. After clamping in the test setup, the effective length becomes 50mm. The test program described hereafter, which is similar to the one that was used for the delrin specimen, was used in the instrument calibration.

Figure 5.18 shows the test results on the steel strip obtained by means of the DSR 2000. As can be seen, a strong resonance effect occurred during the torque controlled frequency sweep test. When a constant torque amplitude of T_{raw} is applied, the signal of θ_{raw} exhibits frequency dependence and a sharp peak value occurs at a test frequency of approximately 25Hz, the so-called resonance frequency. This figure clearly shows that T_{raw} fails to represent T_{sample} . Again, θ_{sample} is slightly smaller than

θ_{raw} .

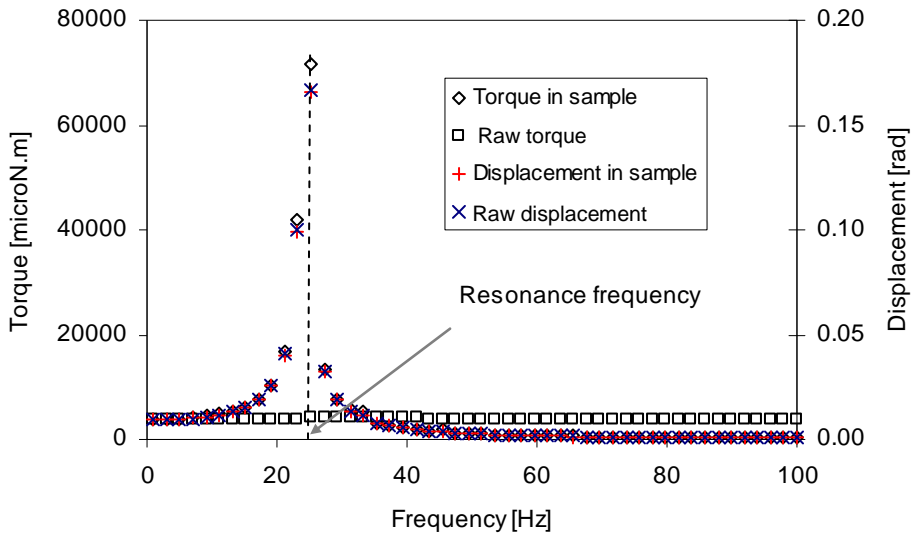


Figure 5.18 Torque controlled frequency sweep test results obtained by means of the DSR 2000 using the stainless steel strip

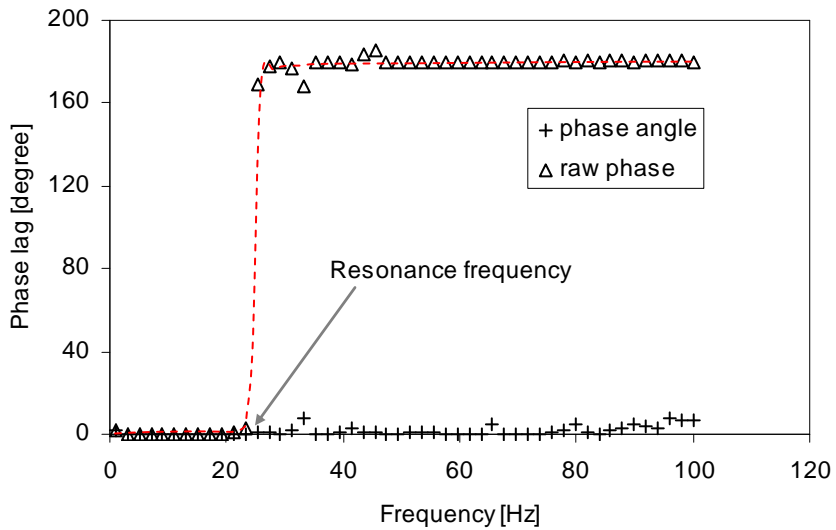


Figure 5.19 Comparison between δ_{sample} (phase angle) and δ_{raw} (raw phase) obtained by means of the DSR 2000 using the stainless steel strip

Figure 5.19 shows that δ_{raw} depends on the test frequency. However, the phase

angle δ_{sample} remains relatively constant. This should be the case since the stainless steel strip used is an elastic material. As indicated in Figure 5.19, δ_{raw} is only comparable with δ_{sample} when the applied frequency is smaller than the resonance frequency. This is in good agreement with the test data obtained on the delrin sample (see Figure 5.16).

When the same tests were done by means of the DSR MCR 101, different results were obtained; this is shown in Figure 5.20. The data shown in this plot were obtained from the frequency sweep test in the torque controlled mode. A huge increase in torque and displacement is observed at the frequency of approximately 12Hz. This frequency is clearly the resonant frequency. Despite of the resonance effect, T_{raw} is exactly equal to T_{sample} . This also holds for the relation between θ_{raw} and θ_{sample} .

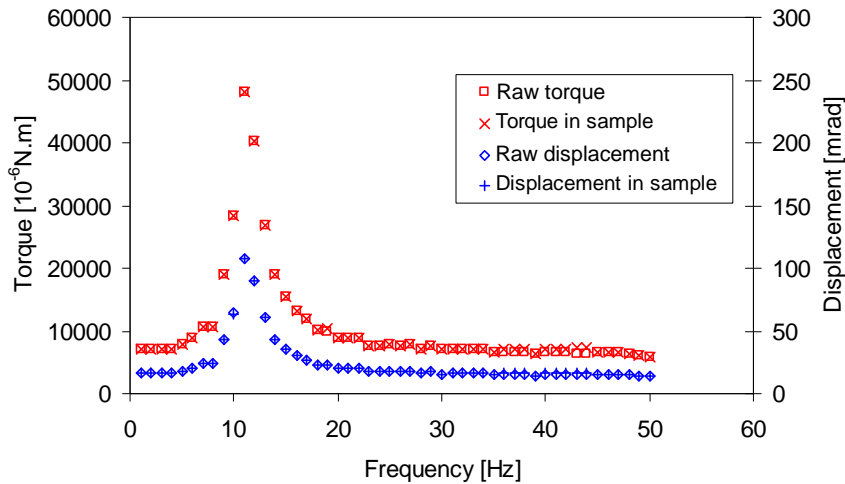


Figure 5.20 Frequency sweep test results under torque controlled mode done by DSR MCR 301 using the stainless steel strip

More tests were performed to check these phenomena by using different test mode, i.e. torque sweep tests with a maximum applied torque of 10N.mm at various frequencies. As can be seen in Figure 5.21, the huge increase in torque and displacement is also observed at the frequency of around 12Hz. As discussed previous, the resonance effect would lead to a nonlinear relationship between the raw torque and displacement. However, a linear relationship as shown in Figure 5.21 is obtained when DRS MCR 101 was applied for the measurements.

Combining all these discussions leads to the conclusion that the data processing of the DSR 2000 differs from the one of DSR MCR 101. The later directly provides the actual torque and displacement in the specimen, which can be directly used for the stress and strain calculations.

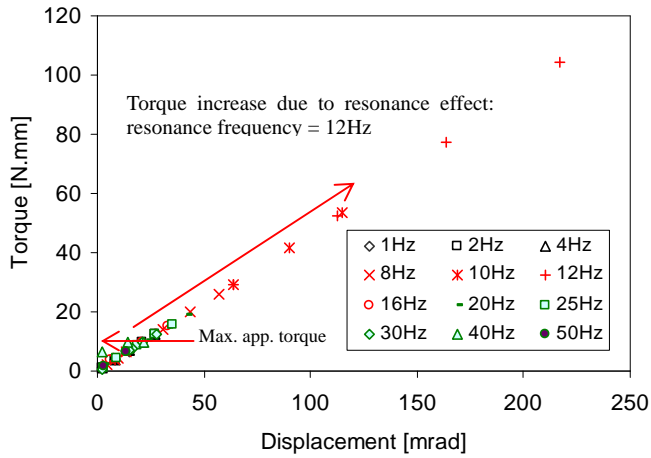


Figure 5.21 Torque sweep tests done by means of the DSR MCR 301 using stainless steel strip

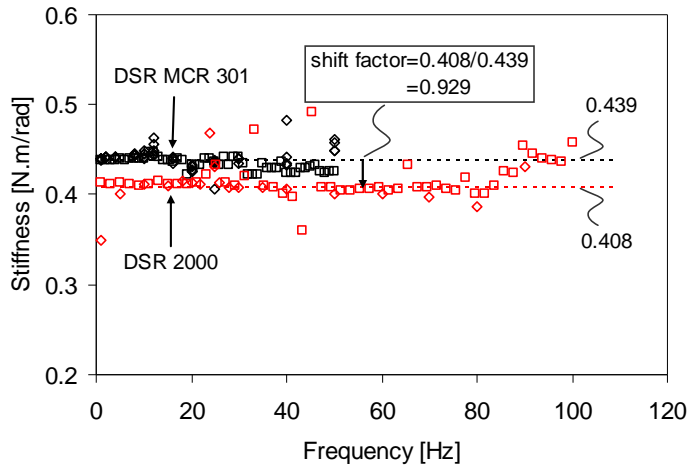


Figure 5.22 Difference between the DSR 2000 and the DSR MCR 301 indicated by test data from the steal strip

To obtain insight into the difference between the DSR 2000 and DSR MCR 301 instruments, the sample stiffness obtained from both instruments was compared. Figure 5.22 shows the measurement results under the same test conditions. Here the stiffness is related to the stainless steel strip with a width of 12.41mm, a thickness of 0.43mm and an effective length of 50mm. As can be observed, the DSR MCR 301 measured a higher stiffness compared with the values obtained from the DSR 2000. Due to data scatter, the representative stiffnesses are indicated by two dashed lines.

These lines are mainly determined based on data at low frequencies since they are less influenced by frequency and thus more reliable. By doing this, the representative stiffness for the DSR MCR 301 is determined as 0.439 N.m/rad, while the corresponding one for the DSR 2000 has a lower value of 0.408N.m/rad. Therefore, the shift factor for the DSR MCR 301 can be determined as 0.929 when the DSR 2000 is chosen as the reference instrument.

5.3.2.4 Dual cantilever bending

From the findings of the DSR calibration presented in the previous sections, it is known that in frequency sweep tests one should examine the dynamic effect on the data output. The frequency dependence of the raw force/displacement could be used to investigate the data processing. Besides dynamic testing, the DMA instruments were also used to perform static tests on the adhesive zone. Therefore, the difference between dynamic and static test modes should be compared. For these reasons, frequency sweep and constant force-rate static tests were performed.

Figure 5.23 gives the overlook of the test set-up and the results of frequency sweep testing under displacement controlled mode by means of the DMA 2980. As observed, the raw displacement and force remain fairly constant as the applied frequency increases. As known from the calibration of the DSR instruments, the resonance effect can only become significant when the test frequency is close to the resonant frequency. Furthermore, the resonant frequency is close to the natural frequency. At this point, the applied test frequency will be compared with the natural frequency of the test item and then the ratio of both is used as an indicator of the resonance effect.

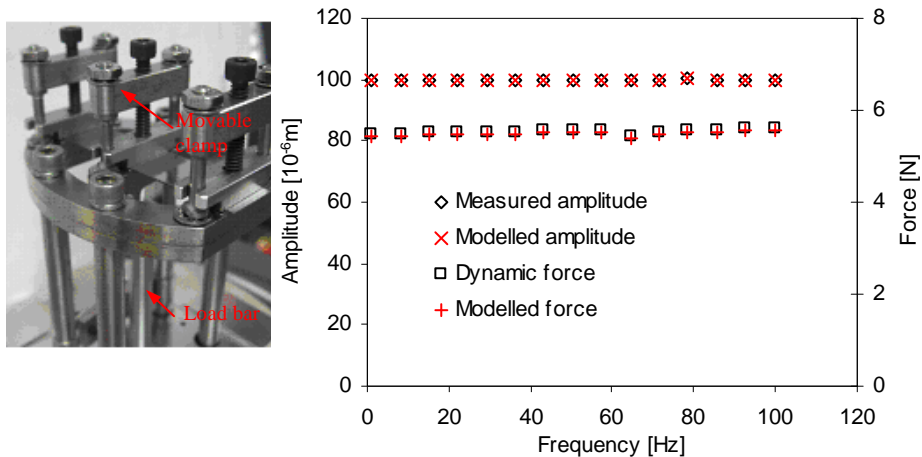


Figure 5.23 Test set-up (left) and typical results of displacement controlled frequency sweep test done by means of the DMA 2980

The test data in Figure 5.23 resulted in a sample stiffness of $K = 55000$ N/m. According to Equation 5.5, it results in a natural frequency $f_n = 215$ Hz. Apparently, this computed natural frequency is beyond the instrument capability (i.e. maximum

frequency of 100Hz) and thus can not be checked directly.

Similar to the DSR calibration, the force and the displacement amplitudes to which the sample is subjected were also computed by means of post data processing. The back-calculation was done using stress and strain divided by the corresponding shape factors. Figure 5.23 shows a comparison between the computed values and the raw output values obtained from the DMA instrument. As observed, the computed values are in good agreement with the output values. This indicates that the DMA 2980 is capable to directly provide the actual force and displacement to which the sample is subjected.

The difference between dynamic and static tests was also investigated. Figure 5.24 presents the test results obtained from a constant displacement-rate controlled test and a frequency sweep test from 1 Hz to 100 Hz. It is observed that the dynamic data is consistent with the static data irrespective of the change in frequency. The linear fit of the data obtained indicates that an overall error is 3.7% for dynamic testing when static testing is used as the reference value.

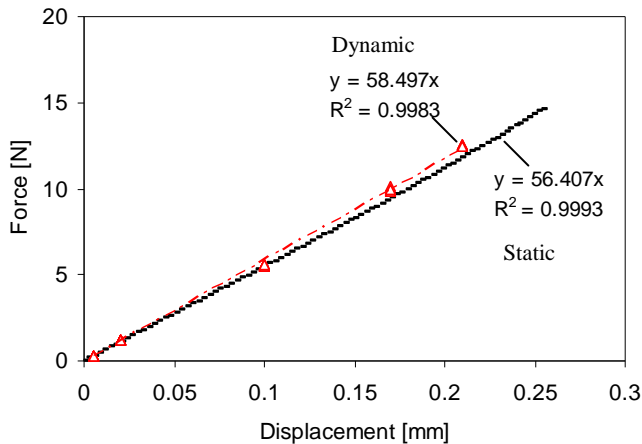


Figure 5.24 Comparison between static and dynamic test results done by DMA 2980

As shown in Figure 5.25, similar results are also obtained for the DMA 800. The computed force and amplitude is identical with the raw ones obtained from data output. With respect to sample stiffness, dynamic tests result in a mean value of 49.67 N/mm. However, static tests show a higher mean value of 58.20 N/mm. Combining these two mean values leads to an estimated error of 14.7% when static testing is selected as the reference.

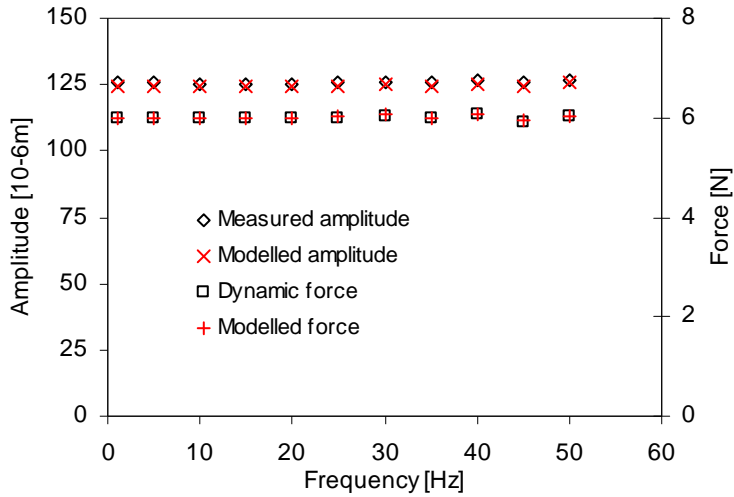


Figure 5.25 Frequency sweep test results by means of DMA 800

Table 5.8 gives the stiffness measurement results obtained from both DMA instruments. Compared with the DMA 800, the error is approximately 3.1% for the DMA 2980 based on the static stiffness data. A maximum error of 14.7% is found in the case of dynamic testing by means of the DMA 800. In general, both DMA instruments are comparable with each other.

Table 5.8 Stiffness measurement results by means of DMA instruments

Instrument	DMA 2980, TUD		DMA 800, WHUT	
	Dynamic test	Static test	Dynamic test	Static test
Test mode				
Sample stiffness [N/mm]	58.50	56.41	49.67	58.20
Error [%]	0.5	-3.1	-14.7	-

5.3.2.5 Correlation between DSR and DMA instruments

As discussed above, the calibration tests for the DMA and DSR instruments were executed under different stress modes, i.e. shear and bending tensile stresses. In order to relate DMA data to DSR data, the material moduli obtained from DSR and DMA testing were compared. Because the calibration sample remains the same, i.e. steel strip, the material modulus, E calculated from DSR and DMA testing should be equal to each other. If different values would occur, it meant that a calibration factor should be introduced to correlate DMA data to DSR data.

According to Equations 5.23 and 5.24, the modulus equation for a rectangular cross section sample, analyzed on the dual cantilever clamp, is as follows.

$$E = \frac{F}{x} \times \frac{l^3 \left[1 + \frac{12}{5} (1 + \nu) \left(\frac{t}{l} \right)^2 \right]}{2wt^3 F_c} = k_1 \times S_1 \quad (5.30)$$

Where:

$$k_1 = \frac{l^3 \left[1 + \frac{12}{5} (1 + \nu) \left(\frac{t}{l} \right)^2 \right]}{2wt^3 F_c}, \text{ shape factor;}$$

$$S_1 = \frac{F}{x}, \text{ sample stiffness.}$$

Based on Equations 5.21 and 5.22, the transfer function for rectangular torsion is written in the form

$$E = G \times 2(1 + \nu) = \frac{\tau}{\gamma} \times 2(1 + \nu) = \frac{6(1 + \nu)l}{Bwt^2} \times \frac{T}{\theta} = k_2 \times S_2 \quad (5.31)$$

Where:

$$k_2 = \frac{6(1 + \nu)l}{Bwt^2}, \text{ shape factor;}$$

$$S_2 = \frac{T}{\theta}, \text{ torsion stiffness.}$$

Based on the specimen geometry, one can obtain $k_1 = 2.567 \times 10^3 \text{ MPa}\cdot\text{mm}/\text{N}$ and $k_2 = 427.2 \text{ MPa}\cdot\text{rad}/(\text{N}\cdot\text{mm})$ with $\nu = 0.3$ via the empirical formulas. Hereafter, these factors will be further checked by using finite element simulations.

ABAQUS package (Version 6.6-1) was used to set up the finite element models. In Figure 5.26, the DSR test set up (bottom) and 3D finite element model (top) are shown. The steel strip and the clamp system are defined as a deformable body. The contact between steel strip and clamps is a fully bonded one obtained by means of a tie element. The effective length between the two clamps is 50mm as indicated in Figure 5.26. The end of the bottom fixed clamp is fully restricted. However, the upper clamp is only allowed to rotation. The type of element used for the steel strip is 8-node hex-structured and the rest is 4-node tetrahedron due to the irregular shapes. The torque is applied at the upper clamp by means of force acting on the edge of the rounded bar and normal to the radial direction. The mesh refinement was checked by varying multiple-levels of mesh density.

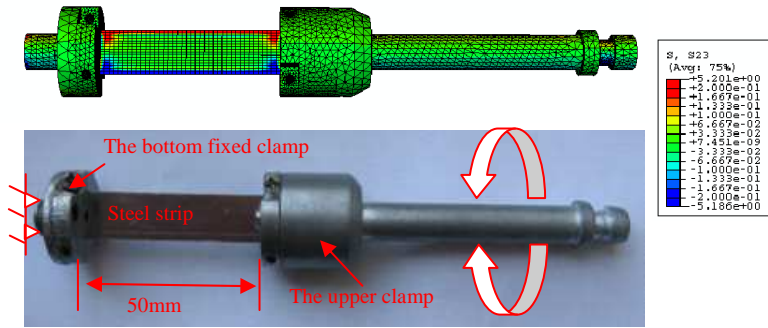


Figure 5.26 DSR test set up (down) and 3D finite element model (upper)

To determine the value of k_2 , the following material parameters are given as input: $E = 2 \times 10^5 \text{ MPa}$ $\nu = 0.3$ for both the stainless steel sample and the clamp system. When a torque of 12.5Nmm was applied, the computed deflection angle obtained from FE modelling was 0.02389 rad. Based on Equation 5.31, the specimen constant k_2 was back-calculated as 382.2MPa.rad/(N.mm).

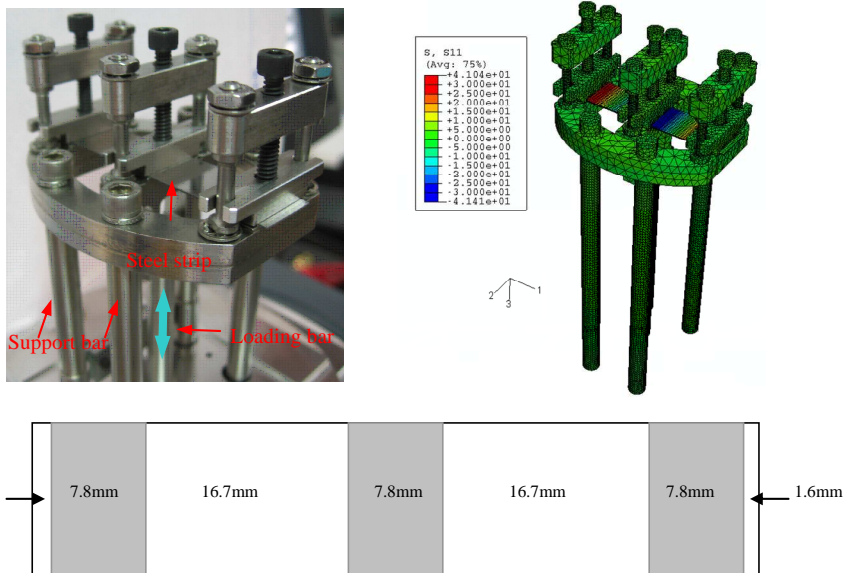


Figure 5.27 DMA test set up (up-left), 3D finite element model (up-right) and clamping positions and sizes on the sample (bottom)

Figure 5.27 shows the DMA test set up (upper-left) and the 3D finite element model (upper-right). The whole set-up is defined as a deformable body. Similarly, the

constraints between the steel strip and clamps are modelled using tie element. The movement at the bottom ends of four support bars are fully limited. The type of element used for the steel strip is an 8-node hex-structured one and for the rest a 4-node tetrahedron is used because of the irregular shapes. To simulate the actual load that is applied by the DMA, the model is loaded by means of concentrated force that is acting on the end of the loading bar. Figure 5.27 also gives an impression of the locations where the clamps contact the sample as indicated by the gray parts. The mesh density was also checked to obtain stable computational results.

To determine the specimen constant k_1 of the DMA set-up, the same material parameters as used for the DSR simulation are used. When a force of 12N was applied via the load bar, the displacement of the load bar computed by means of the FE modelling was 0.1484mm. Based on Equation 5.30, the value of k_1 was calculated as $k_1 = 2.473 \times 10^3 \text{MPa.mm/N}$.

Combining all these discussions leads to the conclusion that the values of k_1 and k_2 determined by means of empirical formula are verified by performing finite element simulations. Hereafter, the values of k_1 and k_2 determined from finite element simulations were used to translate the sample stiffness into material elastic modulus.

Table 5.9 gives the modulus of the steel strip as computed from the DSR and DMA measurements. In Table 5.9, the modulus, E of the steel strip was determined by using Equation 5.30 for DMA measurements and using Equation 5.31 for DSR measurements, respectively. After that, the difference between the various instruments was compared in terms of the modulus. Since the DSR 1000 did not perform tests on the steel strip, the modulus listed in Table 5.9 responsible for the DSR 1000 was estimated from the relation of delrin stiffness measurements by means of the DSR 1000 and DSR 2000.

Table 5.9 The computed modulus of the steel strip by means of DSR and DMA measurements

Instrument	k_1 [MPa.mm/N]	S_1 [N/mm]	k_2 [MPa.rad/(N.mm)]	S_2 [N.mm/rad]	E [Mpa]	Error [%]
DMA 800, WHUT	2473	58.2	-	-	143928.6	3.2
DMA 2980, TUD	2473	56.4	-	-	139477.2	0.0
DSR 101, WHUT	-	-	382.2	439	167785.8	20.3
DSR 2000, TUD	-	-	382.2	408	155937.6	11.8
DSR 1000,TUD	-	-	382.2	458*	174946.2	25.4

Note: *DMA 2980 is the reference instrument; ** is estimated by the relation of delrin stiffness measured by DSR 2000 and DSR 1000.

Based on the test data listed in Table 5.9, a relative instrument calibration was carried out. To do this, a reference instrument is required. It should be noted that both DMA instruments used in this study are able to perform an absolute calibration. The absolute calibration allows to perform the force and displacement (i.e. position) calibration. This procedure ensures the DMA instrument is in good condition. The

data listed in Table 5.9 also show that the error between the DMA 2980 and DMA 800 is fairly small, i.e 3.1%. With respect to DSR instrument, the absolute calibration is more troublesome. As a result, a relative calibration is provided by the manufacturer to examine the DSR instrument.

Combining the discussions above leads to the conclusion that the DMA instruments used in this study seem to be more reliable. For practical reasons, the DMA 2980 was chosen as the reference instrument. By comparing other instruments with this reference instrument, the errors were determined as given in Table 5.9. The errors for other instruments range from 3.2% to 25.4%. This indicates that the instrument accuracy is within $\pm 15\%$.

It should be noted that the errors listed in Table 5.9 are related to the material modulus. For example, the DSR 1000 tends to measure a higher material stiffness compared with the DSR 2000. To minimize the difference, the stiffness obtained from different instruments should be multiplied by a corresponding instrument correction factor.

Similarly, such an approach may also be used to correct the force or displacement. For example, the same material deformation may result in different material load that are measured by different instruments and vice versa. An instrument factor that accounts for such a difference should be assigned to each instrument and then allow to correlate the measurement data obtained from various instruments.

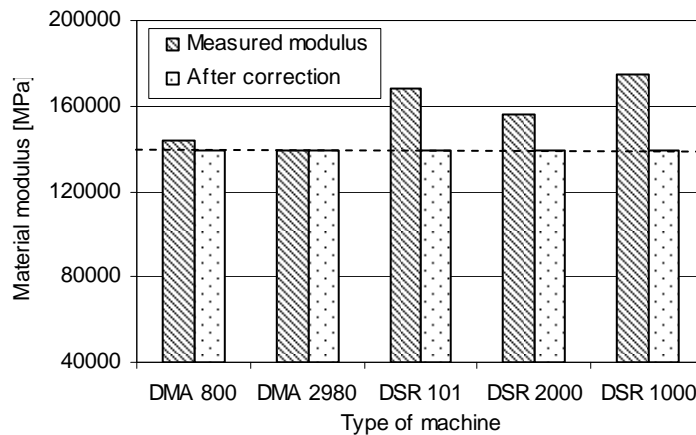


Figure 5.28 Example of using instrument factors to correct various moduli obtained from different instruments into a unique modulus when the DMA 2980 is the reference instrument

Combining all the calibration results leads to the instrument factors as given in Table 5.1. For the purpose of minimizing the data spread, these factors can be used as a multiplier of the measurement data obtained from the various instruments. Figure 5.28 gives an example on modulus correction. As indicated, various moduli obtained from different instruments are corrected into a unique modulus by multiplying the corresponding instrument factors as given in Table 5.1. In this study, all the tests were performed in force or torque controlled mode. It implies that the stress, to which

material is subjected, is more important for data analysis. Considering the fact that various instruments were used for material testing in this study, it was decided to use the instrument factors listed in table 5.1 as a multiplier on the stress to minimize the spread of the fatigue data hereafter.

5.4 Data correction

The results of the instrument calibration indicate that the raw load provided in the data output may not be equal to the real material load depending on the instrument used. Among these five test instruments used in this study, the DSR 1000 and DSR 2000 instruments fail to provide the real T_{sample} and θ_{sample} directly. The other instruments are capable of providing an acceptable output. Therefore, data provided by these two DSR instruments need to be verified and corrected.

As mentioned earlier, the test data produced in the laboratory during the LOT project were reported by the raw variables, e.g. T_{raw} , θ_{raw} and δ_{raw} for the non-standard DSR tests. The stress and strain were then directly calculated using T_{raw} and θ_{raw} and the specimen geometrical factors. The material modulus was obtained by dividing stress by strain. The instrument calibration shows that the mentioned above approach that was used for stress and strain determination may lead to loss of accuracy. Hereafter, the data correction is carried out on the available raw data and the revertent instruments parameters. Detailed information is given in Section 5.2.1.6.

It should be noted that the DSR 2000 and DSR 1000 mainly used for mortar fatigue tests in this study. Only a limited amount of adhesive zone tests were performed by these two DSR instrument. In the following, focus is on the correction of the mortar fatigue data using an Excel spreadsheet. In Section 5.3.2.2, it is shown that the correction calculated by means of the equations used in this Excel spreadsheet is correct.

The following data correction includes the torque, the displacement, phase angle as well as initial total dissipated energy per cycle. The initial dissipated energy per cycle was also involved because it was used as an indicator for mortar fatigue in the initial phase of LOT project [Huurman & Mo 2007]. The initial dissipated energy per cycle was calculated using the following equation:

$$W_i = \pi \times \tau_i \times \gamma_i \times \sin \delta_i \quad (5.32)$$

Where:

- W_i = dissipated energy at the i^{th} cycle, [MPa];
- τ_i = shear stress amplitude at the i^{th} cycle, [MPa];
- γ_i = shear strain amplitude at the i^{th} cycle, [-];
- δ_i = phase angle between maximum stress and strain, [degree];

Figure 5.29 gives a comparison between θ_{raw} and θ_{sample} . It must be noted that the data points in this plot stand for the initial values of θ_{raw} for all of mortar fatigue tests. As observed, θ_{raw} is larger than θ_{sample} since the former consists of the sample

deformation and the contribution of the clamp system. As the displacement reduces, the ratio of θ_{raw} over θ_{sample} increases, indicating that at very small displacements, the difference between θ_{raw} and θ_{sample} becomes significant. It is suggested that special attention should be paid to tests done at displacements smaller than 0.01rad since the deformation of the clamp system may become significant.

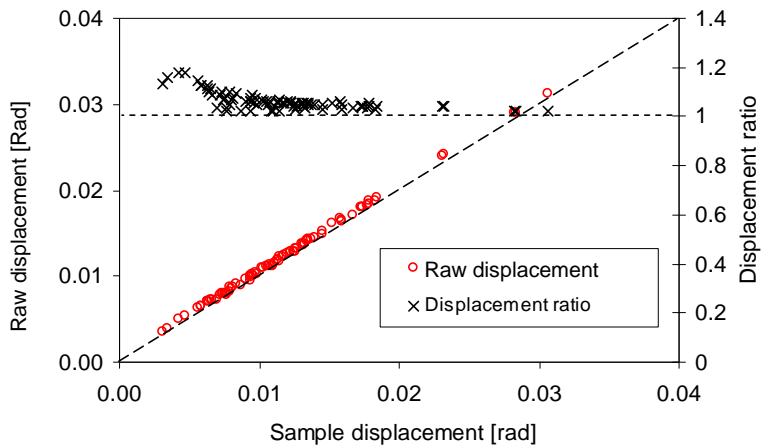


Figure 5.29 θ_{raw} compared with θ_{sample} using the mortar fatigue data obtained from the DSR 1000 and DSR 2000 (displacement ratio = $\theta_{raw} / \theta_{sample}$)

Figure 5.30 shows a comparison between T_{raw} and T_{sample} using all of the mortar fatigue data. As can be seen, a higher T_{raw} results in a higher T_{sample} . However, T_{raw} tends to underestimate T_{sample} because it does not take into account the torque induced by inertia effects. The ratio of T_{raw} over T_{sample} varies from 0.8 to 1.

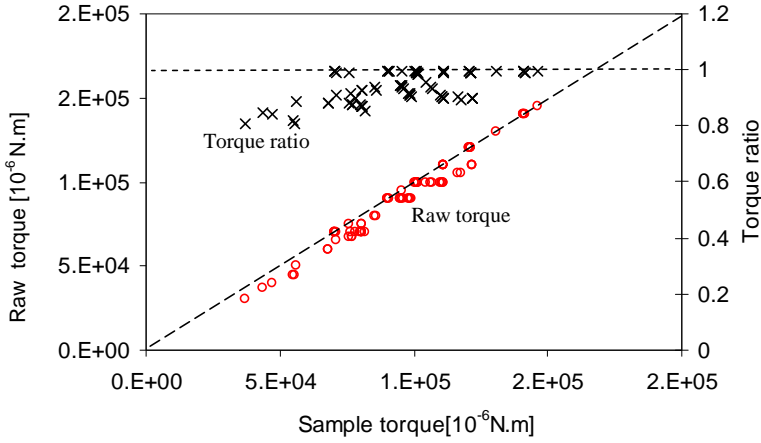


Figure 5.30 T_{raw} compared with T_{sample} using mortar fatigue data

Figure 5.31 shows a comparison between δ_{raw} and δ_{sample} . Most of the data points are close to the line of equality as indicated by the diagonal of the plot. The ratio obtained by $\delta_{raw} / \delta_{sample}$ remains within a range from 0.8 to 1.2.

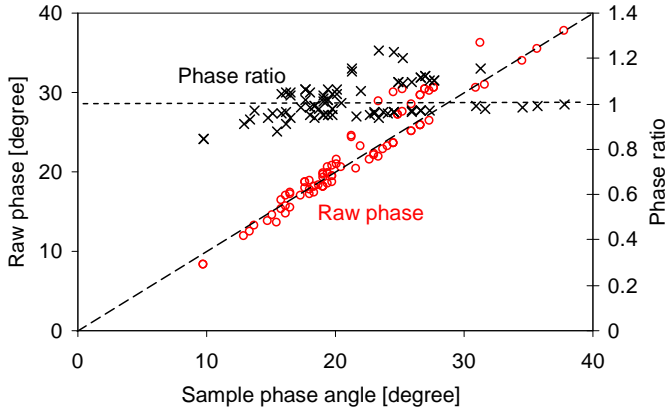


Figure 5.31 δ_{raw} compared with δ_{sample} using mortar fatigue data

Figure 5.32 shows a comparison between the raw initial dissipated energy per cycle and the computed initial dissipated energy per cycle, in which the former is calculated based on the raw variables (T_{raw} , θ_{raw} and δ_{raw}) while the later is dependent on the sample variables (T_{sample} , θ_{sample} and δ_{sample}) obtained by data post processing. As observed, the raw initial dissipated energy per cycle is exactly equal to the computed initial dissipated energy per cycle in the sample. This indicated that almost all of the dissipated energy in the whole test setup is from the test specimen.

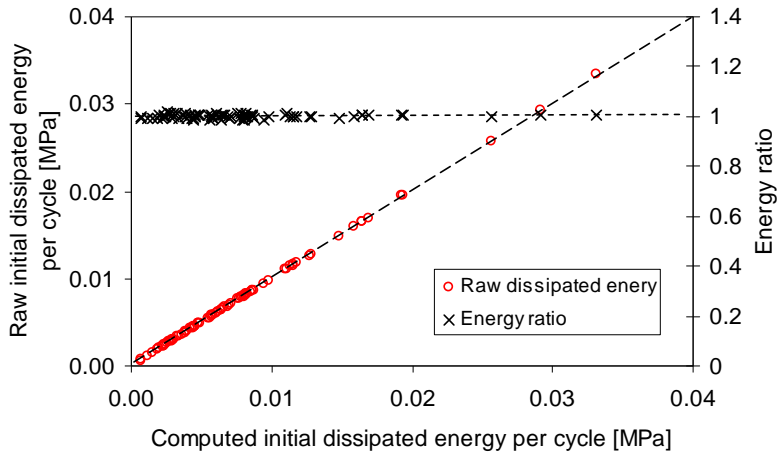


Figure 5.32 Raw dissipated energy compared with computed dissipated energy using mortar fatigue data

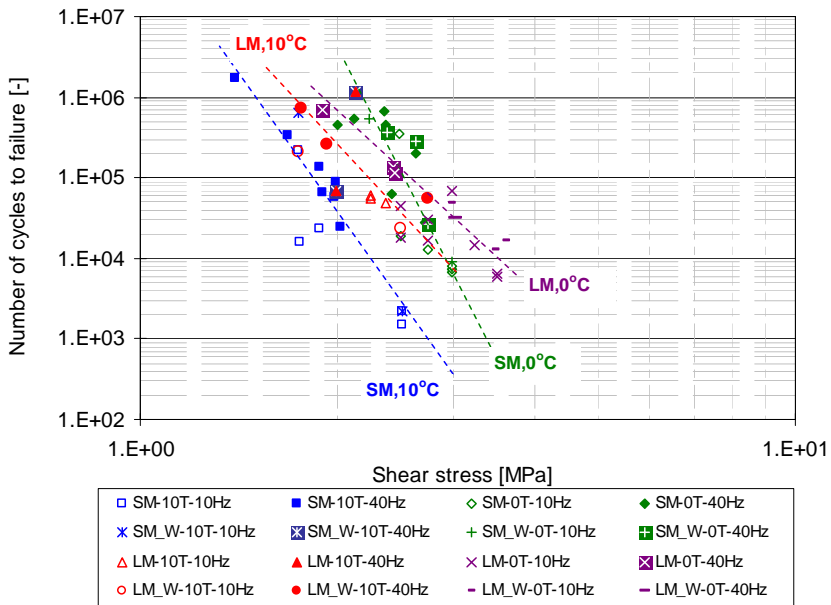


Figure 5.33 Relationship between number of cycles to failure with corrected shear stress by means of T_{sample}

Figure 5.33 shows the relationship between number of cycles to failure and the corrected shear stress in a log-log scale. When comparing these results with the data

obtained from the uncorrected shear stress shown in Figure 4.36 in the previous chapter, it was found that the fatigue lives are shifted to a slightly higher stress level. This is in agreement with the overall relationship between T_{raw} and T_{sample} as shown in Figure 5.30.

5.5 Conclusions

In total two DMA instruments and three DSR instruments were calibrated using different reference samples and different clamp systems. By comparing the calibration data obtained from the above-mentioned instruments, it is concluded that the instrument accuracy is within $\pm 15\%$. This could play an important role in the data scatter.

Among the mentioned above instruments, the DSR 1000 and DSR 2000 are unable to provide the actual torque and radial deflection angle to which the test specimen is subjected. The rest instruments are capable to directly provide this kind of information for the stress and strain calculations.

The raw torque, radial deflection angle and raw phase that were measured by the instrument itself are not exactly equal to the corresponding values to which the specimen is subjected. Demonstration of this is that these variables are frequency dependent when an elastic material is tested. Therefore, the direct calculation of stress and strain based on the raw values may result in loss of accuracy.

A practical procedure that leads to proper test interpretation has been given for the non-standard tests on mortar and adhesive zone specimens (see Appendix 5.1). These non-standard tests can be performed in the standard control mode, i.e. using parallel-plate mode. However, data post processing is needed for proper test interpretation. In this case, strain and stress should be derived from the raw measured values (torque and deflection angle) and the relevant instrument parameters or should be based on the back-calculation of the torque and deflection angle in the specimen as discussed in this chapter. The later approach is proved to be more practical and thus is recommended for other users.

Data correction has been performed and the loss of accuracy due to improper test interpretation was investigated. In the LOT project, the mortar strain tends to be overestimated by a factor of 1.02~1.20. The mortar stress was underestimated by 0~25%. The overall error in the phase angle seems to be limited. The raw initial dissipated energy per cycle is identical with the actual initial dissipated energy per cycle.

A final remark is that checking the measurement data is very necessary for the non-standard tests. To do this, a complete data report from the laboratory is required. This report should consist of detailed input information on instrument parameters, specimen geometry and relevant output data obtained during a test. This information allows to correct the obtained data by means of data post processing.

Appendix 5.1

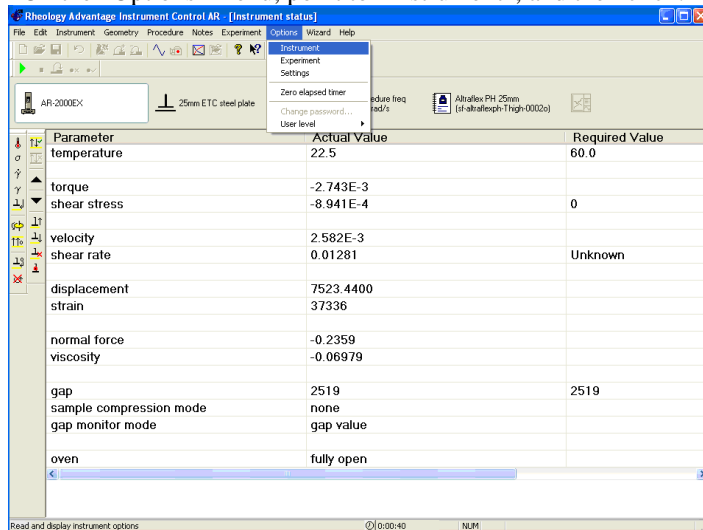
Practical procedure for mortar test using DSR 2000 and DSR 1000

The general procedure for conducting mortar shear testing using the DSR 2000 and the DSR 1000 is described in this appendix. Focus is on how to perform the so-called nonstandard tests by outwitting both instruments and how to obtain the correct data for stress/strain analysis by means of data post processing. Information on sample preparation is thus not described.

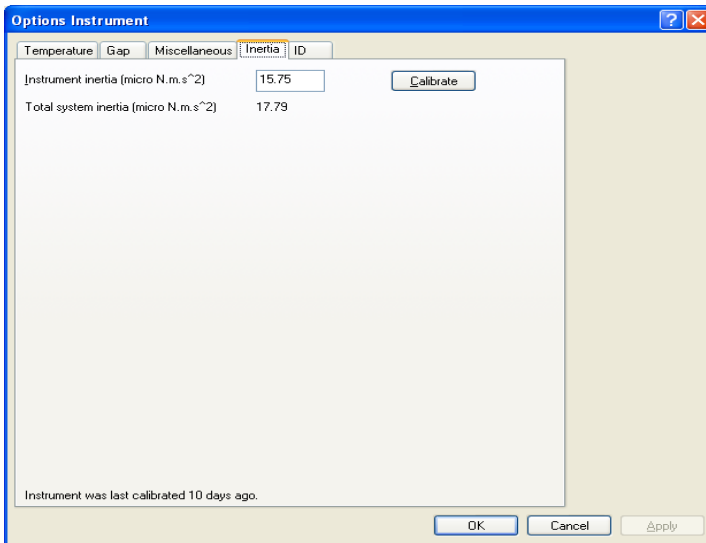
1. Instrument self-calibration

1.1 Instrument inertia calibration

On the “Options” menu, point to “Instrument”, and then click.



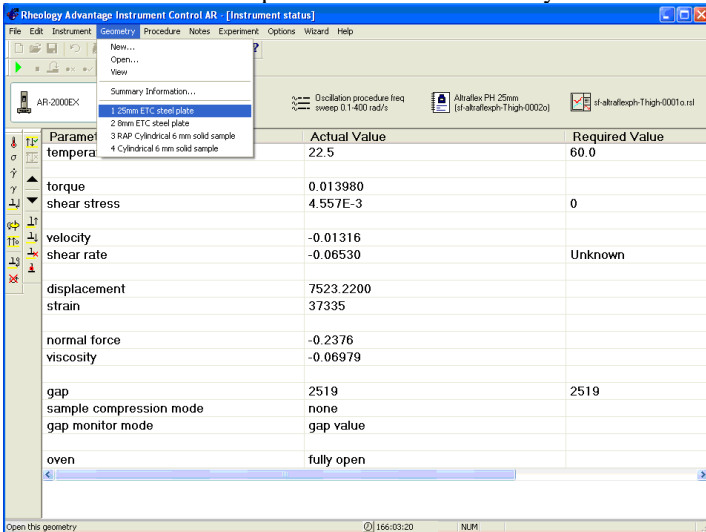
In the Options Instrument, click “Inertia” menu, point to “calibrate” and click.



The instrument will automatically calibrate the instrument inertia. After completing this procedure, it will report the value of the instrument inertia and edit it in the box.

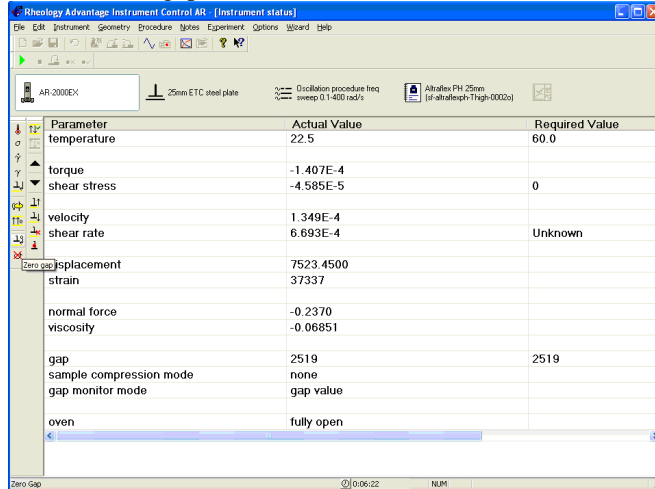
1.2 Select test geometry

On the “Geometry” menu, Click “Open”, select “25mm ETC steel plate”. Or directly click “25mm ETC steel plate” under the “Geometry” menu if available.



1.3 Set zero gap

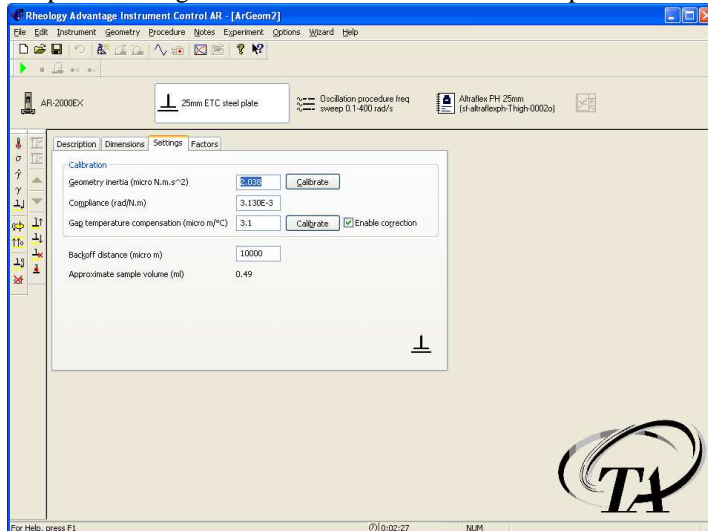
Fix the upper and bottom clamps into the DSR instrument.
 Point to “zero gap” bottom and click.



1.4 Calibrate the geometry inertia and the gap temperature compensation

Highlight the “25mm ETC steel plate”, select the “setting” menu and click the “calibrate” bottom of the geometry inertia (i.e. the clamp plus the mortar specimen).
 After completing, edit the obtained value into the box.

Click the “calibrate” bottom of the gap temperature compensation then edit the temperature range. The instrument will calibrate the parameter automatically.



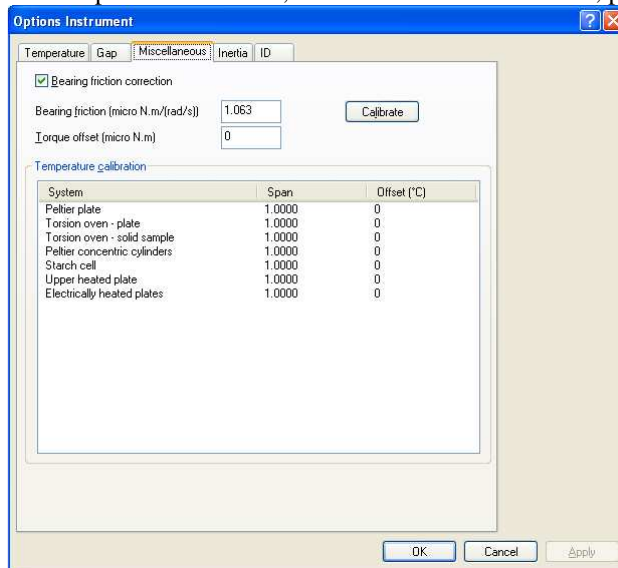
1.5 Calibrate the compliance of the test setup

This step has to be performed manually. It requires performing a static rotation test on a very stiff material by using the same clamp. Use was made of a stone column and a stainless steel strip. Based on the relationship between the applied torque and the induced deflection, the compliance of the test setup can be derived and edited in the required box as instrument input.

1.6 Calibrate the air-bearing friction

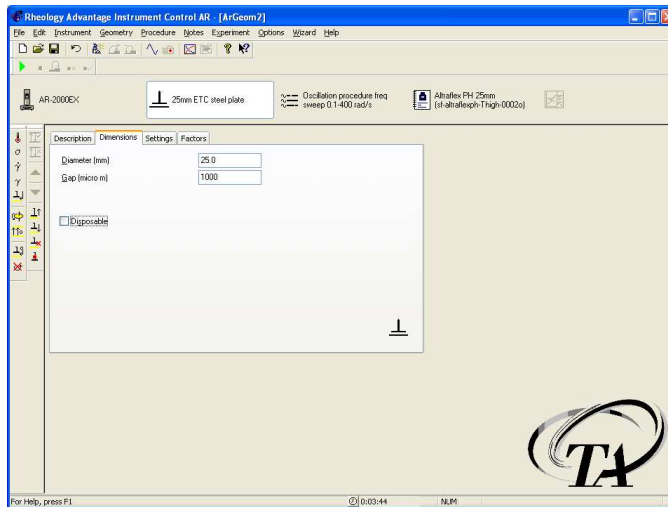
On the “Options” menu, point to “Instrument”, and then click.

In the Options Instrument, click “miscellaneous” menu, point to “calibrate” and click.



1.7 Edit the specimen geometry

Highlight the “25mm ETC steel plate”, select the “dimensions” menu and edit the sample diameter and the gap. The diameter of the sample can be measured and thus the input is known. However, for a nonstandard test beyond the parallel plates, the gap is troublesome. In this step, the instrument is told to perform the standard parallel-plate testing. So it is suggested to use the default value, for example, Diameter = 25mm and Gap = 1000 microm.

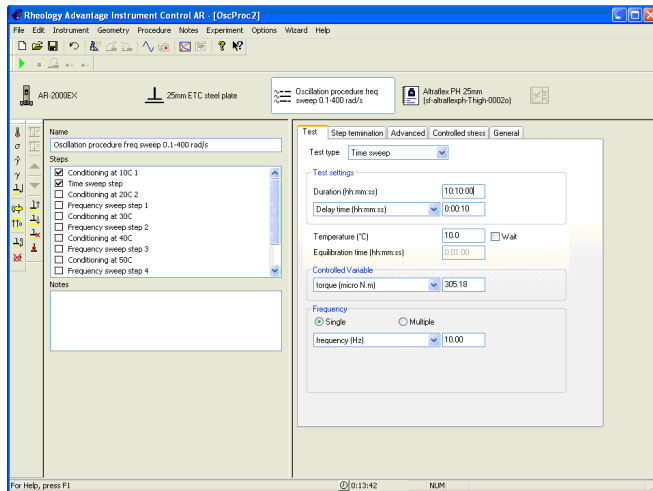


1.8 Edit the test procedure

Highlight the “test procedure”, click the “Test” menu.

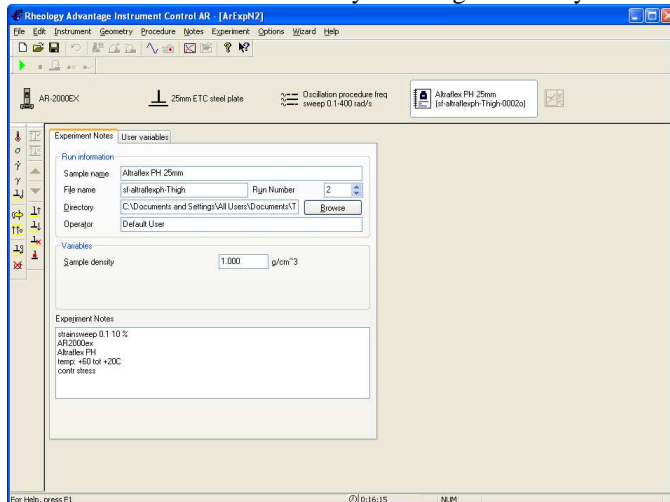
Select “Test type”, e.g. Time sweep for fatigue testing.

Edit all the test settings according to the test requirements from the “Test” menu to the “general” menu one by one.



1.9 Edit the experiment notes

Highlight the “Notes”, click the “Experiment notes” menu and edit the run information. Save the data file by selecting “Directory”.



2. Run the test

3. Data Report

The data report from the laboratory should include the following:

- (1) Instrument self-calibration: moment of inertia, air-bearing friction and compliance.
- (2) Report the inputs of the sample geometry: sample diameter and length.
- (3) Report the variables including time, temperature, frequency, gap, torque, deflection, raw angle, stress in sample, strain in sample and phase angle.

time	temperature	frequency	gap	osc. torque	displacement	raw phase	osc. stress (sample)	strain (sample)	delta	IG1	
s	°C	Hz	micro m	micro N.m	rad	degrees	Pa		degrees	Pa	
1	9.297	10.0	40.00	766	59950	0.0129	27.43	1.280E6	0.053763	23.30	2.380E7
2	13.13	10.0	40.00	766	59950	0.0136	28.68	1.289E6	0.056657	24.06	2.276E7
3	28.92	10.0	40.00	766	59950	0.0141	29.59	1.297E6	0.058959	24.62	2.199E7
4	38.70	10.0	40.00	766	59950	0.0146	30.38	1.303E6	0.060991	25.09	2.137E7
5	48.48	10.0	40.00	766	59950	0.0150	31.08	1.309E6	0.062826	25.50	2.084E7
6	58.23	10.0	40.00	766	59950	0.0154	31.70	1.314E6	0.064473	25.87	2.038E7
7	68.00	10.0	40.00	766	59950	0.0157	32.28	1.319E6	0.066011	26.20	1.990E7
8	77.78	10.0	40.00	766	59950	0.0161	32.73	1.323E6	0.067359	26.43	1.963E7
9	77.78	10.0	40.00	766	59950	0.0161	32.73	1.323E6	0.067359	26.43	1.963E7

- (4) For mortar fatigue tests, report the failure location: close to the steel ring or not. For adhesive zone tests, estimate the percent of adhesive and cohesive failures in accordance to their respective areas and locations.

4. Data post processing: real strain and stress calculation

The data post processing is a must for strain and stress calculations. First of all, export the test data to an Excel sheet and do the following steps:

Step1: determine the torque and displacement in mortar specimen

$$T_{sample} = \frac{\tau_{sample} \times \pi R^3}{2}$$

$$\theta_{sample} = \frac{\gamma_{sample} \times H}{R}$$

Where:

H = gap distance;

R = the radius of the parallel plates, 12.5mm.

Step 2: calculate the mortar stress and strain at the outer edge of the mortar column

$$\tau = \frac{2 \times T_{sample}}{\pi r^3}$$

$$\gamma = \frac{\theta_{sample} \times r}{h_{eff}}$$

Where:

h_{eff} = the effective length of the mortar specimen, 12.742mm.;

r = the radius of mortar specimen, 3mm.

Step 3: the shear complex modulus is determined using

$$|G^*| = \frac{\tau}{\gamma}$$

Step 4: the steps given about are only valid for mortar response measurement and mortar fatigue tests that failure occurs at the middle section. For mortar fatigue tests that specimens failed at the location close to the steel rings (see Figure 4.35), a calibration factor that takes into account the local stress concentration must be introduced:

$$\tau = k_3 \frac{2 \times T_{sample}}{\pi r^3}$$

$$\gamma = k_3 \frac{\theta_{sample} \times r}{h_{eff}}$$

Where:

k_3 = the calibration factor that accounts for local stress concentration, $k_3 = 1.10$.

Similar procedure is also applicable to adhesive zone tests by means of DSR or DMA instruments. In this case, only adhesive zone stress is of interest. Since the definition of the bitumen film thickness is impossible, the calculation of strain and stiffness modulus thus becomes unavailable.

6 ADHESIVE ZONE DAMAGE MODEL

6.1 Introduction

Porous asphalt is a special asphalt mixture with a void content of 20% or more after laying and compaction. In such an open structure, the coarse aggregates form a stone skeleton that creates the load bearing capacity and resistance to permanent deformation. The mortar, made up of fine sand, filler and bituminous binder, binds the aggregates together. An adhesive zone, where the mortar meets the stone surface can thus be defined. Failure of this specific adhesive zone, called adhesive failure, contributes to ravelling of porous asphalt. The prediction of the fatigue life, i.e. the number of cycles of repeated traffic loadings to adhesive failure is thus important for the design of ravelling resistant porous asphalt.

In general, the efficient prediction of the fatigue life must take into account the state of stress to which the material is subjected. Finite element simulations of porous asphalt mixtures showed that the adhesive zones are subjected to 3D states of stress (i.e. a combination of two shear components and one normal stress), which are changing from location to location within the mixtures [Huurman & Mo 2006; Huurman 2008; Mo & Huurman 2007, 2008]. Furthermore, the stress signals that develop in the adhesive zones during tyre passages are far from sinusoidal as commonly applied in classical fatigue tests. Therefore, translation of such complex stress signals into life expectancy requires a damage model that accounts for 3D states of stress and complex stress signals.

This chapter describes the development of a damage model for adhesive zones taking into account the 3D state of stress and complex stress signals. The model is based on extensive laboratory tests on specimens that consist of two stone columns bonded by a bitumen film. In the test program use is made of dynamic mechanical analysers (DMA) and dynamic shear rheometers (DSR). Both uniaxial tension and shear fatigue tests on adhesive zones were performed. The effect of complex stress signals was investigated by application of various force/torque signals, i.e. sinusoidal, haversine and static. The model was further validated by using extra data from test setups which allowed the application of a combination of normal and shear stresses.

6.2 Damage model

6.2.1 Failure criterion

The thickness of the adhesive zone that binds two stone columns together is far smaller than the other two dimensions. The state of stress to which such a zone is subjected, can be explained by one normal stress and two shear components (see Figure 6.1). The strength properties of bitumen in thin films differ significantly from the ones of bulk bitumen [Mack 1957; Majidzadeh & Herrin 1968]. This is especially true for the compressive strength. It is believed that such a thin bitumen film is able to withstand very high compressive stresses. Usually, the failure mode of thin films under compression is different from the one under tensile or shear loads. In general, the tensile and shear stresses are great of importance to investigate the failure of thin films that act as adhesive between two solid substrates. Under mixed shear and tensile

stresses, the failure behaviour of the adhesive zone is expected to be very complex. Several failure criteria have been proposed to explain the combination of shear and tensile stresses [Broek 1991]. For example,

$$\frac{\sigma_n}{\sigma_0} + \frac{\tau}{\tau_0} = 1 \quad (6.1)$$

$$\left(\frac{\sigma_n}{\sigma_0}\right)^2 + \left(\frac{\tau}{\tau_0}\right)^2 = 1 \quad (6.2)$$

Where:

- σ_n = normal tensile stress, positive for tension otherwise negative for compression, [MPa];
- σ_0 = tensile strength, [MPa];
- τ = shear stress, $\tau = (\tau_1^2 + \tau_2^2)^{0.5}$, [MPa];
- τ_i = shear stress component with $i=1, 2$, [MPa];
- τ_0 = shear strength, [MPa].

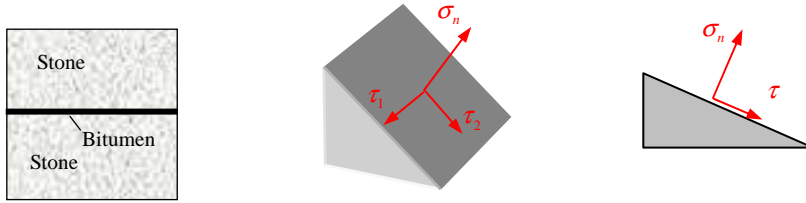


Figure 6.1 Idealized adhesive zone (left), the state of stress in 3D nature (middle) and the 2D representation (right)

Rearranging Equation 6.1 results in the following form:

$$\tau = -\sigma_n \tan(\phi_i) + c \quad (6.3)$$

Where:

- σ_n = normal stress, positive for tension and negative for compression, [MPa];
- ϕ_i = τ_0 / σ_0 angle of internal friction for mixed shear and tensile stresses, [degree];
- c = cohesion, $c = \tau_0$, [MPa].

Equation 6.3 explains that when the adhesive zone is subjected to the combined action of tension and shear stresses, the shear strength at the moment of failure reduces as the tensile stress increases.

The shear strength of the adhesive zone may benefit from the applied normal compressive stress. The reason is that the shear stress acting along the failure plane to

promote failure is opposed by the compressive stress acting across the fracture plane which tends to close the crack and prevent failure. The relation between these two stresses can also be explained by using the internal-friction theory.

$$\tau = -\sigma_n \operatorname{tg}(\phi_c) + c \quad (6.4)$$

Where:

ϕ_c = angle of internal friction for mixed shear and compressive stresses, [degree];

c = cohesion, $c = \tau_0$ [MPa].

By combining Equations 6.1 to 6.4, the relation between the normal and shear stresses can be illustrated by means of the curves as shown in Figure 6.2 depending on what kind of function is used. The states of stress located at the area below the curve will not result in instantaneous failure but will result in fatigue.

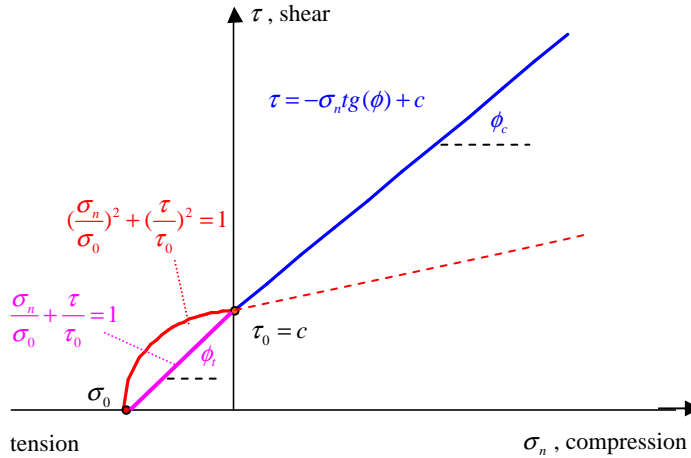


Figure 6.2 Failure envelops for the adhesive zone

It must be noted that the failure behaviour of the adhesive zone may be very complex and the functions described above might not be able to explain this behaviour properly. Figure 6.3 gives an illustration of various potential failure envelopes under mixed shear and normal stresses. To obtain the real failure envelope, it is foreseen that data from the following test conditions are required (see Figure 6.3):

- uniaxial tensile tests;
- pure shear tests;
- the combination of normal tensile and shear tests;
- the combination of normal compressive and shear tests.

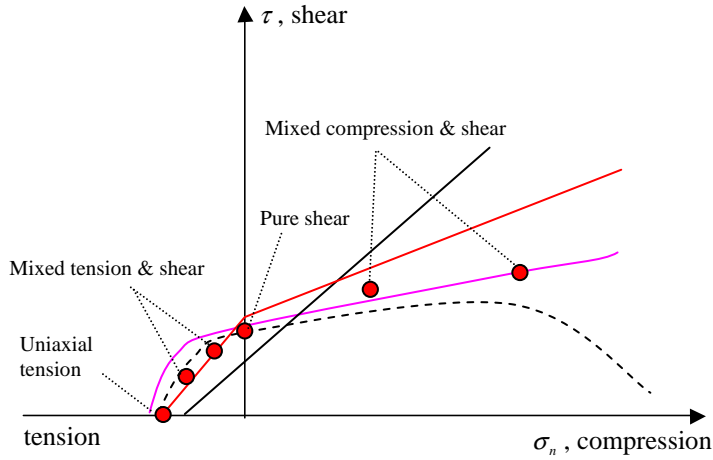


Figure 6.3 Illustration of various failure envelopes under mixed shear and tensile stresses

In the case that the effect of normal tensile stress on shear strength is similar to the effect of normal compressive stress, the failure envelope becomes a straight line (see Figure 6.3).

$$\tau = -\sigma_n \operatorname{tg}(\phi) + c \quad (6.5)$$

Where:

$$\phi = \tau_0 / \sigma_0 \text{ angle of internal friction, [degree].}$$

To determine such a straight line, only two data points are required, indicating that a test program including uniaxial tensile and shear tests can meet such a purpose. Most of all, these tests are commonly used in the laboratory and thus available. However, the extrapolation into the combination of shear and normal stresses needs to be validated.

In reality, the adhesive zone is subjected to the combined action of shear and normal stresses. In most of the cases, such a combined action may not lead to failure. It indicates that the effective stress to which the adhesive is subjected is smaller than the strength. For comparison purpose, the combined action of shear and tensile loading conditions should be transferred into an equivalent uniaxial tensile stress or shear stress. After that, the equivalent tensile or shear stress will be compared with the uniaxial tensile/shear strength. The stress conditions that result in the same/similar ratio of stress over strength may have a same/similar safety capacity for strength design or number of repetitions to failure for fatigue design.

Any combined action of normal and shear stresses can be represented in term of an equivalent shear/tensile stress by using:

$$\tau_e = \sigma_n \operatorname{tg}(\phi) + \tau \leq \tau_0 \text{ for equivalent uniaxial shear stress}$$

$$\sigma_e = \sigma_n + \frac{\tau}{\text{tg}(\phi)} \leq \sigma_0 \quad \text{for equivalent tensile stress} \quad (6.6)$$

Where:

σ_e = equivalent uniaxial tensile stress, [MPa].

τ_e = equivalent uniaxial shear stress, [MPa].

Since the mathematical model for the equivalent uniaxial tensile and shear stress is similar, the following discussions are focused on the equivalent uniaxial tensile stress.

Figure 6.4 is an illustration of how to translate the combined action of shear and normal stresses (red dots) into an equivalent tensile stress (green dots). When the state of stress is below the red line on Figure 6.3, the equivalent tensile stress, σ_e , becomes negative. This indicates compression leading to infinite design life. In this case, a small shear stress and a high compressive stress coexist. As a result, the effect of the compressive stress is strong enough to counteract the effect of the shear stress. Crack closure and no crack opening can be expected under the combination of such stresses. Therefore, it is assumed that the induced damage is limited, or will even not occur when the adhesive zone is subjected to an equivalent tensile stress smaller than zero. Therefore, the following discussion is focussing on situations showing an equivalent tensile stress larger than zero.

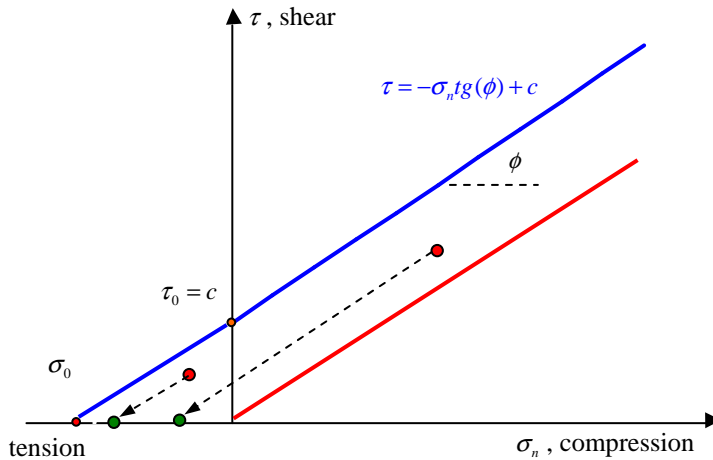


Figure 6.4 Simplified failure criterion for the adhesive zone

Due to the effect of temperature the failure line is expected to change as indicated in Figure 6.5. As the temperature increases, the angle of internal friction ϕ may increase while the tensile and shear strengths, σ_0 and τ_0 , decrease. The increase of ϕ indicates that the benefit of shear strength from the applied normal compressive stress increases with increasing temperatures. If tests are done at various temperatures,

these parameters may also be expressed as functions of temperature.

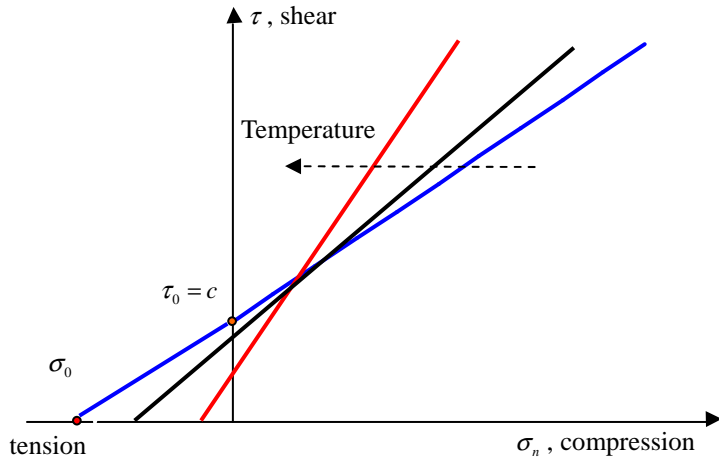


Figure 6.5 Model explanation on the effect of temperature

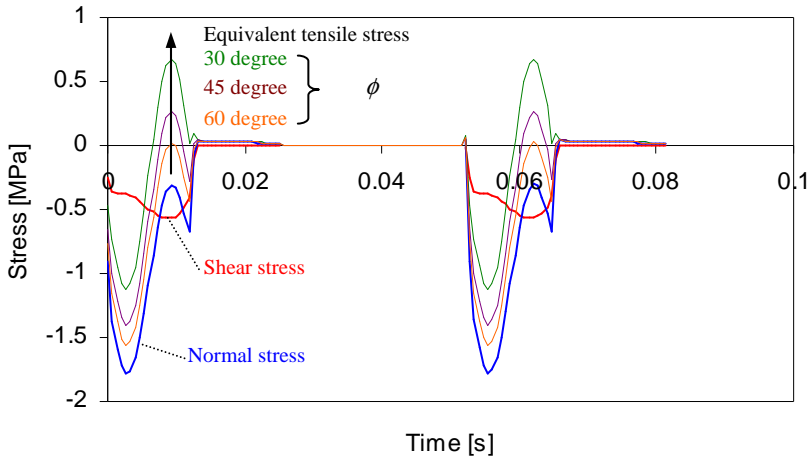


Figure 6.6 Example of translating normal and shear stress-time signals into the corresponding equivalent uniaxial tensile stress-time signal and influence of ϕ

Figure 6.6 gives an example of how to translate the signals of shear and normal stresses into the corresponding equivalent tensile stress. It must be noted that the normal and shear stress-time signals in this figure are obtained from a finite element simulation of porous asphalt. The signals indicate the loads in the adhesive zone during two tyre passages. More information on such finite element simulations can be

found elsewhere [Huurman & Mo 2006; Huurman 2008; Mo & Huurman 2007, 2008]. As indicated, the model described previously can be applied to translate the complex loading conditions to which the adhesive zone is subjected into a simple equivalent uniaxial stress. Figure 6.6 also shows the influence of the angle of internal friction ϕ on the equivalent uniaxial tensile stress σ_e . As can be seen, multiple values of ϕ (i.e. 30° , 45° and 60°) are used to calculate σ_e . σ_e decreases with increasing ϕ .

6.2.2 Fatigue damage under regular signals

In this section, we will discuss a fatigue damage model for the adhesive zone since it is subjected to repeated traffic loads in reality and thus material strength is not good enough for design purpose. Focus is on the fatigue damage under tensile and shear stresses as well as the combination of both stresses. As discussed in Chapter 4, the bitumen layer in the adhesive zone is fairly thin and its thickness is far from uniform due to surface morphology. Furthermore, the stiffness of thin bitumen films is so high that the contribution of the stiff, but non-rigid clamp system on the total deformation can not be neglected [Mack 1957; Majidzadeh & Herrin 1968]. As a result, the accurate determination of adhesive zone strain, if at all definable, becomes troublesome. Thus stress seems to be a more reliable variable for further data analysis than strain. For this reason, investigation of the fatigue behaviour of the adhesive zone will be based on stress only.

In the following discussion, a so-called stress-strength ratio is used as an indicator of fatigue damage. The stress-strength ratio is defined as a ratio of the applied stress amplitude to the static ultimate strength. Apparently, a higher stress-strength ratio indicates that the material is experiencing worse damage per cycle which will result in a shorter fatigue life. As discussed in the previous section, the equivalent uniaxial tensile stress was used as an indicator of the load to which the adhesive zone is subjected. As a result, for a constant stress amplitude and frequency, the fatigue life can be written as the function form,

$$N_f = f\left(\frac{\sigma_e}{\sigma_0}\right) \quad (6.7)$$

Where:

N_f = number of cycles to failure, e.g. fatigue life, [-].

This equation also holds for uniaxial tension and pure shear fatigue following.

$$N_f = f\left(\frac{\sigma_n}{\sigma_0}\right) \quad (6.8)$$

$$N_f = f\left(\frac{\tau}{\tau_0}\right) \quad (6.9)$$

The above discussion is illustrated in Figure 6.7. First of all, it is assumed that only the states of stress located between the blue and red lines may induce damage. These states of stress are identified by σ_e larger than 0. All the points with the same

value of σ_e , indicated by the green line which is parallel with the blue line, have the same fatigue damage behaviour.

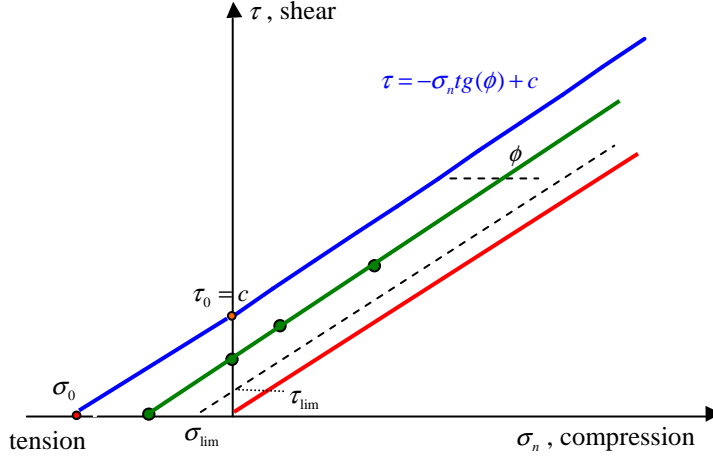


Figure 6.7 Illustration of the lines of fatigue equivalence and fatigue limit

When taking into account the fatigue limit, which is defined as the stress-strength ratio below which the material can withstand an infinite number of loading cycles, Equation 6.6 becomes:

$$N_f = f\left(\frac{\sigma_e - \sigma_{\text{lim}}}{\sigma_0}\right) \quad \text{with} \quad \tau_{\text{lim}} = \sigma_{\text{lim}} \text{tg}(\phi) \quad (6.10)$$

Where:

σ_{lim} = tensile fatigue limit, [MPa];

τ_{lim} = shear fatigue limit, [MPa];

The line for the fatigue limit is also shown in Figure 6.7 by means of the black dashed line.

Usually, the relation between fatigue life and the stress level applied using a constant frequency follows a power law. Therefore, Equations 6.7 and 6.10 are rewritten as follows:

$$N_f = \left(\frac{\sigma_e}{\sigma_0}\right)^{-n} \quad (6.11)$$

and

$$N_f = \left(\frac{\sigma_e - \sigma_{\text{lim}}}{\sigma_0}\right)^{-n} \quad (6.12)$$

Equation 6.11 and Equation 6.12 show two different models that are capable of explaining the fatigue behaviour of the adhesive zone under mixed shear and normal stresses. The parameters of these two models can be determined by combining uniaxial tensile fatigue and pure shear fatigue data. Figure 6.8 shows an example of such a stress-life plot.

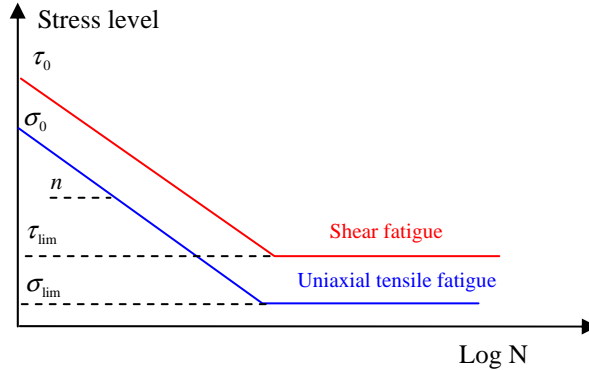


Figure 6.8 Example of the idealized stress-life plot

To determine the fatigue limits, σ_{lim} and τ_{lim} , fatigue tests using very low stress levels are required and these tests are fairly time-consuming. Failure usually occurs after a large number of loading cycles, e.g. 10^7 cycles. For practical reasons, test are normally done using stress levels that result in more than 10^3 cycles and less than 10^7 cycles to failure. Any fatigue model that was developed on the basis of these data would be only valid on such a wide range of cycles. As a result, the model may show its limitations on the predicted fatigue life less than 10^3 cycles or higher than 10^7 cycles.

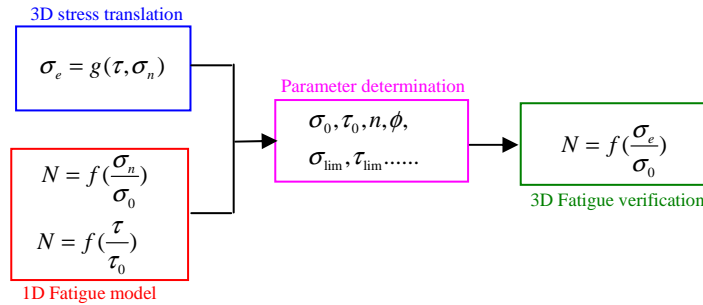


Figure 6.9 Model development for adhesive zone fatigue damage

The discussion above is summarised in Figure 6.9. The final goal of this study is targeted at the fatigue characterization of the adhesive zone under a combination of normal and shear stresses by using a simplified model. It should be possible to determine the parameters of this simplified model by commonly used uniaxial tension

and pure shear test data. As indicated, first of all, a function should be applied to translate the complex 3D state of stress into a simple equivalent uniaxial tensile stress. By combining the 1D fatigue model derived from uniaxial tension and shear fatigue tests, the desired 3D fatigue model can be developed. Finally, the 3D fatigue model must be verified by means of fatigue data obtained from tests in which a combination of shear and normal stresses is applied. The accuracy of the model will increase when more fatigue data under complex stress states are available. Proof of these assumptions will be given later.

6.2.3 Damage accumulation model for complex signals

The procedure used in road engineering for life expectancy determination is illustrated in Figure 6.10. The life expectancy of ravelling of porous asphalt concrete is determined in a similar way. At this moment a tool, i.e. LOT is available for response calculations of porous asphalt. The output from the response calculations is the strain and/or stress to which the adhesive zone is subjected (see Figure 6.11). By using these signals as input for a fatigue model, the life expectancy of the considered material is obtained.

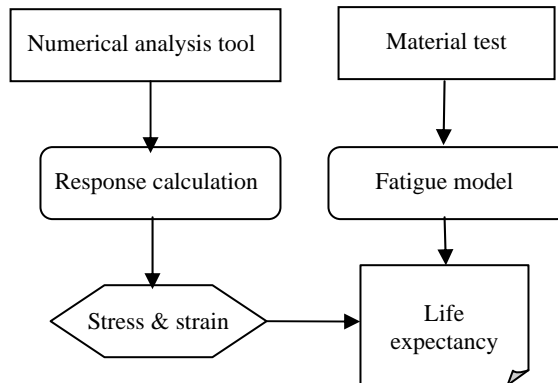


Figure 6.10 Typical procedure of life expectancy determination used in road engineering

Figure 6.11 gives an example of shear and normal stress signals as a function of time obtained from a finite element simulation during two tyre passages on porous asphalt concrete [Mo & Huurman 2007, 2008]. It can be seen that the obtained stress signals are very complex and the shape is unlike the sine-wave that is commonly used for fatigue tests. It is furthermore noted that the obtained shear and normal stress signals differ strongly from location to location throughout the mixture structure. As demonstrated in Chapter 4, the stress signal that was applied on the adhesive zone plays an important role on fatigue life. This indicates that interpretation of these complex stress signals into damage must take into account the influence of stress signal. Tests in which only one single type of stress signal is applied are not enough for analyzing such a problem. It indicates that any desired damage model should at

least be able to explain the damage under various stress signals, e.g. static, repeated load or combinations of these.

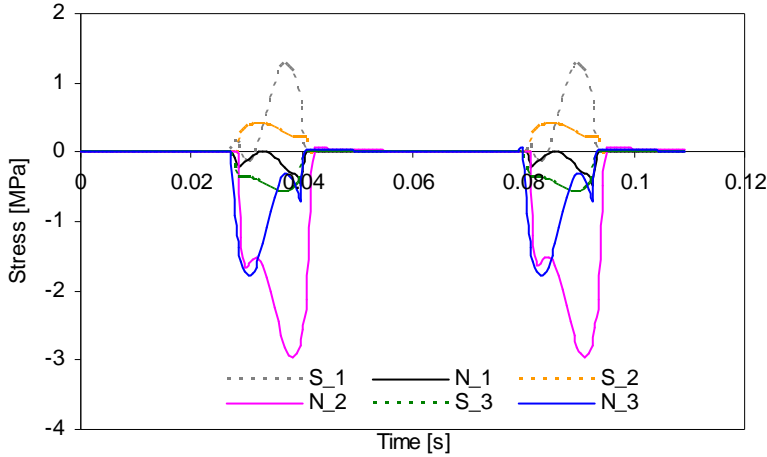


Figure 6.11 Typical shear and normal stress signals obtained from a finite element simulation during for tire passages on porous asphalt concrete (S: shear stress; N: normal stress; Number 1,2 and 3 indicate various locations where the adhesive zone is.) [Mo & Huurman 2007, 2008]

At the start of this project, it was foreseen that a complex state of stress may occur in the adhesive zone and the output of finite element modelling demonstrates this concern. For this reason, a damage model that is capable of explaining the damage development in the adhesive zone under complex tensile or shear stresses was developed [Mo & Huurman et al. 2006; Mo 2007].

$$\frac{dD}{dt} = \dot{D}(\sigma) = \left(\frac{\sigma}{\sigma_0}\right)^n \quad (6.13)$$

Where:

- D = the accumulated damage, [-];
- \dot{D} = the damage rate, [s^{-1}];
- t = time, [s];
- σ = the applied stress, [MPa];
- σ_0 = the nominal strength of the material, [MPa];
- n = model parameter, [-].

For any given stress-time signal the damage accumulation is now described by the following equation

$$D(t) = \int_0^t \dot{D}(\sigma) dt \cong \sum_{i=1}^{k \rightarrow \infty} \dot{D}(\sigma) \Delta t \quad (6.14)$$

The boundary conditions for Equation 6.14 are as follows:

$$D(0) = 0 \quad \text{at } t = 0 \quad \text{for no initial damage} \quad (6.15)$$

$$D(t_f) = 1 \quad \text{at } t = t_f \quad \text{for failure occurs} \quad (6.16)$$

As indicated by Equation 6.14, this damage model makes use of the integral of the stress-time signal raised to the power n . The damage is the sum of damage increments based on a linear cumulative damage rule that is known as Palmgren-Miner's rule [Palmgren 1924; Miner 1945]. This is illustrated in Figure 6.12. The model explains that an increase in stress results in an increase of the damage rate. The resulting damage increases more or less linearly with time.

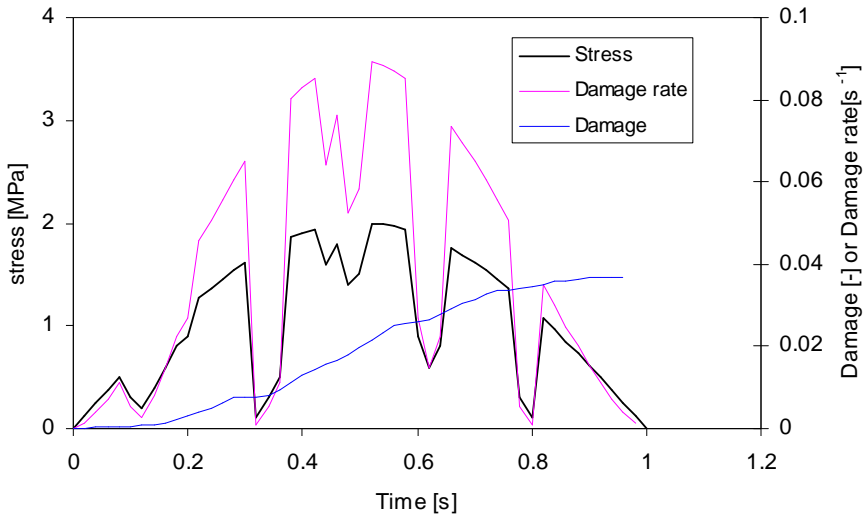


Figure 6.12 Illustration of applied stress and the corresponding damage rate and damage development over time ($n=1.5$, $\sigma_0=10\text{MPa}$)

This damage model was verified against data from monotonic and repeated load tests. Two different bitumen-stone combinations were considered. Monotonic and repeated load uniaxial tensile and shear tests were done. The model is capable of explaining the following phenomena.

(1) For constant stress static tests, the model predicts the duration of time to failure by

$$t_f = \left[\frac{\sigma_0}{\sigma} \right]^n \quad (6.17)$$

A higher applied stress level will result in a shorter duration of time to failure.

(2) For constant force rate tests, the model predicts the ultimate strength at failure by

$$\sigma_f = [(n+1) \times \sigma_0^n \times \dot{\sigma}]^{\frac{1}{1+n}} \quad (6.18)$$

Where:

$\dot{\sigma}$ = the rate of applied stress, [MPa/s].

A higher applied stress rate will result in a higher ultimate strength at failure.

(3) For constant stress amplitude repeated load tests with a signal of $\sigma_a(\sin \omega t + 1)$, the model predicts the number of cycles to failure as

$$N_f = \frac{1}{\int_0^{2\pi/\omega} \left[\frac{\sigma_a(\sin \omega t + 1)}{\sigma_0} \right]^n dt} \quad (6.19)$$

Where:

σ_a = applied stress amplitude, [MPa];

ω = frequency, [rad].

As indicated, an increase in applied stress amplitude will result in a reduced life. An increase of frequency will result in an increase of the number of cycles to failure.

It must be noted that the damage model described above is based on the linear and stress independent accumulative rule. Because of its simplicity, this rule is still widely used. But this rule fails to predict when a sequence of various stress levels is applied [Hwang & Han 1986; Amoz 1990; Fatemi & Yang 1998].

In fact, the damage development is complex during fatigue tests. When a nonlinear damage model is considered, the damage model can be expressed as follows:

$$\frac{dD}{dt} = \left[\frac{\sigma}{\sigma_0} (1-D) \right]^n \quad (6.20)$$

Equation 6.20 indicates that the cumulative amount of damage will affect the rate of damage. In this case, the determination of damage development is not possible unless some physical variables are defined as an indication of fatigue damage. Changes of stiffness modulus and/or the applied strain are usually used for such a purpose [Hwang & Han 1986].

For a constant amplitude fatigue test, the damage is expressed using either of the following two functions:

$$D(N_i) = [E_o - E(N_i)] / [E_o - E(N_f)] \quad (6.23)$$

$$D(N_i) = [\varepsilon_o - \varepsilon(N_i)] / [\varepsilon_o - \varepsilon(N_f)] \quad (6.24)$$

Where:

- E_o = initial modulus, [Mpa];
- $E(N_i)$ = modulus at i -th cycle, [Mpa];
- $E(N_f)$ = modulus at failure, [Mpa].
- ε_o = initial strain, [-];
- $\varepsilon(N_i)$ = strain at i -th cycle, [-];
- $\varepsilon(N_f)$ = strain at failure, [-].

The damage model expresses the damage development over a cycle as

$$D(N_i) = \sum_{i=1}^{N_i} \Delta D_i = \sum_{i=1}^{N_i} \left\{ \frac{\sigma}{[1 - D(N_{i-1})]\sigma_0} \right\}^n \quad (6.25)$$

Therefore, the model parameters are determined by fitting the stiffness modulus or strain data.

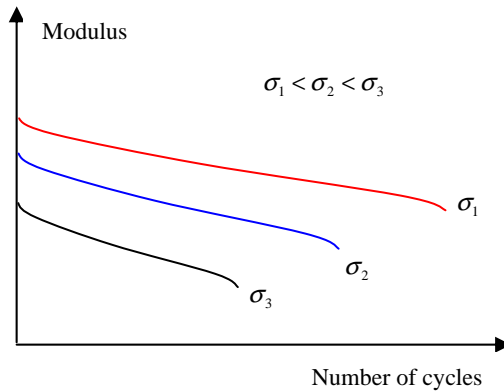


Figure 6.13 Change of stiffness modulus during a fatigue test

Figure 6.13 gives an example of the trends of the change of the stiffness modulus during a fatigue test. By using the change of the stiffness modulus as damage indicator, the value of n at a certain stress level can be determined. By applying various stress levels, the function of $n(\sigma)$ is obtained.

The linear and nonlinear damage rules expressed by Equations 6.13 and 6.20 present different damage accumulation processes (see Figure 6.14). However, both

models will finally predict the same fatigue life for constant amplitude tests.

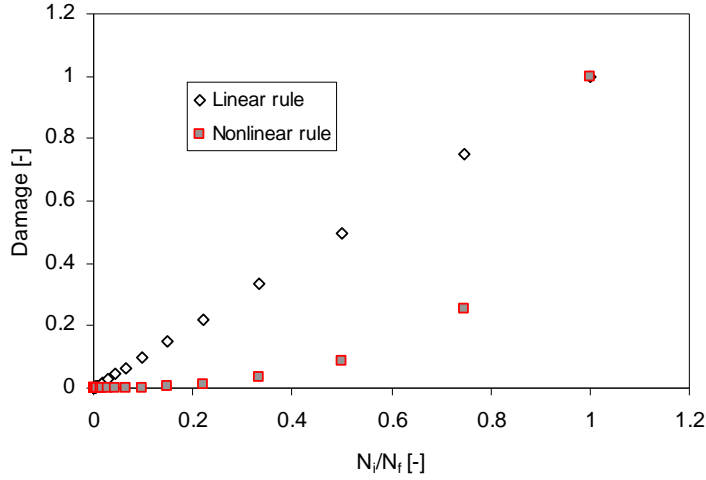


Figure 6.14 Damage as a function of cycle ratio (N_i/N_f) determined by means of linear and nonlinear rules ($n=2.28$)

For example, the linear damage rule predicts the fatigue life as

$$N_f = \frac{1}{D(N_1)} \quad (6.26)$$

For a nonlinear damage rule, the fatigue life is defined as the moment at which the sum of damage increments is equal to 1.

$$D(N_f) = \sum_{i=1}^{N_f} \Delta D_i = \sum_{i=1}^{N_f} \left\{ \frac{1}{[1 - D(N_{i-1})]} \right\}^{n(\sigma)} = 1 \quad \text{with } D(N_0) = 0 \quad (6.27)$$

For a random stress signal, both models explain the moment of failure t_f at $D(t_f) = 1$ independent of damage accumulation process. In this case, the time to failure predicted by the nonlinear damage rule is more accurate than the one predicted by the linear damage rule [Hwang & Han 1986; Amoz 1990; Fatemi & Yang 1998].

$$D(t_f) = \sum_{i=0}^{t_f} \Delta D_i = 1 \quad \text{with } D(t_0) = 0 \quad \text{and } D(t_f) = 1. \quad (6.28)$$

For reasons of simplicity and difficulty in determining the stiffness and strain of the adhesive zone, the linear damage rule has been applied to explain the damage behaviour of the adhesive zone in combination with the equivalent uniaxial tensile

stress.

$$\frac{dD}{dt} = \dot{D}(\sigma_e) = \left(\frac{\sigma_e}{\sigma_0}\right)^n \quad \text{with} \quad \sigma_e = \sigma_n + \frac{\tau}{\text{tg}\phi} > 0, \quad (6.29)$$

otherwise $\dot{D}(\sigma_e) = 0$ when $\sigma_e \leq 0$

Figure 6.15 gives an example of how the damage model translates the complex state of normal and shear stresses into the rate of damage and damage development over time. As mentioned earlier, the normal and shear stress-time signals are obtained from a finite element simulation on porous asphalt concrete during two tyre-passages. As indicated, the damage accumulation after these two tyre passages is approximately 0.0023 by using model parameters of $\sigma_0 = 10\text{MPa}$, $n = 3$ and $\phi = 30^\circ$ (which are arbitrary values). As a result, the fatigue life under such load repetitions is estimated as $2/0.0023 = 870$ cycles based on the linear damage rule. This example shows that the model is capable of analyzing the adhesive zone damage behaviour under complex states of stress. This indicates that life time can be predicted for design purpose.

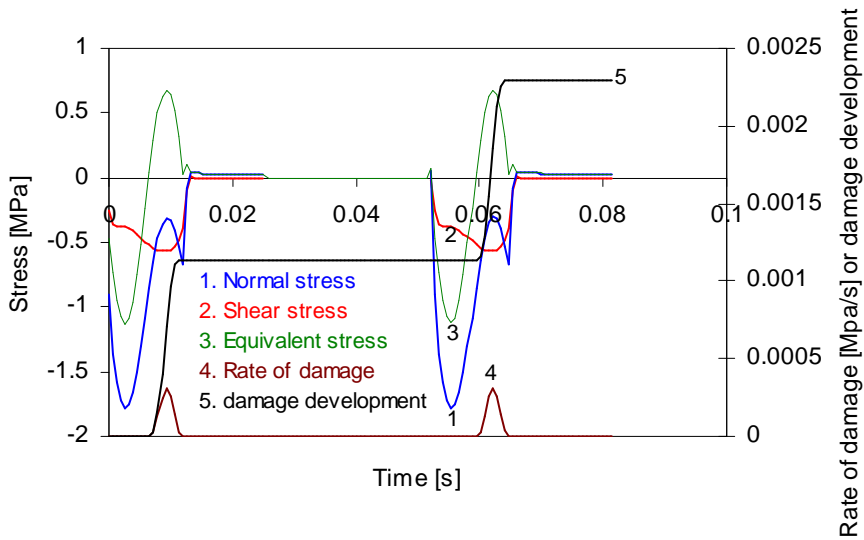


Figure 6.15 Example of how the developed damage model translates the normal and shear stresses into the rate of damage and damage over time ($\sigma_0 = 10\text{MPa}$, $n = 3$ $\phi = 30^\circ$)

Figure 6.16 shows the procedures that were followed to determine the model parameters (σ_0 , n and ϕ) and to verify the model. Initially, the model parameters were only determined by using uniaxial tension and shear test data. To take into account complex stress signals, two distinct loading signals, e.g. static and repeated load stresses were used for the determination of the model parameters. After that, the model was verified by using extra data, coming from tests using a mixture of normal

and shear stresses as well as other signals. Since tests were done at various temperatures, the temperature dependencies of the model parameters could be determined. By incorporating the functions of model parameters σ_0 , n and ϕ on temperature into the damage model, a generalized damage model was obtained.

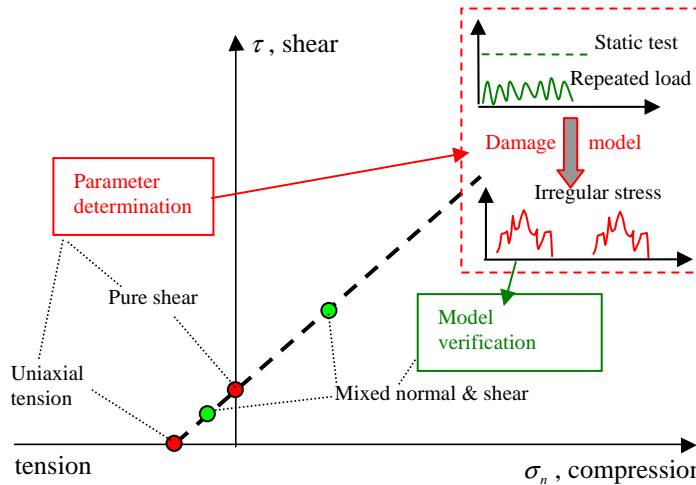


Figure 6.16 Procedures of parameters determination and model verification

6.3 Model parameter determination and model verification

6.3.1 Introduction

In this section, a brief introduction of the tests on the adhesive zone is given. It should be noted that hereafter “stress” means the corrected stresses in which the specimen geometrical and instrument factors are taken into account. More detailed information on these two factors can be found in the previous chapters.

Figure 6.17 shows the test set-ups for the adhesion tests. The applied signals for the tests are shown in Figure 6.18. All tests were done in force controlled or torque-controlled mode. Repeated load tests were done at a frequency of 10Hz. Table 6.1 lists the test plan for parameter determination and model verification. DMA repeated load testing, DMA static testing and DSR repeated load testing were suggested for this purpose. With respect to model verification, extra tests at different temperatures and using different stress signals were performed. It should be mentioned that approximately 200 adhesive zone specimens were tested at temperatures ranging from -10 to 20 °C. In total 8 combinations (2 types of stone, short-term and long-term aged bitumen, water conditioning and no water conditioning) were considered. More detailed information can be found in Chapter 4.

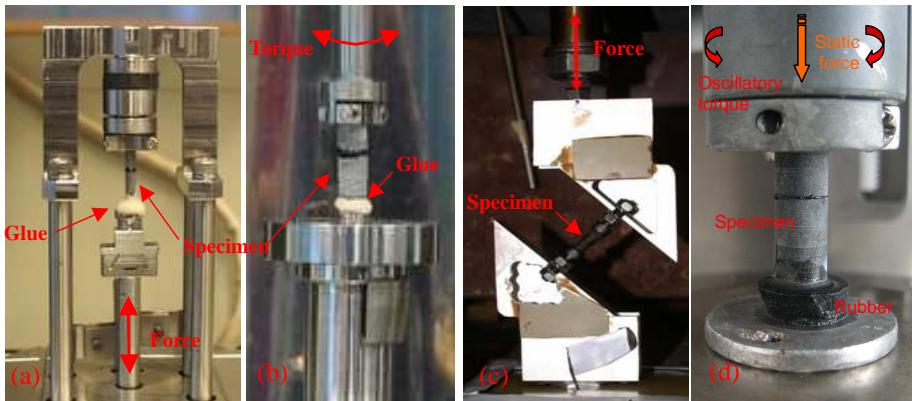


Figure 6.17 Various set-ups for adhesive zone tests (a: DMA uniaxial tension test; b: DSR shear test; c: Oblique shear test with an angle of 45°; d: DSR normal-shear combined test).

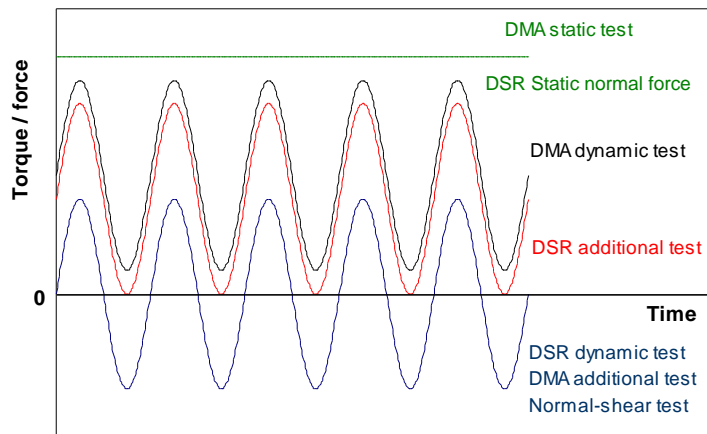


Figure 6.18 Graphical representation of the applied signals in the DMA, DSR and normal-shear combined tests

Table 6.1 Test plan for determination of model parameters and model verification

Test conditions	Bitumen	Short-term aged bitumen (SB)				Long-term aged bitumen (LB)			
	Stone	Sandstone (B)				Greywacke (G)			
	Water condition	Water immersion (W)							
	Material combination	B+SB	B+LB	B+SB_W	B+LB_W	G+SB	G+LB	G+SB_W	G+LB_W
Temperature (°C)									
Parameter determination	DMA dynamic test	0, 10,20	0, 10,20	0,10,20	0,10,20	0, 10,20	0, 10,20	0,10,20	0,10,20
	DMA static test	-10, 20	-10, 20	-	-	-10, 20	-10, 20	-	-
	DSR dynamic test	-10,0, 10,20	-10,0, 10,20	0,10,20	0,10,20	-10,0, 10,20	-10,0, 10,20	0,10,20	0,10,20
Model verification	DSR dynamic test	5	5	5	5	5	5	5	5
	DMA additional Test	10	10	-	-	10	10	-	-
	DSR additional test	10	10	-	-	10	10	-	-
	Oblique shear test	-10,0, 10,20	-10,0, 10,20	-	-	-10,0, 10,20	-10,0, 10,20	-	-
	DSR normal-shear test	10				10			

Note: number, e.g. -10, 0, 10 and 20 is test temperature, °C

6.3.2 Model parameter determination

As mentioned above, the proposed damage model is capable of determining damage development under any stress-time signal. By choice of the model parameters, σ_0 , n and ϕ the damage will reach the value of 1 at the end of test, e.g. at the moment of failure. In the following, the model parameters were determined and optimized by least error fitting:

Step 1: estimate the value of model parameters σ_0 , n and ϕ at each temperature.

Step 2: determine the amount of damage during a single complete cycle in the case of repeated load or the amount of damage during a second in the case of static load for each individual test using

$$D(1) = \sum \left\{ \left[\frac{\sigma_e(t + \Delta t) + \sigma_e(t)}{2} \right]^n \times \Delta t \right\} \quad (6.30)$$

Where:

$D(1)$ = the amount of damage in a single complete cycle or in a second [-];

$\sigma_e(t)$ = the equivalent tensile stress at time t , [MPa];

$\sigma_e(t + \Delta t)$ = the equivalent tensile stress at time $t + \Delta t$, [MPa];

Δt = the time increment, [s].

Step 3: determine the fatigue life in seconds to failure as

$$t_f = 0.1 \times N_f = 0.1 \times \frac{1}{D(1)} \quad \text{for repeated load test} \quad (6.31)$$

$$t_f = \frac{1}{D(1)} \quad \text{for static test} \quad (6.32)$$

Where

N_f = number of cycles to failure for repeated tests with 10Hz;

t_f = time to failure, [s].

Step 4: compute the relative percentage error between the modelled and measured $\log(t_f)$ and apply a solver to minimise the average of the relative errors by alteration of the model parameters.

The results of the procedure discussed above summarized in Table 6.2. As indicated by the correlation coefficients of R^2 in this table, a good fit was obtained for most of material combinations. More detailed discussions on the model parameters will be given later.

As shown in Figure 6.19, the predicted time to failure compares well with the measured time to failure. The data plotted in this figure include the effects of stone-bitumen combination, water immersion, temperature, and type of testing. One can see that the time to failure as predicted by the model is in good agreement with the measured time to failure.

Table 6.2 Summary of determination of model parameters

Temperature [°C]	Material combination	σ_0 [MPa]	n [-]	ϕ [degree]	R^2
-10	B+SB	20.69	3.17	54.8	0.96
	B+LB	18.91	2.57	74.2	0.87
	G+SB	22.21	2.90	66.5	0.45
	G+LB	22.34	2.90	66.2	0.49
0	B+SB	12.85	4.59	27.5	0.98
	B+LB	13.75	4.33	27.1	1.00
	B+SB_W	13.01	4.52	27.0	1.00
	B+LB_W	11.10	5.49	25.1	0.98
	G+SB	11.10	5.49	25.1	1.00
	G+LB	11.93	5.36	24.0	0.95
	G+SB_W	15.03	4.64	22.8	0.39
	G+LB_W	11.93	5.36	24.0	0.96
10	B+SB	14.53	3.09	33.1	0.90
	B+LB	14.89	3.01	32.6	0.69
	B+SB_W	13.24	3.16	31.6	0.09
	B+LB_W	10.99	3.55	30.1	0.66
	G+SB	10.99	3.55	30.1	0.81
	G+LB	8.18	3.83	32.4	0.39
	G+SB_W	9.78	3.03	35.7	0.82
	G+LB_W	8.18	3.83	32.4	0.98
20	B+SB	8.69	2.89	40.4	0.93
	B+LB	7.51	3.33	38.2	0.98
	B+SB_W	10.53	2.69	38.5	1.00
	B+LB_W	9.00	3.15	27.0	0.78
	G+SB	7.49	2.90	44.3	1.00
	G+LB	9.98	2.77	39.6	0.60
	G+SB_W	10.81	2.30	49.6	1.00
	G+LB_W	6.92	3.41	37.0	0.81

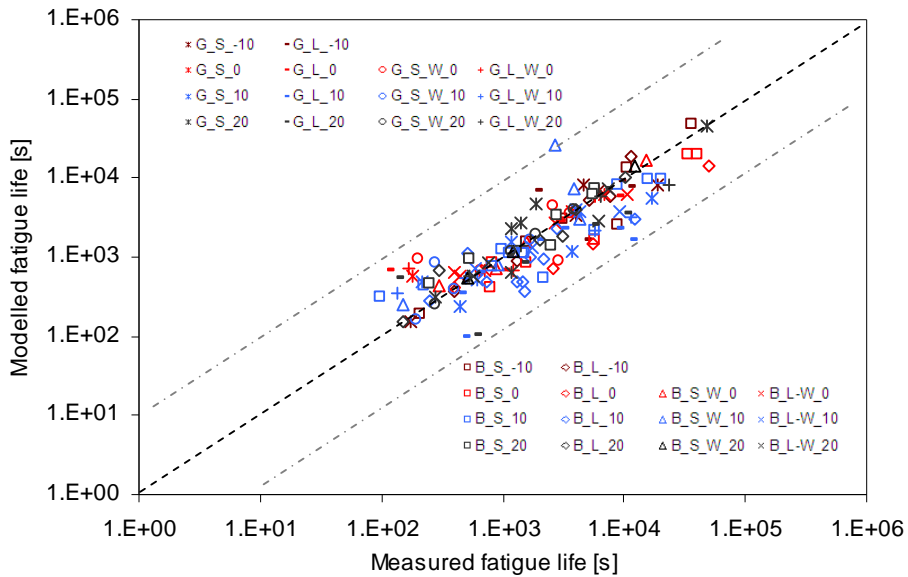


Figure 6.19 Comparison of the predicted and measured life time to failure

Figure 6.20 shows more details of the model's capability to predict life time under both static and repeated loading. Use was made of DMA and DSR repeated test and DMA static test data. Two temperatures, -10°C and 20°C are considered. As can be seen, all data points from the repeated load and static tests are well dispersed along the line of equality. This indicates that the model is capable of explaining life determined by means of static and repeated load tests.

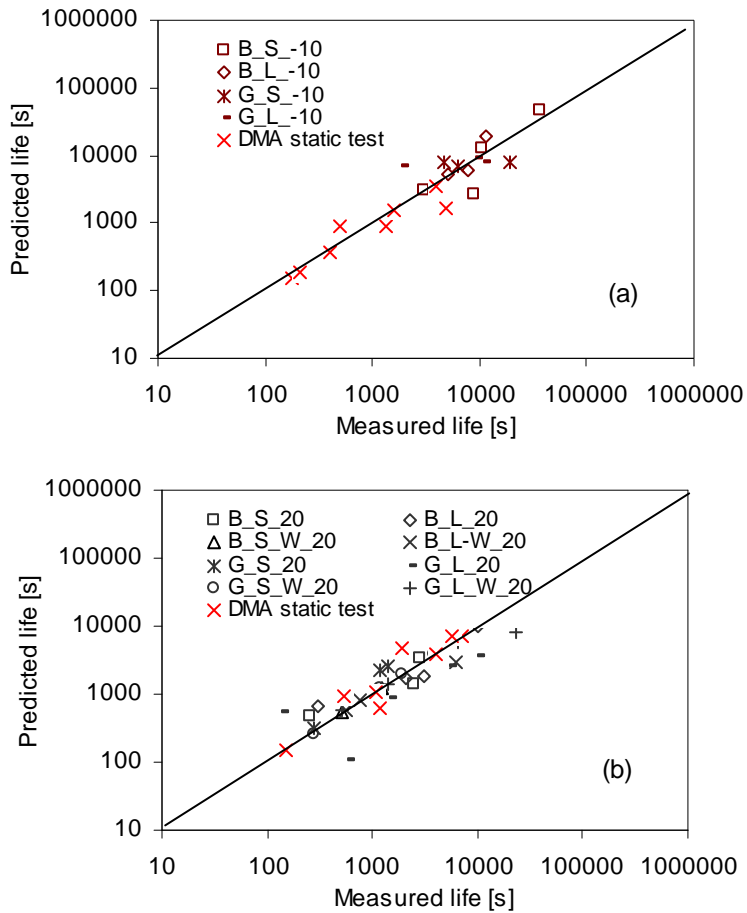


Figure 6.20 Model capability for predicting life time from static and repeated load tests (a: -10°C; b: 20°C)

6.3.3 Model verification

The model above was further validated by comparing the predicted with measured fatigue life time obtained from additional tests. These additional tests were done at additional temperatures and using different stress signals (see 6.18). The data for verifying the model are shown in Figure 6.21. It is stated explicitly that the extra data used for model verification purposes are not used for the model parameter determination shown in Table 6.2 and for fatigue life prediction shown in Figure 6.19.

The model parameters for the additional temperature of 5 °C as shown in Figure 6.21, are obtained by interpolation of the parameters listed in Table 6.2. The DMA and DSR tests performed using additional stress signals, see Figure 6.18, are described by direct application of the parameters listed in Table 6.2. The same holds for describing the combined shear-normal stress tests.

Figure 6.21 indicates that the predicted life time for 5°C correlate well with the measured data. The trends in the tests in which additional stress signals are applied are also described properly. However, it is observed that the fatigue life of the additional DSR and DMA tests as predicted by the damage model tends to be smaller than the measured one. Furthermore, some data points from DMA and DSR additional fatigue tests are out of the boundary. The model is not very sensitive to the DMA additional test data since the predicted life time seems more or less constant while the measured life time varies. The reason for this may be that a pure sine signal is applied for these tests and the healing effect due to the compression period within a cycle may play an important role. A similar trend is also observed on the predicted life time for DSR normal-shear tests, for which a combined action of shear and tensile stresses is applied. The data obtained from the oblique shear tests are described properly. Generally speaking, the proposed model is capable of explaining damage that develops under a combination of normal and shear stresses.

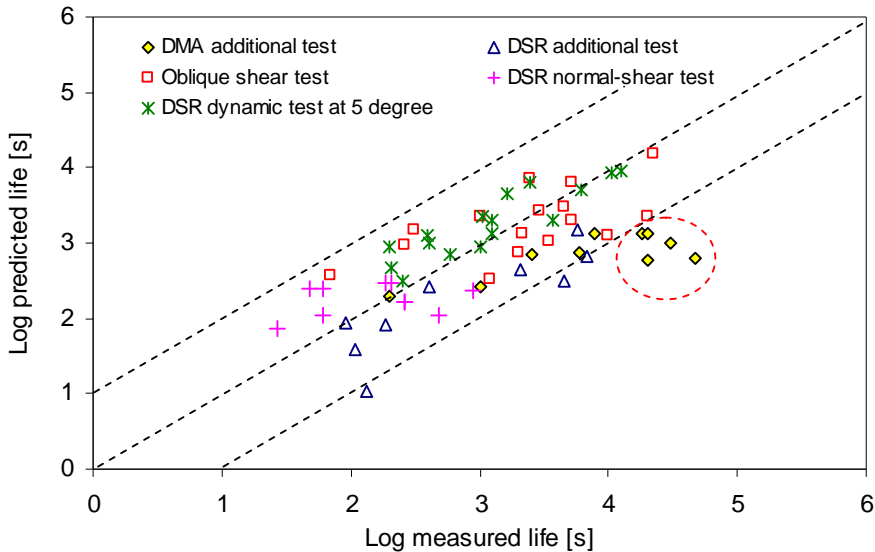


Figure 6.21 Model verification using data obtained from tests at additional temperatures and different stress signals

6.4 Observations on the basis of the model

6.4.1 Temperature dependence of model parameters

Figure 6.22 shows the temperature dependencies of the model parameters. Based on this figure some observations are made which are given below:

- The model parameter σ_0 , which denotes the nominal adhesive strength, tends to increase with reducing temperature. This phenomenon agrees with the temperature dependence of the tensile and shear strength of bitumen in thin films, (see Figures 6.23 and 6.24). As indicated, the values of σ_0 are in the same order of magnitude with the tensile strengths of bitumen in similar thin films

[Majidzadeh & Herrin 1965; Sisko 1968; Marek & Herrin 1968]. However, the values of σ_0 are much higher than the lap-shear strengths of thick bitumen films [Babcock & Statz 1998; Yan & Liang 2001; Khattak & Baladi 2007]. Comparing data reported by several researchers results in the conclusion that no universal relation between the strength of thin bitumen films and temperature can be derived. In general, the strength of thin bitumen films tends to increase as temperature reduces, while the strength tends to decline at very low temperatures. This is in agreement with the relationship between bitumen stiffness modulus and tensile strength as shown in Figure 6.25 [Heukelom & Wijga 1973]. A very high stiffness modulus (low temperature) may result in a low tensile strength.

- The model parameter n is the exponent for the damage development. A lower value of n will result in a relatively faster damage development. As shown, the value of n tends to increase with declining temperature from 20 °C to 0 °C and finally drops down at -10 °C. The initial increase of n indicates that the decrease in temperature has a positive effect on the fatigue resistance of the adhesive zone. However, the sudden drop of n at -10 °C indicates that the damage development of the adhesive zone is rapid at low temperatures.
- The model parameter ϕ is the internal friction angle that indicates the effect of the compressive stress on the shear resistance. A higher value of ϕ results in a stronger positive effect of compressive stress on the shear resistance. As indicated, ϕ tends to decrease when the temperature decreases from 20 °C to 0 °C. However, the sudden increase at -10 °C indicates that the compressive stress may have a significant influence on the shear resistance. The initial decrease of ϕ with decreasing temperatures is in agreement with what can be expected. At high temperature, the bitumen film becomes softer and the chance that the stone columns are touching each other is high resulting in higher ϕ values. The reason for the large value at -10 °C is not clear at this moment and more data at low temperatures is thus required to further explain this phenomenon.

Taking into consideration the temperature dependence of the model parameters, a generalized damage model for the adhesive zone can be written as follows:

$$\frac{dD}{dt} = \dot{D}(\sigma_e) = \left[\frac{\sigma_e}{\sigma_0(T)} \right]^{n(T)} \quad \text{and} \quad \sigma_e = \sigma_n + \frac{\tau}{\tan \phi(T)} \quad (6.33)$$

As indicated in Figure 6.22, these parameters show a linear relation with temperatures ranging from 0 °C to 20 °C. To fully understand the influence of temperature on these parameters, more data at low temperatures are needed. When a generalized model is applied, it is of vital importance to verify the model over a wide range of temperatures and attention must be paid when extrapolating the model to higher and/or lower temperatures.

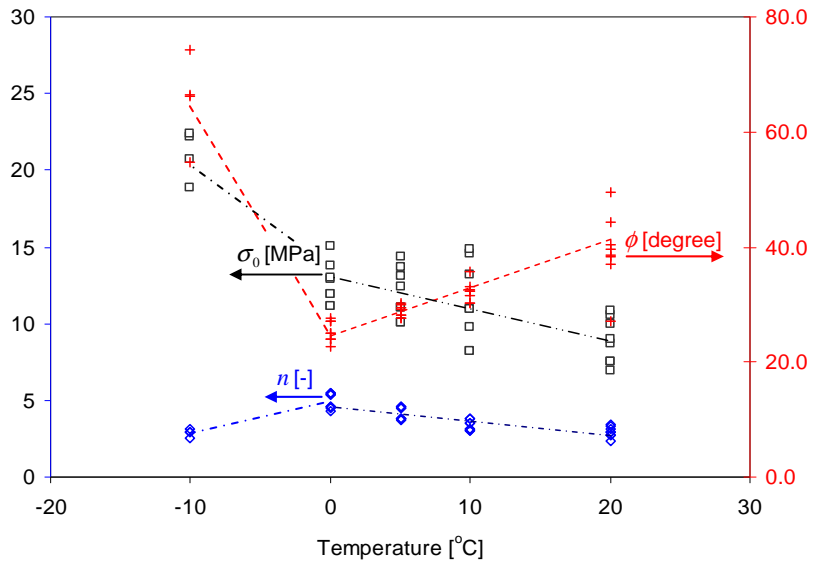


Figure 6.22 Temperature dependencies of model parameters

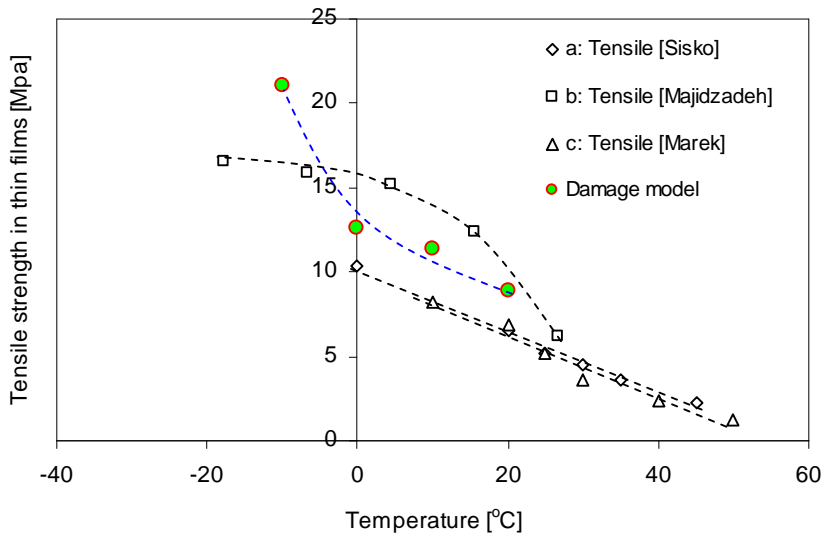


Figure 6.23 σ_0 compared with the tensile strengths of bitumen in thin films (a: data reported by Sisko, film thickness 13 μ m, extension rate 0.1inch/min; b: data reported by Majidzadeh & Herrin, film thickness 20 μ m, extension rate 0.02inch/min ; c: reported by Marek & Herrin, film thickness 20 μ m, extension rate 0.02inch/min)

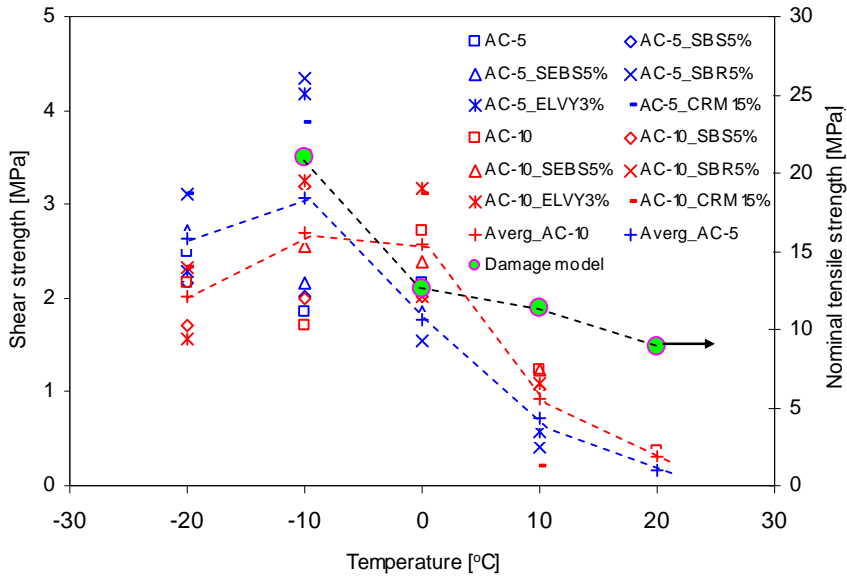


Figure 6.24 σ_0 compared with the lap-shear strengths of various types of bitumen reported by Khattak & Baladi (AC-5 and AC-10: normal bitumen; SBS, SEBS, SBR, ELVY, CRM: polymer modifiers; 3%, 5%, 15%: polymer content; bitumen film 0.13mm, extension rate 0.5cm/min)

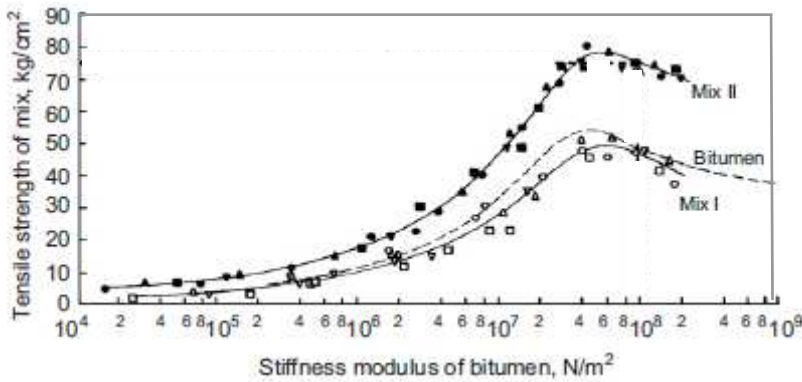


Figure 6.25 Relationship between bitumen stiffness modulus and tensile strength [Heukelom & Wijga 1973]

Figure 6.26 gives an impression of the internal-friction theory for the adhesive zone. The trends in this figure are based on the averages of the model parameters at each temperature. Again, the trends at temperatures ranging from 0°C to 20°C are in agreement with what was predicted. However, at -10°C, the adhesive zone becomes

very strong. For example, the damage model predicts that σ_0 is equal to 23MPa and $\tau_0 = 46\text{MPa}$. Combining these two strengths, a high internal angle of friction of 65° is obtained from the internal-friction theory.

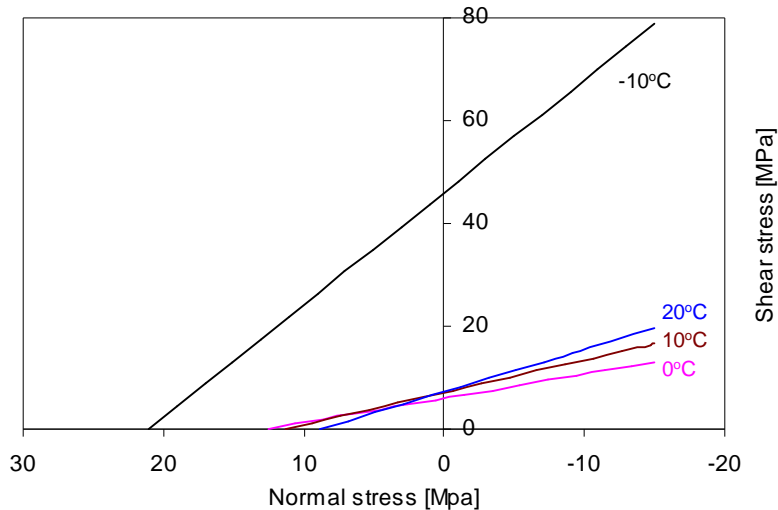


Figure 6.26 Internal-friction theory for the adhesive zone

6.4.2 Model interpretation on effects of aging, water and type of stone

Figures 6.27 to 6.28 show the capability of the model to determine the effects of material combination, stress level as well as temperature on the damage rate. The damage rates at various equivalent stresses are determined by means of Equation 6.29. Please note that a higher damage rate at a given stress level indicates a bitumen-stone combination that is susceptible to damage development. Based on the figures, the following can be observed:

- Higher stress level results in higher damage rate (see Figure 6.27).
- As temperature drops, the damage rate at the same stress level tends to decrease. However, a further decrease in temperature results in an increased damage rate (see Figure 6.27). The influence of temperature on the damage rate indicates that both very low and high temperatures enhance the development of damage.
- Due to the scatter in the fatigue data and the fact that only two data points for each test set are available, it is difficult to come to conclusions on the effects of aging, water conditioning and combinations of both as well as type of stone.
- In general, aging tends to promote the bitumen-stone adhesion and the aging effect seems to be very significant at 20°C as shown in Figure 6.28-a.
- The effect of type of stone on the damage rate is very complex. As shown in Figure 6.28-a, sandstone exhibits a slightly better behaviour than greywacke at 20°C . However, greywacke is much better than sandstone at 0°C (see Figure 6.28-c). At 10°C , both types of stone behave similarly except the combination of G+SB_W (see Figure 6.28-b).
- Water immersion tends to have a negative effect when the short-term aged

bitumen is applied. On long-term aged bitumen, this effect seems to be limited. Compared with short-term aging, it is found that the combination of long-term aging and water conditioning leads to a relatively low damage rate, which further demonstrates that aging has a positive effect on bitumen-stone adhesion.

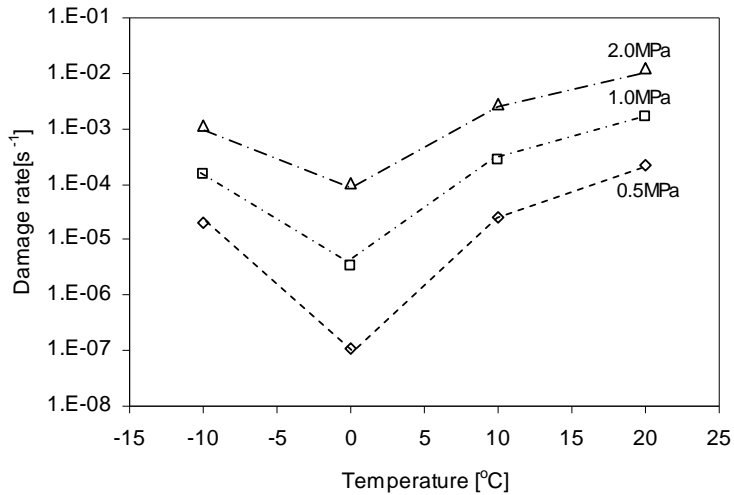


Figure 6.27 Effect of stress level and temperature on the damage rate (values for σ_0 and n are the average at each temperature)

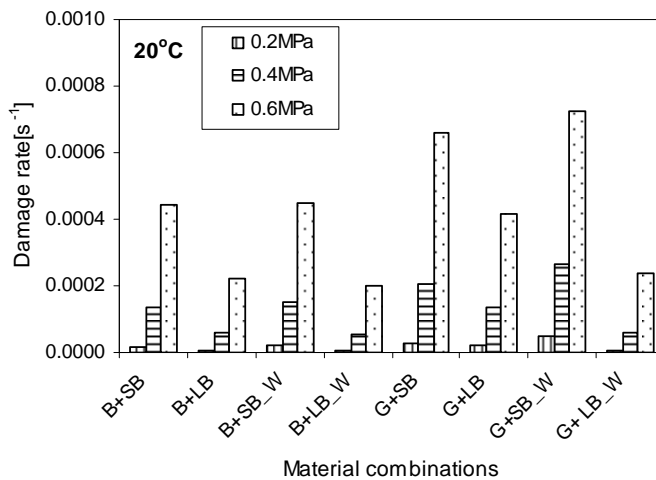


Figure 6.28-a Effects of material combination on damage rate at various stress levels at 20°C

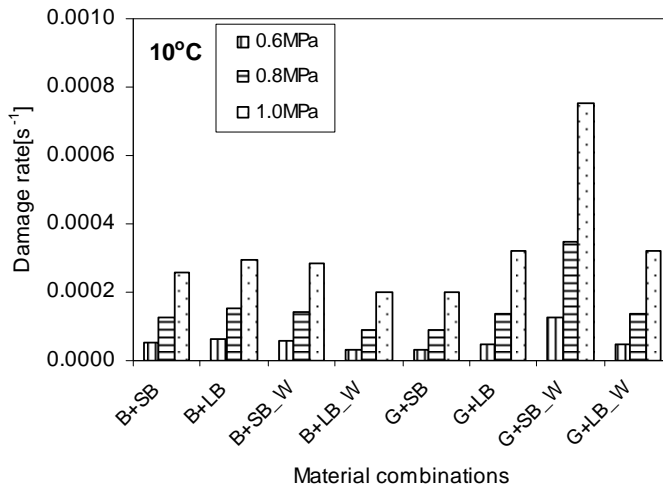


Figure 6.28-b Effects of material combination on damage rate at various stress levels at 10°C

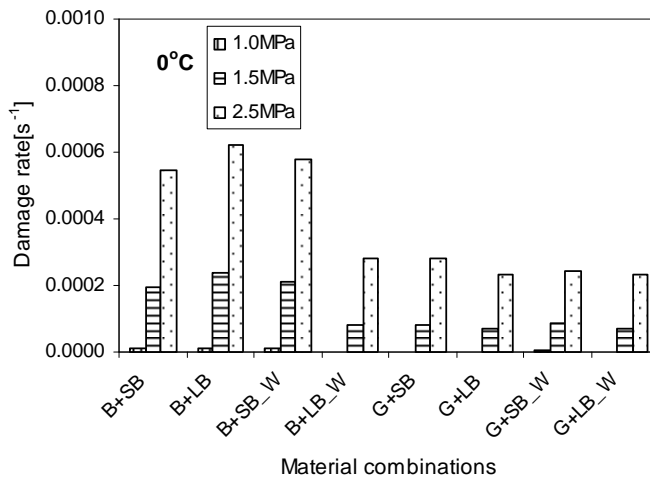


Figure 6.28-c Effects of material combination on damage rate at various stress levels at 0°C

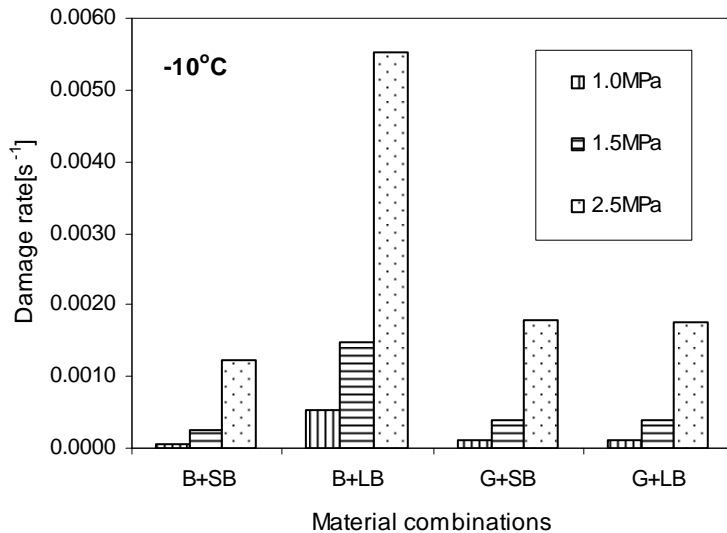


Figure 6.28-d Effects of material combination on damage rate at various stress levels at -10°C

6.4.3 Failure mechanisms

Debonding, or failure of the adhesive zone may occur at different locations within the adhesive zone. The major failure types are cohesive failure in the bitumen film and interfacial adhesive failure along the bitumen-stone boundary. In the first case, the surfaces of both stone columns after debonding are covered by fractured bitumen; in the last case, only one of the surfaces after failure is covered by bitumen. Besides these two cases, other types of failure, e.g. mixed failure may happen within the adhesive zone. Mixed fracture surfaces are characterised by a certain percentage of the area that shows adhesive or cohesive failure.

To investigate the failure mechanisms of various adhesive zones, the fractured surfaces after testing were visually inspected and the percentage of the area that showed adhesive failure was estimated. It must be noted that not all of the fractured surfaces after fatigue failure could be used for such estimations. Some of them were distorted because lack of control at the moment of the failure. For the DSR tests, the failure surfaces tend to be worn off under the function of shear force and finally only the distorted failure surfaces was observed at the end of the test. Therefore, it was difficult to clearly define what type of failure occurred. With respect to other types of test, it was felt that the information on the failure surfaces is more reliable when a pulling-off effect is applied during the test. Because the combined normal stress-shear stress fatigue tests resulted in failure surfaces that easily could be inspected. Only the results of those tests will be presented here (see Figure 6.29).

Figure 6.29 shows the influence of temperature, aging and material combination on the type of failure. Data plotted in this figure include two types of stone, short-term and long-term aged bitumen and four test temperatures ranging from -10 °C to 20 °C. Since the data is obtained by visual inspection it is not exact; three modes of failure

were defined:

- adhesive failure which occurred over an area larger than 70% of the total area;
- mixed failure; in this case, adhesive failure occurred over an area between 30% to 70% of the total area;
- cohesive failure; in this case, adhesive failure occurred over an area less than 30% of the total area.

As shown in Figure 6.29, aging increases the possibility of adhesive failure especially at relatively high temperatures. For short-term aged bitumen (SB) there is an obvious transition temperature for the failure modes. For example, when temperatures are above 5°C, failure tended to be cohesive failure, while adhesive failure seemed dominant at temperatures below 5°C.

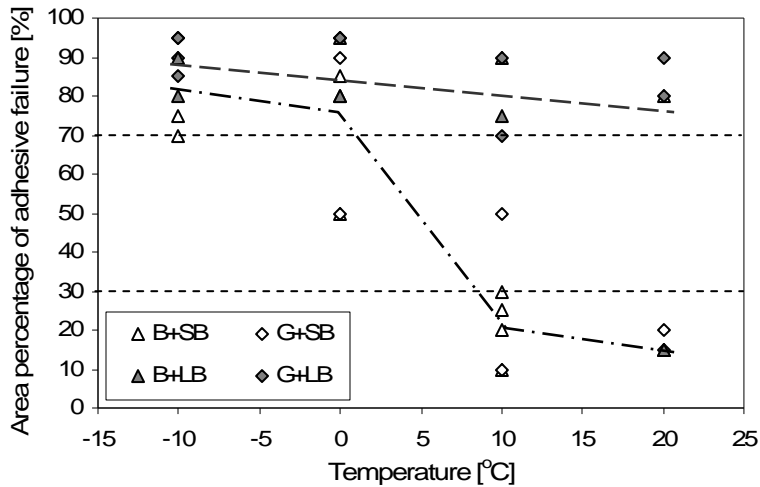


Figure 6.29 Influence of temperature and aging on the percentage of adhesive failure

The change in failure mode can also be used to explain why aging shows a strong positive effect on the damage rate at relatively high temperatures, but a limited effect at low temperatures as shown in Figure 6.28. It also indicates that aging has a more positive effect on cohesion than on bitumen-stone adhesion. Once the adhesive failure occurs prior to cohesive failure, further aging enhances the contribution of adhesive failure.

It must be noted that the aging procedure for the specimen preparation in this study is different from the actual field aging. Thus attention must be paid when using these laboratory-testing data for the analysis of the behaviour of real porous asphalt in the field.

With respect to the type of stone, there is no distinct difference on the failure mode between sandstone (B) and greywacke (G). This may be explained by the

similar relevant properties including surface morphology, surface energy and chemical composition as discussed in Chapter 3.

From all these discussions, it is concluded that the model parameters discussed in this chapter are actually valid for mixed failure modes. Pure adhesive or cohesive failure is difficult to obtain over a wide range of temperature. As indicated in Figure 6.29, the type of failure at -10°C and 20°C may be completely different from each other. However, the model fit shown in Figure 6.20 demonstrates that the developed damage model is capable to explain both of these phenomena. Therefore, it is concluded that the developed damage model can be used to interpret different types of failure due to cohesion and adhesion in the adhesive zone. However, it is also concluded that it is difficult to compare e.g. σ_0 values obtained at different temperatures because at higher temperatures σ_0 seems to be related to cohesive failure while at lower temperatures σ_0 seems to be related to adhesive failure of the adhesive zone.

6.5 Conclusions

A damage model for adhesive zones based on the linear damage accumulation rule was developed. The proposed model is capable of taking into account stress history and 2D states of stress. Model predictions of damage development are in agreement with experimental data.

A generalised model, taking into account the temperature dependency of the model parameters, is proposed. To do this, test data at various temperatures are needed.

The developed damage model can well distinguish the effect of temperature. However, since the tests used in this study did not well capture the effect of water immersion and type of stone as well as aging, the model fitting based on these data also show the similar results. It indicates that the regression results are consistent with the data obtained from laboratory tests.

The above also indicates that improvements on test procedures are needed to distinguish the effects of type of stone, water and aging. For the purpose of material optimization, more tests are suggested to reduce the effect of data scatter.

The visual inspection of the fractured surfaces after testing indicated that different failure mechanisms occurred depending on temperature and amount of aging. Low temperature and extended aging tends to increase the possibility of adhesive failure. The combination of both makes bitumen-stone adhesion extra sensitive to damage.

The developed damage model for the adhesive zone is capable of interpreting the damage development under adhesive failure, cohesive failure and mixed modes of failure.

7 MORTAR FATIGUE MODEL

7.1 Introduction

In porous asphalt mixtures, the mortar binds the stone particles together. Failure within mortar bridges that connect the coarse stone particles, the so-called cohesive failure, may contribute to the development of ravelling. The complex 3D characteristics of tyre-pavement interaction create a very complex state of stress. In combination with the heterogeneous mixture geometry, this indicates that multiaxial loadings will play a very important role in the prediction of the fatigue life. Besides the complex 3D state of stress, the signals of stress components are complex and are not alike the conventional sinusoidal stress wave that is commonly used for fatigue testing. Combining these facts, one should realize that the mortar fatigue in porous asphalt is a problem of complex multiaxial loadings. As a result, the development of any mortar fatigue model must take into account the effects of 3D states of stress and complex stress signals.

The aim of this chapter is to develop a mortar fatigue model based on the dissipated energy concept. It must be noted that the proposed model will be used to interpret the mortar stress and strain signals obtained from finite element simulations of porous asphalt such that the mortar fatigue life can be estimated. To perform tests using complex 3D loadings that reflect the actual mortar loadings is difficult or even impossible. For this reason, model development has to make use of the data from simple uniaxial tensile or shear fatigue tests. The proposed model can and will be verified by using extra data from other fatigue tests in which more complex stress states were applied. However, in this study, attempt to perform combined tensile-shear fatigue tests by means of the available DSR and DMA was unsuccessful. For this reason, the model will be developed by the use of DSR shear fatigue data without further verification.

7.2 Multiaxial fatigue failure

7.2.1 Energy criteria

Special attention has been paid to the energy-based criteria of multiaxial fatigue. Several reviews and comparisons of existing energy-based criteria can be found elsewhere [Garud 1981; Macha & Sonsino 1999; Aleksander & Ewald 2005; Lagoda & Ogonowski 2005]. These criteria have used different kinds of strain energy, i.e. elastic strain energy, hysteresis energy or the sum of both energies, as the damage parameter [Garud 1981, Ellyin & Golos 1998; Ellyin & Xia 1993; Lee, Kim et al 2003]. Identification and calculation of the components of strain energy under cyclic and random loading can be found elsewhere [Lachowicz 2001]. The energies described above can be from a specific material volume or plane. The former considers that the energies due to volume change and distortion are associated with damage. In later use is made of the energies from normal and shear stresses acting on a specific plane. The so-called critical plane is the plane showing the maximum energy by choice of the orientation of the plane in a 3D system. From a review of literature it appeared that the criteria which are taking into account the energy in the critical plane appear promising [Aleksander & Ewald 2005, Lagoda & Ogonowski

2005]. However, it is difficult or even impossible to find the critical plane from infinite orientations under a complex multiaxial state of stress in 3D systems.

7.2.2 Hysteresis energy criteria

When a solid is subjected to cyclic loadings, the graph of stress against strain is frequently a closed loop. The area of this loop is equal to the energy dissipated per unit volume per cycle. Many observations have made use of this quantity and of its variation with stress and with repeated application of constant stress. It is commonly believed that the dissipated energy is for the larger part translated into heat. A small part of the dissipated energy will contribute to damage. Dissipated energy was thus used as an indicator of fatigue damage of various materials. Erber (1993) stated that the sustained hysteresis is a necessary condition for fatigue and is related to the rate of damage accumulation. An estimate of the fatigue life can thus be based on the relations between the area of stress-strain hysteresis loops and the number of cycles to failure. Dimove and Andonova (1995) reported that the relationship between the hysteresis energy per cycle and the number of cycles to failure of low-alloy steel followed a power law. Sugimoto and Sasaki (2006) proposed a fatigue model for structural plywood under panel shear load based on the dissipated energy per cycle. The proposed model can explain the observed phenomenon that the fatigue life at higher loading frequencies was longer than that at low frequencies.

The dissipated energy concept was also used to explain the fatigue behaviour of bituminous materials [van Dijk 1975; Pronk & Hopman 1990; Khalid & Carpenter 2006; Jaeseung et al 2006]. Research done by van Dijk (1975) showed that a unique relationship exists between the total dissipated energy dissipated per volume and the number of cycles to failure.

$$W_{total} = AN_f^z \quad \text{with} \quad W_{total} = \sum_{i=1}^{N_f} W_{i-cycle} = \frac{N_f W_{initial_cycle}}{\psi} \quad (7.1)$$

Where:

- W_{total} = total dissipated energy, [J/m³];
- N_f = number of cycles to failure, [-];
- W_{i_cycle} = dissipated energy in i-th cycle, [J/m³];
- $W_{initial_cycle}$ = initial dissipated energy per cycle;
- A, Z = model constant, [-];
- ψ = factor, [-]. For displacement controlled tests: $1 < \psi \leq 1.5$; for force controlled tests: $0.5 \leq \psi < 1$;

Hopman et al (1992) proposed a fatigue model for asphalt mixtures based on the initially dissipated energy per cycle:

$$N_f = \frac{1}{T_c} \left(A \Psi \frac{T_c}{W_{initial_cycle}} \right)^{\frac{1}{1-Z}} \quad (7.2)$$

Where:

T_c = the loading cycle time;

$\psi = 1.2$ obtained from displacement controlled fatigue tests using sinusoidal load signals.

Some other researchers defined the dissipated energy ratio (DER) based on the change in dissipated energy between the i -th cycle and $i+1$ -th cycle divided by the dissipated energy in the i -th cycle:

$$DER = \frac{W_{i+1_cycle} - W_{i_cycle}}{W_{i_cycle}} \quad (7.3)$$

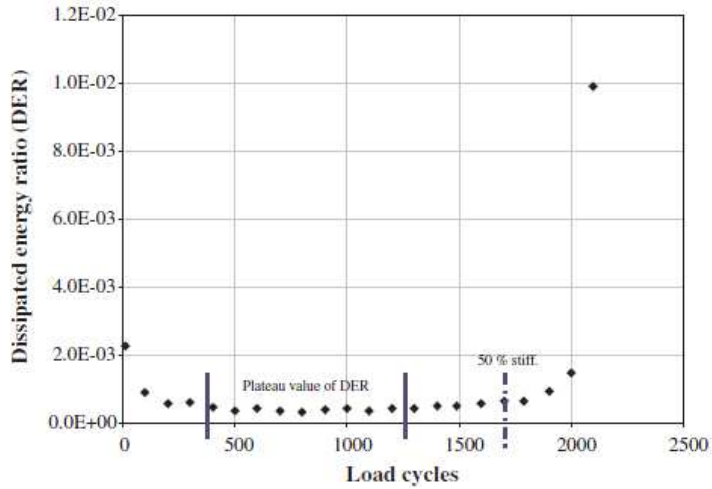


Figure 7.1 The dissipated energy ratio (DER) versus number of load cycles [Ghuzlan & Carpenter 2006]

Plotting the value of DER against load cycles (see Figure 7.1) in a constant load test gives a curve that decreases during the first portion of loading, remains constant (plateau value as indicated in Figure 7.1) for quite some time and then increases rapidly. The moment of true failure, N_{ff} , is defined at the point where the value of DER increase rapidly. The plateau value of DER shows a strong relationship with the true failure [Ghuzlan and Carpenter 2006, Shen & Carpenter 2005]:

$$N_{ff} = A(PV)^B \quad (7.4)$$

Where:

N_{ff} = number of cycles to true failure;

PV = the plateau value of DER;

A, B = model constants.

Numerous multiaxial fatigue failure criteria based on the dissipated energy concept have been reported [Garud 1981; Macha & Sonsino 1999]. However, the effectiveness of these individual methods varies strongly with materials, fracture mechanisms and loading conditions. No universal model has been applied to various materials under complex multiaxial loadings. Garud (1981) proposed the sum of the hysteresis energies per cycle from various stress components, as the damage parameter that influences the fatigue life under multiaxial loadings.

$$W_{initial_cycle} = \sum W_{ij} = \int \sigma_{ij} d\varepsilon_{ij} = CN_f^{-\beta} \quad (7.5)$$

Where:

- $\sum W_{ij}$ = the sum of hysteresis loop areas from various stress components during a complete cycle;
- σ_{ij} = stress components, [Mpa];
- ε_{ij} = strain components;
- C, β = material constants;

To better relate the hysteresis energy per cycle to the axial and torsional fatigue data, various weight coefficients smaller than 1 have been introduced on shear hysteresis energy [Garud 1981; Macha & Sonsino 1999; Andrews & brown 1989].

7.3 Mortar multiaxial fatigue model

In this section, focus is on the development of a mortar fatigue model under multiaxial loadings. At the moment, the tool that allows performing response calculations on porous asphalt concrete already exists [Huurman 2008, Huurman & Mo 2007]. The tool is making use of the linear visco-elastic properties of mortar as material inputs without taking into account damage accumulation during the calculation. The output of the response calculations provides mortar stress and strain signals at any location within the mixture. By combining the mortar load signals, e.g. hysteresis loops and a fatigue model based on the dissipated energy concept, the life expectancy of the mortar is obtained. Illustration of this will be given hereafter.

Figure 7.2 gives an example of mortar stress-time signals obtained from a 2D finite element simulation during four tyre passages on porous asphalt [Mo & Huurman 2007, 2008]. As observed, the obtained stress signals are very complex and the shapes are much different from the sine-wave that is commonly used for fatigue tests. The state of stress also differs strongly from location to location throughout the mixture structure (see Location a and b). Further analysis of the stress/strain signals indicate that there is no predominant direction of stress that allows for the prediction of mortar failure. It appears that interpretation of these complex stress signals into fatigue damage must take into account the influence of stress history and the effect of 3D loadings.

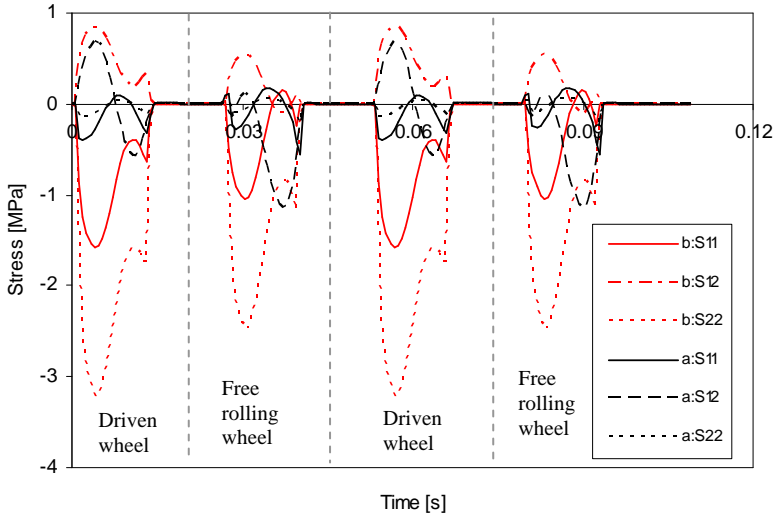


Figure 7.2 Example of mortar stress signals obtained from a 2D finite element simulation as a function of four tyre passages (each driven wheel is followed by a free rolling wheel) (a, b: different locations; S11,12,22: stress components)

On the basis of the above, use is made of a mortar fatigue model based on the sum of the dissipated energy from various stress components as proposed by Grand (1981). According to Equation 7.4, the number of cycles to failure can be explained as the function of the sum of dissipated energy per cycle using a power law form:

$$N_f = \left(\frac{W_{initial_cycle}}{W_0} \right)^{-b} \quad \text{with} \quad W_{initial_cycle} = \sum W_{ij} = \int \sigma_{ij} d\varepsilon_{ij} \quad (7.6)$$

Where:

- W_0 = the energy limit that will lead to failure within one cycle, [MPa];
- b = model constant, [-].

In reality, the relationship between the initial dissipated energy per cycle and the number of cycles to failure may not be well explained by a simple power law described above. For example, Equation 7.1 indicates the following function.

$$N_f = \left(\frac{W_{initial_cycle}}{A\Psi} \right)^{\frac{1}{z-1}} \quad (7.7)$$

Where:

$$\frac{W_{initial_cycle}}{\Psi} = \frac{W_{total}}{N_f}, \quad \text{the mean dissipated energy per cycle, [MPa].}$$

In Equation 7.7, three parameters are needed to be known for life prediction on the basis of $W_{initial_cycle}$. The parameters ψ ($0.5 \leq \psi < 1$ for force controlled mode) is not a constant value but depends on test materials and test conditions. Fatigue life predictions based on this function thus require to estimate the value of ψ firstly. For this reason, ψ should be correlated with some variables that are available both from testing and finite element modelling, for example, stress, strain or dissipated energy. The general formulation can be explained by

$$\Psi = g(\sigma_{ij}, \epsilon_{ij}, W_{ij} \dots) \quad (7.8)$$

As indicated above, the proposed fatigue model makes use of the integral of the stress-strain signals, e.g. initial dissipated energy due to volume change and distortion, within a complete loading cycle. The fatigue parameter is the sum of initial dissipated energy per cycle. The model explains that an increase in initial dissipated energy per cycle results in a decrease of fatigue life.

Illustration of the model will be done using the data as plotted in Figure 7.2. Plotting the stresses against the corresponding strains shown in Figure 7.2 gives the hysteresis loops in Figure 7.3. The area of these hysteresis loops can be determined by using the following equation.

$$W_{initial_cycle} = \sum W_{ij} = \int \sigma_{ij} d\epsilon_{ij} = \sum \left\{ \frac{\sigma_{ij}(t + \Delta t) + \sigma_{ij}(t)}{2} \times [\epsilon_{ij}(t + \Delta t) - \epsilon_{ij}(t)] \right\} \quad (7.9)$$

The sum of dissipated energy, $\sum W_{ij}$ from different stress and strain components as the function of each passage of driven wheel is then determined as 0.000464MPa and 0.000218MPa for Location a. By combination of any known model parameters, e.g. $W_0 = 0.5$ MPa and $b = 2.5$, one can estimate the life expectancy by using Equation 7.6.

$$N_f = \left(\frac{W_{initial_cycle}}{W_0} \right)^{-b} = \left(\frac{0.000464}{0.5} \right)^{-2.5} = 3.82 \times 10^7 \quad \text{for each driven wheel at Location a}$$

$$N_f = \left(\frac{W_{initial_cycle}}{W_0} \right)^{-b} = \left(\frac{0.000218}{0.5} \right)^{-2.5} = 2.52 \times 10^8 \quad \text{for each free rolling wheel Location a}$$

Similarly, one can also compute the fatigue life according to Equation 7.7 when the related model parameters are known. It must be noted that the value of ψ varies strongly with different values of $W_{initial_cycle}$. Proof of this will be given later. For reasons of simplification, ψ was assumed to be a constant in other studies [van Dijk 1975; Hopman 1990]. However, one should be careful in using this assumption.

When different stress magnitudes in a spectrum are considered, the Palmgren-Miner linear damage hypothesis are usually used for design purpose. Failure occurs at

$$\sum_i^k \frac{n_i}{N_i} = 1 \tag{7.10}$$

Where:

N_i = the number of cycles to failure of a constant stress reversal σ_i ;

n_i = the number of repeated cycles of a constant stress reversal σ_i .

Combining the stress spectrum at Location a as shown in Figure 7.2 leads to an estimated number of 1.66×10^7 repetitions of such four wheel passages.

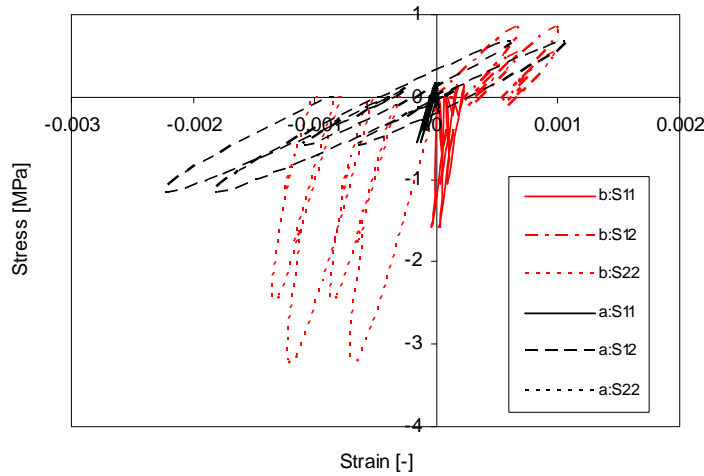


Figure 7.2 The hysteresis loops obtained from the stress and strain data in Figure 7.1 (a, b: different locations; S11,12,22: stress components)

For simple uniaxial tensile or shear fatigue tests, the state of stress to which the test material is subjected is known. For these tests, the energy is dissipated in one direction. On the basis of fatigue data, the described model parameters, W_0 and b can be determined by fitting the initial dissipated energy per cycle with the number of cycles to failure. Similarly, A and Z can be determined by fitting the mean dissipated energy per cycle or the total dissipated energy with the number of cycles to failure.

7.4 Mortar fatigue results

In this study, shear and bending fatigue tests were considered for the mortar fatigue testing program. However, as stated earlier, DMA bending fatigue testing was not successful. Data on bending fatigue are thus not available for model development. Therefore, the discussions hereafter are related to mortar fatigue data obtained by

means of the DSR.

As mentioned above, the initial dissipated energy per unit volume per cycle will be used as a damage parameter of mortar fatigue for practical reasons. For mortar shear fatigue testing, a sinusoidal oscillation torque was applied to the specimen in the torque-controlled mode. The induced radial deflection angle and the phase lag between torque and radial deflection angle were measured accordingly. The transfer functions that are required to translate torque into stress and displacement into strain, have been derived based on finite element simulations. More information can be found in Chapter 4.

$$\tau = k_3 \frac{2 \times T}{\pi \times r^3} \quad (7.11)$$

$$\gamma = k_3 \frac{r \times \theta}{h_{\text{eff}}} \quad (7.12)$$

Where:

τ = shear stress, [MPa];

T = torque, [N.mm];

r = specimen radius, 3mm;

γ = shear strain, [-];

θ = deflection angle, [rad];

h_{eff} = specimen effective height, 12.742mm;

k_3 = the calibration factor that accounts for stress concentration, $k_3 = 1.05$.

The sample stress can be expressed by

$$\tau = \tau_0 \sin \omega t \quad (7.13)$$

Where:

τ_0 = amplitude of shear stress, [MPa];

ω = angular frequency, [rad/s].

The sample strain will be oscillatory with a frequency equal to the applied frequency and lagging by a phase angle δ .

$$\gamma = \gamma_0 \sin(\omega t - \delta) \quad (7.14)$$

Where:

γ_0 = amplitude of shear strain, [MPa];

δ = phase angle, [rad];

The initial dissipated energy per unit volume per cycle, which is equal to the area of the hysteresis loop obtained by plotting the stress against the strain, is calculated by

$$\begin{aligned}
 W_{initial_cycle} &= \int_0^{1cycle} [(\tau_0 \sin \omega t) \times \frac{d(\gamma_0 \sin(\omega t - \delta))}{dt}] dt \\
 &= \int_0^{1cycle} \tau_0 \sin \omega t \times [\omega \gamma_0 \cos(\omega t - \delta)] dt \\
 &= \pi \tau_0 \gamma_0 \sin \delta
 \end{aligned}
 \tag{7.15}$$

Figure 7.3 gives a typical example of the change in dissipated energy per cycle over the number of cycles. In torque controlled mode, the strain amplitude as well as the phase angle of each cycle increase with increasing number of cycles. As a result, the dissipated energy increases with increasing number of load cycles. Apparently, the trend can be divided into three periods. Firstly an increase is observed after starting the test. Then a steady increase can be observed and finally the dissipated energy increases rapidly at the end of the test. The increase after starting the test indicates that the test is not in a steady state and thus the initial dissipated energy per cycle $W_{initial_cycle}$ should not be determined based on the first few cycles. As shown in this figure, the dissipated energy per cycle at the beginning of the steady stage, (which is defined in the figure), is chosen as the energy-based damage parameter hereafter.

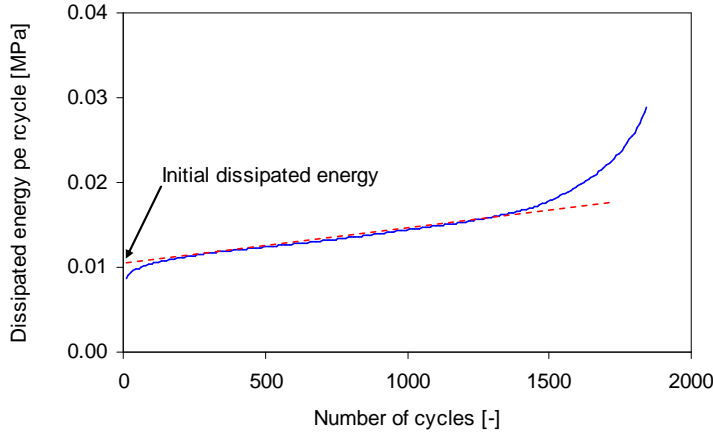


Figure 7.3 Change of dissipated energy per cycle over the number of cycles

7.5 Determination of model parameters

7.5.1 Initial dissipated energy per cycle

Figure 7.4 shows the measured number of cycles to failure N_f that is plotted against the initial dissipated energy per cycle $W_{initial_cycle}$ on a log-log scale. Data shown in this plot include 16 test combinations (short-term and long-term aging, with and without water conditioning, 2 temperatures and 2 frequencies). As indicated the number of cycles to failure follows a linear relation with the initial dissipated energy per cycle on a log-log scale. This demonstrates the previous assumption that the relationship between the number of cycles to failure and the initial dissipated energy

may follow a power law form as explained by Equation 7.6.

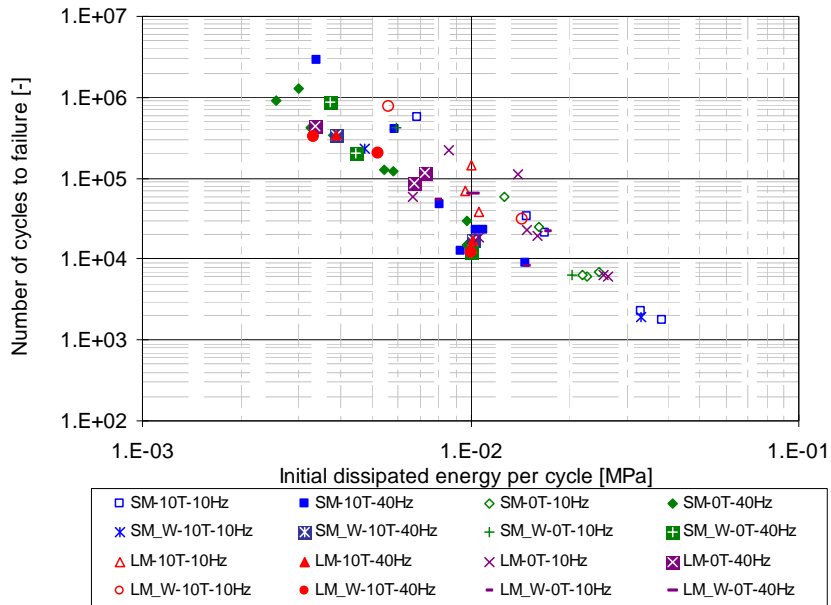


Figure 7.4 Relation between fatigue life and initial dissipated energy per cycle (hereafter, SM: short-term aged mortar; LM: long-term aged mortar; W: water conditioning; 0T and 10T: test temperatures of 0°C and 10°C; 10Hz and 40Hz: test frequencies.)

Table 7.1 Model parameters and model fit based on initial dissipated energy

Temperature	Material	w_0 [MPa]	b [-]	R^2
0°C	SM	0.453	2.748	0.93
	SM_W	0.440	2.685	0.83
	LM	0.530	2.677	0.91
	LM_W	0.514	2.727	0.57
10°C	SM	0.518	2.760	0.84
	SM_W	0.526	2.593	0.98
	LM	0.503	2.755	0.72
	LM_W	0.500	2.704	0.61

Based on the data shown in Figure 7.4, the values of w_0 and b can be determined by the method of least square fitting. In the fitting procedure, the relative error between the predicted number of cycles to failure and the measured number of cycles to failure is minimized on log-log scale. For each combination the model

parameters were determined for the temperatures at which tests were done. The obtained fits are summarized in Table 7.1. As indicated by the correlation coefficient of R^2 , the model shows a good fit with the test data. As shown in Figure 7.5, the number of cycles to failure as predicted by the model is in good agreement with the actual number of cycles to failure as measured.

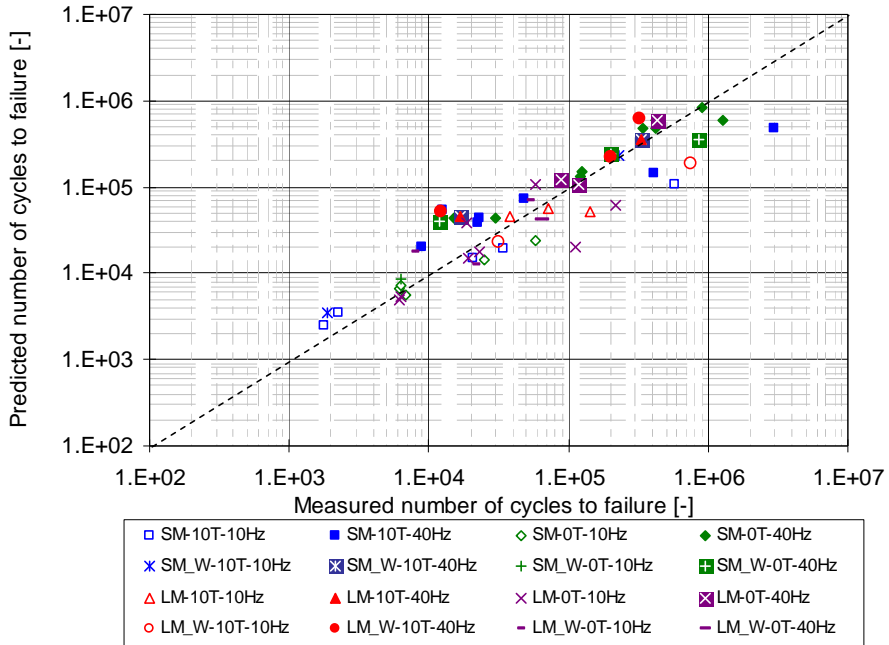


Figure 7.5 Comparison of the predicted and measured number of cycles to failure based on initial dissipated energy per cycle

7.5.2 Mean dissipated energy per cycle

Figure 7.6 shows the measured number of cycles to failure plotted against the mean dissipated energy per cycle, $\frac{\Delta W_{ij}}{\Psi}$, on a log-log scale. It must be noted that the mean

dissipated energy per cycle is equal to the ratio between the total dissipated energy and the number of cycles to failure. Plotting the number of cycles to failure against the total dissipated energy results in the relation as shown in Figure 7.7. Again, data shown in these two plots include 16 test combinations as mentioned earlier. As indicated the number of cycles to failure follows a linear relation with the mean dissipated energy per cycle on a log-log scale.

On the basis of fatigue data shown in Figure 7.6 or Figure 7.7, the described model parameters, A and Z can be determined by means of regression according to either Equation 7.7 or Equation 7.1. Table 7.2 gives the fitting results and Figure 7.8 gives an expression of the accuracy of model fit. As can be observed, the model is in good agreement with the measured data.

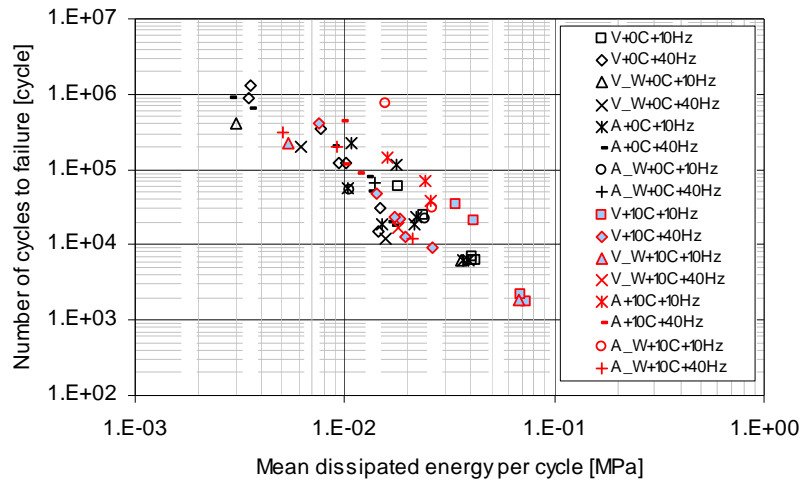


Figure 7.6 Relation between fatigue life and the mean dissipated energy per cycle

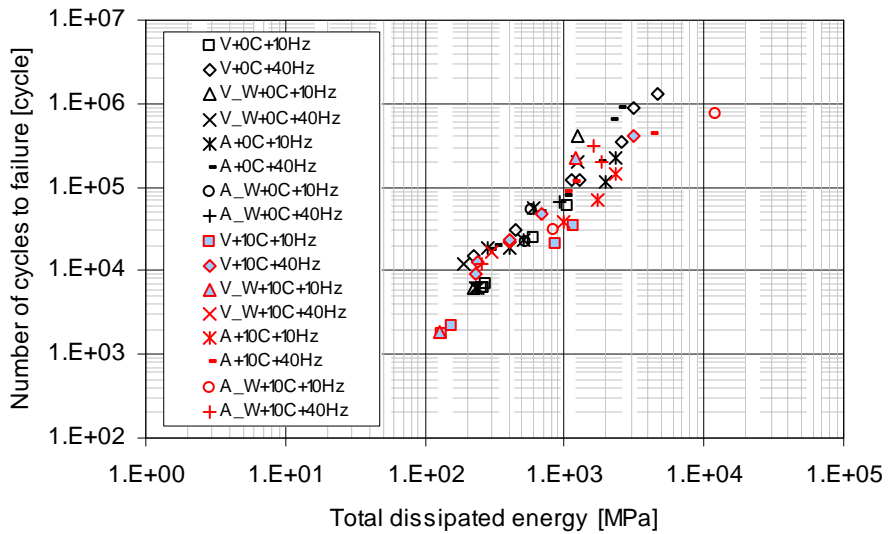


Figure 7.7 Relation between fatigue life and the total dissipated energy

Table 7.2 Model parameters and model fit based on total dissipated energy

Temperature	Material	A [MPa or 10^6J/m^3]	Z [-]	R^2
0 °C	SM	0.732	0.621	0.91
	SM_W	0.732	0.621	0.91
	LM	0.852	0.617	0.95
	LM_W	0.852	0.617	0.53
10 °C	SM	0.870	0.620	0.89
	SM_W	0.870	0.620	0.99
	LM	0.825	0.650	0.74
	LM_W	0.825	0.650	0.86

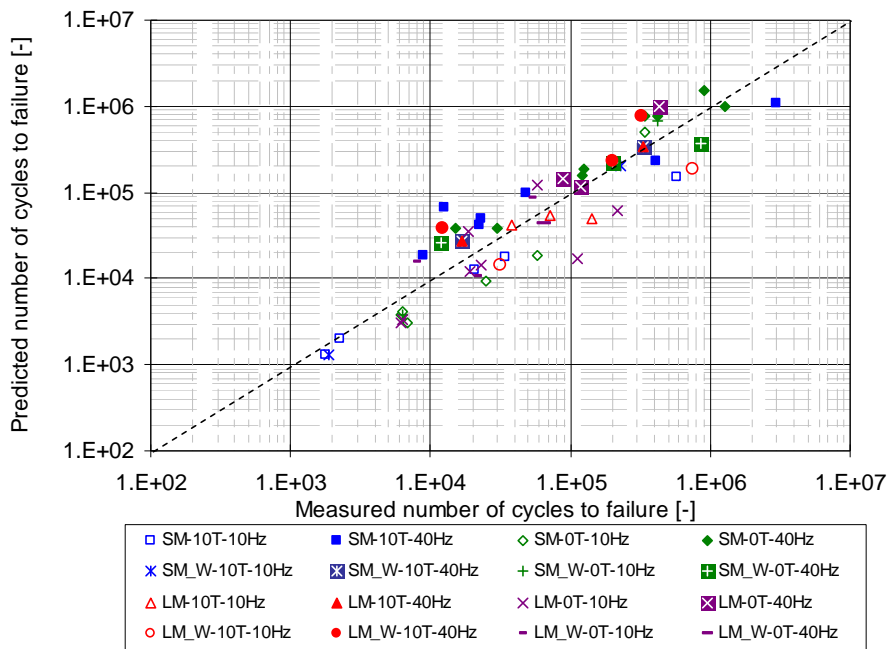


Figure 7.8 Comparison of the measured and predicted number of cycles to failure based on the mean dissipated energy per cycle

With respect to the model parameter Z , it has been observed that Z does not vary too much for common asphalt mixes and this value can therefore be taken as a constant for practical purposes (e.g. $Z = 0.66$) [van Dijk 1975; Molenaar 2007]. In this study, it is also observed that Z shows a limited variation (from 0.617 to 0.650 as listed in Table 7.2). It should be noted that this observation is based on test data obtained from only one type of bitumen (SBS polymer modified bitumen) and one type of mortar composition.

The relation between Z and b in the model based on initial dissipated energy per cycle can be approximately explained by using:

$$b \approx \frac{1}{1-Z} \tag{7.16}$$

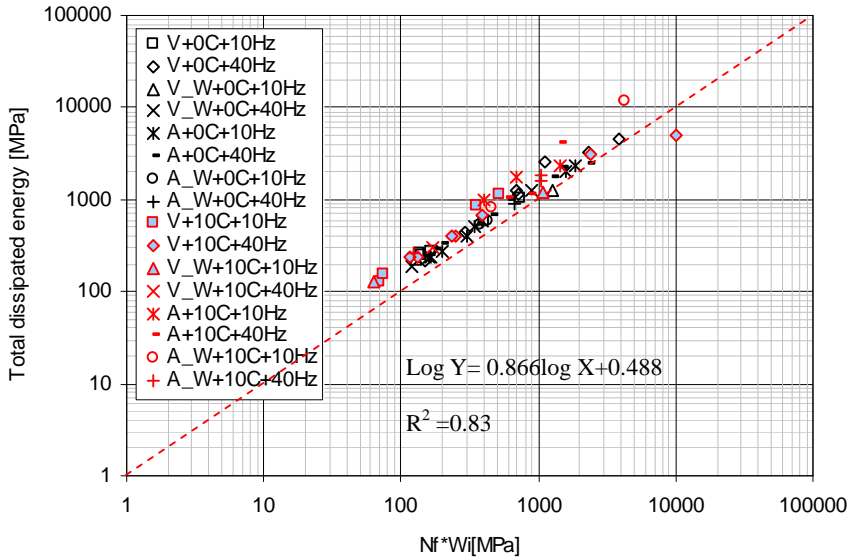


Figure 7.9 Relationship between the $N_f \times W_{initial_cycle}$ and W_{total}

The parameter Ψ is the ratio of $N_f \times W_{initial_cycle}$ to W_{total} , (e.g. $\Psi = \frac{N_f \times W_{initial_cycle}}{W_{total}}$).

Figure 7.9 shows the relationship between the $N_f \times W_{initial_cycle}$ and W_{total} . As indicated, W_{total} is larger than $N_f \times W_{initial_cycle}$ and a linear relationship is observed on log-log scale. This demonstrates that the value of Ψ is not a constant value, but a correction factor that can take many values.

Figure 7.10 gives an impression of the values Ψ can take. Based on this figure, some observations are made which are given below:

- Ψ tends to increase as temperature reduces from 10°C (red points) to 0 °C (black points);
- Ψ tends to increase with increasing frequencies from 10Hz to 40Hz (see V+0C+10Hz versus V+0C+40Hz).
- Ψ tends to increase with extended aging (see V+0C+10Hz versus A+0C+10Hz).
- A higher load level leads to a larger amount of initial dissipated energy per cycle, and thus resulting in a smaller value of Ψ .

- A very small amount of initial dissipated energy per cycle may lead to a value of Ψ approaching to 1, meaning $N_f \Rightarrow \infty$ and no damage occurs.

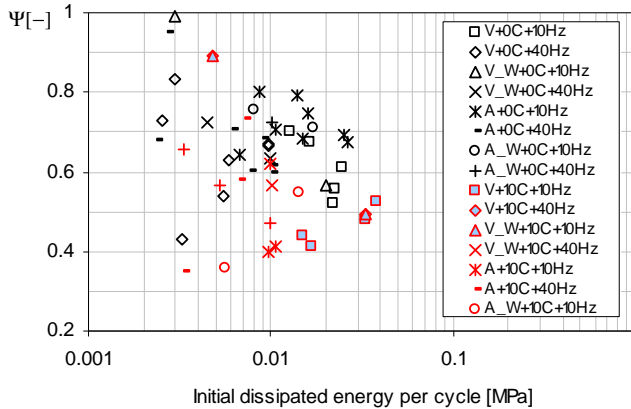


Figure 7.10 Relationship between $W_{initial_cycle}$ and Ψ

In general, one can conclude that Ψ depends on the frequency, temperature, load level as well as aging degree. One might also argue that the bitumen type and the composition of the mortar might also have an influence. This however can not be investigated since only one type of bitumen and one type of mortar were used in this study.

7.5.3 Practical mortar fatigue model

The above indicates that mortar fatigue can be described using either the initial dissipated energy per cycle or the mean dissipated energy per cycle (that is, the total dissipated energy divided by N_f). Both models give very good results compared with the measured number of cycles to failure.

With respect to the life prediction on the basis of the mortar stress and strain signals obtained from response calculations, the model based on the initial dissipated energy per cycle is more practical than the model based the mean dissipated energy per cycle. As mentioned, the response calculations are performed only provide limited information; only the initial dissipated energy per cycle can be determined, but the mean dissipated energy per cycle or the total dissipated energy can only be known after failure.

In reality, the dissipated energy per cycle will change as a function of the amount of damage that is developing in the mortar bridges that connect the coarse particles in the porous asphalt mixture. This change is not known in advance and the value of Ψ can therefore not be estimated. Given the limitations of the current model, the fatigue life predictions which will be discussed later, are therefore based on the initial dissipated energy per cycle.

7.6 Conclusions

A practical mortar fatigue model based on the dissipated energy concept is developed for the life predictions under complex multiaxial loading conditions. The fatigue parameter makes use of the initial dissipated energy per cycle. Model parameters can be determined on the basis of the commonly used fatigue tests. This approach gives very good results in explaining the laboratory fatigue data. Only data from the DSR shear fatigue tests is available. For this reason the model could not be verified against data at other stress conditions. For this reason the model should be applied with some care.

8 MODEL APPLICATION & VERIFICATION

8.1 Introduction

In this chapter, the mortar fatigue model and the adhesive zone damage model discussed in the previous chapters are applied to predict the life expectancy of porous asphalt. To do this, finite element simulations of porous asphalt under repeated traffic loadings are required. Numerical models that enable such simulations were first developed in the CAPA-3D finite element platform [Huurman & Mo et al. 2006; Mo & Huurman et al. 2007, 2008]. During the LOT project, further model development was done by application of the ABAQUS finite element package and finally formed a tool, named Lifetime Optimization Tool, LOT [Huurman 2008; Huurman & Mo 2007; Huurman & Woldekidan 2007]. The tool contains 2D idealized, 3D idealized and 2D photo geometrical models of porous asphalt. These geometrical models represent the mixture's structural geometry on meso-scale. The finite element models enable the translation of the geometry of the mixture, the mortar's visco-elastic response and traffic surface loadings into in-mixture stress and strain signals. Given the scale of the geometrical models, after simulation, stress and strain signals are available at any location in the modelled mixture structure. Combined with the discussed fatigue and damage models, the stress and strain signals in the mortar may be utilised to determine the fatigue life of the mortar bridges. Similarly, signals of adhesive zone stress may be utilised to determine the adhesive zone life expectancy.

From the above it should be clear that LOT forms a tool that is able to predict the ravelling lifespan of porous asphalt. The tool combines models of; traffic surface loading, mixture geometry (volumetrics), mortar response, mortar fatigue and adhesive zone damage.

For the purpose of validation a full-scale ravelling test was done at the Research Association for Underground Transportation Facilities (STUVA) in Cologne, Germany. For this test use was made of the STUVA Accelerated Pavement Test (APT) [van Hinthem 2008; RWTH 2007; Huurman & Molenaar et al. 2008]. In the APT four types of porous asphalt were tested. In two mixtures, use was made of greywacke stone while the other mixtures were made using sandstone. For both types of stone the performance of a bitumen-rich and low-void-ratio mixture was compared to a bitumen-poor and high-void-ratio mixture. In total, 7×10^5 wheel load applications were applied at 80km/h. Ravelling developed on all of the mixtures. During the APT the development of ravelling damage was monitored by laser texture measurements. At the end of the APT ravelling damage was also assessed by detailed visual inspection by a qualified Dutch visual inspector of DVS.

In this chapter, LOT simulations of the four types of porous asphalt mixtures involved in the ravelling APT are carried out. Use is made of the 2D idealized model, which has been demonstrated to be a more practical tool compared with 3D idealized and 2D photo models [Huurman 2008]. The model geometry was generated on the basis of the available knowledge after construction. This implied that the actual volumetric properties were used in the simulations. With respect to the mortar behaviour, the properties of laboratory prepared mortar were compared with those of the mortar collected from the actual porous asphalt mixture constructed at the STUVA

test section. This ensured that the proper mortar behaviours were used as model input. Besides the model geometry and material behaviour, the loading of the model is also of great importance. The test set-up at STUVA is a circular test track. As a result, the tyre-pavement interaction is significantly different from a real vehicle riding on a normal road. To obtain insight into the complex tyre-pavement contact stress distributions for the real STUVA load, a research was carried out at Eindhoven University of Technology [Lopez & Steen 2007]. The results of the above research were used to simulate the tyre-pavement interaction at the STUVA test section.

Using these inputs, the model provided the stress and strain signals in the mortar and the stress signal in the adhesive zone. The fatigue and damage models enabled to translate the computed stress and/or strain into life expectancies, e.g. number of passages to cause failure.

Finally, the computed lifetime (e.g. number of passages to cause failure) is compared to the actual ravelling damage as determined by means of the results of laser texture measurements and visual inspection. As will be discussed later, LOT focuses on the critical contact where failure occurs first. As a result, LOT gives an indication of the initiation of ravelling and the computed life expectancy does not directly correlate with the lifespan of the porous asphalt. Furthermore, the evolution of ravelling can not be explained by LOT. For this reason, a ravelling evolution model is proposed to correlate the computed life expectancy with the life span, e.g. the maintenance moment.

8.2 Finite element simulation

Geometry, loading, boundary conditions and material properties are the critical issues in finite element modelling. In the following these relevant issues will be discussed. Effort is made to get the simulations as closely as possible to the situations that occur at the STUVA APT.

8.2.1 Geometry

8.2.1.1 Structural geometry of porous asphalt

The spatial modelling of the actual structure of porous asphalt concrete is a great challenge. The structure of porous asphalt at meso-scale is very complex as it includes aggregates with a wide range of sizes and irregular shapes. It should be known that there are thousands of mineral particles including coarse and fine aggregates even in a small volume of porous asphalt. Due to this a huge amount of degrees of freedom is required to model each individual aggregate. Solving such a 3D model will be very time consuming and impractical if not impossible with the capability of modern computers. Modelling of the structure of porous asphalt thus asks for simplifications. These simplifications, however, may not affect the capabilities of the model to represent the mixture structure.

The aggregates in porous asphalt are gap graded, i.e. a large amount of coarse aggregates combined with a small amount of fine materials. As a result, porous asphalt concrete is an open material with a void ratio larger than 20% by volume. Figure 8.1 gives a cross-section image of porous asphalt obtained from the STUVA APT sections [Khedoe & Moraal 2008]. The finer aggregates are mixed with the bitumen to form the mortar that surrounds and glues the coarser aggregates. The

coarser aggregates form a stone skeleton throughout the whole structure. This implies that coarse aggregates play an important role in the structural stability and force transmission within the mixture, whereas the mortar acts mainly as an agent that acts to bind the coarse aggregates.

Figure 8.1 gives an example of the real structural geometry of porous asphalt. To enable structural modelling, the structure of porous asphalt is simplified to the following phases: (1) coarse aggregates, i.e. larger than 2mm; represented by spherical grains with an equivalent size; (2) mortar consisting of bitumen, filler and fine aggregates, i.e. smaller than 2mm; (3) air voids and (4) the adhesive zones where the mortar meets the stone surface.



Figure 8.1 Image of the cross-section of porous asphalt concrete [Khedoe & Moraal 2008]

8.2.1.2 Simplified structural geometry for simulations

In this study, Use is made of a 2D idealized model. The model geometry is generated by using LOT which was developed during the LOT project. For this reason, only a brief introduction will be given hereafter. For more detailed information the reader is referred to [Huurman 2008; Huurman & Mo 2007; Huurman & Woldekidan 2007].

Figure 8.2 gives an overview of the 2D idealized model obtained on the basis of the discussed simplifications [Huurman 2008]. As shown in this figure, the idealized model considers perfectly round spheres bound together via mortar bridges. The stone particles are modelled by using rigid bodies. Modelling the aggregate particles as rigid bodies is acceptable given the huge difference in stiffness between stone mineral and mortar. The stone particles themselves are not visible and formed by implementation of restraints forming rigid bodies. The model consists of three layers of stone particles enclosed in a mortar film. The mortar films closer to the middle of the model (see the blue box) are of special interest therefore they are modelled using a finer element mesh.

Only the five particles (see red box) closest to the centre of the model are fitted with a layer of thin elements that represent the adhesive zone. This adhesive zone is modelled by using an ABAQUS element (code: COH2D4) and each node has two degrees of freedom, e.g. normal and tangential traction components.

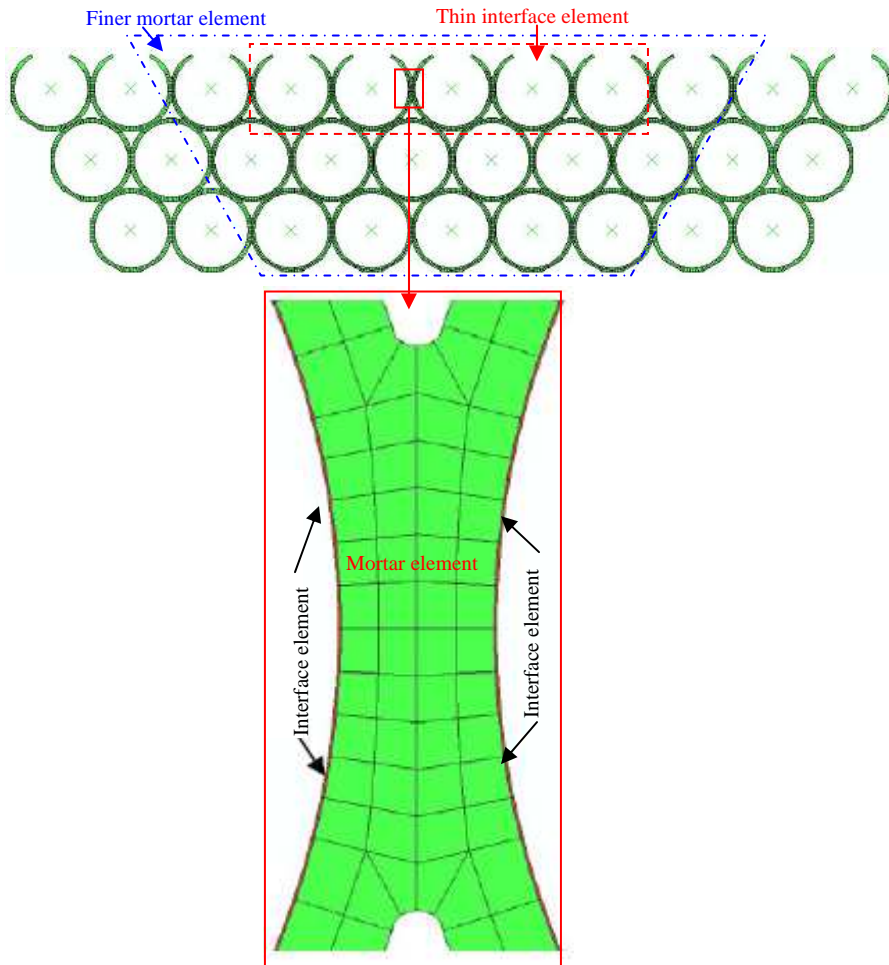


Figure 8.2 Overview of the 2D idealized model [Huurman 2008]

The model is rigidly restrained at locations where mortar bridges form the outer boundary of the model. The discussed mesh refinement indicates that the model is aiming to be accurate in the central part consisting of five particles. The remainder of the model is made so that the effects of boundary conditions are negligible in the central area of the model.

In the 2D model use is made of rigid body stone particles to limit the mathematical size of the model. For the same reason the mortar film surrounding the particles is modelled less accurately at the edges of the model.

The meshes of the idealized model are generated by the LOT input generator on the basis of some parameters including aggregate grading, bitumen content, and air void content as well as other volumetric properties. More detailed information can be

found elsewhere [Huurman 2008].

8.2.1.3 STUVA mixtures and simulations

LOT is a mechanistic tool for determination of the ravelling performance of porous asphalt. Similarly, LOT also can serve as a tool for performance analyses for the paved porous asphalt concrete in the field. In this case, the analysis uses knowledge obtained from the compacted porous asphalt concrete as used in the STUVA APT sections. Hereafter, examples will be given based on the performance prediction of the various porous asphalt concrete sections of the STUVA circular APT.

As mentioned before, accurate information of especially aggregate grading, bitumen content, air void content after compaction (degree of compaction) will be of great importance for performance analyses. The actual volumetric properties, especially the real achieved void content, must be used as model input.

In the following discussions, focus is on the real properties of the STUVA mixtures after production and compaction. Most of the required information was available from additional research performed on a number of cores taken from the STUVA test slabs [Khedoe & Moraal 2008].

Four different double-layered porous asphalt mixtures were tested in the STUVA circular APT. In all cases the lower layer consisted of porous asphalt 11/16 mm with a void content of 18.8vol% and 4.2wt% bitumen. Variations were in the top layer, see Table 8.1.

Table 8.1 Top layer mixture composition [van Hinthem 2008]

Mixture	A	B	C	D
Aggregate	Greywacke	Greywacke	Sandstone	Sandstone
Grading	4/8 mm	4/8 mm	4/8 mm	4/8 mm
Bitumen content, wt%	6.6	5.0	7.1	5.4
Desired void content, vol%	20	26	20	26
Bitumen	Cariphalt XS, SBS modified			
Filler	Wigro 60K with 25% hydrated lime			

As indicated in Table 8.2 Mixture B had a void content of 27.4%. Please note that the 2D idealized model discussed above is based on hexagonal close-packing and the maximum void content of such a close-packing by single spheres is approximately 25.95%. A higher void ratio would lead to a situation in which the spheres in the packing no longer make contact. This means that the LOT procedure that translates mixture volumetrics into idealized model geometry has its limitations. Indications are that the procedure works to a maximum void ratio of 23.5%.

As mentioned above, the actual void content should be reflected in the model geometry. To overcome this limitation of the model, it was decided that the life expectancy of a mixture with a void content above 23.5% was going to be made use of a curve which relates life to void content. This curve was developed by making a number of calculations at void contents lower than 23.5%.

As listed in Table 8.2, all other mixtures had actual void contents higher than 23.5% except for Mixture C. The life expectancies of these mixtures need to be determined by means of extrapolation using the design life vs void content curve mentioned above.

The model is also limited in simulating mixtures with relatively low void contents. The reason is that the void content is controlled by the distance between neighbouring rigid spheres in the model. However, the minimum air void is obtained when the neighbouring particles are directly in contact with each other. It has been shown that the LOT procedure works for void content as low as 18%. Due to the limitations of the model, simulations were done for three void contents, e.g. 18%, 20% and 23.25%.

Table 8.2 also shows that the actual grading of various STUVA mixtures is comparable to the design grading used in the laboratory [Khedoe & Moraal 2008]. For this reason, the design grading was used to determine the equivalent grain sizes for these four mixtures. At the moment of writing this thesis, information on the actual bitumen contents of the STUVA mixtures was not available. Therefore, the bitumen content for the mixture design was used to represent the actual bitumen contents of the STUVA mixtures.

Table 8.2 Relevant properties of the STUVA mixtures against mix design [Khedoe & Moraal 2008]

Particle size, mm			Grading, wt%								
			Mixture A				Mixture B				Mixture C
Lower limit	upper limit	Equivalent	STUVA	Mix design	STUVA	Mix design	STUVA	Mix design	STUVA	Mix design	
8	11.2	9.5	6.7	6.7	3.0	6.9	4.0	12.7	4.9	13.2	
5.6	8	6.7	50.7	53.7	51.1	55.4	51.8	59.4	54.6	61.4	
2	5.6	3.3	32.5	28	34.4	28.9	28.7	15.4	29.4	15.9	
Sand+filler			13.7	11.6	11.5	8.8	15.4	12.5	11.1	9.5	
Equivalent grain size[mm]			-	5.84	-	5.84	-	6.51	-	6.51	
Bitumen content, wt%			-	6.6	-	5.0	-	7.1	-	5.4	
Void content, vol%			24.3	20	27.4	26	21.6	20	25	26	
Computed void content, vol%						18, 20 , 23.25					

Based on the information listed in Table 8.2, the model geometries for various mixtures were generated using the LOT generator. The guide on how to use this tool is available elsewhere [Huurman & Mo 2007]. For each mixture, three void contents, e.g. 18%, 20% and 23.25%, were computed to determine the relationship of design life versus void content. Using this relationship, the design lives at high void contents which are beyond the model capability were estimated by means of extrapolation.

8.2.2 Loading

8.2.2.1 LOT Loading

The surface loading of the model should reflect the actual traffic loading as well as

possible. Some researchers published the results of 3D contact stresses measurements between a road surface and a tyre [Seitz 1971. de Beer 1997; Blab 1999; Lopez 2008]. On the basis of the available information on tyre-pavement contact forces, a scaled-down method that enables to translate the tyre-pavement interactions into the meso-scale mechanics of porous asphalt concrete has been developed for LOT [Huurman & Milne et al. 2003; Milne & Huurman et al. 2004; Huurman 2008]. In LOT, the model is loaded by simulating the moving tyre contact forces induced by a real vehicle riding on a road. The load generator of LOT is able to simulate the loading induced by free rolling and driven wheels. More detailed information can be found elsewhere [Huurman 2008]

8.2.2.2 *STUVA Loading*

The test set-up at STUVA is a circular test track (see Figure 8.3). The load consisted of a 50 kN wheel load applied via a Good Year 425R65 super single tyre inflated up to 0.850 MPa, driving at a speed of 80km/h. The length of the contact patch of this tyre under the test conditions is 294 mm [Lopez & Steen 2007]. The tyre-pavement interaction is significantly different from a real vehicle riding on a normal road. The tyres at the STUVA set-up are forced to ride in a circle which causes the tyre to rotate around a vertical axis through the centre of the contact patch. This effect is known as turn-slip and the result is an increase of, mainly, the transversal forces and a net moment around the vertical axis [Lopez & Steen 2007]. This indicates that any simulation of the STUVA mixture load must take into account the effect of turn-slip. It also indicates that the LOT load signals that were derived from the normal vehicle riding were not useful in the simulations for the STUVA test set-up. New load signals thus became necessary.



Figure 8.3 Overview of APT at STUVA (left) and some parallelograms that combined make the test section (right)

8.2.2.3 *New insights into STUVA loading*

To obtain insight into the tyre-pavement contact stress distributions of the test set-up at STUVA, measurements and finite element modelling of the tyre-pavement contact was carried out at Eindhoven University of Technology [Lopez & Steen 2007]. This research provided ample information to simulate correctly the tyre-pavement contact at the STUVA APT section. In the following, some main findings obtained from the measurements and simulations on tyre-pavement interaction done at Eindhoven

University of Technology will be given. By combining these findings, the new loading signals for 2D idealized model to simulate the STUVA APT section were derived.

First of all, dynamic simulation results indicated that the contact forces for two different travelling velocities (1.5 km/h and 80 km/h) are identical (see Figure 8.4). Lopez and Steen thus concluded that that the inertia and damping effects due to increasing the velocity from 1.5 to 80km/h can be neglected and that the contact vertical forces can be determined from a static calculation [Lopez & Steen 2007].

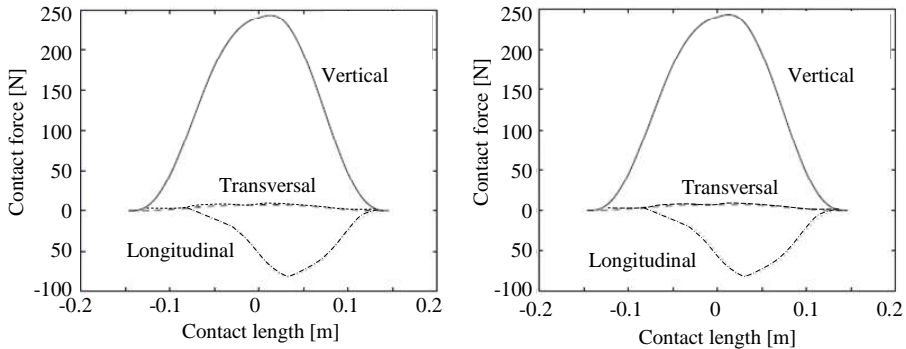


Figure 8.4 Computed tire contact forces on a square patch of 0.01m×0.01m by means of 3D finite element models (left: 1.5 km/h, right: 80 km/h) [Lopez & Steen 2007]

The second finding was that the effect of turn-slip significantly changes the contact stress distributions. Figure 8.5 gives an illustration of the slip velocities at the contact area (blue arrows) and the resulting forces acting on the road (red arrows). Figure 8.6 depicts the resulting longitudinal and transversal contact stress distributions at the tyre patch.

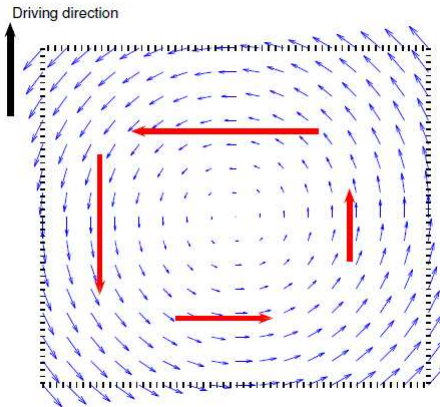


Figure 8.5 Illustration of the turn-slip velocity field (blue arrows) on the contact patch and the resulting longitudinal and transversal forces (red arrows) [Lopez & Steen 2007].

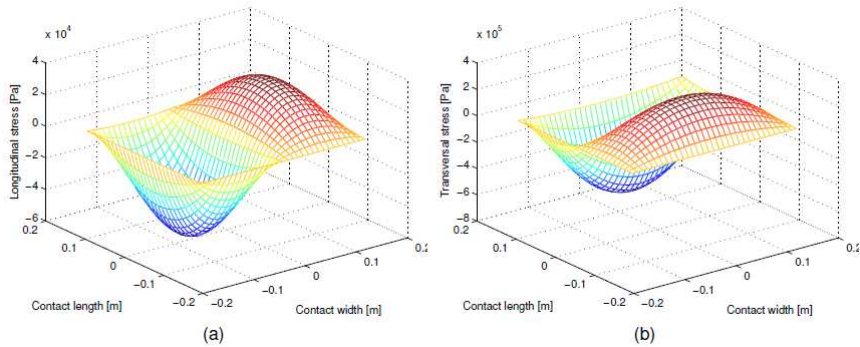


Figure 8.6 Estimated contact stress distributions due to turn-slip (a: Longitudinal stress, b: Transversal stress) [Lopez & Steen 2007]

The contact stress distributions in Figure 8.6 have further been used by Lopez and Steen to estimate the average longitudinal and transversal forces. Figure 8.7 gives the estimated results on various blocks under the tyre patch.

Combining Figures 8.4 and 8.7 lead to the 3D contact forces as applied on the STUVA accelerated pavement test sections. They are shown by the curves in Figure 8.8.

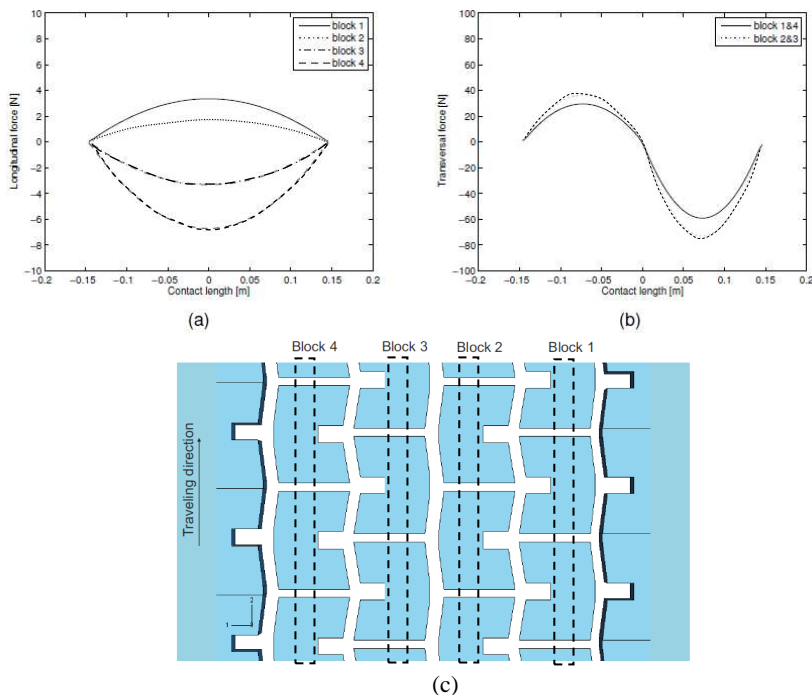


Figure 8.7 Estimated contact forces on a area of 10^{-4} m^2 due to turn-slip (a: Longitudinal stress, b: Transversal stress) and positions where the turn-slip forces have been computed (strips of 0.01 m width) [Lopez & Steen 2007]

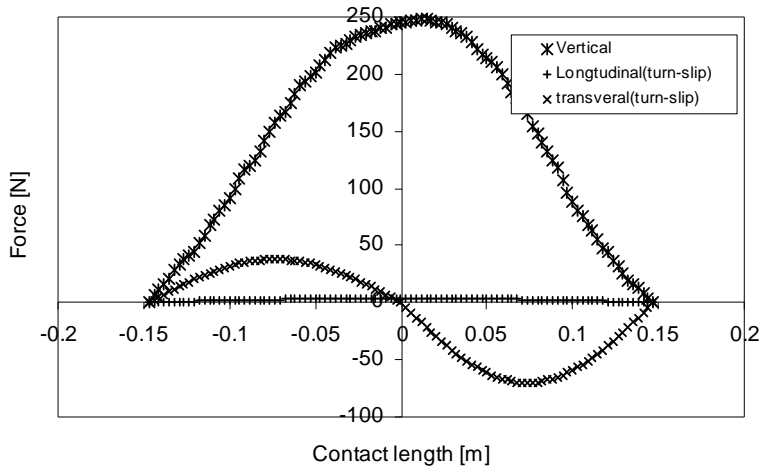


Figure 8.8 Estimated 3D contact forces for STUVA accelerated pavement test based on Lopez and Steen's research (contact area: 10^{-4} m^2)

8.2.2.3 Determination of new model loading

On the basis of the speed and tyre contact length, the corresponding loading time of the moving tyre on a certain location can be computed as 0.01323 second. In combination of 3D contact forces as shown in Figure 8.8, one can obtain the basic time functions for the vertical, longitudinal and transversal stresses to simulate the moving 3D tyre contact stresses applied on the STUVA test sections. As indicated in Figure 8.9, high values of contact pressure and shear stress were applied for simulations. This also appeared to occur in reality because during the STUVA APT, there was a lot of tyre wear. This indicates that indeed a lot of shear occurred between the tyre and pavement surface.

The 3D stress contribution can not directly be applied in the 2D idealized model. As observed in Figure 8.9, the longitudinal stress is very limited when compared with the other two directions. For this reason, only the transversal and vertical stresses were applied in the 2D idealized model.

In this study, the traffic surface loading was transferred to the forces that act on the individual stones. These forces were determined by the stresses in the transversal and vertical directions multiplied by the foot print of individual stone particles. To simulate the moving wheel loads, all of individual stone particles at the model surface are loaded simultaneously according the time functions given in Figure 8.9. In this way, a complete load cycle during a tyre passage was simulated.

Figure 8.10 gives an example of force signals on the individual particles during two tyre passages. To save the computational time, the load case applied to the model only consists of one axle and a long rest period after loading.

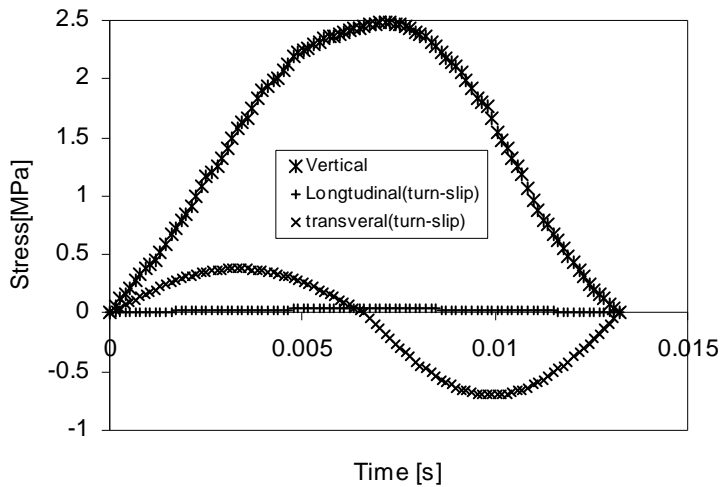


Figure 8.9 Basic time functions for simulating the vertical, longitudinal and transversal stress, respectively to simulate the moving 3D tyre contact stresses

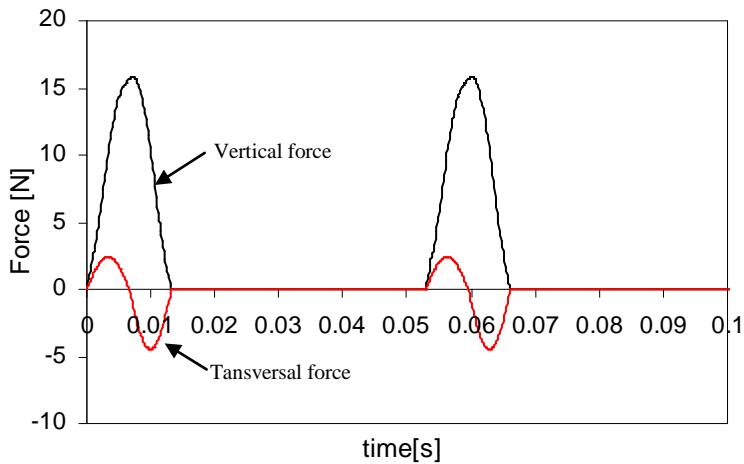


Figure 8.10 Example of load signals applied on the individual surface particles during two tyre passages

8.2.3 Material properties

8.2.3.1 Mortar response

Since the stone particles in the model are represented by rigid bodies, only the response properties of the mortar and the adhesive zone are required as input. It is known that pavement materials like porous asphalt normally have a life expectancy that is larger than 10^6 cycles. The amount of damage that accumulates during a single

load cycle is thus negligible and may be neglected in structural response calculations. For this reason a linear response model that does not incorporate damage development can be applied in the mixture response simulations. Of course this model needs to be visco-elastic, so allowing computing dissipated energy. Use was made of a two-term Prony series constitutive model [Huurman & Woldekidan 2007].

$$E(t) = E_0 \cdot \left(1 - \sum_{i=1}^2 \alpha_i (1 - \exp(-t/t_i))\right) \quad (8.1)$$

Where:

$E(t)$ = stiffness as function of time, [MPa];

E_0 = instantaneous stiffness, [MPa];

t = time, [s];

t_1, t_2 = time constants, [s];

α_1, α_2 = stiffness reduction parameters.

Use is made of parameters that were determined for LOT on the basis of 23 Direct Tension Relaxation Tests, 6 DSR frequency sweep tests, 2 DMA dual cantilever bending tests and 4 DMA uniaxial frequency sweep tests. By combining these tests a complete insight into mortar response over a range of frequencies and temperatures was obtained [Huurman & Woldekidan 2007]. It is noted that all response measurements were done on the same mortar as discussed in this thesis.

After the completion of the APT at STUVA, the actual mortar was carefully collected from hot and loose mixtures [Khedoe & Moraal 2008]. The obtained mortar was used for the preparation of mortar samples for DSR testing as described in Chapter 4. Two response measurements were carried out by means of DSR frequency sweep tests.

Figures 8.11 and 8.12 show a comparison of the rheological response between the short-term aged mortar prepared in the laboratory and the STUVA mortar obtained from the mixtures. As indicated by the master curves in these figures, one can observe that the variation between two tests that were done on the same mortar is significant thus implying that the procedure of sample preparation may play an important role. Further observation shows that the data obtained from one of the STUVA mortar samples (STUVA-2) is comparable to those obtained from one of the short-term aged mortar samples (SAM-1). Differences can only be observed in the phase angle master curves at lower frequencies. These figures also indicate that the properties of short-term aged mortar may partly overlap with the properties of the STUVA mortar, especially at relatively high frequencies.

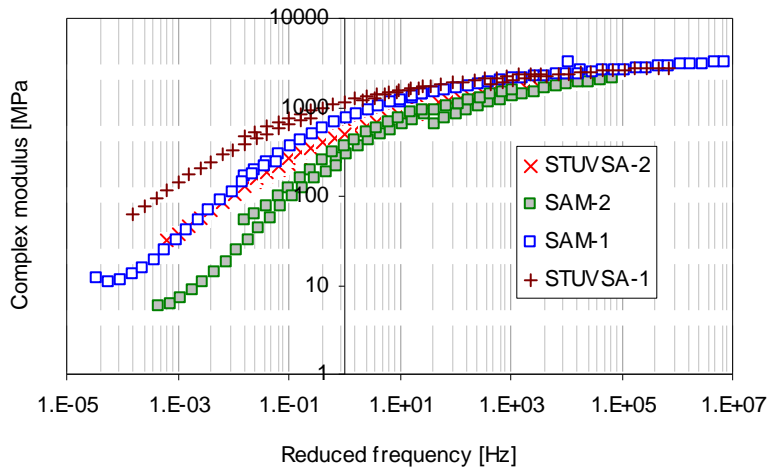


Figure 8.11 Complex modulus master curves for the short-term aged (SAM) and STUVA mortar at a reference temperature of 10°C

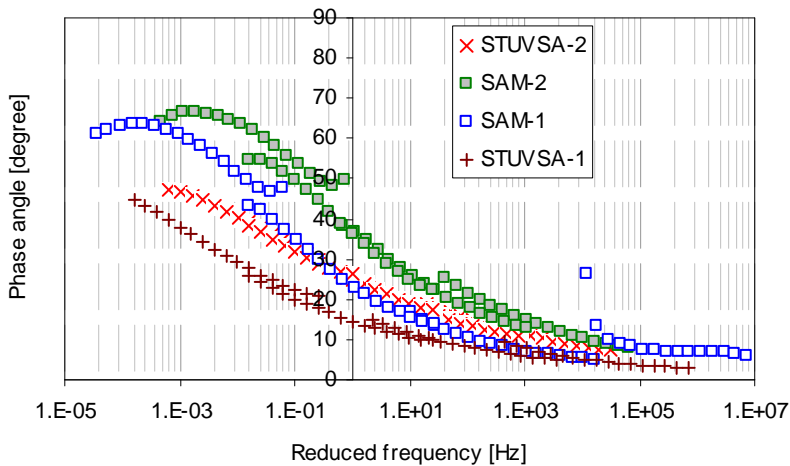


Figure 8.12 Phase angle master curves for short-term aged and STUVA mortar at a reference temperature of 10°C

As mentioned earlier, the APT at STUVA has been applied at 80 km/h and the loading time of such a moving tyre on a certain location was computed as 0.01323 second. Furthermore, it was assumed that the same period of time is needed to allow mortar completely relax after loading. Combining the loading and relaxation time resulted in the corresponding loading frequency of approximately 40Hz. This frequency was regarded as the predominant frequency for the mortar loading during

APT at the STUVA. Taking into account the frequency dependence of mortar response, the determination of the mortar properties used for the following simulations should be as accurate as possible at such a frequency window.

On the basis of the above, it was concluded that the visco-elastic behaviour of the STUVA mortar is similar to that of the short-term aged mortar at a frequency of 40Hz. At the time of writing this thesis, only a limited amount of data was available for the STUVA mortar. Based on these limited data, the accurate determination of model parameters is difficult. As a result hereof, the parameters determined from the short-term aging mortar, which was prepared in the laboratory, were used as input for the model. Table 8.3 gives the input parameters that followed from that work.

Table 8.3 Response inputs for STUVA APT simulations

Parameters	Mortar response parameters						Adhesive zone Stiffness	
	E_0	t_1	t_2	α_1	α_2	ν	k_n	k_s
Short-term aged	4250	0.016	0.311	0.9469	0.025	0.45	425000	146000

8.2.3.2 Adhesive zone Response

In LOT, the adhesive zone in the structural models is assumed to be very thin, 0.01 mm, compared to the thickness of mortar bridges which are in the order of 0.4 to 0.5 mm. As a result any relative movement between two stones translates into mortar deformation for approximately 95%, while adhesive zone deformation accounts for only 5% of the total deformation. This clearly indicates that the exact response properties of the adhesive zone are far less relevant than the response properties of the mortar. Furthermore response measurements on adhesive zones are difficult if not impossible due to difficulties in controlling the measurement and defining the adhesive zone thickness. More discussions on determination of the thickness of the adhesive zone can be found elsewhere [Huurman 2008].

Given the previous it was decided to estimate the stiffness of adhesive zones on the basis of mortar stiffness. Use is made of the following equations [Huurman 2008]. Table 8.3 lists relevant adhesive zone stiffnesses.

$$k_n = \frac{E^*}{0.01 \text{ mm}} \quad (8.2)$$

$$k_s = \frac{G^*}{0.01 \text{ mm}} \quad (8.3)$$

Where:

k_n, k_s = normal and shear stiffness of the adhesive zone, [MPa/mm].

8.3 Material fatigue and damage models

8.3.1 Mortar fatigue model

Similar to the STUVA mortar response measurements, the real mortar obtained from the STUVA mixtures was used to prepare the mortar specimens for DSR fatigue testing as described in Chapter 4. Only a limited amount of fatigue tests was done on

the STUVA mortar [Khedoe & Moraal 2008]. The fatigue behaviour of the STUVA mortar was compared with the fatigue data of the laboratory prepared mortar. As shown in Figure 8.13, the fatigue behaviour of the STUVA mortar can be well predicted by the fatigue model that was determined on the basis of short-term aged mortar fatigue data except for one data point. From this it was concluded that the fatigue behaviour of the STUVA mortar is comparable with the one of the laboratory prepared short-term aged mortar. Table 8.4 gives the parameters of the fatigue model that may represent the STUVA mortar.

Table 8.4 Parameters of the fatigue model for the STUVA mortar

Temperature [°C]	Material combination	W_0 [MPa]	b [-]	Mixtures
10	Short-term aged mortar	0.518	2.760	A, B, C, D

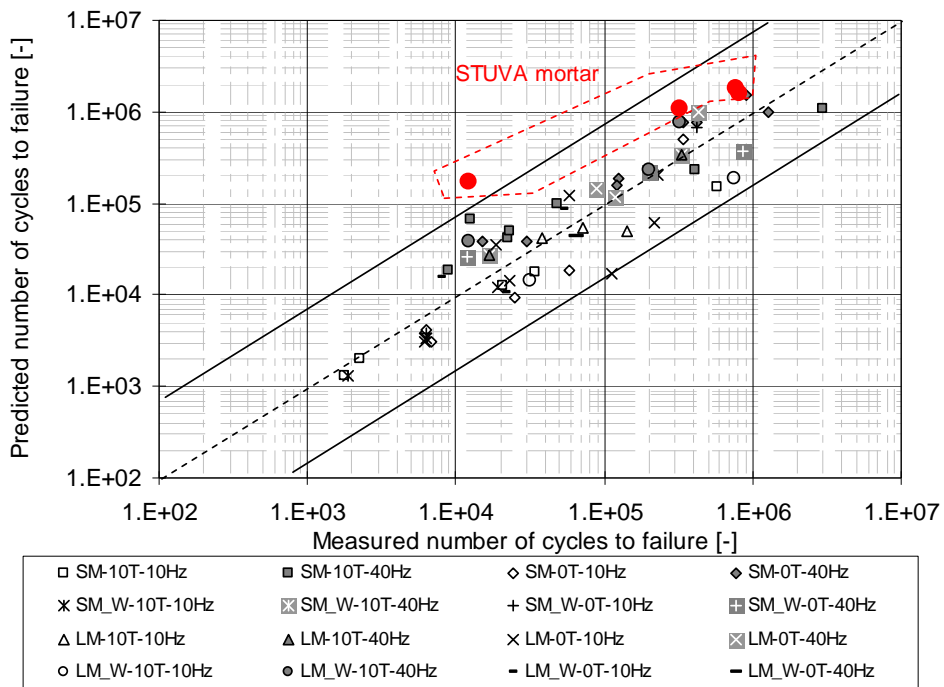


Figure 8.13 Fatigue behaviour of the STUVA mortar in relation to laboratory prepared mortar (SM: short-term aged mortar; LM: long-term aged mortar; W: water conditioning; 0T and 10T: test temperatures of 0°C and 10°C; 10Hz and 40Hz: test frequencies)

8.3.2 Adhesive zone damage model

At the time of writing this thesis, information on the fatigue behaviour of the real STUVA adhesive zones was not available. It was foreseen that it is difficult or

impossible to drill a core with diameter of 3mm and height of 10 mm from a real porous asphalt concrete. Testing on such a small specimen is believed to be troublesome. Furthermore, translation of the test results into material stress becomes impossible since the geometry of the real adhesive zone is very complex and thus remains unknown. Due to the limitations mentioned above, use was made of the damage model that was developed on the basis of the laboratory prepared adhesive zone data. Considering the fact that the APT at the STUVA was done under a controlled surface temperature of the test section of 10°C and that the STUVA mixtures were not subjected to long-termed aging, it was assumed that the behaviour of the STUVA adhesive zones should approach the behaviour of laboratory prepared short-term aged adhesive zones. Table 8.5 lists the adhesive zone damage model parameters applicable for the STUVA adhesive zones.

Table 8.5 Model parameters of the adhesive zones

Temperature [°C]	Material combination	σ_0 [MPa]	n [-]	ϕ [degree]	Mixture
10	B+SB	14.53	3.09	33.1	C, D
	G+SB	10.99	3.55	30.1	A, B

Note: B+SB=Sandstone + short-term aged bitumen; G+SB= Greywacke + short-term aged bitumen

8.4 Results and discussions

In the 2D idealized model, the main particle of interest is the central particle on the upper row. Since this particle is far away from the model boundaries, the effect of boundary conditions on the computational results is expected to be relatively small. This stone particle has four contacts with the surrounding material. Each contact is numbered based on its location, as presented in Figure 8.14. As indicated by the red dots in the centre of each contact, four nodes are standing for the mortar bridges and are selected for stress analysis. Similarly, four nodes standing for the adhesive zones are also selected at the stone-mortar interface. Due to very limited thickness, the adhesive zone is not visible in this figure. Hereafter, the analysis will focus on these eight nodal locations as indicated in Figure 8.14.

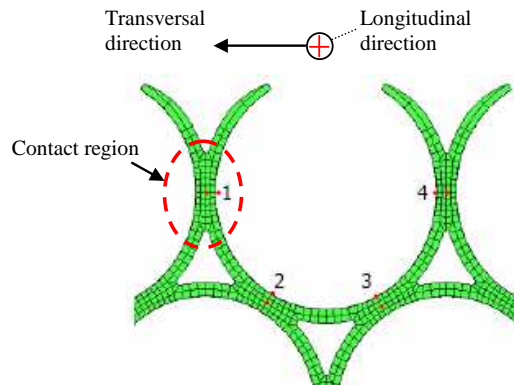


Figure 8.14 Four contacts of the central stone particle and the selected nodal

locations for stress analysis [Huurman 2008; Huurman & Mo 2007]

8.4.1 Life estimation based on adhesive zone damage

The finite element modelling of the STUVA mixtures provided the development of relevant stress components during a tyre passage. Figure 8.15 gives an example of adhesive zone stresses. The corresponding development of the equivalent tension stress and the evolution of the damage are given in Figure 8.16.

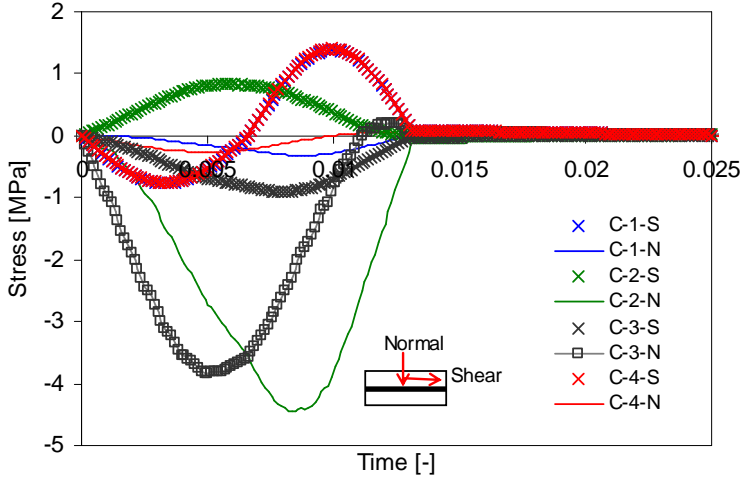


Figure 8.15 Normal and shear stress development during a tyre passage on the basis of the simulation on Mixture D with 18% void content (C-1, 2, 3, and 4: Contact number as indicated in Figure 8.15; S: shear stress; N: normal stress.)

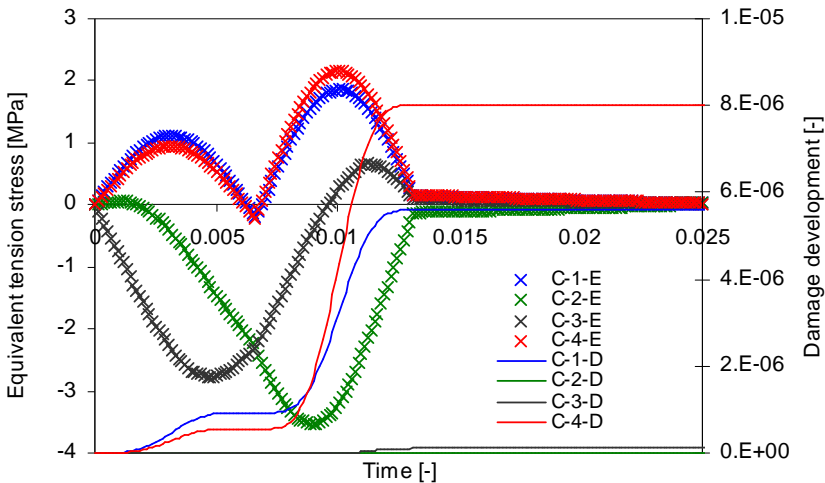


Figure 8.16 Corresponding equivalent tension stress and damage development on the basis of the stress signals given in Figure 8.15. (C-1, 2, 3, and 4: Contact number

as same as in Figure 8.15; E: Equivalent tension stress; D: damage development.)

In Figure 8.16, the equivalent tension stress that represents the combination effect of normal and shear stresses at any given time is determined as follows.

$$\sigma_e(t) = \sigma_n(t) + \frac{|\tau(t)|}{tg\phi} \quad (8.4)$$

Where:

σ_e = equivalent tensile stress, [MPa];

σ_n = normal stress, [MPa], (- for compression and + for tension);

τ = the shear stress, [MPa];

ϕ = the internal friction angle, [°];

t = time, [s].

The damage development is then determined by the sum of the various damage increments.

$$D(t) = \sum_{i=1}^m \left[\frac{\sigma_e(t_{i+1}) + \sigma_e(t_i)}{2\sigma_0} \right]^n \times \Delta t \quad \text{for } [\sigma_e(t_{i+1}) + \sigma_e(t_i)] > 0 \quad \text{otherwise } D(t) = 0 \quad (8.5)$$

Where

$D(t)$ = the accumulated damage at time $t = \sum_{i=1}^m t_i$;

$\sigma_e(t_i)$ = the equivalent tensile stress at time t_i , [MPa];

$\sigma_e(t_{i+1})$ = the equivalent tensile stress at time t_{i+1} , [MPa];

Δt = $t_{i+1} - t_i$, the time increment, [s],

σ_0 = model parameter, [MPa];

n = model parameter.

The life expectancy of the adhesive zone is determined by the reciprocal of the cumulative damage in one cycle.

$$N = \frac{1}{D(1)} \quad (8.6)$$

Where

N = predicted life expectancy, [repetition];

$D(1)$ = the accumulative damage in one repetition.

On the basis of the above, the life expectancies of various mixtures with various void contents are summarised in Table 8.6. As indicated in this table, the computed life expectancies vary strongly at various contacts even for the same simulation. Among these four contacts, Contact 4 is the most critical location having the maximum damage accumulation and thus the smallest life expectancy in all of the cases. It indicates that failure will occur firstly at Contact 4 and thus the life expectancy of Contact 4 is responsible for the initiation of loss of stone, i.e. ravelling. For this reason, this critical contact is taken into account in the following discussions.

Table 8.6 Summary of the computed life expectancies of various mixtures with various void contents

Mixture	Void content	Damage Life	Contact 1	Contact 2	Contact 3	Contact 4
A (Greywacke)	18%	D(1)	5.851E-06	3.045E-11	1.269E-08	1.086E-05
		N	1.709E+05	3.284E+10	7.877E+07	9.207E+04
	20%	D(1)	9.229E-06	4.270E-11	2.029E-08	1.373E-05
		N	1.083E+05	2.342E+10	4.929E+07	7.283E+04
	23.25%	D(1)	1.404E-05	5.271E-08	2.788E-06	2.160E-05
		N	7.124E+04	1.897E+07	3.600E+05	4.630E+04
B (Greywacke)	18%	D(1)	1.013E-05	1.862E-08	5.311E-07	1.479E-05
		N	9.874E+04	5.370E+07	1.883E+06	6.761E+04
	20%	D(1)	1.145E-05	5.050E-11	1.431E-07	1.689E-05
		N	8.737E+04	1.980E+10	6.988E+06	5.922E+04
	23.25%	D(1)	2.965E-05	1.794E-10	5.906E-07	4.464E-05
		N	3.372E+04	5.574E+09	1.693E+06	2.240E+04
C (Sandstone)	18%	D(1)	4.258E-06	4.279E-11	1.004E-07	6.026E-06
		N	2.349E+05	2.337E+10	9.956E+06	1.659E+05
	20%	D(1)	5.290E-06	6.055E-11	1.393E-07	7.497E-06
		N	1.890E+05	1.652E+10	7.179E+06	1.334E+05
	23.25%	D(1)	8.119E-06	6.896E-10	5.029E-07	1.224E-05
		N	1.232E+05	1.450E+09	1.988E+06	8.173E+04
D (Sandstone)	18%	D(1)	5.601E-06	4.208E-11	1.044E-07	8.009E-06
		N	1.785E+05	2.377E+10	9.582E+06	1.249E+05
	20%	D(1)	6.686E-06	4.203E-11	1.422E-07	9.524E-06
		N	1.496E+05	2.379E+10	7.034E+06	1.050E+05
	23.25%	D(1)	1.526E-05	2.625E-10	4.975E-07	2.219E-05
		N	6.552E+04	3.809E+09	2.010E+06	4.506E+04

Based on the data listed in Table 8.6, the relationship of life expectancies versus void contents for different mixtures can be established. Figure 8.17 shows the critical life expectancies that are plotted against the void contents. As mentioned earlier, the

2D idealized model is not capable of making simulations for mixtures with void contents above 23.5%. Due to this limitation, simulations on Mixtures A, B and D with void contents 24.3%, 27.4 and 25.0% respectively are impossible. As a result, use is made of extrapolation on the basis of data obtained from the simulations with void contents below 23.5%. The obtained void content versus life expectancy relationships are indicated by the dashed lines drawn in Figure 8.17., the life expectancies due to adhesive failure of the STUVA mixtures can be estimated by plotting the void content of the STUVA mixtures in the relationships (see the solid points in Figure 8.17). Table 8.7 lists the life expectancies of the STUVA mixtures at their actual void contents. The relationship between the predicted life expectancies and the observed ravelling damage after APT at the STUVA will be discussed latter.

Table 8.7 The estimated life expectancies of the STUVA mixtures on the basis of the actual achieved void contents

Mixture	A	B	C	D
Achieved void content [%]	24.3	27.4	21.6	25.0
Life expectancy [cycle]	2.00E+04	4.50E+03	1.05E+05	2.50E+04
Ranking [-]	3	4	1	2

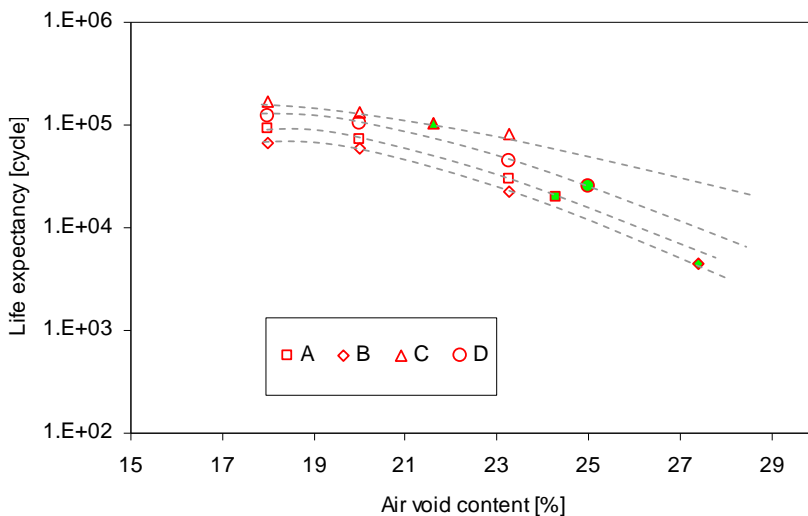


Figure 8.17 Relationship between life expectancy and void content (dashed curves) and estimation of the life expectancies for the STUVA mixtures based on the actual achieved void contents (green solid points)

8.4.2 Life estimation based on mortar fatigue

Similarly, the finite element modelling of the STUVA mixtures provided the

development of relevant mortar stress and strain components during a tyre passage. Figure 8.18 gives an example of mortar stresses. When these stresses are plotted against the respective strains, one can obtain the stress-strain hysteretic loops as indicated in Figure 8.19.

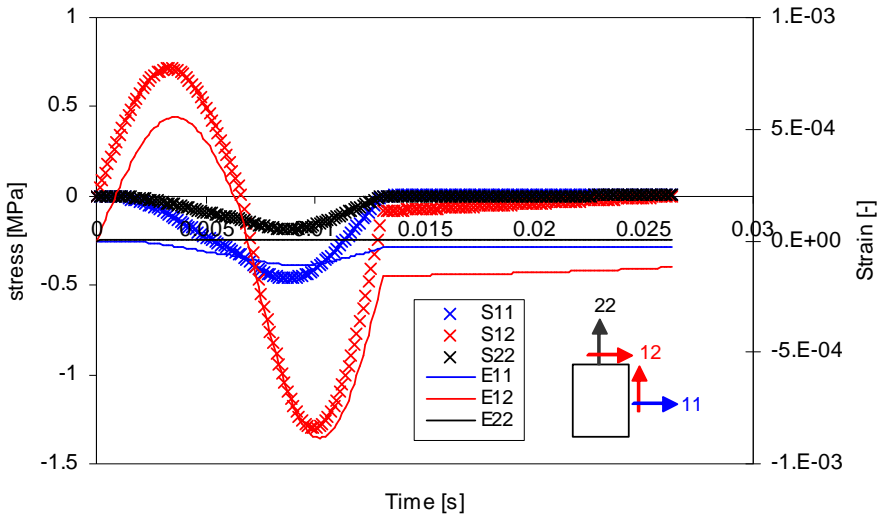


Figure 8.18 Example of stress and strain development in the mortar bridge during the tyre passage (Contact 1 of Mixture D with 18% void content)

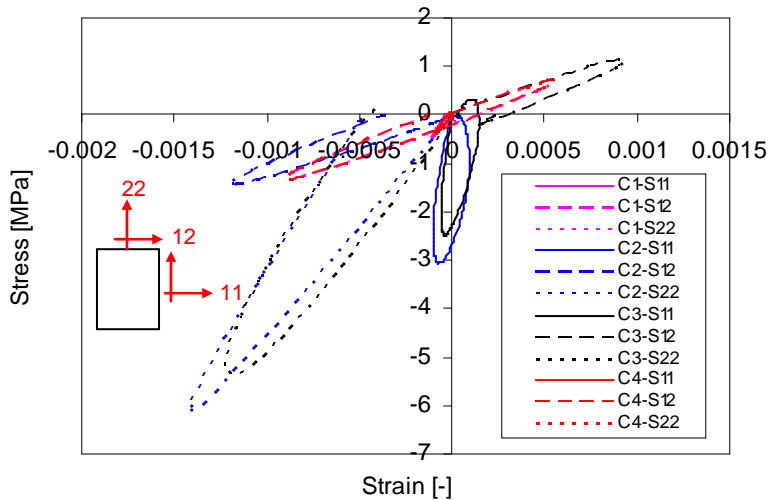


Figure 8.19 Example of stress-strain hysteretic loops at various mortar bridges based on the simulation of Mixture D with 18% void content (C1, 2, 3 and 4: contact number; S11, 12 and 22: stress components)

As discussed in the previous chapter, the initial dissipated energy per cycle is used as an indication of the fatigue damage. High levels of initial dissipated energy per cycle indicate that the mortar is subjected to high stress levels and thus can only withstand a small amount of repetitions before failure, whereas a very low initial dissipated energy per cycle indicates that the mortar can withstand a very large number of repetitions before fatigue failure. The relationship between the initial dissipated energy per cycle and the number of cycles to fatigue can be explained as follows.

$$N = \left[\frac{W_{initial_cycle}}{W_0} \right]^{-b} \quad (8.7)$$

Where:

W_0 = the energy limit, [MPa];

$W_{initial_cycle}$ = the total dissipated energy per cycles during the initial stage, [MPa];

b = model constant.

In the case of 2D fatigue loadings in the simulations of various mixtures hereafter, $W_{initial_cycle}$ is equal to the sum of the dissipated energies W_{ij} from all of the three stress components. Based on the stress and strain signals obtained from finite element simulations, the value of $W_{initial_cycle}$ can be determined by the total area of various hysteretic loops.

$$W_{initial_cycle} = \sum W_{ij} = \int \sigma_{ij} d\varepsilon_{ij} = \sum \left[\frac{\sigma_{ij}(t + \Delta t) + \sigma_{ij}(t)}{2} \right] \times [\varepsilon_{ij}(t + \Delta t) - \varepsilon_{ij}(t)] \quad (8.8)$$

Where:

σ_{ij} = stress components, [MPa];

ε_{ij} = strain components.

On the basis of the above, the life expectancies due to cohesive failure within the mortar bridges were calculated and the results are summarised in Table 8.8. As indicated in this table, the computed life expectancies in the mortar bridges vary strongly dependent on the contact locations. Among these four contacts, Contact 2 is the most critical location having the maximum dissipated energy and thus the smallest life expectancy in all of the cases. It indicates that failure will occur firstly at Contact 2 and thus the life expectancy of Contact 2 is responsible for the initiation of loss of stone, i.e. ravelling, in case of cohesive failure. For this reason this critical contact is considered in discussions following hereafter.

Table 8.8 Summary of life expectancies of the mortar bridges

Mixture	Void content	Energy Life	Contact 1	Contact 2	Contact 3	Contact 4
A (Greywacke)	18%	Wini	2.79E-04	2.58E-03	1.94E-03	2.79E-04
		N	1.05E+09	2.27E+06	4.95E+06	1.06E+09
	20%	Wini	3.15E-04	2.91E-03	2.20E-03	3.14E-04
		N	7.51E+08	1.63E+06	3.52E+06	7.59E+08
	23.25%	Wini	4.71E-04	5.03E-03	2.67E-03	4.69E-04
		N	2.48E+08	3.60E+05	2.06E+06	2.50E+08
B (Greywacke)	18%	Wini	3.26E-04	2.28E-03	1.75E-03	3.26E-04
		N	6.84E+08	3.18E+06	6.64E+06	6.86E+08
	20%	Wini	3.59E-04	2.89E-03	2.21E-03	3.58E-04
		N	5.24E+08	1.66E+06	3.50E+06	5.27E+08
	23.25%	Wini	6.21E-04	5.19E-03	3.92E-03	6.19E-04
		N	1.15E+08	3.30E+05	7.13E+05	1.17E+08
C (Sandstone)	18%	Wini	2.44E-04	2.07E-03	1.58E-03	2.43E-04
		N	1.53E+09	4.18E+06	8.81E+06	1.54E+09
	20%	Wini	2.77E-04	2.36E-03	1.81E-03	2.76E-04
		N	1.07E+09	2.88E+06	6.05E+06	1.08E+09
	23.25%	Wini	4.91E-04	4.16E-03	3.23E-03	4.84E-04
		N	2.21E+08	6.05E+05	1.22E+06	2.30E+08
D (Sandstone)	18%	Wini	3.05E-04	2.51E-03	1.92E-03	3.05E-04
		N	8.20E+08	2.44E+06	5.15E+06	8.24E+08
	20%	Wini	3.38E-04	2.74E-03	2.09E-03	3.37E-04
		N	6.19E+08	1.92E+06	4.04E+06	6.23E+08
	23.25%	Wini	5.89E-04	4.93E-03	3.81E-03	5.87E-04
		N	1.34E+08	3.81E+05	7.70E+05	1.35E+08

Similarly, the relationship of life expectancies induced by cohesive failure at various void contents for different mixtures was also established. Figure 8.20 shows the critical life expectancies of mortar bridges that are plotted against the void contents. Again, due to the limitations of the 2D idealized model, the life expectancies of mortar of the STUVA mixtures have been estimated by means of extrapolation. The life expectancies of the mortar bridges of the STUVA mixtures are indicated by the green solid points. The number of load repetitions is given in Table 8.9. The relationship between the predicted life expectancies of the mortar bridges and the ravelling damage after APT at the STUVA will be discussed in combination with the life expectancies of the adhesive zones. This is because ravelling will only occur in the weakest link in the stone contact region, e.g. adhesive failure or cohesive failure.

Table 8.9 Mortar life expectancies for the STUVA mixtures taking into account the achieved void contents

Mixture	A	B	C	D
Achieved void content [%]	24.3	27.4	21.6	25
Life expectancy [cycle]	2.00E+05	4.00E+04	1.40E+06	1.50E+05
Ranking [-]	2	4	1	3

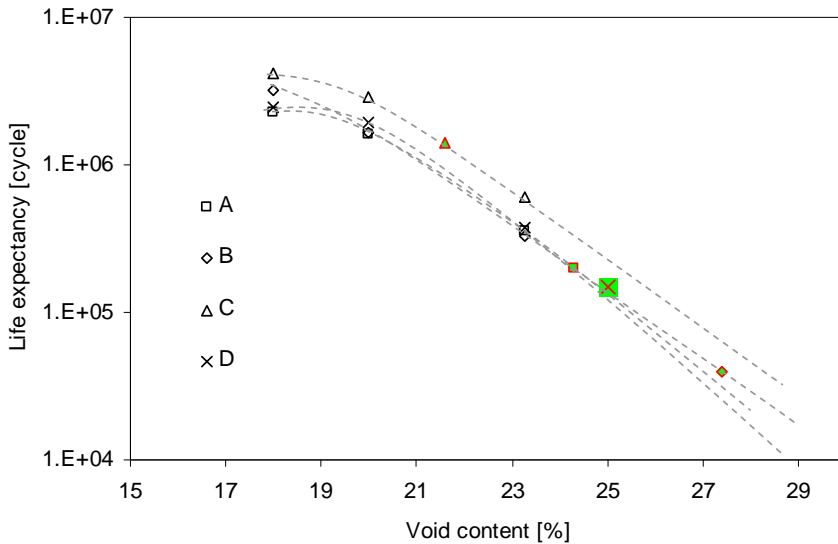


Figure 8.20 Relationship between mortar life expectancy and void content

8.4.3 Causes of ravelling

8.4.3.1 Adhesive failure vs cohesive failure

As discussed in the previous sections, the life expectancies of the mortar bridges and the adhesive zones were estimated. By comparing these two, the weak link with respect to ravelling was obtained. Table 8.10 gives the life expectancies of the adhesive zones against those of the mortar bridges. As indicated, the life expectancies of the adhesive zones are an order of magnitude smaller than the life expectancies of the mortar bridges for all of the STUVA mixtures. At this point, the adhesive zone seems to be more decisive for ravelling compared to the mortar bridges.

Table 8.10 Life expectancies of the adhesive zones against the mortar bridges

Mixture	A	B	C	D
Adhesive zones life expectancy ⁽¹⁾	2.00E+04	4.50E+03	1.05E+05	2.50E+04
Mortar life expectancy ⁽²⁾	2.00E+05	4.00E+04	1.40E+06	1.50E+05
Life ratio ^{(2)/(1)}	10.0	8.9	13.3	6.0
Type of failure [-]	Adhesive Failure	Adhesive failure	Adhesive failure	Adhesive failure
Critical life expectancy	2.00E+04	4.50E+03	1.05E+05	2.50E+04

Table 8.11 gives a comparison of fatigue lives of the mortar, adhesive zone and stone mortar-stone system at 10°C. The laboratory fatigue test data show that either the fatigue life of the stone-mortar-stone specimen or the fatigue life of the adhesive zone is much smaller than the life of the mortar. This means that failure may not firstly happen in the undisturbed mortar when it is subjected to the same/similar stress level as the adhesive zone. It should be noted that the stone-mortar-stone system represents an idealized stone contact region. The failure of such a system after being subjected to shear fatigue was examined and it was found that the system failed at a location which was very close to the stone surface. This type of failure can be defined as cohesive failure in the bitumen interlayer rather than in the mortar. More information is given to Chapter 4.

Table 8.11 Comparison of fatigue lives of the mortar, adhesive zone and stone mortar-stone system at 10°C

Test conditions	Shear stress	Stone-mortar-stone system	Adhesive zone	Mortar
	MPa	N ₁	N ₂	N ₃
B_SB_10°C	1.296	2.22E+03	3.00E+04	1.10E+07
B_LB_10°C	1.296	6.42E+03	2.00E+04	4.30E+07
B_SB_W_10°C	1.296	1.74E+03	9.00E+03	8.50E+06
G_SB_10°C	1.296	2.07E+03	4.20E+03	1.10E+07
G_LB_10°C	1.296	1.92E+03	5.20E+03	4.30E+07
G_SB_W_10°C	1.296	1.44E+03	4.05E+03	8.50E+06

Figure 8.21 gives a comparison of the short-term aged mortar, the adhesive zones and the stone-mortar-stone system tested at 10°C. The computational results indicate that the shear stresses in the adhesive zones and mortar bridges are in the order of 1.5 to 3MPa. Combining this with the fatigue data shown in Figure 8.21, one can observe that the adhesive zone is more punished than the mortar bridge at such a stress level.

The discussions given above indicate that among the material components in the contact region where the mortar binds the stone columns together, the adhesive zone tended to be the weak link to ravelling. However, it must be noted that this is based on

some specific conditions, especially for specimen preparation and simulations on idealized mixtures in this study. In reality, the geometry of the stone contact region is complex and the stress state differs significantly from the idealized specimens tested in the laboratory. As a result, failure may have various choices of location. Therefore, validation of the weak link observed in the laboratory should compare with the actual pavement performance.

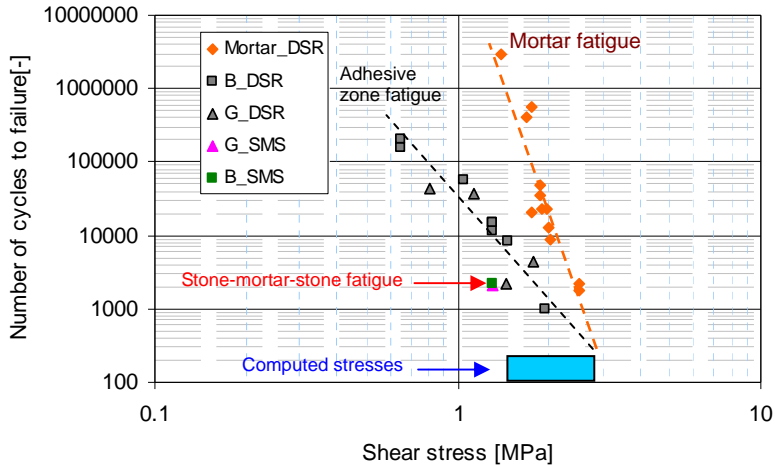


Figure 8.21 Compare DSR fatigue data among the mortar, adhesive zone (B_DSR, G_DSR) and stone-mortar-mortar system (G_SMS, B_SMS) at 10°C and short-termed aging

8.4.3.2 Effect of void content

Figure 8.22 gives the general trends of the computed life expectancy of the adhesive zones and mortar bridges on increased void contents. It should be noted that there are many factors that can influence the void content in porous asphalt concrete. Among these factors, the aggregate grading and bitumen content are important issues as well as the degree of compaction. Given a controlled grading and bitumen content, the obtained void content is directly related to the degree of compaction. High void contents indicate poor compacted asphalt concrete, while low void contents indicate well or over compacted asphalt concrete.

In Figure 8.22, only the effect of degree of compaction is considered. The simulations were done by using a constant aggregate grading and bitumen content, while different void contents were taken into account. As observed, the mortar life expectancy is more sensitive to void content compared with the adhesive zone life expectancy. As a result, the types of failure that may occur shifts from adhesive failure to cohesive failure when the void content is beyond the critical void content as indicated in Figure 8.22. This indicates that porous asphalt mixtures with high degrees of compaction tend to fail in adhesive zone (adhesive failure), while those with low degrees of compaction tend to fail in the mortar bridge (cohesive failure).

The above also indicates that LOT can serve as a tool for the purpose of quality control of mixtures. In this case, the desired void content after compaction should not be in the susceptible range at which life expectancy is changing rapidly. As indicated in Figure 8.22 the life expectancy reduces to 14% for the mortar bridge and 43% for the adhesive zone as the void content increases from 18% to 23.25%. Molenaar and Meerkerk et al. (2006) conducted a study on the performance of the single layer porous asphalt concrete based on the SHRP-NL database and found that the void content lower than 24% is critical to prevent premature ravelling within 5 years. Combining the computed results and the actual performance of porous asphalt leads to the conclusion that the critical void content responsible for the premature ravelling exists and LOT may use to explain this phenomenon. It should be noted that this critical void content may depend on the type of porous asphalt, i.e. PA11/16 or PA 4/8. In any case, the model results must be validated by means of the real mixture ravelling performance.

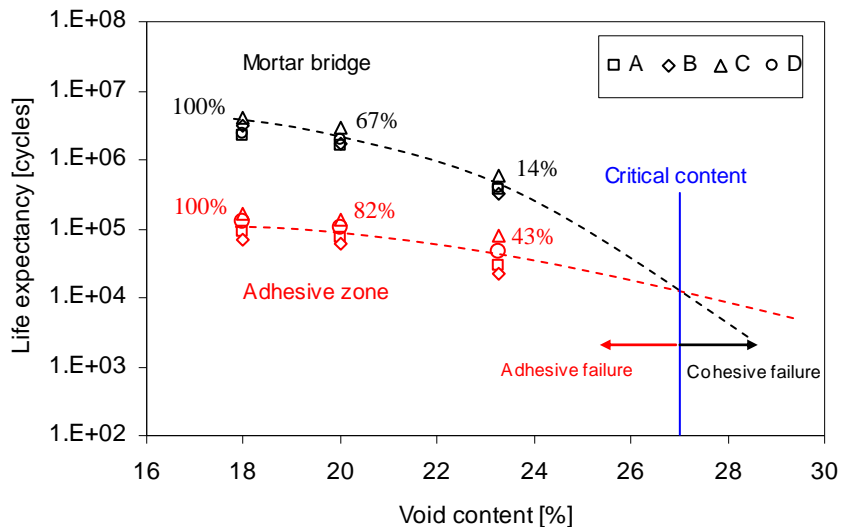


Figure 8.22 General trends of the computed life expectancies of the adhesive zones and mortar bridges (A, B, C and D: type of mixture)

8.4.4 Ravelling damage prediction

In this section, the relationship between the computed life expectancy and the measured ravelling in the STUVA mixtures will be discussed.

During the APT, a total of 700,000 wheel load repetitions were applied to the four different types of mixtures discussed above. The test conditions were 10°C without considering the effects of water ingress and long-term aging of binder. During application of the 700,000 repeated loadings ravelling developed. At the end of the APT the ravelling damage of each section was determined by means of two independent methods [RWTH 2007]. The first method is based on interpretation of highly accurate texture measurements. Figure 8.23 gives an example of surface

texture after APT. Due to local loss of aggregate the surface texture will become rougher. From the difference of between the initial texture and the texture after 700,000 cycles the so-called *Integral der differenzen(IDD)* was computed from the laser data. This IDD is a commonly used measure for ravelling damage and larger IDD indicates larger change of texture and thus more ravelling damage [RWTH 2007; Hurman & Molenaar 2008].

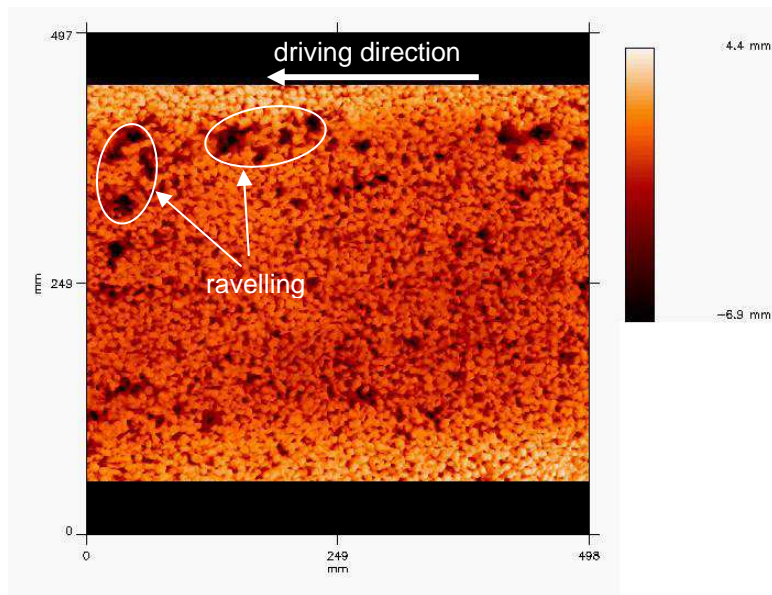


Figure 8.23 Impression of ravelling damage after APT [RWTH 2007]

The second method is a visual inspection conducted by a Dutch qualified inspector. In this approach the wheel track in each section was subdivided in smaller subsections. For each subsection an assessment of ravelling damage was made and a damage value was assigned accordingly (see Table 8.12). More detailed information is given in Appendix 8.1.

Table 8.12 Relation between ravelling assessment and damage value [RWTH 2007;Huurman 2008; Miradi 2009]

Damage value	Ravelling assessment and percentage of ravelling
0	No damage
L=1	Light damage, incidental loss of stone, 6-10%
M=2	Moderate damage, loss of one or more clusters of stone, 11-20%
E=3	Severe damage, continuous track of stone loss, >20%

Table 8.13 gives a summary of the computational results and the ravelling damage assessment. Figure 8.24 shows a comparison between the computed life expectancy

and the ravelling damage after 7×10^5 load cycles. In this figure, the results of texture measurement and visual inspection are plotted against the lives computed for these four types of mixtures. As observed, the general trend is that the shorter the predicted life, the more the damage is introduced to that mixture during the ravelling test. The largest deviation from this trend is observed for Mixture A in the case of the texture measurement. The trend of computed life is in good agreement with ravelling assessment by means of visual inspection.

Table 8.13 Summary of the calculated life expectancy and the damage assessment after 7×10^5 load cycles

Mixture	Ravelling evaluation [RWTH 2007]			Model simulation	
	Integral der differenzen, IDD [mm]	Visual inspection [-]	Ranking [-]	Computed Life [cycle]	Ranking [-]
A	0.0367	21	3	$2.00E+04$	3
B	0.0423	32	4	$4.50E+03$	4
C	0.0116	16	1	$1.05E+05$	1
D	0.0266	21	2	$2.50E+04$	2

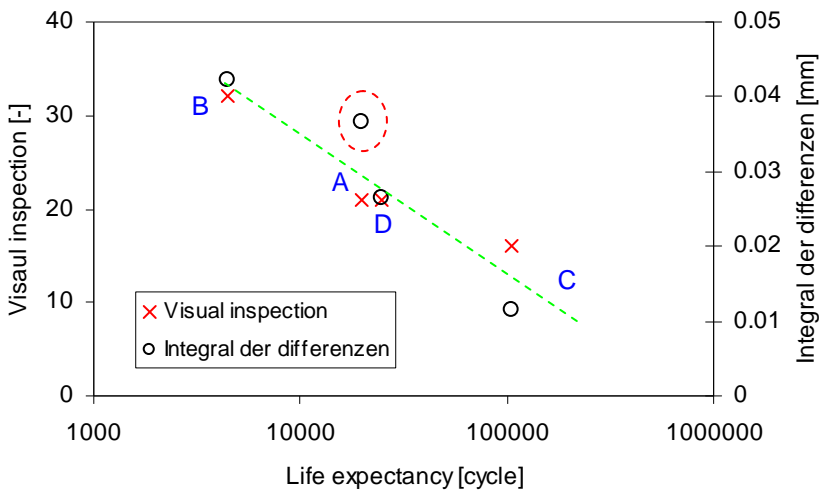


Figure 8.24 Comparison between the computed life and the ravelling damage after 7×10^5 load cycles

8.4.5 Prediction of lifespan and the maintenance moment

LOT simulations on porous asphalt will provide the life expectancy on the critical contact point. The process of damage propagation leading to the actual loss of stone

and visible damage is not incorporated in the model. As a result, the computed life expectancy gives an indication of the initiation of ravelling damage. However, compared with 7×10^5 load cycles during the STUVA APT, the computed life expectancy of the best mixture is only approximately 1×10^5 cycles. Furthermore, ravelling developed during the APT at the STUVA and after 7×10^5 load cycles the tested mixtures did not completely ravel. The above indicates that the computed life expectancy does not directly relate to either the lifespan or the maintenance moment. It was felt that the real lifespan and the maintenance moment may be much longer than the computed life expectancy. Therefore, it is of great interest to correlate the computed life expectancy to the real lifespan (time to mill old porous asphalt and lay new porous asphalt) or the moment for preventive and/or temporary maintenance.

In real pavements ravelling damage develops over years of trafficking. For a pavement with a 12-year service life, the first piece of surface stone may well ravel away within the first month of trafficking. The previous indicates that ravelling is a visual damage that slowly develops in real pavements. In order to predict ravelling damage for pavement preservation, the following two questions need to be answered.

- When does ravelling start? The answer to this question allows determining the time for preventive maintenance.
- What is the evolution of ravelling damage as a function of pavement service life? The answer to this question enables to estimate the time for temporary maintenance and the time for resurfacing.

With respect to the first question, LOT may serve as a tool to predict the initiation of ravelling. Combining LOT computed life with a model that is capable to explain the evolution of ravelling damage, the real lifespan and the moment of maintenance become predictable. Of course, this is very useful for planning pavement preservation strategies.

In the following, a ravelling evolution model is proposed based on the relationship between the amount of ravelling and the age of the top porous asphalt layers. By defining the degree of damage at the moment that ravelling initiates the proposed ravelling evolution model is capable to estimate the lifespan and the moment of maintenance.

8.4.5.1 Ravelling evolution in real pavements

Figure 8.25 gives an example of the amount of ravelling in relation to the age of porous asphalt surface layers. More data can be found elsewhere [Miradi 2009]. The cumulative lifespan distribution of porous asphalt as determined by the Road and Hydraulic Engineering Division (RHED) of the Dutch Ministry of Transport is also given in Figure 8.26. It should be noted that ravelling is decisive for the lifespan of porous asphalt in most of the cases. Therefore, the curve of cumulative lifespan distribution also gives an indication of ravelling development over the years.

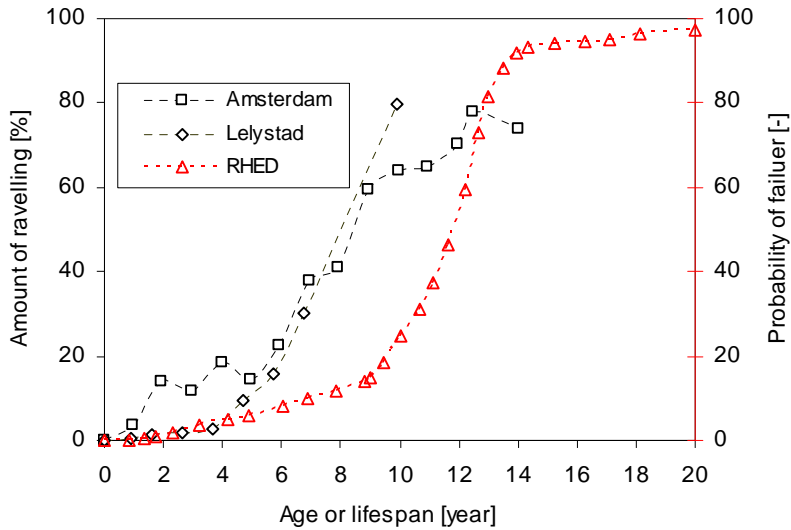


Figure 8.25 Amount of ravelling in relation to the age of porous asphalt layers (Amsterdam: 84.7Km main road; Lelystad: 2.35.9Km main road.) and the cumulative lifespan distribution as determined by RHED [Miradi 2009]

8.4.5.2 Ravelling evolution model

A ravelling evolution model has been reported on the basis of SHRP-NL database [Sweere 1995].

$$\ln\left(\frac{Raf}{100 - Raf}\right) = \beta_0 + \beta_1 \times Lft \quad (8.9)$$

Where:

- Raf = percentage of ravelling, $0 < Raf < 100$, [%];
- Lft = serve life, [year];
- β_0, β_1 = model parameters.

Similarly, the following model was used to explain the ravelling evolution in the STUVA APT sections.

$$\ln\left(\frac{Raf}{100 - Raf}\right) = \beta_0 + \beta_1 \times N \quad (8.10)$$

At the time of writing this thesis, the actual amount of ravelling Raf in the STUVA APT is unavailable. Indication was that Raf might be expressed by means of IDD using the following equation

$$Raf = \frac{IDD}{IDD_0} \times 100 \tag{8.11}$$

Where:

IDD_0 = the reference value IDD at which $Raf = 100$, [mm].

As indicated in Table 8.13, the total score for each mixture varies from 16 to 32 after 700000 load repetitions. It should be noted that this total score of visual inspection is the sum of 24 subsections which are assigned by a damage weight varying from 0 to 3 (see Appendix 8.10). As a result, the total score of 24, 48 and 72 is directly related to light, moderate and severe damage, respectively (see Figure 8.26).

Figure 8.26 shows the linear relationship between the total score and IDD. Furthermore, an average of the amount of ravelling is assigned to each level of ravelling damage. By doing this, one can obtain that the IDD value responsible for severe damage, i.e. $Raf = 30\%$ was determined as 0.0955mm. Based on a linear rule, the IDD_0 value accounting for completely ravelling, $Raf = 100\%$ was thus determined as 0.318mm.

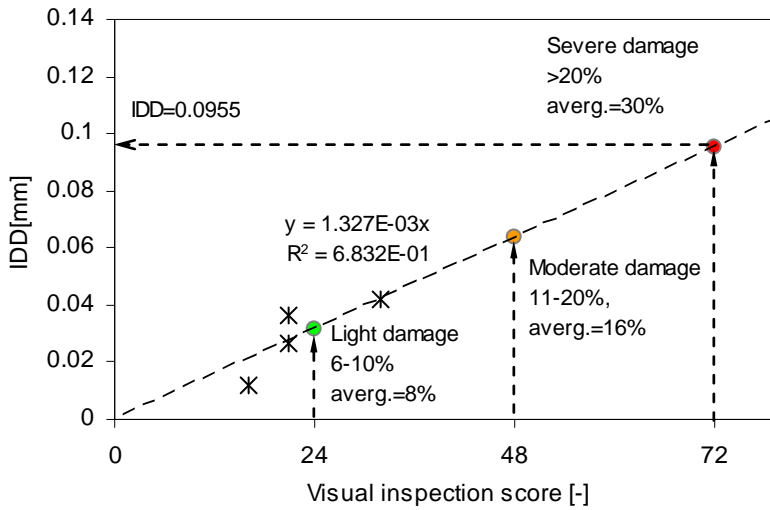


Figure 8.26 Relationship between the visual inspection score, IDD and the amount of ravelling

On the basis of above, the ravelling evolution model is rewritten as the function of IDD .

$$\ln\left(\frac{IDD}{0.318 - IDD}\right) = \beta_0 + \beta_1 \times N \tag{8.12}$$

Equation 8.12 shows that model parameters β_0 and β_1 can be determined by means of least square method if the measurement results of IDD after different load repetitions are available.

At the moment of writing this thesis, only the IDD value after 700000 load repetitions was available. Because of this limitation, the parameters were determined using the following procedure.

- (1) When $N=0$, the amount of ravelling should be zero. However, the model shows its limits at this point. Therefore, it was assumed that the amount of ravelling is fairly very small, i.e. $raf \Rightarrow 0$ when $N=0$. For this reason, $Raf=0.0001\%$ was chosen and this result in $\beta_0 = -13.816$.
- (2) Combining the IDD value after 700000 load repetitions leads to the determination of the other parameter β_1 (see Table 8.15).

Table 8.14 Model parameters and model prediction

Mixture	β_0	$\beta_1 \times 10^{-5}$	$Raf @ N_{LOT} [\%]$	$N @ Raf = 20\%$	$N @ Raf = 75\%$
A	-13.816	1.683	0.00014	7.386E+05	8.863E+05
B	-13.816	1.706	0.00011	7.286E+05	8.743E+05
C	-13.816	1.506	0.00049	8.253E+05	9.903E+05
D	-13.816	1.632	0.00015	7.617E+05	9.140E+05

Figure 8.27 gives the computed ravelling development of the four STUVA mixtures by means of the model parameters given in Table 8.14. As illustrated, the ravelling model is capable to explain the relative ravelling development of the four STUVA mixtures. By combining the LOT computed lives, it is found that except for Mixture C, the model predicted a similar amount of ravelling at the number of load cycles equal to the life expectancy for all other mixtures. The deviation of Mixture C indicates the importance of accurate determination of the model parameters.

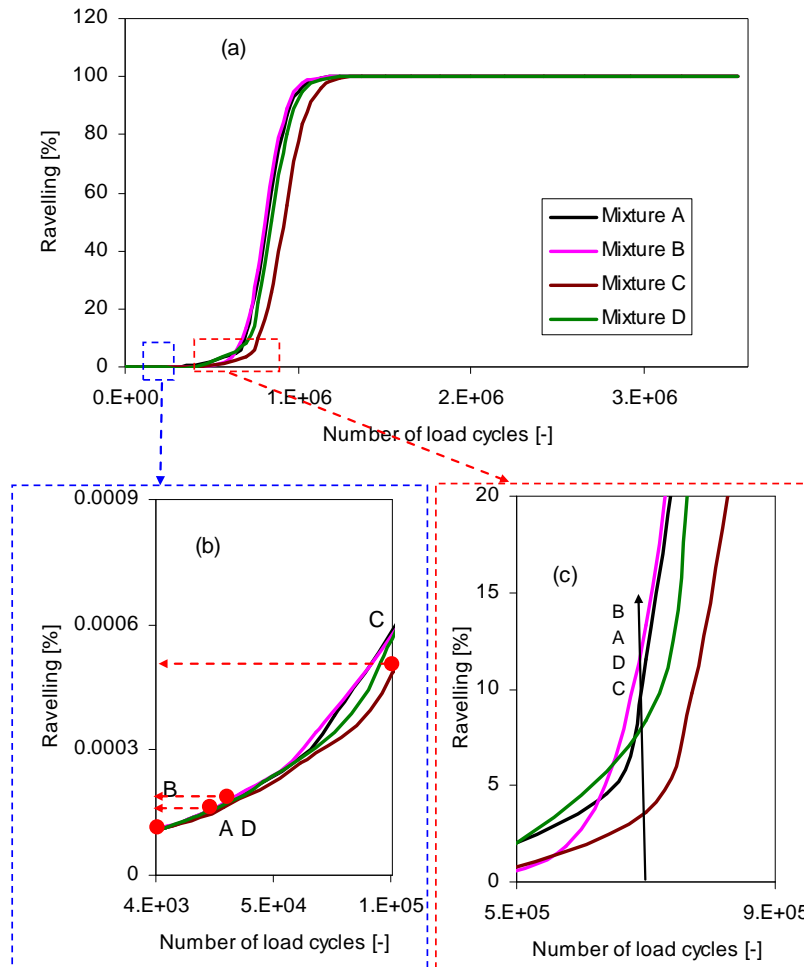


Figure 8.27 Modelled ravelling development of the four STUVA mixtures (a: the overview; b: zoom-in at the number of load cycles equal to the life expectancy; c: zoom-in at 700000 load cycles.)

It must be noted that the above indications are only based on the measurement results of IDD value after 700000 cycles. More data after different load repetitions are needed to come to a conclusion. Despite of the drawback of lacking of data, the model still exhibits its capability on explaining ravelling development.

Therefore, the following was proposed. By rewriting the model, one may obtain a model that allows to predict the lifespan (i.e. when $Raf \approx 100\%$) and the maintenance moment (i.e. when $Raf = 20\%$) as follows

$$N = \frac{\ln\left(\frac{Raf}{100 - Raf}\right) - \beta_0}{\beta_1} \quad (8.13)$$

In Equation 8.13, β_0 could be estimated using the initial condition of $Raf \Rightarrow 0\%$ when $N = 0$, i.e. $\beta_0 = -13.816$. After that, the other parameter β_1 can be determined on the basis of LOT computational results using the following relation:

$$\ln\left(\frac{Raf_0}{100 - Raf_0}\right) = \beta_0 + \beta_1 \times N_{LOT} \quad (8.14)$$

Where:

N_{LOT} = LOT computed life, [cycle];

Raf_0 = the amount damage as ravelling initiates, i.e. $Raf_0 = 0.0002\%$. This value is an average of the four STUVA mixtures

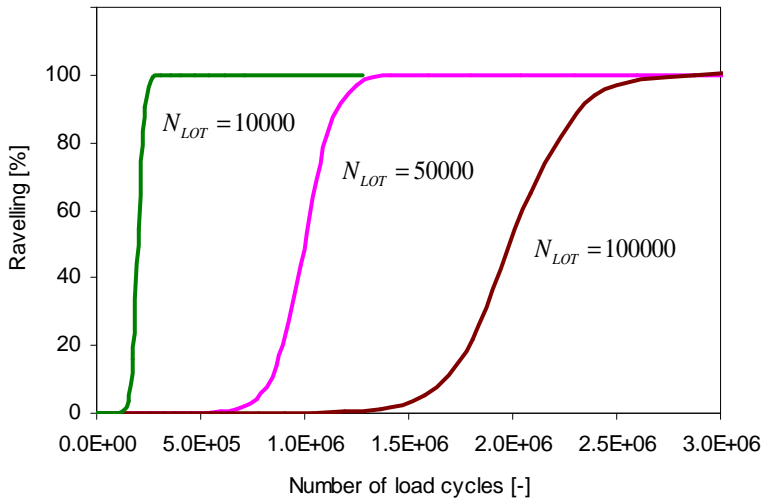


Figure 8.28 Illustration of ravelling models based on LOT computed life

Figure 8.28 gives an illustration of a few models which are based on LOT computed lives. It is clearly shown that the proposed method enables to predict the ravelling development and thus information on the life span or maintenance moment becomes available.

The above was intended to discuss a possible method to correlate the LOT computed life to the actual life. This method takes into account when ravelling initiates and how ravelling develops over time. Validation of the proposed method is very necessary and use can be made of the APT measurement results of IDD after different load repetitions if available.

8.5 Conclusions

A 2D idealized model is used for ravelling analysis of the four STUVA mixtures. Finite element simulations take into account the actual volumetric properties in-situ, the complex tyre-pavement contact stresses and the response of the STUVA mortar as well as the fatigue damage models of the adhesive zone and mortar. Based on the computed results, it is concluded that the developed adhesive zone and mortar fatigue damage models explain the ravelling damage at the STUVA sections well.

The damage model of the adhesive zone is capable of translating complex stress signals into accumulative damage development. The model results in logical life expectancies responsible for the initiation of ravelling at the STUVA sections. The number of cycles to ravelling is computed in a range of 10^3 ~ 10^5 cycles, which is smaller than the total of 700,000 cycles as were applied during APT.

The mortar fatigue model has been demonstrated to be capable to deal with the complex stress and strain signals. Combining the fatigue model with the mortar stress and strain signals leads to reasonable life expectancies due to mortar failure. The life expectancies of the four STUVA mixtures were estimated in a range of 10^4 ~ 10^6 cycles.

The computed live span of mortar bridges is higher than the computed live span of adhesive zones. This is in good agreement with fatigue data from laboratory tests on stone-mortar-stone systems. Indications are that the adhesive zone tends to be the weak link in the stone contact region.

The above leads to the conclusion that the design life due to adhesive failure should be used for evaluation of the ravelling resistance of the four types of mixture used in the STUVA APT sections.


It is concluded that the computed lives of the four STUVA mixtures compare well with the assessment of ravelling damage. In general, a shorter computed life will strongly indicate more ravelling damage.

The final remark is that LOT simulation focuses on the critical stone-to-stone contact region where failure may occur firstly. As a result, LOT simulation explains the initiation of ravelling while visible ravelling damage in real pavements tends to develop over years. Taking this into account it is logical to note that LOT appears to be conservative. The computed life expectancy is not directly related to the actual lifespan of porous asphalt or the maintenance moment. However, a good correlation between these two can be expected when taking into account ravelling evolution.

Appendix 8.1

Ravelling assessment after 7×10^5 load cycles by means of visual inspection

LOT 2-laags ZOAB plaat

Dienst Verkeer en Scheepvaart  Gedetailleerde visuele inspectie

Datum: 10-May-07
 Waarnemer: R.J. van Gent

Rundlaufanlage - STUVA - KEULEN

Toestand
 ■ Fabriekshal
 ■ Kunstlicht
 □

Wegdek
 ■ Droog
 □ Opdrogend
 □ Nat

score: (L=1; M=2; E=3)

Het oppervlak naast de voegovergangen bij de platen is buiten beschouwing gelaten

Even deel van de plaat			Oneven deel van de plaat			
	A	B	C	A	B	C
D4	32	L	0	0		
	31				0	L
D3	30	L	L	0		
	29				L	L
D2	28	E	L	L		
	27				E	L
D1	26	M	0	L		
	25				M	0
SCORE	7	2	2	6	3	1

21

Even deel van de plaat			Oneven deel van de plaat			
	A	B	C	A	B	C
C4	24	L	L	0		
	23				M	L
C3	22	0	0	L		
	21				L	0
C2	20	L	0	0		
	19				L	0
C1	18	M	L	0		
	17				L	L
SCORE	4	2	1	5	2	2

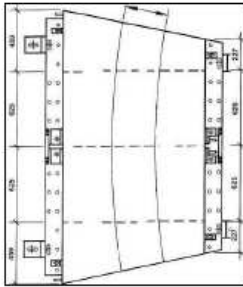
16

Even deel van de plaat			Oneven deel van de plaat			
	A	B	C	A	B	C
B4	16	M	L	L		
	15				M	L
B3	14	M	M	L		
	13				M	L
B2	12	M	M	0		
	11				M	L
B1	10	E	M	L		
	9				M	0
SCORE	9	7	3	8	3	2

32

Even deel van de plaat			Oneven deel van de plaat			
	A	B	C	A	B	C
A4	8	M	0	0	M	L
	7					
A3	6	L	L	0	0	L
	5					
A2	4	M	L	0	L	0
	3					
A1	2	M	M	L	M	L
	1					
SCORE	7	4	1	5	3	1

21



gat buiten inspectiegebied

vreemde schuine streep over plaat

ERNST VAN DE RAFELING
 0: geen schade
 L: af en toe een steentje weg
 M: één of meer clusterjes weg
 E: een spoor steentjes weg

PLAATS OP DE PLAAT
 A = rafeling langs buitenrand band
 B = rafeling onder de band
 C = rafeling langs binnenrand band

Note: the wheel track of each mixture was subdivided into 24 (4x2x3) smaller subsections.

9 CONCLUSIONS & RECOMENDATIONS

9.1 Introduction

In this final chapter the main conclusions of this research are summarized and some recommendations are given respectively in the following three parts: experimental work, fatigue/damage models and model application and verification.

9.2 Conclusions

9.2.1 *Conclusions related to experimental work*

- It was shown that test specimens at meso-scale for adhesive zone and mortar testing can be produced successfully and tested.
- The adhesive zone and mortar fatigue behaviour at meso-scale can be captured by utilisation of the DMA and DSR instruments.
- The idealized adhesive zone represented by two stone columns glued by a thin bitumen interlayer can well explain the behaviour of the region where the mortar meets the stone surface, i.e. the adhesive zone.
- Mechanics analysis at micro-scale showed that complex stress distributions develop in the adhesive zone due to stone surface morphology.
- The stone-mortar-stone system can successfully be used to identify the weak link, e.g. cohesive failure or adhesive failure that will cause ravelling in the stone contact region.

9.2.2 *Conclusions related to fatigue/damage models*

- The equivalent uniaxial tensile stress on the basis of the internal-friction theory taking into account both normal and shear stresses, is a good indicator of the stresses that actually occur.
- The adhesive zone damage model is based on the linear damage accumulation rule combined with the equivalent uniaxial tensile stress. Model parameters can be obtained by combination of commonly used uniaxial tensile tests and shear tests. Model validation can be done using test data obtained under combined normal and shear stresses.
- The damage development of the adhesive zone is sensitive to temperature.
- The adhesive zone exhibits two failure mechanisms; adhesive failure at the bitumen-stone interface and cohesive failure within the thin bitumen interlayer. Adhesive failure becomes predominant at low temperatures and after aging.
- A mortar fatigue model can be described using models based on dissipated energy.
- Although incorrect in principle, the dissipated energy per cycle in the initial phase of fatigue tests is a much more practical indicator for fatigue life determination purposes than the total energy dissipated during a fatigue test.
- Since a mortar fatigue model based on the initial dissipated energy per cycle was adopted, effects of complex stress and strain signals can be taken into account.

9.2.3 Conclusions related to model application and verification

- The ranking of life expectancy explained by LOT is in good agreement with the results of full scale tests in which ravelling was introduced by a real truck tyre travelling at 80 km/h.
- The potential type of failure (i.e. adhesive v.s. cohesive failure) is predictable by comparing the live span of mortar bridges to adhesive zones. The prediction can be verified by laboratory tests on stone-mortar-stone systems and/or the real pavement performance in-situ.
- It has been shown that it is possible that ravelling is a type of mixture damage that may be introduced by repeated mechanical action only.
- Pavement life as expected by LOT is approximately 3% to 10% of the real life time at which 20% ravelling occurs.
- It has been shown that LOT is an excellent tool to rank the performance of mixtures.

9.3 Recommendations

9.3.1 Recommendations related to experimental work

- It was found that stone morphology plays an important role in the adhesive zone performance. It is therefore recommended to further improve the protocol for adhesive zone specimen preparation such that specimens with a known and realistic morphology are obtained.
- For the purpose of material optimization, more adhesive zone tests are required to reduce the effect of data scatter.
- It is recommended to apply a more severe protocol for water immersion in the future. A study into determination of the most realistic protocol should precede any decision on this point. This protocol should include effect of freeze-thaw cycles and allow sufficient time for diffusion.
- Since local stress concentration (i.e. 9.82% higher than the uniform stress) occurs in the mortar specimen, it is recommended to redesign the mortar specimen by means of finite element simulation.
- Repeated load uniaxial tensile tests on a more powerful DMA instrument with a load capacity larger than 100N are recommended for mortar fatigue.

9.3.2 Recommendations related to fatigue/damage models

- The parameters of the adhesive zone damage model show temperature dependency. It is thus recommended to develop a generalized damage model by taking into account this dependency. Hereto test data obtained over a wide range of temperatures and on various bitumen-stone combinations should be generated.
- The effect of friction in the adhesive zone due to direct stone surface contact should be investigated.
- Improvements of the available adhesive zone damage model should consider the healing effect of compressive adhesive zone stresses.
- Since the DSR instrument proved to be capable of performing combined normal-shear tests, it is recommended to apply such tests for quick parameter determination. This will reduce the required number of time-consuming fatigue

tests.

- The mortar fatigue model should be used with some care since it has not been validated against data at other stress conditions that differ from shear. Bending and uniaxial tensile tests are thus recommended for the purpose of model validation. In particular, the effect of compressive stress on fatigue damage should be distinguished from the effect of tensile and shear stresses.
- The parameters of the mortar fatigue model developed show limited variation with frequency, temperature and aging. It should be noted that this observation is based on test data for one type of mortar only. Indications are that a universal dissipated energy based fatigue model for asphalt mixtures exists. On the basis of the previous it is recommended that tests on various types of mortar are performed to establish a generalized mortar fatigue model.

9.3.3 Recommendations related to model application and verification

- LOT is susceptible for mixture geometry which is amongst others indicated by mixture compaction. Because of this significant differences exist between LOT calculations on the basis of mixture design inputs and calculations on the basis of in situ mixture inputs. It is thus recommended that performance assessment should also take into account the quality of construction by consideration of the in situ mixture volumetric composition instead of the mixture recipe.
- Since LOT computed life is not directly related the actual life span, it is recommended to set up the relation between these two values on the basis of the ravelling development of the four STUVA mixtures if available.
- LOT should be further validated at extremely low and high temperatures since these temperatures may be critical for ravelling damage.

References

- ABAQUS (2006). ABAQUS User's Manual, Version 6.6.
- Airey GD, Brown SF (1998). Rheological performance of aged polymer modified bitumens. *Journal of the Association of Asphalt Paving Technologists* 67:66–100.
- Aleksander K, Ewald M (2005). A Review of critical plane orientations in multiaxial fatigue failure criteria of metallic materials, *International Journal of Fracture*, 134 (2005):267-304.
- Amoz BM (1990). A cumulative damage theory for fatigue life prediction, *Engineering Fracture Mechanics* 37(2): 341-347.
- Anderson DA, Cristensen DW, Bahia HU, Dongre R, Sharma MG, Antle CE, Button J (1994). Binder characterization and evaluation volume 3: physical characterization, SHRP-A-369, National Research Council, Washington DC.
- Andrews RM, Brown MW (1989). Elevated temperature out-of-phase fatigue behaviour of a stainless steel. *Biaxial, Multiaxial Fatigue*, Publication 3, London.
- Anton Paar Ltd, <http://www.anton-paar.com>.
- Anton Paar Ltd, DSR MCR 301 User's Manual.
- Babcock GB, Statz RJ, Larson DS (1998). Study of asphalt binders using lap shear bonds. Technical report, E.I. DuPont de Nemours Inc., Wilmington, Delaware.
- Bahia HU, Hanson DI, Zeng M, Zhai H, Khatri MA, Anderson RM (2001). Characterization of modeified asphalt binders in Superpave mix design, NCHRP report 459, National Academy press, Washington D.C.
- Beer De M, Fisher C, Jooste FJ (1997). Determination of pneumatic tyre/pavement interface contact stresses under moving loads and some effects on pavements with thin asphalt surfacing layers, *Proceedings of 8th international conference on asphalt pavements*, Seattle, USA.
- Blab R (1999). Introducing improved loading assumptions into analytical pavement models based on measured contact stresses, *Proceedings of 3rd International Conference Accelerated Pavement Testing*, Reno, NV, 1999.
- Bourne SJ, Willemsse EJ (2001). Elastic stress control on the pattern of tensile fracturing around a small fault network at Nash Point, UK, *Journal of Structural Geology* 23, 1753–1770.
- Broek D (1991). *Elementary Engineering Fracture Mechanics*. Boston: Kluwer Academic Publishers.
- Cao TW (2007). Investigation of the mechanical behavior of asphalt-aggregate adhesion, Master thesis, Wuhan University of Technology.
- Chang WV (1994). Application of acoustic emission to study the cohesive and adhesive strength of asphalt, SHRP-A-682, National Research Council, Washington DC.
- Copeland A, Youtcheff J, Kringos N, Scarpas A, Mahadevan S (2006). Determination of bond strength as a function of moisture content at the aggregate-mastic interface, 10th International Conference of Asphalt Pavements, Canada, vol.1, pp.709-718.
- Copeland A, Youtcheff J, Kringos N, Scarpas A, Mahadevan S (2006). Determination of Bond Strength as a Function of Moisture Content at the Aggregate-Mastic Interface, 10th International Conference on Asphalt Pavements, pp.709-718.
- Copeland AR, Youtcheff JS, Shenoy A (2007). Moisture Sensitivity of Modified Asphalt Binders: Factors Influencing Bond Strength, 86th Transportation Research Board.
- Copeland AR (2007). Influence of moisture on bond strength of asphalt-aggregate systems, Ph.D thesis, Vanderbilt University.
- Dimov DM, Andonova MM (1995). Fatigue life prediction of pressure vessels using an energy based approach, *Strength of material*, 27:75-81.
- Ellyin F, Xia Z (1993). A general fatigue theory and its application to out-of-phase cyclic

- loading, *Journal of Engineering Materials and Technology*, 115(1993):411-416
- Ellyin F, Golos K (1988). Multiaxial fatigue damage criterion. *Journal of Engineering Materials and Technology*, 101:63-68
- Elvik R, Greibe P (2005). Road safety effects of porous asphalt: a systematic review of evaluation studies. *Accident Analysis & Prevention*, 37(3): 515-522
- Erber T (1993). Hysteresis and Fatigue, *Annals of Physics*, 224:157-192.
- Fatemi A, Yang L (1998). Cumulative fatigue damage and life prediction theories: a survey of the state of the art for homogeneous materials, *International Journal of Fatigue*, 20(1): 9-34.
- Frolov AF, Vasieva VV, Frolova EA, Ovchinnikova VN (1983). Strength and structure of asphalt films, *Chemistry and Technology of Fuels and Oils*, 19 (8):415- 419.
- Frolov AF, Frolova EA, Stepanov AG, Kanevskii IM (1984). Models of asphalt film in asphaltic concrete - film structure and strength, *Chemistry and Technology of Fuels and Oils*, 20(9): 456-459.
- Garud YS (1981). A new approach to the evaluation of fatigue under multiaxial loadings. *Journal of Engineering Materials and Technology*, 103:118-125
- Garud YS (1981). Multiaxial fatigue: a survey of the state-of-the-art. *Journal of Test and Evaluation*, 9:165-178.
- Hagos ET (2008). The effect of aging on binder properties of porous asphalt concrete aging, PhD thesis, Civil Engineering & Geosciences, Delft University of Technology.
- Heukelom W, Wijga P(1973). Bitumen testing: an introduction to the use of test methods at the Koningkijke/Shell-Laboratorium, Amsterdam.
- Hofstede J (2007). Test results of dynamic shear-normal tests with bitumen at different temperatures, Adhesion Institute, Delft University of Technology, Netherlands.
- Hopman PC, Pronk Ac, Kunst PAJC, Molenaar AAA, Molenaar JMM (1992). Application of the visco-elastic properties of asphalt concrete. *Proceedings of the 7th International Conference on Asphalt pavements*, Nottingham, 1:73-88.
- Huurman M, Milne TI, van de ven MFC, Scarpas A (2003). Development of a structure FEM for road surfacing seals, ICCES, Corfu, Greece.
- Huurman M, Mo LT, Molenaar AAA, Wu SP (2006). Ravelling in porous asphalt concrete, Road Construction Conference in Ede, the Netherlands.
- Huurman M, Mo LT (2007). Lifetime Optimisation Tool, Fatigue in mortar and adhesive zones; measurements, test interpretation and determination of model parameters, Delft University of Technology, Laboratory of Road and Railway engineering, Report 7-07-170-2, the Netherlands.
- Huurman M, Mo LT (2007). Lifetime Optimisation Tool, User's Guide, Delft University of Technology, Laboratory of Road and Railway engineering, Report 7-07-170-5, The Netherlands.
- Huurman M, Woldekidan MF (2007). Mortar response; measurement, test interpretation and determination of model parameters, Report 7-07-170-3, September 2007, Delft University of Technology, the Netherlands.
- Huurman M (2008). Lifetime Optimisation Tool, LOT, Main Report, Report 7-07-170-1, Delft University of Technology, the Netherlands.
- Huurman M, Molenaar A., van Reizen F, Hofman R, Schreyer J (2008). Accelerated testing of double layer porous asphalt wearing courses, APT'08 Program & Proceedings. Madrid.
- Hwang W, Han Sk (1986). Cumulative damage model and Multi-stress fatigue life prediction, *Journal of Composite Materials*, 20:125-153.
- Jaeseung K, Roque R, Birgisson B (2006). Interpreting dissipated energy from complex modulus data, *Road Materials and Pavement Design*, 7 :223-245
- Kanitpong K, Bahia H (2003). Role of adhesion and thin film tackiness of asphalt binders in moisture damage of HMA, *Journal of the Association of Asphalt Paving Technologists*

- 72:502-528.
- Kanitpong K, Bahia H (2004). Test method to determine aggregate/asphalt adhesion properties as an indication of potential susceptibility to moisture damage, The Wisconsin Highway Research program, The Wisconsin Department of Transportation, February, 2004.
- Kanitpong K, Bahia H (2005). Relating adhesion and cohesion of asphalts to effect of moisture on laboratory performance of asphalt mixtures, Transportation Research Record, 1901:33-43.
- Khalid GA, Carpenter SH (2006). Fatigue damage analysis in asphalt concrete mixtures using the dissipated energy approach, Canada Journal of Civil Engineering, 33:890-901
- Khattak MJ, Baladi GY, Drzal LT (2007). Low temperature binder-aggregate adhesion and mechanistic characteristics of polymer modified asphalt mixtures, Journal of Materials in Civil Engineering, 19 (5):411-422.
- Khedoe RN, Moraal J (2007). Sample preparation and laboratory testing for the LOT research program, Report 7-07-170-4, Delft University of Technology.
- Khedoe R, Moraal J (2008). Lifetime Optimisation Tool, additional laboratory testing for validation purposes, Delft University of technology, Laboratory of Road and Railway engineering , Report 7-07-170-6.
- Lachowicz CT (2001). Calculation of the elastic-plastic strain energy density under cyclic and random loading, International Journal of Fatigue, 23:643-652.
- Lagoda T, Ogonowski P (2005). Criteria of multiaxial random fatigue based on stress, strain and energy parameters of damage in the critical plane, Materialwissenschaft und Werkstofftechnik. 36:429-437
- Lee BL, Kim KS, Nam KM (2003). Fatigue analysis under variable amplitude loading using an energy parameter, International Journal of Fatigue, 25(2003): 621-631
- Little D, Jones D (2003). Chemical and Mechanical Processes of Moisture Damage in Hot-Mix Asphalt Pavements, Moisture Sensitivity of Asphalt Pavements: A National Seminar, San Diego, CA, Transportation Research Board.
- Lopez A, Steen R (2007), Prediction of Tyre/Road Contact Stress Distributions. Report DCT 2007.106, Dynamics and Control Group, Eindhoven University of Technology, Eindhoven , The Netherlands.
- Macha E, Sonsino CM (1999). Energy criteria of multiaxial fatigue failure, Fatigue & Fracture of Engineering Materials & Structures, 22: 1053-1070
- Mack C (1957). Physical properties of asphalts in thin films, Industrial and Engineering Chemistry, 49(3):422-427.
- Majidzadeh K, Herrin M (1965). Modes of failure and strength of asphalt films subjected to tensile stresses, Highway Research Record, 67:98-121.
- Marek CR, Herrin M (1968). Tensile behavior and failure characteristics of asphalt cements in thin film. Proceedings of the Association of Asphalt Paving Technologists 37: 387-421.
- Milne TI, Huurman M, van de ven MFC, Jenkins KJ, Scarpas A, Kasbergen C (2004). Towards mechanistic behavior of flexible road surfacing seals using a prototype FEM model, Eighth Conference on Asphalt Pavements for South Africa, Sun City.
- Miner MA (1945). Cumulative damage in fatigue, Journal of Applied Mechanics 67: A159-A164.
- Miradi M (2004). Neural network models predict ravelling and analyse material/construction properties, Proceedings of the 6th IASTED International Conference, Hawaii, USA.
- Miradi M, Molenaar AAA (2006). Application of artificial neural network (ANN) to PA lifespan: forecasting models. IEEE World Congress on Computational Intelligence. Canada.
- Miradi M (2009). Knowledge discovery and pavement performance, intelligent data mining, Ph.D thesis, Civil Engineering and Geosciences, Delft University of Technology.
- Mo LT, Huurman M, Wu SP, Molenaar AAA, T.W. Cao TW (2006). Damage accumulation model for monotonic and dynamic shear fracture of asphalt-stone adhesion, Theoretical

- and Applied Fracture Mechanics, 46(2):140-147.
- Mo LT (2007). Tensile failure and fatigue of asphalt-aggregate adhesion, Lab report, Wuhan University of Technology.
- Mo LT, Huurman M, Wu SP, Molenaar AAA (2007). Finite element analysis and experimental study on tensile fatigue behaviour of asphalt-stone adhesion, Fatigue and fracture engineering materials and structure, 30(9): 823 - 831
- Mo LT, Huurman M, Wu SP, Molenaar AAA (2007). Investigation into stress states in porous asphalt concrete on the basis of FE-modelling, Finite Element Analysis and Design, 43(4):333-343.
- Mo LT, Huurman M, Wu SP, Molenaar AAA (2008). 2D and 3D meso-scale finite element models for ravelling analysis of porous asphalt concrete, Finite Element Analysis and Design, 44 (4):186-196.
- Mo LT, Huurman M, Wu SP, Molenaar AAA (2009). Ravelling investigation of porous asphalt concrete based on fatigue characteristics of bitumen-stone adhesion and mortar, Materials and Design, 30:170-179.
- Molenaar AAA (2007). Road material: Part III Asphalt materials, Lecture note CT 4850. Delft University of Technology, the Netherlands.
- Molenaar AAA, Meerkerk AJJ, Miradi M, van der Steen T (2006) Performance of porous asphalt concrete. Journal of Association of Asphalt Paving Technologists, 75:1053-1094.
- Muraya PM (2007). Permanent deformation of asphalt mixes, PhD thesis, Civil Engineering & Geosciences, Delft University of Technology,.
- Nguyen T, Byrd E, Bentz D, Seiler J (1996). Development of a method for measuring water-stripping resistance of asphalt/siliceous aggregate mixtures, NISTIR 5865, Transport Research Board, National Research Council, Washington D.C..
- Nielsen CB (2006). Durability of porous asphalt - international experiences, Danish Road institute technical note 41, Road ministry of transport and Energy, Denmark.
- Nielsen CB, Bendtsen H (2006). Noise reducing pavements-evaluation workshop, Road Directorate, Danish Road Institute. ISBN 87-91177-96-0
- Nielson CB (2007). Ravelling of porous asphalt pavements assessment of test sections, Road Directorate, Denmark, 2007.
- Nielsen CB, Raaberg J, Van Vliet D (2007). Microstructural characterization of porous pavements, Advanced Characterization of Pavement Soil Engineering Materials, 1-2: 791-801
- Palmgren A (1924). Die Lebensdauer von Kugellagern. Verfahrenstechnik, Berlin, 68:339-341.
- Pronk AC, Hopman PC (1990). Energy dissipation: the leading factor of fatigue, Highway Research: Sharing the Benefits, Proceedings of the Conference of the United States Strategic Highway Research Program, London.
- RWTH Aachen (2007) Institut für Straßenwesen Aachen, Lifetime Optimisation Tool (LOT), Schlussbericht.
- Scarpas A (1993). CAPA Finite Elements System-Version 2.6, FEMA User's Manual, Faculty of Civil Engineering, Delft University of Technology, Delft, Netherlands, 1993
- Seitz n, Hußmann AW (1971). Force and displacements in contact area of free rolling tires, Precedings SAE inc. No. 710626, Montreal.
- Swart JH (1997). Experience with porous asphalt in the Netherlands, European conference on porous asphalt, Madrid, Spain 1997.
- Shell Bitumen (2003), Cariphalte XS, Multi-purpose elastomeer gemodificeerd bindmiddel, Poducinformate 1539NL01
- Shen SH, Carpenter SH (2005). Application of the dissipated energy concept in fatigue endurance limit testing, Journal of the Transportation Research Board, 1929:165-173.
- Sisko AW (1968). Tensile strength of asphalt films and road life, Highway Research Record, 231:62-67.
- Sugimoto T, Sasaki Y (2006). Effect of loading frequency on fatigue life and dissipated energy

- of structural plywood under panel shear load, *Wood Science and Technology*, 40: 501–515
- Sweere GTH, van Zwieten J, Eijbersen MJ, huipen H. Wegerhardingen op termijn bekeken, Technisch verslag SHRP-NL periode 1990-1995.
- TA Instruments, DMA User's Manual
- TA Instruments, DSR User's Manual
- van der Zwan J, Goeman T, Gruis H, Swart J, Oldenburger R (1990). Porous asphalt wearing courses in the Netherlands: state of the art review, *Transportation Research Record* 1265:95-110.
- van Dijk W (1975). Practical fatigue characterization of bituminous mixes, *Journal of the Association of Asphalt Paving Technologists*, 62:38-74.
- van Lent D (2008). Aggregate characterization in relation to bitumen-aggregate adhesion. Master's thesis, Delft University of Technology, the Netherlands.
- van Hinthem PE (2008). LOT-rundlauffanage, vervaardiging en transport asfaltproefplaten, Heijmans infra.
- Wiki, Harmonic oscillator; http://en.wikipedia.org/wiki/Harmonic_oscillator
- Wiki, Poisson's ratio; http://en.wikipedia.org/wiki/Poisson's_ratio
- Wiki, Young's modulus; http://en.wikipedia.org/wiki/Young%27s_modulus
- Wu SP, Pang L, Mo LT, Chen YC, Zhu GJ (2009). Influence of aging on the evolution of structure, morphology and rheology of base and SBS modified bitumen, *Construction and Building Materials*, 23(2):1005-1010.
- Yan XL, Liang CY (2001). Study of the shear adhesiveness between bitumen and rock. *China Journal of Highway Transport*, 14:25-29.
- Youtcheff J, Aurilio V (1997). Moisture sensitivity of asphalt binders: evaluation and modeling of the pneumatic adhesion test results, 42nd Annual Conference of Canadian Technical Asphalt Association, Ottawa, Ontario, Polyscience Publications Inc.

CURRICULUM VITAE

- May 18th 1979: Born in Wuming county, Nanning city, Guangxi Zhuang Autonomous Region, China
- September 1992-
July 1995: Wuming Junior High School, Guangxi Zhuang Autonomous Region, China
- September 1995-
July 1998: Wuming Senior High School, Guangxi Zhuang Autonomous Region, China
- September 1998-
July 2002: Bachelor at Materials Science & Engineering, Wuhan University of Technology, P.R. China.
Thesis entitled " Mix and Structure Design of Asphalt Pavement in Xiangfan-Shiyan Freeway, Hubei Province "
- September 2002-
July 2004: Master at Materials Science & Engineering, Wuhan University of Technology, P.R. China.
Thesis entitled " Preparation and Research of Electrically Conductive Asphalt Concrete "
- Since June 2005: Ph.D research at Road & Railway Engineering, Delft University of Technology (65%) carried out in cooperation with Key Laboratory for Silicate Materials Science and Engineering of Ministry of Education, Wuhan University of Technology (35%)

Publications related to this Ph.D research

- [1] Huurman M, **Mo LT**, Woldekidan MF. Mechanistic design of silent asphalt mixtures and its validation, accepted for presentation and publication by AAPT 2010.
- [2] **Mo LT**, Huurman M, Wu SP, Molenaar AAA (2009). Fatigue characteristics and damage model development of bitumen-stone adhesive zone, TRB 88th Annual Meeting, Washington DC.
- [3] **Mo LT**, Huurman M, Wu SP, Molenaar AAA (2009). Ravelling investigation of porous asphalt concrete based on fatigue characteristics of bitumen-stone adhesion and mortar, *Materials & Design*, 30(1):170-179.
- [4] **Mo LT**, Huurman M, Wu SP, Molenaar AAA (2008). 2D and 3D meso-scale finite element models for ravelling analysis of porous asphalt concrete, *Finite Element Analysis and Design*, 44 (4):186-196.
- [5] **Mo LT**, Huurman M, Wu SP, Molenaar AAA (2007). Investigation into stress states in porous asphalt concrete on the basis of FE-modelling, *Finite Element Analysis and Design*, 43(4):333-343.
- [6] **Mo LT**, Huurman M, Wu SP, Molenaar AAA (2007). Finite element analysis and experimental study on tensile fatigue behaviour of asphalt-stone adhesion, *Fatigue and Fracture Engineering Materials and Structure*, 30(9): 823 - 831
- [7] Huurman M, **Mo LT**, Woldekidan MF, Medani TO (2007). Advanced pavement analysis techniques, 9th Conference on Asphalt Pavements for South Africa (CAPSA), Botswana.
- [8] Huurman M, **Mo LT** (2007). Lifetime Optimisation Tool, Fatigue in mortar and adhesive zones; measurements, test interpretation and determination of model parameters, Delft University of Technology, Laboratory of Road and Railway engineering, Report 7-07-170-2, the Netherlands.
- [9] Huurman M, **Mo LT** (2007). Lifetime Optimisation Tool, User's Guide, Delft University of Technology, Laboratory of Road and Railway engineering, Report 7-07-170-5, the Netherlands.
- [10] **Mo LT**, Huurman M, Wu SP, Molenaar AAA, Cao TW (2006). Damage accumulation model for monotonic and dynamic shear fracture of asphalt-stone adhesion, *Theoretical and Applied Fracture Mechanics*, 46(2):140-147.
- [11] Huurman M, **Mo LT**, Molenaar AAA, Wu SP (2006). Ravelling in porous asphalt concrete, Road Construction Conference in Ede, the Netherlands.

PROPOSITIONS

1. Although roads can be designed on the basis of many of the known, they are paved with miles of the unknown.
2. The assumption that ravelling is a type of surface defect and thus has nothing to do with the pavement structure is incorrect.
3. A material model provides more valuable information than individual measurements do.
4. Fatigue characterization of bituminous materials without taking into account the shape of the load signal and the load history is an unnecessary and incorrect simplification of reality.
5. Life is not easy even for a lazy person.
6. It is not who you know, it is who knows you. *[Jeffrey Gitomer. Little Black Book of Connections]*
7. Doing Ph.D research is a great job. It is a continuing learning process with a lot of challenges and surprises, and you even get paid.
8. China is changing, but can't change instantly since it has a history of more than five thousand years, which bears great influence on the Chinese people.
9. When the creditor lends the debtor one Euro the latter normally needs to pay back one Euro or more. Such a rule does not always exist at the level of nations. China is the largest creditor country to the United States of America. However, this debtor nation has tricky ways to return less.
10. The current financial crisis is a good example of the fact that the global problems facing the world today are not at all things beyond our control. Instead, all the global threads facing us today are problems entirely of our own making.

The propositions are considered opposable and defensible and as such have been approved by the promoters Prof. dr. ir. A.A.A. Molenaar and Prof. dr. S.P. Wu.

STELLINGEN

1. Hoewel wegen ontworpen kunnen worden op basis van bestaande kennis, zijn ze verhard met kilometers aan ontbrekende kennis.
2. De aanname dat rafeling een oppervlakschade is, en dus geen relatie vertoont met de verhardingsconstructie, is niet correct.
3. Een materiaalmodel geeft meer waardevolle informatie dan individuele metingen.
4. De bepaling van de vermoeiingseigenschappen van bitumineuze materialen zonder rekening te houden met de vorm van het lastsignaal en de belastinggeschiedenis is een onnodige en een onjuiste vereenvoudiging van de werkelijkheid.
5. Het leven is niet gemakkelijk, zelfs niet voor een lui persoon.
6. Het gaat er niet om wie jij kent, het gaat erom wie jou kent.
7. Het verrichten van promotie-onderzoek is een geweldige baan. Het is een continu leertraject met veel uitdagingen en verrassingen waarvoor je ook nog betaald wordt.
8. China verandert, maar dat kan niet instantaan. Haar geschiedenis van meer dan vijf duizend jaar heeft hiervoor te veel invloed op de Chinese bevolking.
9. Als een crediteur één Euro leent aan een debiteur, dan zal de laatste over het algemeen minimaal één Euro moeten terugbetalen. Deze regel geldt niet altijd op het niveau van naties. China is de grootste crediteur van de Verenigde Staten van Amerika. Deze debiteur heeft echter sluwe manieren om minder terug te betalen.
10. De huidige financiële crisis is een goed voorbeeld van het feit dat de wereldwijde problemen die ons bedreigen, zeker niet buiten onze controle vallen. Integendeel, alle huidige wereldwijde problemen zijn volledig door ons gecreëerd.

Deze stellingen worden oponeerbaar en verdedigbaar geacht en zijn als zodanig godgekeur door de promotors, Prof. dr.ir A.A.A. molenaar en Prof. dr. S.P.Wu.